East European Journal of Physics

East European Journal of Physics

ORIGINAL PAPERS

East European Journal of Physics

NONLINEAR DYNAMO IN OBLIQUELY ROTATING STRATIFIED ELECTROCONDUCTIVE FLUID IN AN UNIFORMLY MAGNETIC FIELD

Michael I. Kopp[a]*, Anatoly V. Tur[c], Konstantin N. Kulik[a], Volodymyr V. Yanovsky[a,b]*

[a]Institute for Single Cristals, Nat. Academy of Science Ukraine,
Nauky Ave. 60, Kharkiv 31001,Ukraine
[b]V.N. Karazin Kharkiv National University
4, Svoboda Sq., Kharkiv, 61022, Ukraine
[c]Universite Toulouse [UPS], CNRS, Institute of Research for Astrophysics and Planetology
9 avenue du Colonel Roche, BP 44346, 31028 Toulouse Cedex 4, France
*Corresponding Author: michaelkopp0165@gmail.com
Received December 20, 2018; revised January 22, 2020; accepted January 28, 2020

In this paper, we investigated a new large-scale instability that arises in an obliquely rotating convective electrically conducting fluid in an external uniform magnetic field with a small-scale external force with zero helicity. This force excites small-scale velocity oscillations with a small Reynolds number. Using the method of multiscale asymptotic expansions, we obtain the nonlinear equations for vortex and magnetic disturbances in the third order of the Reynolds number. It is shown that the combined effects of the Coriolis force and the small external forces in a rotating conducting fluid possible large-scale instability. The linear stage of the magneto-vortex dynamo arising as a result of instabilities of α -effect type is investigated. The mechanism of amplification of large-scale vortex disturbances due to the development of the hydrodynamic α - effect taking into account the temperature stratification of the medium is studied. It was shown that a «weak» external magnetic field contributes to the generation of large-scale vortex and magnetic perturbations, while a «strong» external magnetic field suppresses the generation of magnetic-vortex perturbations. Numerical methods have been used to find stationary solutions of the equations of a nonlinear magneto-vortex dynamo in the form of localized chaotic structures in two cases when there is no external uniform magnetic field and when it is present.
KEY WORDS: equations of magnetic hydrodynamics in Boussinesq approximation, Coriolis force, multi-scale asymptotic expansions, small-scale non-helical turbulence, α -effect, chaotic structures

As is known, the problems of generation of magnetic fields of planets, stars, galaxies and other space objects are studied within the framework of dynamo theory. For the first time, the term «dynamo» in connection with the generation of magnetic fields is introduced by Larmor [1]. In his opinion, hydrodynamic motion of an electroconductive fluid could engender a magnetic field by acting as the dynamo. In the linear theory or kinematic dynamo with the small magnetic energy compared to the medium motion kinetic energy, the magnetic forces hardly influence the medium flow. Currently, the kinematic theory of dynamo is practically built [2-11]. In this theory a significant role belongs to rotational motion of space bodies which generates various waves (e.g. Rossby or inertial waves) and vortex motions (geostrophic, etc. [12-19]). In particular, under the influence of the Coriolis force the initial mirror-symmetric turbulence turns into helical one characterized by breakdown of the mirror symmetry of the turbulent fluid motion. The invariant $J_s = \overline{\vec{v} rot \vec{v}}$ is the important topological characteristic of helical turbulence. It measures the knottedness of vortex field force lines [20]. It was shown in [21] that the generation of large-scale field occurs under the action of turbulent e.m.f. proportional to the mean magnetic field $\vec{\varepsilon} = \alpha \overline{\vec{H}}$. Coefficient α is proportional to the mean helicity of the velocity field $\alpha \sim \overline{\vec{v} rot \vec{v}}$ and is so called α -effect. The generation properties of helical turbulence were considered not only in magnetic hydrodynamics or in electroconductive media, but in conventional hydrodynamics as well. For the first time the hypothesis that helical turbulence may generate large-scale vortices was reported in [22]. It was based on the formal similarity of the equations of magnetic field induction $\vec{H}$ and those for vorticity $\vec{\omega} = rot \vec{v}$.

However, as proved in [23], the α -effect cannot occur in an incompressible turbulent fluid because of the symmetry of the Reynolds stress tensor in the averaged Navier-Stokes equations. Thus, for the appearance of the hydrodynamic α -effect, one helicity of turbulence is not enough, other factors of symmetry breaking of turbulent flow are needed. As shown in [24] and [25], these factors are compressibility and temperature gradient in gravitational field, respectively. The effect of generation of large-scale vortex structures (LSVS) by helical turbulence is called vortex dynamo. The vortex dynamo mechanisms were developed with reference to the turbulent atmosphere and ocean. The theory of convective vortex dynamo was built in [25-31].

According to this theory, helical turbulence gives rise to a large-scale instability leading to the formation of a convective cell interpreted as a huge vortex of tropical cyclone type. There are many papers which deal with LSVS

generation and take into account the effects of the rotation [32-37]. Just another α -effect is reported in [38], where turbulent fluid motion is modelled by means of an external small-scale force $\vec{F}_0$. This model is characterized by parity violation (at zero helicity: $\vec{F}_0 rot \vec{F}_0 = 0$). The effect of generation of large-scale disturbances by such a force is called anisotropic kinetic α -effect, or AKA-effect [38]. The mentioned paper consideres the large-scale instability in an incompressible fluid by means of the method of asymptotic multi-scale expansions. This method uses the Reynolds number $R = \frac{v_0 t_0}{\lambda_0} \ll 1$ as a small parameter for small-scale pulsations of the velocity v_0 caused by the small-scale force. In real situations, because of the low kinematic viscosity, the Reynolds number number is large. However, in reality, the small scale turbulence generates turbulent viscosity. The Reynolds number calculated with this turbulent viscosity is not large $R = \frac{v_0 t_0}{\lambda_0} \ll 1$. For this reason, the theory presented below can be applied approximately to real objects.

It is evident that applicability of kinematic theory of magnetic and vortex dynamos is limited. After a certain time, the intensified fields (vortex and magnetic ones) begin to affect the flows. In this case the behavior of the magnetic field and the motion of the meduim must be considered self-consistently, i.e. in the frame of the nonlinear theory. The observed magnetic fields of real objects exist probably just in nonlinear mode. So, the nonlinear theory [39] appears to be very important. In this paper the nonlinear theory of magnetic dynamo is based on generalization of the theory of mean field (see e.g. [7]) taking into account the nonlinear effects.

However, the theory of mean field does not allow us to determine the principal order at which the instability occurs from the whole hierarchy of perturbations. Therefore, an alternative for construction of a nonlinear dynamo theory is the method of multi-scale asymptotic expansions [38]. This method allows to construct the nonlinear theories of vortex dynamo for compressible media [40-41], as well as for convective media with a helical external force [30-31]. The asymptotic multi-scale method is used to reveal large-scale instability in the thermally stratified conductive medium in the case of helicity of small-scale velocity and magnetic fields [42-43]. Development of this large-scale instability in a convective electroconductive medium engenders the generation of both vortex and magnetic fields as well. Self-consistent or nonlinear theory of magneto-vortex dynamo in a convective electroconductive medium with small-scale helicity was built in [43].

In this work, the possibility of the formation of stationary chaotic large-scale structures in magnetic and vortex fields was shown for the first time. The particular case of the formation of large-scale stationary magnetic structures was also considered in this work. These structures were classified as stationary solutions of three types: nonlinear waves, solitons and kinks. Qualitative estimations of the linear stage [42] for solar conditions allow to set a good agreement of the characteristic scales and times of the formed hydrodynamic structures with those of the structures found experimentally [44].

In the above-mentioned papers helical turbulence was considered as a priori known, or the problem of its generation was examined independently [45]. The question naturally arises about the possibility of generation of large-scale vortices (hydrodynamic and magnetic) in rotating media under the action of a small-scale force with zero helicity $\vec{F}_0 rot \vec{F}_0 = 0$. The example of LSVS generation in a rotating incompressible fluid is found in [46]. The development of this large-scale instability in obliquely rotating fluid gives rise to nonlinear large-scale helical structures of Beltrami vortex type, or to localized kinks with internal helical structure. In [47] the new hydrodynamic α -effect found in [46] was generalized to the case of electroconductive fluid. The corresponding large-scale instability leads to the generation of LSVS and magnetic fields. The nonlinear stage of this instability gives chaotic localized vortices and magneic structures. As is known [48-49], a large-scale motion caused by nonuniform heating in a gravitation field (free convection) exists in convective zones of the Sun and other stars, as well as in the core of the Earth and other planets. The convection in which the rotation axes of the medium and uniform magnetic field coincide with the direction of gravitation vector, was studied in detail in [49]. However, for astrophysical problems it is important to consider the case when the directions of the rotation axes and of magnetic fields are perpendicular, or do not coincide with each other. The role of azimuthal magnetic field significantly increases for convective fluid layers located in the equatorial region of the rotating object. As known from the theory of magnetic dynamo [2-7], the toroidal magnetic field in the Earth's crust and in the atmosphere of the Sun exceeds the poloidal magnetic field.

The aim of this work is to study generation and nonlinear evolution of vortices and magnetic fields in a rotating stratified electoconductive fluid in an external uniform magnetic field under the action of the nonhelical force $\vec{F}_0$.

Suppose that the vector of angular rotation velocity $\vec{\Omega}$ is deviated from the vertical direction OZ, and the vector of the external magnetic field $\bar{B}$ is located in the horizontal plane XOY perpendicular to the direction of the gravity force $\vec{g}$ (Fig. 1). This geometry is most suitable for the description of dynamo processes in rotating space objects. The results obtained in the present work can be applied for various astrophysical problems.
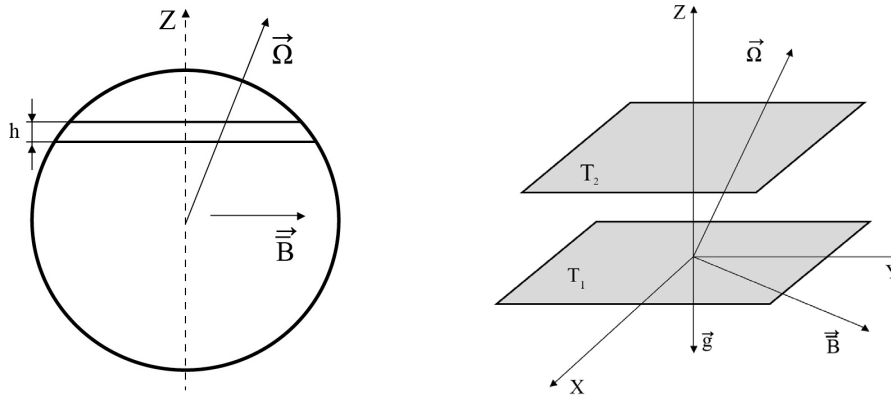
Fig.1. Shows schematically a thin layer of rotating electroconductive fluid of astrophysical object. For the general case the angular velocity $\vec{\Omega}$ is inclined to the plane (X,Y) where the induction vector $\overline{B}$ of uniform magnetic filed is located. The gradient of equilibrium temperature is directed vertically downwards: $T_1 > T_2$ - heating from below.

BASIC EQUATIONS AND FORMULATION OF THE PROBLEM

Consider the dynamics of perturbed state of the electroconductive fluid located in the constant gravitation $\vec{g}$ and magnetic $\vec{B}$ fields with the constant temperature gradient $\nabla \overline{T}$ in the system of rotating coordinates:

$$\frac{\partial v_i}{\partial t} + v_k \frac{\partial v_i}{\partial x_k} = \nu \frac{\partial^2 v_i}{\partial x_k^2} - \frac{1}{\overline{\rho}} \frac{\partial P}{\partial x_i} + 2\varepsilon_{ijk} v_j \Omega_k + \frac{\varepsilon_{ijk}\varepsilon_{jml}}{4\pi\overline{\rho}} \frac{\partial B_l}{\partial x_m}(B_k + \overline{B}_k) +$$

$$+ ge_i \beta\Theta + F_0^i \tag{1}$$

$$\frac{\partial B_i}{\partial t} = \varepsilon_{ijk}\varepsilon_{knp} \frac{\partial}{\partial x_j}\left(v_n(B_p + \overline{B}_p)\right) + \nu_m \frac{\partial^2 B_i}{\partial x_k^2} \tag{2}$$

$$\frac{\partial \Theta}{\partial t} + v_k \frac{\partial \Theta}{\partial x_k} - Ae_k v_k = \chi \frac{\partial^2 \Theta}{\partial x_k^2} \tag{3}$$

$$\frac{\partial v_i}{\partial x_i} = \frac{\partial B_i}{\partial x_i} = 0 \tag{4}$$

Here v_i, P, B_i, Θ are the perturbations of velocity, pressure, magnetic field induction and fluid temperature $(i = x, y, z)$. $\overline{B}_i = const$ is the induction of the external homogeneous magnetic field; $\overline{\rho}$ is the equilibrium density of the medium $\overline{\rho} = const$, ν, χ are fluid viscosity and thermal conductivity coefficients respectively, $\nu_m = \dfrac{c^2}{4\pi\sigma_c}$ is the magnetic viscosity coefficient. σ_c is coefficient of electrical conductivity of the medium and β is thermal expansion coefficient. The system of magnetic hydrodynamic eqs. (1)-(4) is written in the Boussinesq approximation [48] and describes the evolution of disturbances relative to the equilibrium state given by the constant temperature gradient $\nabla \overline{T} = -A\vec{e}$ $(A > 0)$ and the hydrostatic pressure: $\nabla\left(\overline{P} + \dfrac{\overline{B}^2}{8\pi}\right) = \overline{\rho}\vec{g}$. Here we neglect the centrifugal forces, since the condition $g \gg \Omega^2 r$, where r is the characteristic radius of fluid rotation, is satisfied. Now let us formulate the problem with the geometry shown in Fig. 1. Consider a thin layer (with the thickness h) of a rotating electoconductive fluid in which the lower and the upper surfaces have the temperatures T_1 and T_2, respectively. We suppose $T_1 > T_2$, i.e. heating from below. In this case the direction of the temperature gradient $\nabla \overline{T} = \vec{A}$ coincides with the direction of the gravitation field $\vec{g} = -g\vec{e}_z$. Here $\vec{e} = (0,0,1)$ is the unit vector in the direction of the axis Z. The temperature profile $\overline{T}$ depends linearly on the vertical coordinate z: $\overline{T}(z) = T_1 - \dfrac{T_1 - T_2}{h} \cdot z$. The vector of angular rotation velocity $\vec{\Omega} = (\Omega_1, \Omega_2, \Omega_3)$ is constant (solid-body rotation) and inclined with respect to the plane (X,Y) where is the vector of homogeneous magnetic field $\vec{\overline{B}} = (\overline{B}_1, \overline{B}_2, 0)$.

Eq. (1) contains the external force $\vec{F}_0$. It models the source of external excitation in the medium of small-scale and high-frequency fluctuations of the velocity field $\vec{v}_0$ with the small Reynolds number $R = \dfrac{v_0 t_0}{\lambda_0} \ll 1$. Here we will consider the non-helical external force $\vec{F}_0$ with the following properties:

$$divf\vec{F}_0 = 0, \ \vec{F}_0 rot\vec{F}_0 = 0, \ rot\vec{F}_0 \neq 0, \ \vec{F}_0 = f_0 \vec{F}_0 \left(\frac{x}{\lambda_0}; \frac{t}{t_0} \right) \tag{5}$$

where λ_0 is the characteristic scale, t_0 is the characteristic time, f_0 is the characteristic amplitude of the external force. Now choose the external force in a rotating coordinate system in the form:

$$F_0^z = 0, \ \vec{F}_0 = f_0 \left(\vec{i} cos\varphi_2 + \vec{j} cos\varphi_1 \right),$$

$$\varphi_1 = \vec{\kappa}_1 \vec{x} - \omega_0 t, \qquad \varphi_2 = \vec{\kappa}_2 \vec{x} - \omega_0 t, \tag{6}$$

$$\vec{\kappa}_1 = \kappa_0 \left(1,0,0 \right), \ \vec{\kappa}_2 = \kappa_0 \left(0,1,0 \right).$$

It is evident that this external force satisfies all the conditions (5). Let us consider the dimensionless variables in eqs. (1)-(4). For convenience we keep the same notation as for dimensional variables:

$$\vec{x} \rightarrow \frac{\vec{x}}{\lambda_0}, \quad t \rightarrow \frac{t}{t_0}, \quad \vec{v} \rightarrow \frac{\vec{v}}{v_0}, \quad \vec{F}_0 \rightarrow \frac{\vec{F}_0}{f_0},$$

$$\vec{B} \rightarrow \frac{\vec{B}}{B_0}, \quad \overline{\vec{B}} \rightarrow \frac{\overline{\vec{B}}}{B_0}, \quad \Theta \rightarrow \frac{\Theta}{\lambda_0 A},$$

$$t_0 = \frac{\lambda_0^2}{\nu}, \quad f_0 = \frac{v_0 \nu}{\lambda_0^2}, \quad P \rightarrow \frac{P}{P_0}, \quad P_0 = \overline{\rho} \frac{\nu v_0}{\lambda_0}.$$

Here v_0, B_0, P_0 are the characteristic values of small-scale pulsations of the velocity, magnetic field and pressure. In the dimensionless variables eqs.(1)-(3) take the form:

$$\frac{\partial v_i}{\partial t} + R v_k \frac{\partial v_i}{\partial x_k} = \frac{\partial^2 v_i}{\partial x_k^2} - \frac{\partial P}{\partial x_i} + \varepsilon_{ijk} v_j D_k + \frac{Q}{RPm} \varepsilon_{ijk} \varepsilon_{jml} \frac{\partial B_l}{\partial x_m} (B_k + \overline{B}_k) +$$

$$+ e_i \frac{Ra}{RPr} \Theta + F_0^i \tag{7}$$

$$\frac{\partial B_i}{\partial t} - Pm^{-1} \frac{\partial^2 B_i}{\partial x_k^2} = R\varepsilon_{ijk} \varepsilon_{knp} \frac{\partial}{\partial x_j} \left(v_n (B_p + \overline{B}_p) \right) \tag{8}$$

$$\frac{\partial \Theta}{\partial t} + R v_k \frac{\partial \Theta}{\partial x_k} - R e_k v_k = Pr^{-1} \frac{\partial^2 \Theta}{\partial x_k^2} \tag{9}$$

Whithe new temperature $\Theta \rightarrow \Theta / R$ and magnetic field $B \rightarrow B / R$ we obtain finally:

$$\frac{\partial v_i}{\partial t} + R v_k \frac{\partial v_i}{\partial x_k} = \frac{\partial^2 v_i}{\partial x_k^2} - \frac{\partial P}{\partial x_i} + \varepsilon_{ijk} v_j D_k + R\tilde{Q} \varepsilon_{ijk} \varepsilon_{jml} \frac{\partial B_l}{\partial x_m} B_k +$$

$$+ \tilde{Q} \varepsilon_{ijk} \varepsilon_{jml} \frac{\partial B_l}{\partial x_m} \overline{B}_k + e_i \widetilde{Ra} \Theta + F_0^i \tag{10}$$

$$\frac{\partial B_i}{\partial t} - Pm^{-1} \frac{\partial^2 B_i}{\partial x_k^2} = R\varepsilon_{ijk} \varepsilon_{knp} \frac{\partial}{\partial x_j} \left(v_n B_p \right) + \varepsilon_{ijk} \varepsilon_{knp} \frac{\partial}{\partial x_j} \left(v_n \overline{B}_p \right) \tag{11}$$

$$\frac{\partial \Theta}{\partial t} - Pr^{-1} \frac{\partial^2 \Theta}{\partial x_k^2} = -R v_k \frac{\partial \Theta}{\partial x_k} + e_k v_k \tag{12}$$

$$\frac{\partial v_i}{\partial x_i} = \frac{\partial B_i}{\partial x_i} = 0 \tag{13}$$

Here we use the following dimensionless parameters: $\widetilde{Ra} = \dfrac{Ra}{Pr}$, $Ra = \dfrac{g\beta A\lambda_0^4}{\nu\chi}$ is the Rayleigh number in the

scale λ_0; $D_i = \dfrac{2\Omega_i\lambda_0^2}{\nu}$ - the rotation parameter in the scale λ_0 ($i = 1,2,3$) connected with the Taylor number

$Ta_i = D_i^2$; $\tilde{Q} = \dfrac{Q}{Pm}$, $Q = \dfrac{\sigma_c B_0^2 \lambda_0^2}{c^2 \rho\nu}$ - the Chandrasekhar number, $Pm = \dfrac{\nu}{\nu_m}$ - the magnetic Prandtl number, $Pr = \dfrac{\nu}{\chi}$ --

the Prandtl number. The small parameter of asymptotic expansion is the Reynolds number $R = \dfrac{v_0 t_0}{\lambda_0} \ll 1$ and the

parameters D, $\tilde{Q}$ and $\widetilde{Ra}$ are arbitrary and do not affect the scheme of asymptotic expansion. The presence of the small parameter ($R \ll 1$) in the system of eqs. (10)-(13) allows us to apply the theory of multi-scale asymptotic expansions (see e.g. [30-31], [38]). In contrast to the theory of mean field [2-7] we can consistently see the dynamics of disturbances for different spatial and temporal scales in each order by R. In particular, in the zero order of R, small-scale and high-frequency oscillations of the velocity $\vec{v}_0$ are excited by the external force $\vec{F}_0$ acting at the equilibrium state. Obviously, the dynamics of small-scale fields depends on external factors such as rotation and stratification of the medium, magnetic and gravitation fields, etc. These oscillations are characterized by zero average values. Nevertheless, the nonlinear interactions in some orders of the perturbation theory give rise to the terms which do not vanish at averaging. In the next section, we consider in detail how to find the solvability conditions for the multi-scale asymptotic expansion, which define the evolution equations for large-scale perturbations.

EQUATIONS FOR LARGE-SCALE FIELDS

In accordance with the method of construction of asymptotic equations [30-31], [38] let us present spatial and temporal derivatives in eqs. (10)-(13) in the form of the asymptotic expansion:

$$\frac{\partial}{\partial t} \to \partial_t + R^4 \partial_T, \quad \frac{\partial}{\partial x_i} \to \partial_i + R^2 \nabla_i \tag{14}$$

where ∂_i and ∂_t are the derivatives with respect to the fast variables $x_0 = (\vec{x}_0, t_0)$, whereas ∇_i and ∂_T are the derivatives with respect to the slow variables $X = (\vec{X}, T)$. The variables x_0 and X may be referred to as small- and large-scale variables, accordingly. While constructing the nonlinear theory we present the variables $\vec{V}$, $\vec{B}$, P in the form of the asymptotic series:

$$\vec{V}(\vec{x}, t) = \frac{1}{R}\vec{W}_{-1}(X) + \vec{v}_0(x_0) + R\vec{v}_1 + R^2\vec{v}_2 + R^3\vec{v}_3 + \cdots$$

$$\vec{B}(\vec{x}, t) = \frac{1}{R}\vec{B}_{-1}(X) + \vec{B}_0(x_0) + R\vec{B}_1 + R^2\vec{B}_2 + R^3\vec{B}_3 + \cdots \tag{15}$$

$$\Theta(\vec{x}, t) = \frac{1}{R}T_{-1}(X) + T_0(x_0) + RT_1 + R^2T_2 + R^3T_3 + \cdots$$

$$P(x) = \frac{1}{R^3}P_{-3} + \frac{1}{R^2}P_{-2} + \frac{1}{R}P_{-1} + P_0(x_0) + R(P_1 + \overline{P}_1(X)) + R^2 P_2 + R^3 P_3 + \cdots$$

Let us substitute the expansions (14)-(15) into the system of eqs. (10)-(13). Then we select the terms of the same orders of R up to the degree R^3 and obtain the equations of multi-scale asymptotic expansion. The algebraic structure of the asymptotic expansion of eqs. (10)-(13) of different orders in R is presented in Appendix A. Here it is shown that the basic secular equations, i.e. those for large-scale fields, are obtained in the order R^3

$$\partial_t W_{-1}^i - \nabla_k^2 W_{-1}^i + \nabla_k \overline{(v_0^k v_0^i)} = -\nabla_i \overline{P}_1 + \tilde{Q}\varepsilon_{ijk}\varepsilon_{jml}\left(\nabla_m \overline{(B_0^l B_0^k)}\right) \tag{16}$$

$$\partial_t B_{-1}^i - Pm^{-1}\nabla_k^2 B_{-1}^i = \varepsilon_{ijk}\varepsilon_{knp}\nabla_j \overline{(v_0^n B_0^p)} \tag{17}$$

$$\partial_T T_{-1} - Pr^{-1}\nabla_k^2 T_{-1} = -\nabla_k \overline{(v_0^k T_0)} \tag{18}$$

Using the convolution of the tensors $\varepsilon_{ijk}\varepsilon_{jml} = \delta_{km}\delta_{il} - \delta_{im}\delta_{kl}$, $\varepsilon_{ijk}\varepsilon_{knp} = \delta_{in}\delta_{jp} - \delta_{ip}\delta_{jn}$ and the denotations $\vec{W} = \vec{W}_{-1}, \vec{H} = \vec{B}_{-1}$ obtain eqs. (16)-(17) in the following form:

$$\partial_T W_i - \nabla_k^2 W_i + \nabla_k \overline{(v_0^k v_0^i)} = -\nabla_i \overline{P}_1 + \tilde{Q}\left(\nabla_k \overline{(B_0^i B_0^k)} - \frac{\nabla_i}{2} \overline{(B_0^k)^2} \right) \tag{19}$$

$$\partial_T H_i - Pm^{-1}\nabla_k^2 H_i = \nabla_j \overline{(v_0^i B_0^j)} - \nabla_j \overline{(v_0^j B_0^i)} \tag{20}$$

Eqs. (16)-(18) are supplemented with the secular equations derived in Appendix A:

$$-\nabla_i P_{-3} + \varepsilon_{ijk} W_j D_k + e_i \widetilde{Ra} T_{-1} = 0, \quad W_{-1}^z = 0,$$

$$W_{-1}^k \nabla_k W_{-1}^i = -\nabla_i P_{-1} + \tilde{Q}\varepsilon_{ijk}\varepsilon_{jml}\left(\nabla_m B_{-1}^l B_{-1}^k + \nabla_m B_{-1}^l \overline{B}_k \right),$$

$$\varepsilon_{ijk}\varepsilon_{knp}\left(\nabla_j W_{-1}^n B_{-1}^p + \nabla_j W_{-1}^n \overline{B}_p \right) = 0,$$

$$W_{-1}^k \nabla_k T_{-1} = 0, \quad \nabla_i W_{-1}^i = 0, \quad \nabla_i B_{-1}^i = 0.$$

To obtain the system of eqs. (16)-(18) which decribe the evolution of large-scale fields we have to reach the third order of the perturbation theory. This is a rather typical phenomenon when applying the method of multiscale expansions. As seen from eqs. (16)-(17), the large-scale temperature T_{-1} does not influence the dynamics of the large-scale field of the velocity $\vec{W}_{-1}$ and the magnetic field $\vec{B}_{-1}$, therefore let us confine ourselves to investigation of eqs. (16)-(17). These equations acquire a closed form after calculation of the correlation functions, i.e. the Reynolds stresses $\nabla_k \overline{(v_0^k v_0^i)}$, the Maxwell stresses $\nabla_k \overline{(B_0^i B_0^k)}$ and the turbulent e.m.f. $\mathcal{E}_n = \varepsilon_{nij} \overline{v_0^i B_0^j}$. Calculation of these correlation functions is significantly simplified due to the «quasi-two-dimensional» approximation which is often used for description of large-scale vortices and magnetic fields in many astrophysical and geophysical problems. In the framework of this approximation we consider the large-scale derivative with respect to Z as more important than horizontal derivatives, i.e.

$$\nabla_Z \equiv \frac{\partial}{\partial Z} \gg \frac{\partial}{\partial X}, \frac{\partial}{\partial Y}.$$

Therefore, the geometry of large-scale fields has the following form:

$$\vec{W} = \left(W_1(Z), W_2(Z), 0 \right), \vec{H} = \left(H_1(Z), H_2(Z), 0 \right) \tag{21}$$

For the «quasi-two-dimensional» problem the system of eqs. (14)-(15) is simplified:

$$\partial_T W_1 - \nabla_Z^2 W_1 + \nabla_Z \overline{(v_0^z v_0^x)} = \tilde{Q}\nabla_Z \overline{(B_0^z B_0^x)} \tag{22}$$

$$\partial_T W_2 - \nabla_Z^2 W_2 + \nabla_Z \overline{(v_0^z v_0^y)} = \tilde{Q}\nabla_Z \overline{(B_0^z B_0^y)} \tag{23}$$

$$\partial_T H_1 - Pm^{-1}\nabla_Z^2 H_1 = \nabla_Z \overline{(v_0^x B_0^z)} - \nabla_Z \overline{(v_0^z B_0^x)} \tag{24}$$

$$\partial_T H_2 - Pm^{-1}\nabla_Z^2 H_2 = \nabla_Z \overline{(v_0^y B_0^z)} - \nabla_Z \overline{(v_0^z B_0^y)} \tag{25}$$

$$\partial_T T_{-1} - Pr^{-1}\nabla_Z^2 T_{-1} + \nabla_Z \left(\overline{v_0^z T_0} \right) = 0 \tag{26}$$

To have eqs. (22)–(26) in the closed form we use the solutions of the equations for small-scale fields in the zero order in R obtained in Appendix B. Then it is necessary to calculate the correlators contained in the system (22)-(26). The technical aspect of this problem is considered in detail in Appendix C. The calculations performed here make possible to obtain the following closed equations for large-scale fields of the velocity (W_1, W_2) and the magnetic fields (H_1, H_2):

$$\partial_T W_1 - \nabla_Z^2 W_1 + \nabla_Z \left(\alpha_{(2)} \cdot (1 - W_2) \right) = 0 \tag{27}$$

$$\partial_T W_2 - \nabla_Z^2 W_2 - \nabla_Z \left(\alpha_{(1)} \cdot (1 - W_1) \right) = 0 \tag{28}$$

$$\partial_T H_1 - Pm^{-1}\nabla_Z^2 H_1 + \nabla_Z \left(\alpha_H^{(2)} \cdot H_2 \right) = 0 \tag{29}$$

$$\partial_T H_2 - Pm^{-1}\nabla_Z^2 H_2 - \nabla_Z \left(\alpha_H^{(1)} \cdot H_1 \right) = 0 \tag{30}$$

where the nonlinear coefficients $\alpha_{(1)}$, $\alpha_{(2)}$, $\alpha_H^{(1)}$, $\alpha_H^{(2)}$ have the form:

$$\alpha_{(1)} = \frac{f_0^2}{2} \cdot \frac{D_1 q_1 Q_1 (1 - W_1)^{-1}}{4(1-W_1)^2 q_1^2 \tilde{Q}_1^2 + \left[D_1^2 + W_1(2 - W_1) + \mu_1 \right]^2 + \xi_1},$$

$$\alpha_{(2)} = \frac{f_0^2}{2} \cdot \frac{D_2 q_2 Q_2 (1 - W_2)^{-1}}{4(1-W_2)^2 q_2^2 \tilde{Q}_2^2 + \left[D_2^2 + W_2(2 - W_2) + \mu_2 \right]^2 + \xi_2},$$

$$\alpha_H^{(1)} = f_0^2 \cdot \frac{D_1(1-W_1)Pm\tilde{Q}_1(1 + \overline{B}_1 / H_1)}{\left(1 + Pm^2(1-W_1)^2 \right) \cdot \tilde{\xi}_1},$$

$$\alpha_H^{(2)} = f_0^2 \cdot \frac{D_2(1-W_2)Pm\tilde{Q}_2(1 + \overline{B}_2 / H_2)}{\left(1 + Pm^2(1-W_2)^2 \right) \cdot \tilde{\xi}_2}.$$

The expressions which denote $q_{1,2}$, $Q_{1,2}$, $\tilde{Q}_{1,2}$, $\mu_{1,2}$, $\sigma_{1,2}$, $\chi_{1,2}$, $\xi_{1,2}$, $\tilde{\xi}_{1,2}$ are also presented in Appendix C. The coefficients $\alpha_{(1)}$, $\alpha_{(2)}$ and $\alpha_H^{(1)}$, $\alpha_H^{(2)}$ correspond to the nonlinear HD α-effect and the nonlinear MHD α-effect, respectively. Thus, we have obtained the self-consistent system of nonlinear evolution equations for the large-scale perturbations of the velocity and magnetic field which further are called the equations of nonlinear magneto-vortex dynamo. It should be noted that the mechanism of dynamo «works» only due to the effect of rotation of the medium. If this rotation is absent ($\Omega = 0$), then the diffuse spreading of large-scale fields occurs. In the absence of heating ($\nabla \overline{T} = 0$) and of external magnetic field ($\overline{B} = 0$) eqs. (27)-(28) coincide with the results found in [47]. In the case of non-electroconductive fluid ($\sigma = 0$) with the temperature gradient ($\nabla \overline{T} \neq 0$) we obtain the same results as in [50]. In the limit of non-electroconductive ($\sigma = 0$) and homogeneous fluid ($\nabla \overline{T} = 0$) we obtain the results of [46]. To study this dynamo model, it is necessary at first to consider the evolution of small perturbations and then to examine the nonlinear effects.

LARGE-SCALE INSTABILITY

Let us consider the behavior of small perturbations of the field of velocity (W_1, W_2) and the magnetic fields (H_1, H_2). Then expand the nonlinear coefficients $\alpha_{(1,2)}$ and $\alpha_H^{(1,2)}$ in eqs. (27)-(30) into the Taylor series with respect to the small values (W_1, W_2), (H_1, H_2):

$$\alpha_{(1,2)} \cdot (1 - W_{1,2}) \approx \alpha_0^{(1,2)} - \alpha_{1,2}^{(H)} \cdot H_{1,2} - \alpha_{1,2}^{(W)} \cdot W_{1,2}, \quad \alpha_0^{(1,2)} = const,$$

$$\alpha_H^{(1,2)} \cdot H_{1,2} \approx \alpha_{0H}^{(1,2)} + \tilde{\alpha}_H^{(1,2)} \cdot H_{1,2} - \beta_W^{(1,2)} \cdot W_{1,2}, \quad \alpha_{0H}^{(1,2)} = const. \tag{31}$$

After substituting (31) into eqs. (27)-(30) we obtain the linearized system of equations :

$$\partial_T W_1 - \nabla_Z^2 W_1 - \alpha_2^{(H)} \cdot \nabla_Z H_2 - \alpha_2^{(W)} \cdot \nabla_Z W_2 = 0 \tag{32}$$

$$\partial_T W_2 - \nabla_Z^2 W_2 + \alpha_1^{(H)} \cdot \nabla_Z H_1 + \alpha_1^{(W)} \cdot \nabla_Z W_1 = 0 \tag{33}$$

$$\partial_T H_1 - \nabla_Z^2 H_1 + \tilde{\alpha}_H^{(2)} \cdot \nabla_Z H_2 - \beta_W^{(2)} \cdot \nabla_Z W_2 = 0 \tag{34}$$

$$\partial_T H_2 - \nabla_Z^2 H_2 - \tilde{\alpha}_H^{(1)} \cdot \nabla_Z H_1 + \beta_W^{(1)} \cdot \nabla_Z W_1 = 0, \tag{35}$$

where the constant coefficients $\alpha_{1,2}^{(H)}, \alpha_{1,2}^{(W)}, \tilde{\alpha}_H^{(1,2)}, \beta_W^{(1,2)}$ have the following form:

$$\alpha_{1,2}^{(H)} = \frac{f_0^2 D_{1,2}}{2} \cdot Q\overline{B}_{1,2} \left[\frac{(2-Ra)(2-Q\overline{B}_{1,2}^2)\left(4(D_{1,2}^2-Ra)+(Ra+1)^2+7\right)}{4\left(4+(D_{1,2}^2-Ra)^2\right)^2} + \frac{Q\overline{B}_{1,2}^2 - 2(Ra-1)}{4\left(4+(D_{1,2}^2-Ra)^2\right)} \right], \quad (36)$$

$$\alpha_{1,2}^{(W)} = \frac{f_0^2 D_{1,2}}{2} \cdot \left[\frac{(2-Ra)(2-Q\overline{B}_{1,2}^2)\left(D_{1,2}^2-Ra-2\right)}{\left(4+(D_{1,2}^2-Ra)^2\right)^2} + \frac{Q\overline{B}_{1,2}^2 + Ra\left(1-Q\overline{B}_{1,2}^2\right)}{2\left(4+(D_{1,2}^2-Ra)^2\right)} \right], \quad (37)$$

$$\tilde{\alpha}_H^{(1,2)} = \frac{f_0^2 D_{1,2}}{4} \cdot \left[\frac{2+Ra-Q\overline{B}_{1,2}^2+\overline{B}_{1,2}(2+Ra)}{4+(D_{1,2}^2-Ra)^2} - \frac{\overline{B}_{1,2}(2+Ra)\left(4(D_{1,2}^2-Ra)+(Ra+1)^2+7\right)}{\left(4+(D_{1,2}^2-Ra)^2\right)^2} \right], \quad (38)$$

$$\beta_W^{(1,2)} = f_0^2 \cdot \frac{D_{1,2}\overline{B}_{1,2}(2+Ra)\left(D_{1,2}^2-Ra-2\right)}{\left(4+(D_{1,2}^2-Ra)^2\right)^2} - \frac{f_0^2}{4} \cdot \frac{D_{1,2}\overline{B}_{1,2}Ra}{4+(D_{1,2}^2-Ra)^2} \quad (39)$$

To obtain the system of equations (32)-(35) we use a simplification when the equality of Prandtl numbers is equal to unity: $Pr = Pm = 1$. As seen from eqs. (32)-(35), in the presence of external magnetic field the coefficients $\alpha_{1,2}^{(H)}$ and $\beta_W^{(1,2)}$ define the positive feedback in the self-consistent dynamics of the fields $W_{1,2}$ and $H_{1,2}$. Now let us find the solution of the linear system of eqs. (32)-(35) in the form of plane waves with the wave vector $\vec{K} \parallel OZ$:

$$\begin{pmatrix} W_{1,2} \\ H_{1,2} \end{pmatrix} = \begin{pmatrix} \mathcal{W}_{1,2} \\ \mathcal{H}_{1,2} \end{pmatrix} exp\left(-i\omega T + iKZ\right) \quad (40)$$

After substituting (40) into the system (32)-(35) we obtain the dispersion equation:

$$\left[\left(K^2-i\omega\right)^2 - K^2\left(\alpha_1^{(W)}\alpha_2^{(W)} + \alpha_2^{(H)}\beta_W^{(1)}\right) \right]\left[\left(K^2-i\omega\right)^2 - K^2\left(\tilde{\alpha}_H^{(1)}\tilde{\alpha}_H^{(2)} + \alpha_1^{(H)}\beta_W^{(2)}\right) \right] +$$

$$+K^4\left(\tilde{\alpha}_H^{(1)}\alpha_2^{(H)} - \alpha_1^{(H)}\alpha_2^{(W)}\right)\left(\alpha_1^{(W)}\beta_W^{(2)} - \tilde{\alpha}_H^{(2)}\beta_W^{(1)}\right) = 0 \quad (41)$$

Analysis of dispersion equation (41) in the absence of external magnetic field $\overline{B}_{1,2} = 0$

It is obvious that without external magnetic field $\overline{B}_{1,2} = 0$ the coefficients $\alpha_{1,2}^{(H)}$ and $\beta_W^{(W)}$ vanish, and (41) breaks down into two independent equations:

$$\left[\left(K^2-i\omega\right)^2 - \alpha_1^{(W)}\alpha_2^{(W)}K^2 \right]\left[\left(K^2-i\omega\right)^2 - \tilde{\alpha}_H^{(1)}\tilde{\alpha}_H^{(2)}K^2 \right] = 0 \quad (42)$$

where the coefficients $\alpha_{1,2}^{(W)}$, $\tilde{\alpha}_H^{(1,2)}$ do not depend on $\overline{B}_{1,2}$. Dispersion eq. (42) corresponds to the physical situation when small perturbations of vortex and magnetic fields independently gain in intensity due to development of large-scale instability such as α-effect. Using the frequency $\omega = \omega_0 + i\Gamma$ from eq. (42) we find:

$$\Gamma_1 = Im\,\omega_1 = \pm\sqrt{\alpha_1^{(W)}\alpha_2^{(W)}}\,K - K^2 \quad (43)$$

$$\Gamma_2 = Im\,\omega_2 = \pm\sqrt{\tilde{\alpha}_H^{(1)}\tilde{\alpha}_H^{(2)}}\,K - K^2 \quad (44)$$

Solutions (43) show the instability at $\alpha_1\alpha_2 > 0$ for large-scale vortex perturbations with the maximum instability increment $\Gamma_{1max} = \frac{\alpha_1\alpha_2}{4}$ at the wave numbers $K_{1max} = \frac{\sqrt{\alpha_1\alpha_2}}{2}$. Similarly, for magnetic perturbations the instability increment $\Gamma_{2max} = \frac{\tilde{\alpha}_H^{(1)}\tilde{\alpha}_H^{(2)}}{4}$ reaches its maximum at the wave numbers $K_{2max} = \frac{\sqrt{\tilde{\alpha}_H^{(1)}\tilde{\alpha}_H^{(2)}}}{2}$. If $\alpha_1\alpha_2 < 0$ and

$\tilde{\alpha}_H^{(1)} \tilde{\alpha}_H^{(2)} < 0$, then, instead of instability damped oscillations arise with the frequences $\omega_{01} = \sqrt{\alpha_1 \alpha_2} K$ and $\omega_{02} = \sqrt{\tilde{\alpha}_H^{(1)} \tilde{\alpha}_H^{(2)}} K$, respectively. It is clear that in the considered linear theory the coefficients $\alpha_1^{(W)}$, $\alpha_2^{(W)}$, $\tilde{\alpha}_H^{(1)}$, $\tilde{\alpha}_H^{(2)}$ depend not on the amplitudes of the fields, but on the rotation parameters $D_{1,2}$, the Rayleigh number Ra and the amplitude of the external force f_0. Now let us analyze the dependence of these coefficients on the dimensionless parameters. For simplicity let us assume that the dimensionless amplitude of the external force is $f_0 = 10$. Use of the given level of the dimensionless force signifies the choice of a certain level of steady background of small-scale and fast oscillations. It is convenient to replace the Cartesian projections D_1 and D_2 in the coefficients $\alpha_1^{(W)}$, $\alpha_2^{(W)}$, $\tilde{\alpha}_H^{(1)}$, $\tilde{\alpha}_H^{(2)}$ by their projections in the spherical coordinate system (D, ϕ, θ). The coordinate surface $D = const$ is a sphere, where θ is the latitude $\theta \in [0, \pi]$, ϕ is the longitude, $\phi \in [0, 2\pi]$ (see Fig. 2).
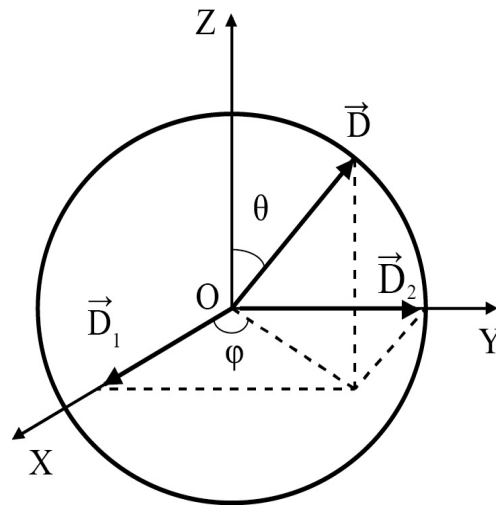
Fig. 2. The case, when the external magnetic field $\bar{B} = 0$ shows the relationship of the Cartesian projections of the rotation parameter $\vec{D}$ (or the angular velocity vector of rotation $\vec{\Omega}$) with their projections in a spherical coordinate system.

Let us analyze the dependences of the coefficients α_1, α_2, $\tilde{\alpha}_H^{(1)}$, $\tilde{\alpha}_H^{(2)}$ on the effect of rotation and stratification. For simplicity assume that $D_1 = D_2$, which corresponds to the fixed longitude value $\varphi = \pi/4 + \pi n$, where $n = 0,1,2...k$, k are integer. In this case the coefficients for vortex and magnetic perturbations are

$$\alpha = \alpha_1^{(W)} = \alpha_2^{(W)} = f_0^2 \sqrt{2} D \sin \theta \times$$

$$\times \frac{4\left(D^2 \sin^2 \theta - 2Ra - 4\right)(2 - Ra) + \frac{Ra}{2}\left((D^2 \sin^2 \theta - 2Ra)^2 + 16\right)}{\left((D^2 \sin^2 \theta - 2Ra)^2 + 16\right)^2}, \tag{45}$$

$$\alpha_H = \tilde{\alpha}_H^{(1)} = \tilde{\alpha}_H^{(2)} = \frac{f_0^2 \sqrt{2}}{2} \cdot \frac{D(2 + Ra)\sin \theta}{(D^2 \sin^2 \theta - 2Ra)^2 + 16} \tag{46}$$

respectively. As can be seen from these relations, at the poles $(\theta = 0, \theta = \pi)$ generation of vortex and magnetic perturbations is inefficient, since $\alpha, \alpha_H \to 0$. It means that the large-scale instability occurs in the case when the vector of angular rotation velocity $\vec{\Omega}$ deviates from the axis Z. For homogeneous medium $Ra = 0$ the generation of large-scale vortex and magnetic disturbances is due to the action of an external small-scale non-helical force and the Coriolis force [47]. The coefficient α of vortex perturbations for a rotating stratified electroconductive fluid coincides with the analogous coefficient α for a rotating stratified non-electroconductive fluid obtained in [50]. Therefore, the conclusions of this paper concerning the increase of vortex perturbations may be applied to the problem considered

here. The dependence of the coefficient α on the parameter of fluid stratification (the Rayleigh number Ra) at the fixed value of latitude $\theta = \pi/2$ and $D = 2.5$ is presented in the left part of Fig. 3.
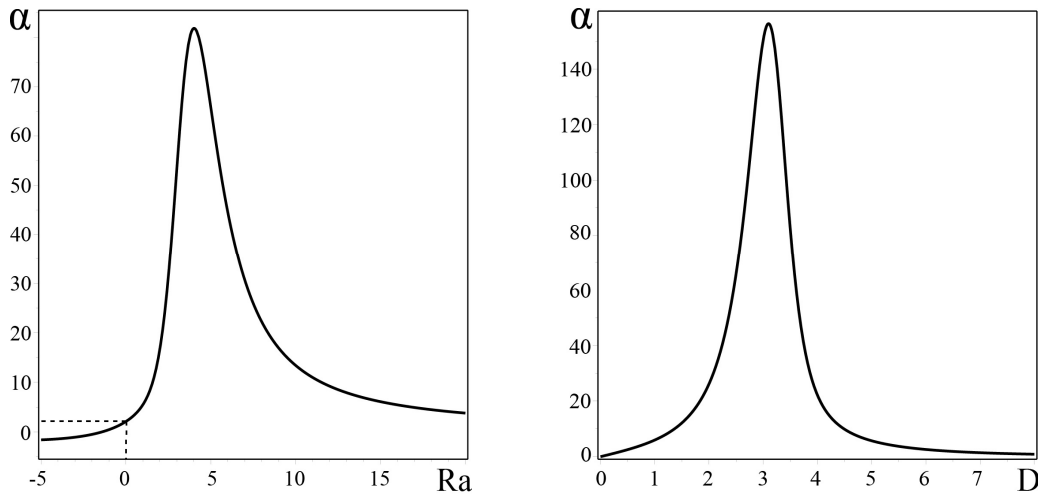
Fig. 3. On the left the plot of α - effect of parameter stratification of the medium Ra (Rayleigh number), and on the right the plot of the α - effect of the parameter of rotation D .

As can be seen, the temperature stratification ($Ra \neq 0$) may increase significantly the coefficient α and, consequently, generate large-scale vortex perturbations faster than in the homogeneous medium. This effect is particularly significant at $Ra \to 5$. When the Rayleigh number increases the value of the coefficient α decreases. Now let us consider the influence of the rotation of the medium on the coefficient α . For this purpose, we consider the value of the Rayleigh number as $Ra = 5$ at $\theta = \pi / 2$. For this case the functional dependence $\alpha(D)$ is presented in the right part of Fig. 3. One can see that at a certain value of the rotation parameter D the coefficient α reaches its maximum $\alpha_{\max}$. With increasing of D the coefficient α smoothly tends to zero, i.e. α -effect is suppressed by the rotation of the medium. Now consider the dependence of the coefficient α_H on the parameters of stratification and rotation (Ra and D , respectively) at the latitude $\theta = \pi / 2$. The dependence of the coefficient α_H on the stratification parameter (the Rayleigh number Ra) at $\theta = \pi / 2$ and $D = 2.5$ is shown in the left part of Fig. 4.
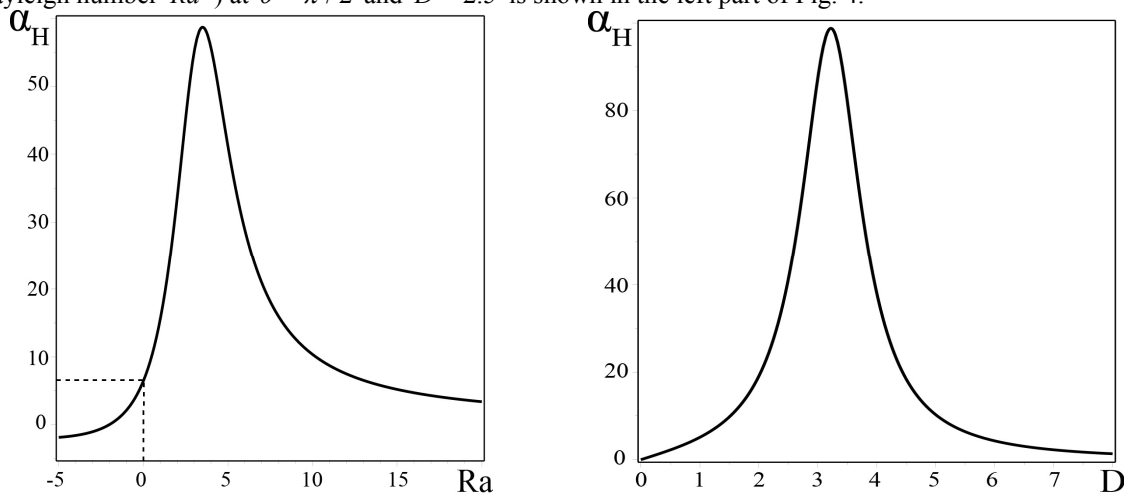
Fig. 4. On the left, the plot of α_H - effect of parameter stratification of the medium Ra (Rayleigh number), and on the right the plot of the α_H - effect of the parameter of rotation D .

We can see that the temperature stratification ($Ra \neq 0$) significantly increases coefficient α_H , and, consequently, generates the large-scale perturbations faster than in homogeneous medium. Magnetohydrodynamic α -effect (or α_H -effect) also increases at «slow» rotation up to the maximum value α_{Hmax} . Then with the rise of the parameter D the coefficient α_H decreases, but its sign does not change. The analysis of the dependence $\alpha_H(D)$ shows that at

«fast» rotation of the medium MHD α-effect is also suppressed (see the right part of Fig. 4). Similar phenomenon, i.e. suppression of α-effect by the rotation of turbulent medium is shown in [51].
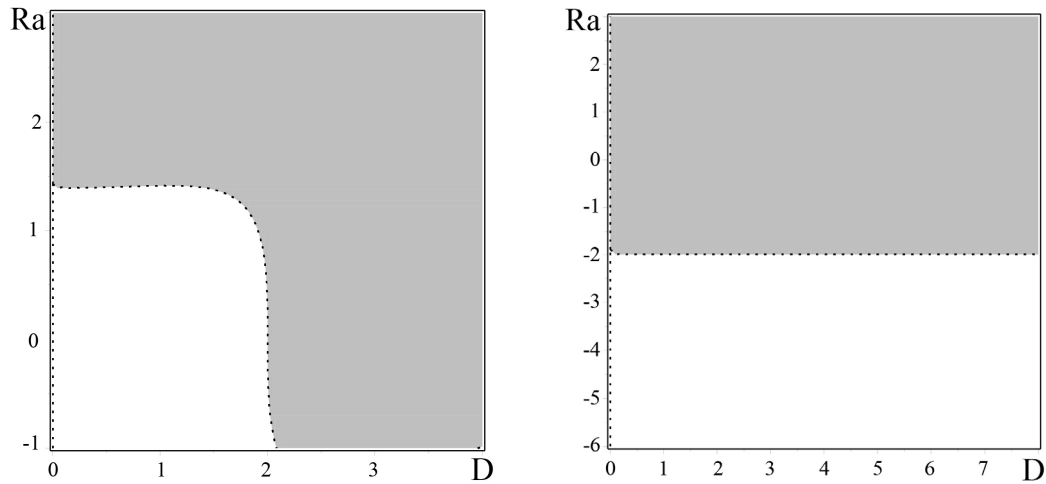
Fig. 5. On the left the plot for α in the plane (D, Ra), where the gray color shows the region corresponding to positive values $\alpha > 0$ (unstable solutions), and the white shows negative values α. On the right is the plot for α_H in the plane (D, Ra), where the gray color shows the region corresponding to positive values $\alpha_H > 0$ (unstable solutions), and the white to negative values α_H.

Fig. 5 shows the plot which represents the influence of rotation and stratification on α and α_H-effects in the plane (D, Ra). Here the regions of instability $\alpha > 0, \alpha_H > 0$ are highlighted in gray. We choose the values of rotation and stratification parameters D and Ra for the latitudinal angles $\theta = \pi / 2$ we plot the dependences of the growth rate of the vortex Γ_1 and magnetic Γ_2 perturbations on the wave numbers K. These plots have the typical form of α-effect (see Fig. 6).
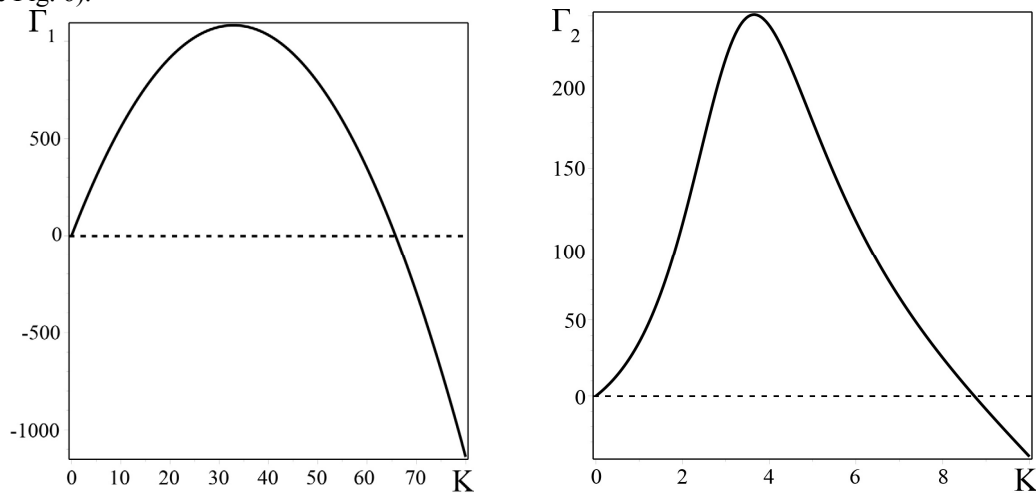
Fig. 6. On the left is the plot of the dependence of the instability increment for α-effect on the wave numbers K; on the right is a plot of the dependence of the instability increment for the α-effect on the wave numbers K. The plots are constructed for fixed parameters of stratification $Ra = 5$ and rotation $D = 2.5$.

Analysis of dispersion equation (41) in the presence of the external magnetic field

Let us study eq. (41) at $\overline{B}_{1,2} \neq 0$. In this case it is transformed into the biquadratic equation :

$$(K^2 - i\omega)^4 - b(K^2 - i\omega)^2 + a = 0, \tag{47}$$

where

$$b = K^2 \left(\alpha_1^{(W)} \alpha_2^{(W)} + \alpha_2^{(H)} \beta_W^{(1)} + \tilde{\alpha}_H^{(1)} \tilde{\alpha}_H^{(2)} + \alpha_1^{(H)} \beta_W^{(2)} \right) = K^2 \tilde{b},$$

$$a = K^4 \left(\tilde{\alpha}_H^{(2)} \alpha_2^{(W)} \left(\alpha_1^{(W)} \tilde{\alpha}_H^{(1)} + \alpha_1^{(H)} \beta_W^{(1)} \right) + \alpha_2^{(H)} \beta_W^{(2)} \left(\alpha_1^{(H)} \beta_W^{(1)} + \tilde{\alpha}_H^{(1)} \alpha_1^{(W)} \right) \right) = K^4 \tilde{a}.$$

The solution of eq. (47) has the form:

$$K^2 - i\omega = \pm K\sqrt{\frac{\tilde{b}}{2} \pm \frac{1}{2}\sqrt{\tilde{b}^2 - 4\tilde{a}}} \qquad (48)$$

Since we are interested in increasing solutions, it is easy to find the growth rate of large-scale instability from eq. (48):

$$\Gamma = Im\omega = \Lambda K - K^2, \qquad (49)$$

where $\Lambda = \sqrt{\frac{\tilde{b}}{2} \pm \frac{1}{2}\sqrt{\tilde{b}^2 - 4\tilde{a}}}$ is the coefficient for vortex and magnetic perturbations which has a positive value at

$\tilde{b}^2 > 4\tilde{a}$. The maximum growth rate of instability $\Gamma_{max} = \Lambda^2/4$ is achieved for the wave numbers $K_{max} = \Lambda/2$. In the right part of Fig. 9 is shown the dependence of the growth rate Γ of large-scale instability (49) on the wave numbers K for given values of the inclination angle $\theta = \pi/2$, the amplitude of the extenal force $f_0 = 10$ and the dimensionless parameters $D = 2.5$, $Ra = 5$, $Q = 10$, $\overline{B} = 0.5$. The form of this plot is typical for α-effect (see Fig. 6). As in the previous Section, it is convenient to replace the Cartesian projections $D_{1,2}$ and $\overline{B}_{1,2}$ by their projections in the spherical coordinate system (see Fig. 7).
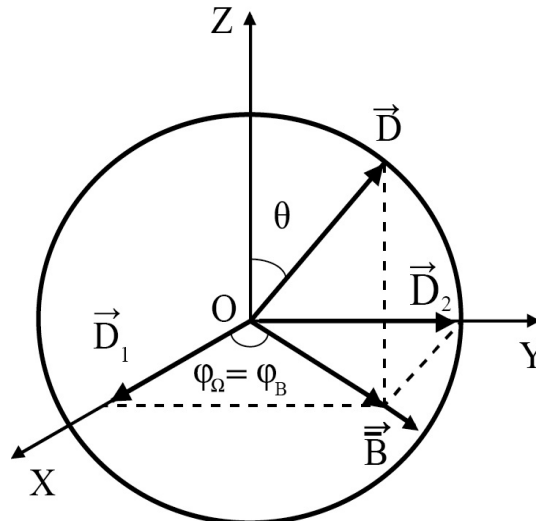
Fig. 7. Here is shown the relationship of the Cartesian projections of the rotation parameter $\vec{D}$ (or the angular velocity vector of rotation $\vec{\Omega}$) with their projections in a spherical coordinate system. The direction of the external magnetic field $\overline{B}$ is chosen so that the angles φ of deviation from the axis OX for the rotation vector φ_Ω and for magnetic field φ_Ω and magnetic field φ_B coincide i.e. $\varphi_\Omega = \varphi_B$.

Now let us analyze the dependences of the growth rate Λ on the effects of rotation D, stratification Ra and the external magnetic field $\overline{B}$. For simplicity assume that $D_1 = D_2$ and $\overline{B}_1 = \overline{B}_2$, and this corresponds to the fixed value of the angle $\varphi_\Omega \approx \varphi_B = \pi/4 + \pi n$, where $n = 0,1,2...k$, k is an integer. In this case the coefficients $\alpha_{1,2}^{(W)}, \alpha_{1,2}^{(H)}, \tilde{\alpha}_H^{(1,2)}, \beta_W^{(1,2)}$ have the form :

$$A = \alpha_1^{(W)} = \alpha_2^{(W)} = f_0^2 \sqrt{2} D\sin\theta \times$$

$$\times \left[\frac{\left(D^2\sin^2\theta - 2Ra - 4\right)(2 - Ra)(4 - Q\overline{B}^2)}{\left((D^2\sin^2\theta - 2Ra)^2 + 16\right)^2} + \frac{Ra(2 - Q\overline{B}^2) + Q\overline{B}^2}{4\left((D^2\sin^2\theta - 2Ra)^2 + 16\right)}\right] \qquad (50)$$

$$B_H = \alpha_1^{(H)} = \alpha_2^{(H)} = \frac{f_0^2}{8} DQ\overline{B}\sin\theta \times$$

$$\times\left[\frac{4(4-Q\overline{B}^2)(2-Ra)\left(2(D^2\sin^2\theta-2Ra)+(Ra+1)^2+7\right)}{\left(16+(D^2\sin^2\theta-2Ra)^2\right)^2}+\frac{Q\overline{B}^2-4(Ra-1)}{16+(D^2\sin^2\theta-2Ra)^2}\right],\qquad(51)$$

$$A_H=\tilde{\alpha}_H^{(1)}=\tilde{\alpha}_H^{(2)}=\frac{f_0^2\sqrt{2}}{2}\cdot\frac{D\left(2+Ra-\dfrac{Q\overline{B}}{2}+\dfrac{\sqrt{2}}{2}(2+Ra)\overline{B}\right)\sin\theta}{(D^2\sin^2\theta-2Ra)^2+16}-$$

$$-f_0^2\cdot\frac{2D\overline{B}(2+Ra)\sin\theta}{\left((D^2\sin^2\theta-2Ra)^2+16\right)^2}\cdot\left((2(D^2\sin^2\theta-2Ra)+(Ra+1)^2+7\right),\qquad(52)$$

$$B_W=\beta_W^{(1)}=\beta_W^{(2)}=f_0^2\cdot\frac{4D\overline{B}(2+Ra)\sin\theta}{\left((D^2\sin^2\theta-2Ra)^2+16\right)^2}\cdot\left(D^2\sin^2\theta-2Ra-4\right)-$$

$$-\frac{f_0^2}{4}\cdot\frac{D\overline{B}Ra\sin\theta}{(D^2\sin^2\theta-2Ra)^2+16}.\qquad(53)$$
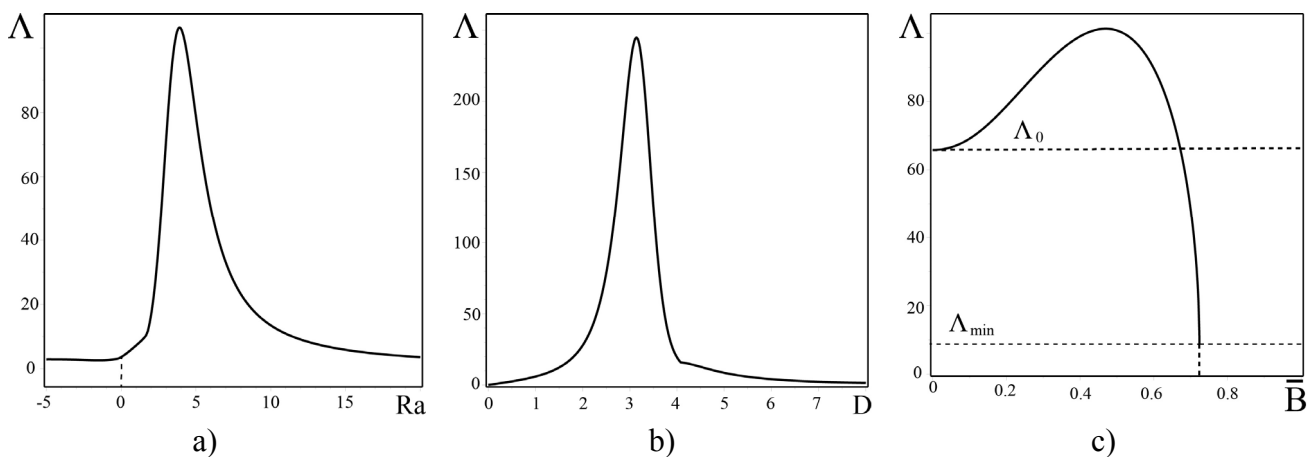
Fig. 8. a) is the plot of the dependence of the Λ -effect on the stratification parameter of the medium Ra (the Rayleigh number); b) is the plot of the dependence of the Λ -effect on the parameter of rotation of the medium D ; c) is the plot of the dependence of the Λ -effect on the external magnetic field $\overline{B}$.

Fig. 8a shows the dependence of the coefficient Λ on the Rayleigh number Ra at the fixed latitude values $\theta=\pi/2$ and the dimensionless numbers $D=2.5$, $Q=10$, $\overline{B}=0.2$. Assume that the amplitude of the external force $f_0=10$. In Fig. 8a the value of the coefficient Λ at $Ra=0$ (homogeneous medium) are shown by dashed lines. We can see, with the increase of the Rayleigh number $Ra\to5$ the coefficient Λ considerably exceeds its value for a homogeneous medium, i.e. reaches its peak magnitude. Further increase of the parameter Ra leads to a drop of the value of Λ and, consequently, to less intense generation of the magneto-vortex perturbations. Let us choose the Rayleigh number e.g. on the level of $Ra=5$ and find the dependence of the coefficient Λ on the rotation parameter D at the external magnetic field $\overline{B}=0.2$ and $Q=10$. The plot presented in Fig. 8b shows the dependence $\Lambda(D)$. Here we observe the increase of Λ to a certain maximum value Λ_{max} for $D\approx3$. With the increase of the parameter D the value of Λ diminishes, and generation of magneto-vortex perturbations becomes less efficient. «Fast» rotation of the medium also suppresses the considered Λ -effect. To clarify the influence of the homogeneous magnetic field $\overline{B}$ on Λ -effect, let us consider the following parameters: $D=2.5$, $Ra=5$, $Q=10$. Fig. 8c presents the dependence $\Lambda(\overline{B})$. The upper dashed line indicates the level Λ_0 corresponding to the case when the external magnetic field is absent: $\overline{B}=0$. As seen from this figure, the increase of the magnetic field value gives intensification of the magneto-

vortex pertubations up to a certain level $\Lambda_{max} \sim 100$. The lower dashed line in Fig. 8c shows the minimum level of the coefficient $\Lambda_{min} \approx 9.63$ which corresponds to the value of the magnetic field $\overline{B} \approx 0.72$ for the given parameters D, Ra and Q. This implies that «strong» external magnetic field suppresses the considered Λ-effect. For the parameters $D = 2.5$, $Ra = 5$, $Q = 10$ and $\overline{B} = 0.5$ one can find the dependence of the coefficient Λ on the angle of deviation θ for the vector of the angular rotation velocity $\vec{\Omega}$ from the vertical direction OZ. This function $\Lambda(\theta)$ is presented in the left part of Fig. 9.
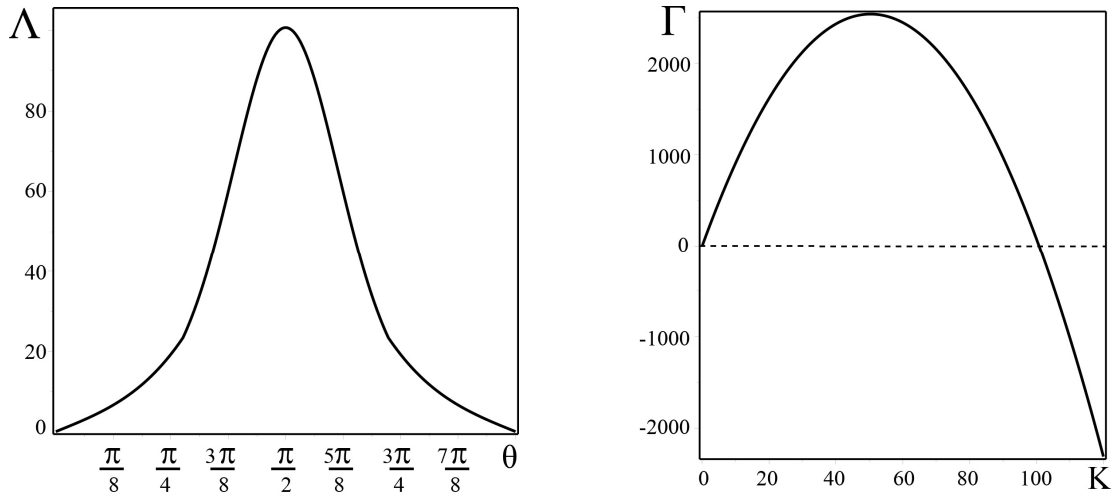
Fig. 9. On the left the plot of the dependence of the Λ-effect on the angle of inclination θ of the angular velocity vector $\vec{\Omega}$; on the right the plot of the dependence of the instability increment for the Λ-effect on the wave numbers K.

The generation magneto-vortex perturbations does not occur $(\Lambda \to 0)$ at $\theta \to 0$ or $\theta \to \pi$ (the pole), whereas at $\theta \to \pi/2$ (the equator) is more effective.

NONLINEAR STATIONARY STRUCTURES

When the amplitude of the perturbations $W_{1,2}$ and $H_{1,2}$ increase due to the development of large-scale instability, the linear theory which we consider in the previous Section becomes inapplicable. The evolution of these perturbations is described by the nonlinear system of eqs. (27)-(30). Now study the instability saturation which leads to the formation of nonlinear stationary structures. To describe these structures, let us put $\partial_T W_1 = \partial_T W_2 = \partial_T H_1 = \partial_T H_2 = 0$ in the system of eqs. (27)-(30), and then integrate these equations over to Z:

$$\frac{d\tilde{W}_1}{dZ} = -\frac{f_0^2 \sqrt{2} D q_2 Q_2}{16\tilde{W}_2^2 q_2^2 \tilde{Q}_2^2 + \left[D^2 + 2(1-\tilde{W}_2^2) + 2\mu_2\right]^2 + 4\xi_2} + C_1 \tag{54}$$

$$\frac{d\tilde{W}_2}{dZ} = \frac{f_0^2 \sqrt{2} D q_1 Q_1}{16\tilde{W}_1^2 q_1^2 \tilde{Q}_1^2 + \left[D^2 + 2(1-\tilde{W}_1^2) + 2\mu_1\right]^2 + 4\xi_1} + C_2 \tag{55}$$

$$\frac{dH_1}{dZ} = \frac{f_0^2 \sqrt{2} D \tilde{W}_2 \tilde{Q}_2 (2H_2 + \overline{B}\sqrt{2})}{(1+\tilde{W}_2^2)\left[16\tilde{W}_2^2 q_2^2 \tilde{Q}_2^2 + \left[D^2 + 2(1-\tilde{W}_2^2) + 2\mu_2\right]^2 + 4\xi_2\right]} + C_3 \tag{56}$$

$$\frac{dH_2}{dZ} = -\frac{f_0^2 \sqrt{2} D \tilde{W}_1 \tilde{Q}_1 (2H_1 + \overline{B}\sqrt{2})}{(1+\tilde{W}_1^2)\left[16\tilde{W}_1^2 q_1^2 \tilde{Q}_1^2 + \left[D^2 + 2(1-\tilde{W}_1^2) + 2\mu_1\right]^2 + 4\xi_1\right]} + C_4 \tag{57}$$

Here $\tilde{W}_1 = 1 - W_1$, $\tilde{W}_2 = 1 - W_2$; C_1, C_2, C_3 and C_4 are arbitrary integration constants. In order to obtain eqs.

(54)-(57) we put the Prandtl numbers $Pr = Pm = 1$, and substitute the Cartesian projections for $D_{1,2}$ and $\overline{B}_{1,2}$ in the coefficients $\alpha_{(1,2)}$, $\alpha_H^{(1,2)}$ by their projections in the spherical coordinate system (see Fig. 7). For simplicity we use the values of the angles $\varphi_\Omega = \varphi_B = \pi/4$ and $\theta = \pi/2$. In this case, the expressions for $q_{1,2}$, $Q_{1,2}$, $\tilde{Q}_{1,2}$, $\mu_{1,2}$, $\sigma_{1,2}$, $\chi_{1,2}$, $\xi_{1,2}$ are also simplified:

$$q_{1,2} = 1 + \frac{QH_{1,2}(2H_{1,2} + \overline{B}\sqrt{2})}{2(1 + \tilde{W}_{1,2}^2)} - \frac{Ra}{1 + \tilde{W}_{1,2}^2}, \qquad Q_{1,2} = 1 - \frac{Q(2H_{1,2} + \overline{B}\sqrt{2})^2}{4(1 + \tilde{W}_{1,2}^2)},$$

$$\mu_{1,2} = QH_{1,2}(2H_{1,2} + \overline{B}\sqrt{2}) + Q^2 H_{1,2}^2 (2H_{1,2} + \overline{B}\sqrt{2})^2 \cdot \frac{1 - \tilde{W}_{1,2}^2}{4(1 + \tilde{W}_{1,2}^2)} -$$

$$- Ra \cdot \frac{1 + \tilde{W}_{1,2}^2 + QH_{1,2}(2H_{1,2} + \overline{B}\sqrt{2}) \cdot \frac{1 - \tilde{W}_{1,2}^2}{1 + \tilde{W}_{1,2}^2}}{1 + \tilde{W}_{1,2}^2},$$

$$\xi_{1,2} = 2\Xi_{1,2} + 2\tilde{W}_{1,2}^2 \Pi_{1,2} - 2\tilde{W}_{1,2}^2(1 - \tilde{Q}_{1,2}^2)\Pi_{1,2} - 2(1 - q_{1,2}^2)\Xi_{1,2} + \Xi_{1,2}\Pi_{1,2} + \chi_{1,2}\tilde{W}_{1,2}^2 + \chi_{1,2}(1 + \sigma_{1,2}),$$

$$\Xi_{1,2} = -\frac{4\tilde{W}_{1,2}^2 \tilde{Q}_{1,2} Ra}{1 + \tilde{W}_{1,2}^2} + \frac{2\tilde{W}_{1,2}^2 Ra^2}{\left(1 + \tilde{W}_{1,2}^2\right)^2} + Ra \cdot \frac{1 + \tilde{W}_{1,2}^2 + QH_{1,2}(2H_{1,2} + \overline{B}\sqrt{2}) \cdot \frac{1 - \tilde{W}_{1,2}^2}{1 + \tilde{W}_{1,2}^2}}{1 + \tilde{W}_{1,2}^2},$$

$$\Pi_{1,2} = \frac{4 q_{1,2} Ra}{1 + \tilde{W}_{1,2}^2} + \frac{2 Ra^2}{\left(1 + \tilde{W}_{1,2}^2\right)^2} - Ra \cdot \frac{1 + \tilde{W}_{1,2}^2 + QH_{1,2}(2H_{1,2} + \overline{B}\sqrt{2}) \cdot \frac{1 - \tilde{W}_{1,2}^2}{1 + \tilde{W}_{1,2}^2}}{1 + \tilde{W}_{1,2}^2},$$

$$\sigma_{1,2} = \frac{QH_{1,2}(2H_{1,2} + \overline{B}\sqrt{2})}{4(1 + \tilde{W}_{1,2}^2)} \cdot \left[4(1 + \tilde{W}_{1,2}^2) + QH_{1,2}(2H_{1,2} + \overline{B}\sqrt{2}) \right],$$

$$\chi_{1,2} = \frac{Ra}{1 + \tilde{W}_{1,2}^2} \cdot \left[Ra - \left(2(1 - \tilde{W}_{1,2}^2) + QH_{1,2}(2H_{1,2} + \overline{B}\sqrt{2}) \right) \right],$$

$$\tilde{Q}_{1,2} = 1 - \frac{QH_{1,2}(2H_{1,2} + \overline{B}\sqrt{2})}{2(1 + \tilde{W}_{1,2}^2)} + \frac{Ra}{1 + \tilde{W}_{1,2}^2}.$$

Eqs. (54)-(57) constitute the nonlinear dynamic system in 4-dimensional phase space in which phase flow divergence is (equal to) zero. Therefore, the system of eqs. (54)-(57) is conservative. The search for the Hamiltonian of this system is a very difficult task, as the integration is complicated by the dependence of the nonlinear coefficients $\alpha_{(1,2)}$, $\alpha_H^{(1,2)}$ on the fields ($\vec{W}$, $\vec{H}$), that takes it beyond the class of elementary functions. A complete qualitative analysis of this system is extremely complicated because of a high dimensionality of the phase space and large number of the parameters in the system. According to the general ideas, we can expect that this system of conservative equations may contain structures of resonance and non-resonance tori in the phase space and, consequently, chaotic stationary structures of hydrodynamic and magnetic fields. The considered system of nonlinear eqs. (54)-(57) can be studied using the Poincaré cross-section method.

STATIONARY CHAOTIC STRUCTURES IN THE ABSENCE OF EXTERNAL MAGNETIC FIELD $\overline{B} = 0$.

Let us build the Poincaré cross-sections using the standard Mathematica programs for the trajectories in the phase space for the case of rotating electroconductive fluid stratifified with respect to temperature ($Ra \neq 0$) without the external magnetic field $\overline{B} = 0$. All the numerical calculations are performed for the following parameters: $f_0 = 10$, $D = 2$, $Q = 1$, $Ra = 0.1$ and the constants $C_1 = 1, C_2 = -1$, $C_3 = -0.5, C_4 = 0.5$. For the initial conditions $W_1(0) = 1.25$, $\tilde{W}_2(0) = 1.25$, $H_1(0) = 1.4$, $H_2(0) = 1.4$ the Poincaré cross-sections presented in Fig. 10a-10b demonstrate regular trajectories for the velocity and magnetic fields. With the increase of the initial perturbation velocity $\tilde{W}_1(0) = 1.398$, $\tilde{W}_2(0) = 1.398$, $H_1(0) = 1.4$, $H_2(0) = 1.4$ the regular trajectories become chaotic. They correspond to the Poincaré cross-sections shown in Fig. 10c-10d.

Fig. 10. In the figures a) and b) are shown the Poincaré sections for a trajectory with initial conditions $\tilde{W}_1(0) = 1.25$, $\tilde{W}_2(0) = 1.25$, $H_1(0) = 1.4$, $H_2(0) = 1.4$. These are trajectories of regular type, which are wound on the tori. The figures c) and d) correspond to Poincaré sections for a trajectory with initial conditions $\tilde{W}_1(0) = 1.398$, $\tilde{W}_2(0) = 1.398$, $H_1(0) = 1.4$, $H_2(0) = 1.4$. These pictures show stochastic layers, to which belong the corresponding chaotic trajectories. The calculations were carried out for the case $\overline{B} = 0$.

Fig. 11a-11d present the dependence of the stationary large-scale fields on the altitude Z. It was obtained numerically for the initial conditions corresponding to the Poincaré cross-sections presented in Fig. 10a-10d. These figures show also the emergence of stationary chaotic solutions for magnetic and vortex fields. To prove the existence of chaotic regime of stationary large-scale fields, we use also the method of autocorrelated function. As is known (see

e.g. [52]), the autocorrelated function $K(\tau)$ is the value which characterizes the intensity of chaos. It is defined as averaging of the product of random functions $P(t)$ and $P(t+\tau)$ at the moment of time t and $t+\tau$, respectively, over «large» interval of time Δt : $K(\tau) = \lim\limits_{\Delta t \to \infty} \dfrac{1}{\Delta t} \int\limits_0^{\Delta t} P(t)P(t+\tau)dt$. So we consider the coordinate Z as the time t, whereas the product $P(t)P(t+\tau)$ consists of 16 components:

$$P(t)P(t+\tau) = \begin{bmatrix} \tilde{W}_1(t) \\ \tilde{W}_2(t) \\ H_1(t) \\ H_2(t) \end{bmatrix} \begin{bmatrix} \tilde{W}_1(t+\tau) & \tilde{W}_2(t+\tau) & H_1(t+\tau) & H_2(t+\tau) \end{bmatrix}$$

a)

b)

c)

d)

Fig. 11. The upper plots (a), b)) show the dependence of the velocity and magnetic field on the height Z for the numerical solution of equations (54)-(57) with the initial conditions $\tilde{W}_1(0) = 1.25$, $\tilde{W}_2(0) = 1.25$, $H_1(0) = 1.4$, $H_2(0) = 1.4$. This dependence corresponds to regular motions of the Poincaré section which are shown in Fig. 10a-10b. Plots (c),d)) show the similar dependence for the numerical solution of equations (54)-(57) with the initial conditions: $\tilde{W}_1(0) = 1.398$, $\tilde{W}_2(0) = 1.398$, $H_1(0) = 1.4$, $H_2(0) = 1.4$. This chaotic dependence corresponds to the Poincaré sections in Fig. 10c-10d.

Fig. 12. The plot of the dependence of the autocorrelation function $K_{\tilde{W}_1\tilde{W}_1}$ on time τ for a trajectory with initial conditions

$\tilde{W}_1(0) = 1.398$, $\tilde{W}_2(0) = 1.398$, $H_1(0) = 1.4$, $H_2(0) = 1.4$ (chaotic motion).

Fig. 13. A rectilinear dependence of the autocorrelation function $K_{\tilde{W}_1\tilde{W}_1}$ in logarithmic scales from the time interval τ for strongly chaotic motion.

The plot of the dependence of the autocorrelated function for the component $K_{\tilde{W}_1\tilde{W}_1}$ on the time τ is presented in Fig. 12. The case of chaotic motion corresponds to the section of the trajectory with the exponential decay of the function $K_{\tilde{W}_1\tilde{W}_1}$. It is evident that in this region, the autocorrelation function $K_{\tilde{W}_1\tilde{W}_1}$ on a logarithmic scale is approximated as a straight line (see Fig. 13). The data presented in Fig. 13 allow to determine the characteristic correlation time $\tau_{cor} \approx 1324$ of the stationary random process $P_{\tilde{W}_1}$. If we take into account the introduced definition of «time» t, it becomes clear that we have found the estimated value of the altitude $Z_{cor} \approx 1324$ corresponding to onset of chaotic motion of the large-scale fields. In Fig. 11c-11в are shown the chaotic solutions for the velocity and magnetic fields of $Z \approx 90$ height which is much less than Z_{cor}. However, even in this case one can see the start of the complex intricate trajectory for the large-scale fields with the increase of the altitude Z. Therefore, such trajectories cannot be plotted. Thus, with the increase of the altitude Z up to critical value Z_{cor}, the quasi-periodic motion of the stationary large-scale fields becomes chaotic.

STATIONARY CHAOTIC STRUCTURES IN THE PRESENCE OF EXTERNAL MAGNETIC FIELD $\overline{B} \neq 0$.

Using the standard Matematica programs we construct the Poincaré cross-sections of trajectories in the phase space for the nonlinear system of eqs. (54)-(57) with the external homogeneous magnetic field. All the numerical calculations are carried out for the following dimensionless parameters: $f_0 = 10$, $D = 2$, $Q = 1$, $Ra = 0.1$, $\overline{B} = 0.1$ and the constants $C_1 = 1, C_2 = -1$, $C_3 = -0.5, C_4 = 0.5$. In Fig. 14a-14b are shown regular trajectories of

the velocity and magnetic fields built at the numerical solutions of eqs. (54)-(57) with the following initial conditions : $\tilde{W}_1(0) = 1.31$, $\tilde{W}_2(0) = 1.31$, $H_1(0) = 1.4$, $H_2(0) = 1.4$. These trajectories correspond to quasi-periodic character of motion for large-scale perturbations of the velocity $(\tilde{W}_{1,2})$ and magnetic fields $(H_{1,2})$. By increasing only the amplitudes of the initial values of perturbations for the magnetic field $\tilde{W}_1(0) = 1.31$, $\tilde{W}_2(0) = 1.31$, $H_1(0) = 1.8$, $H_2(0) = 1.8$ we find that the quasi-periodic motion transforms into chaotic. This case demonstrates the Poincaré cross-sections shown in Fig. 14c-14d.
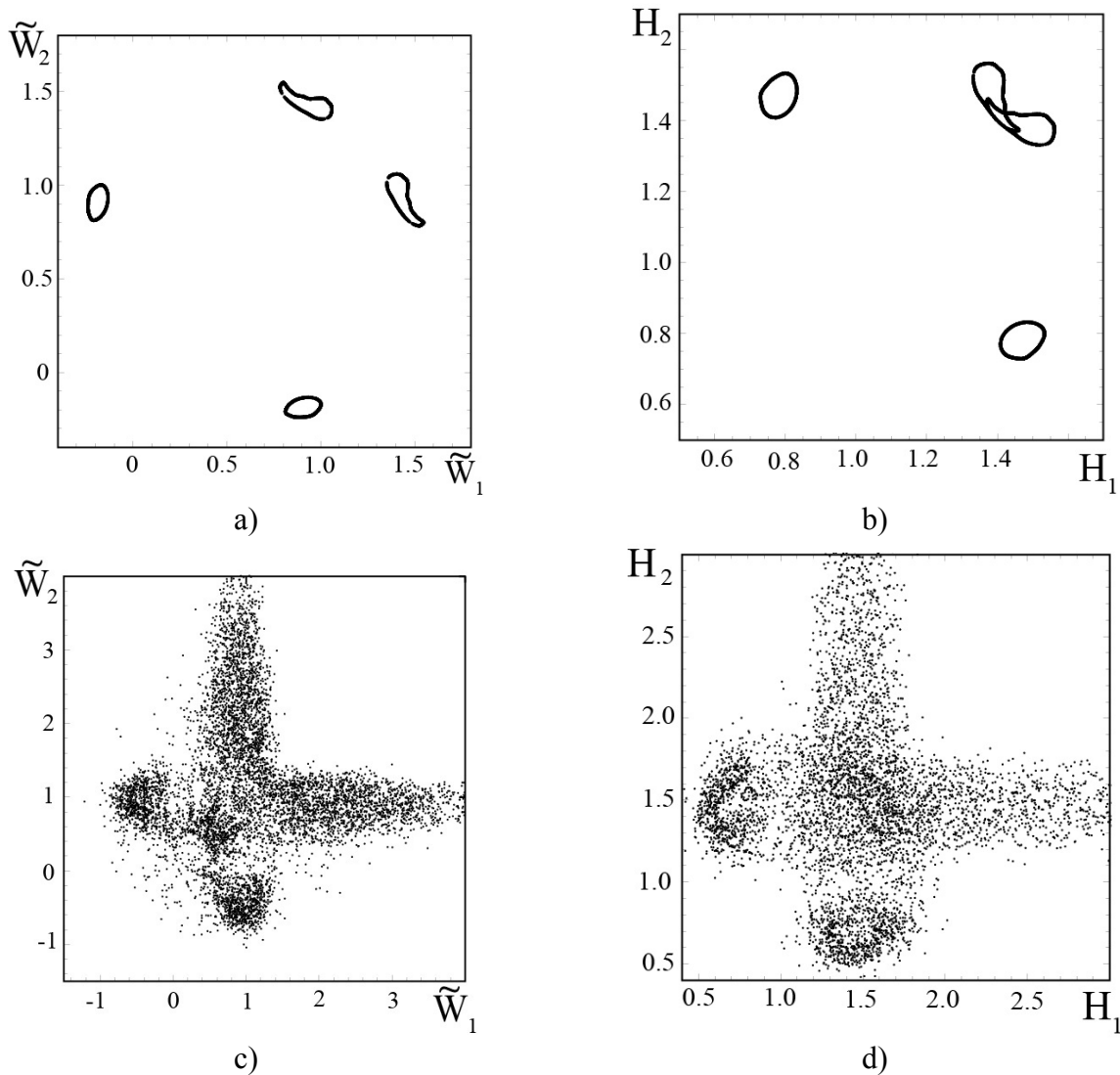

a)

b)

c)

d)
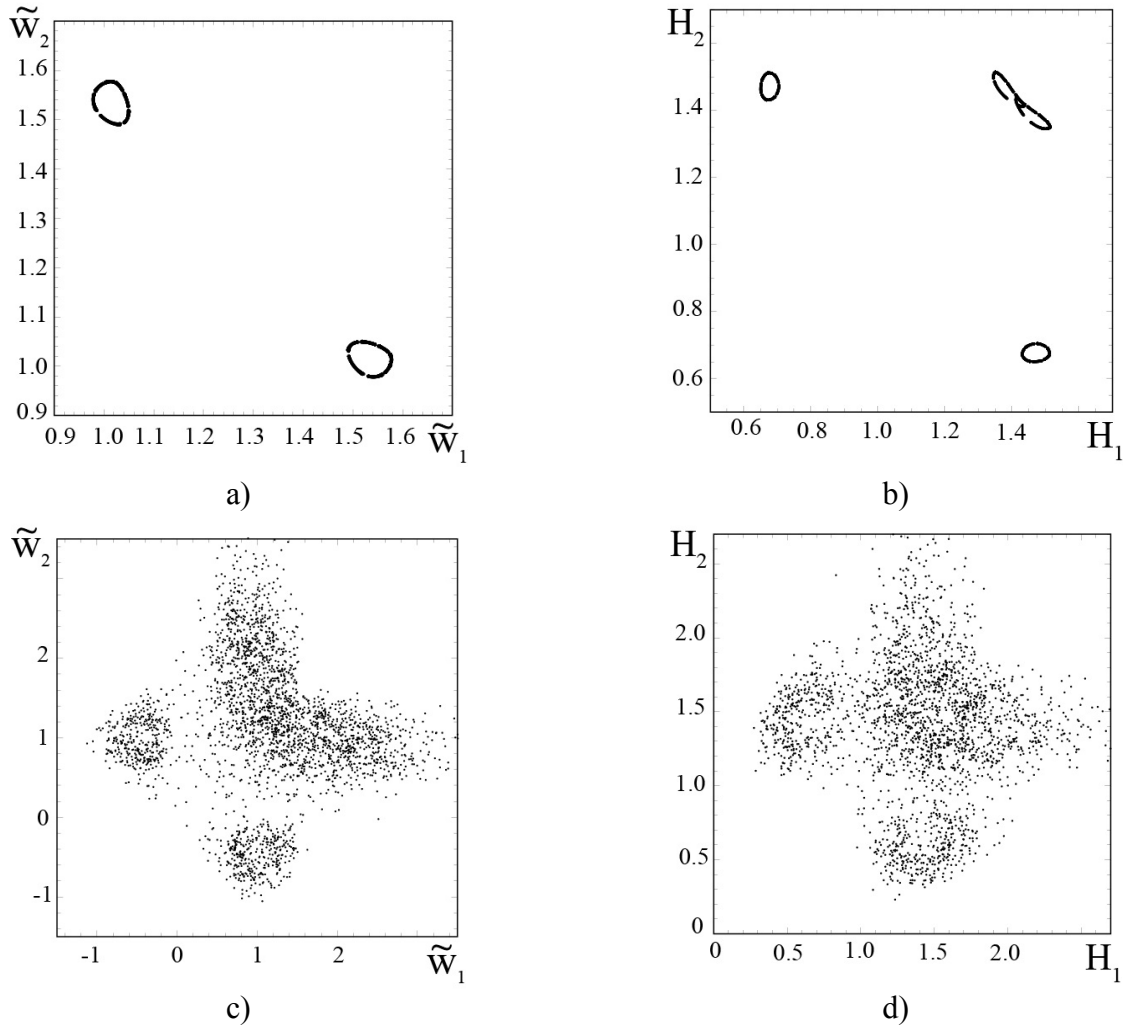
Fig. 14. The figures a) and b) shown the Poincaré sections for a trajectory with initial conditions $\tilde{W}_1(0) = 1.31$, $\tilde{W}_2(0) = 1.31$, $H_1(0) = 1.4$, $H_2(0) = 1.4$. This is a regular type of trajectory, which is wound on the tori. The figures c) and d) correspond to Poincaré sections for a trajectory with initial conditions $\tilde{W}_1(0) = 1.31$, $\tilde{W}_2(0) = 1.31$, $H_1(0) = 1.8$, $H_2(0) = 1.8$. These pictures show stochastic layers, to which belongs the corresponding chaotic trajectory. The calculations were carried out for the case $\overline{B} = 0.1$.

Using the initial data for the regular ($\tilde{W}_1(0) = 1.31$, $\tilde{W}_2(0) = 1.31$, $H_1(0) = 1.4$, $H_2(0) = 1.4$) and chaotic ($\tilde{W}_1(0) = 1.31$, $\tilde{W}_2(0) = 1.31$, $H_1(0) = 1.8$, $H_2(0) = 1.8$) trajectories, we can build numerically the dependence of the stationary large-scale fields on the altitude Z (see Fig. 15a-15d). The emergence of stationary chaotic solutions for the magnetic and vortex fields is also shown in Fig. 15c-15d. To confirm the onset of chaotic regime of the stationary large-scale fields we plot the dependence of the autocorrelated function for the component $K_{\tilde{W}_1 \tilde{W}_1}$ on time τ (see Fig. 16). The trajectories of chaotic motion correspond to the part of the plot with the exponential decay of function $K_{\tilde{W}_1 \tilde{W}_1}$ in Fig. 16. In the logarithmic scale of the autocorrelated function $K_{\tilde{W}_1 \tilde{W}_1}$ this part is approximated by a straight line (see Fig. 17). Using this plot it is easy to find the estimated value of the characteristic correlation time for a stationary random process: $\tau_{cor} \approx 2000$. The obtained value of the correlation time corresponds to the altitude

$Z_{cor} \approx 2000$. Above this value arise strongly chaotic stationary structures of the large-scale fields. In Fig. 15c-15d are shown chaotic solutions for the velocity and magnetic fields at the altitude $Z \approx 50$ which is significantly less than Z_{cor} . It is evident that for Z tending to a critical value Z_{cor} the motion trajectories become more intricate and, finally, completely chaotic.

a)   b)

c)   d)
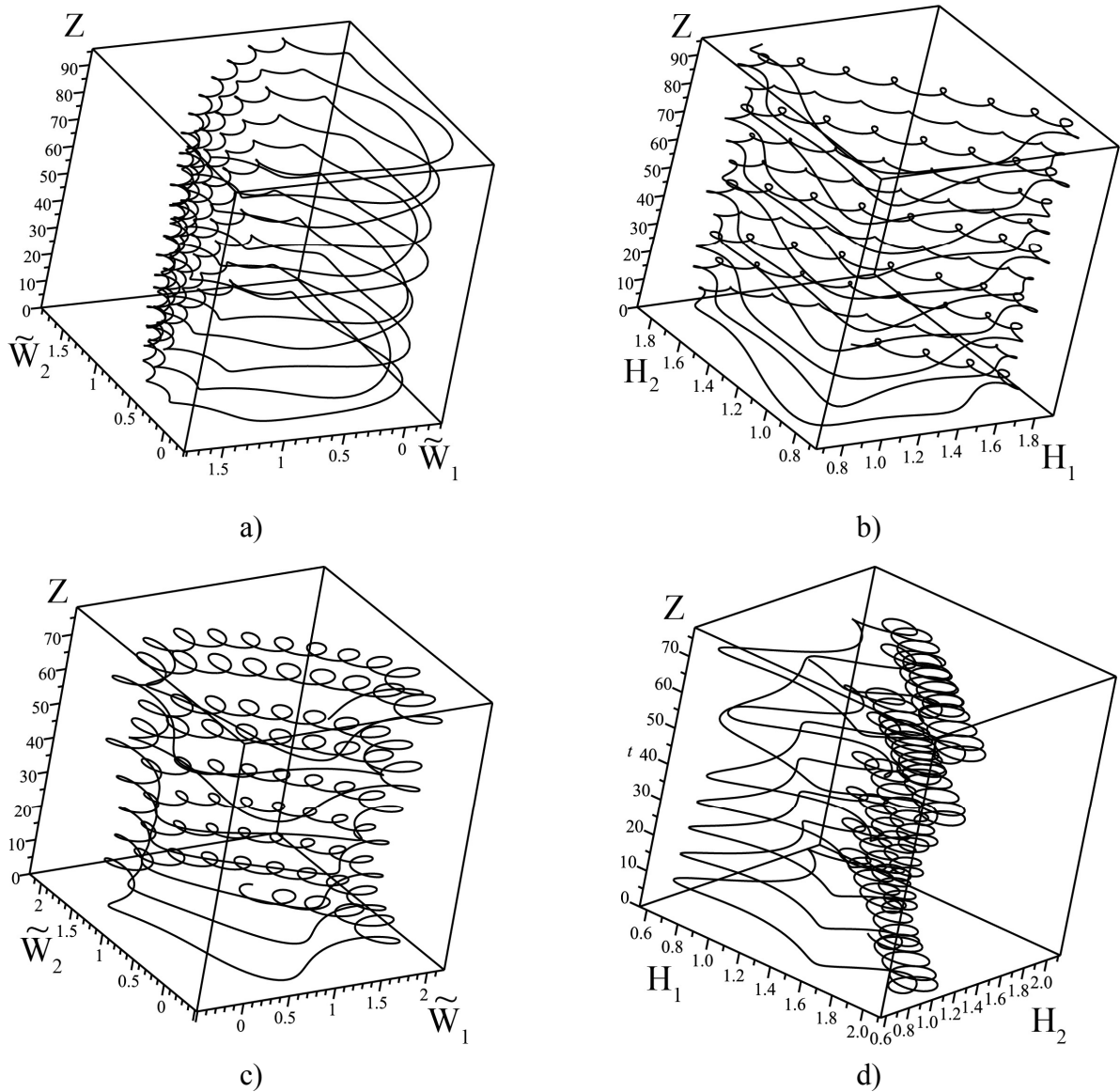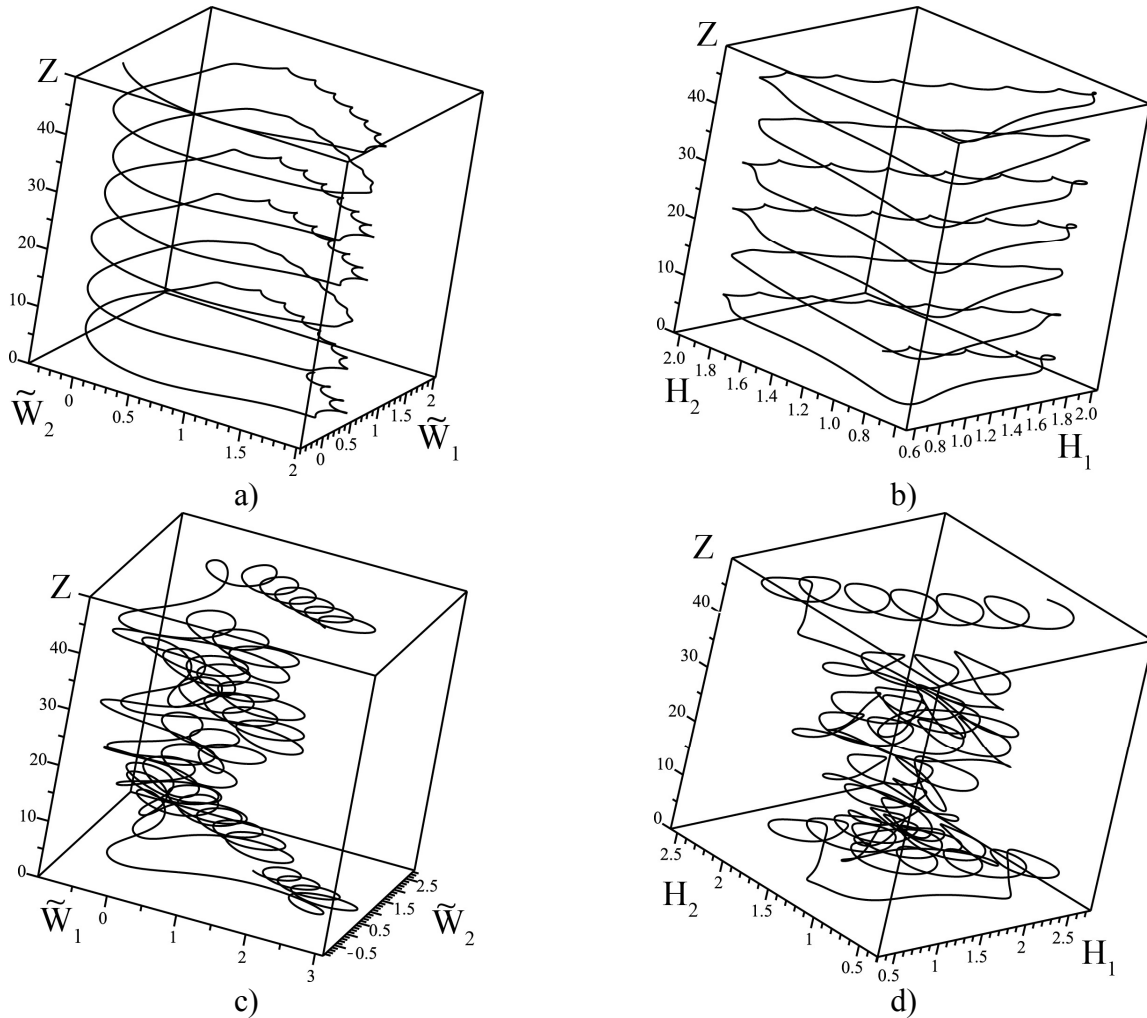
Fig. 15. The upper part (a),b)) shows the dependence of the velocity and magnetic field on the height Z for the numerical solution of equations (54)-(57) with the initial conditions $\tilde{W}_1(0) = 1.31$, $\tilde{W}_2(0) = 1.31$, $H_1(0) = 1.4$, $H_2(0) = 1.4$. This dependence corresponds to regular motions of the Poincaré section shown on top of Fig. 14a-14b. Below (c), d)) show a similar dependence for the numerical solution of equations (54)-(57) with the initial conditions: $\tilde{W}_1(0) = 1.31$, $\tilde{W}_2(0) = 1.31$, $H_1(0) = 1.8$, $H_2(0) = 1.8$. This chaotic dependence corresponds to the Poincaré sections shown at the bottom in Fig. 14c-14d
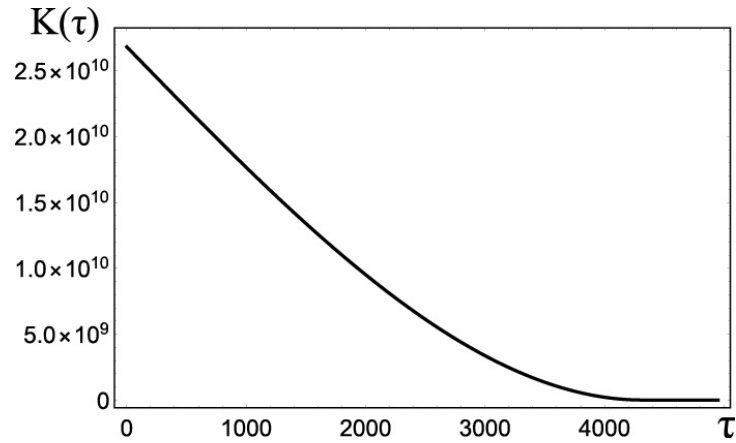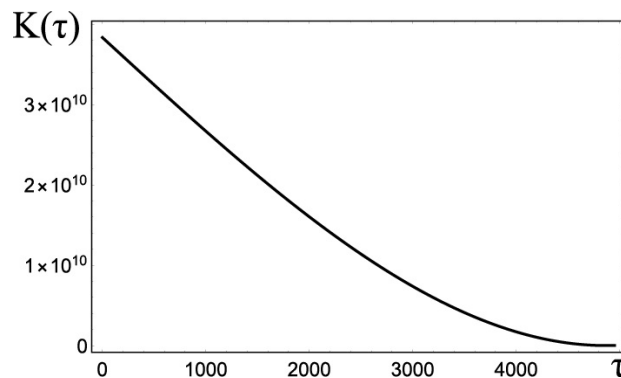

Fig. 16. The plot of the dependence of the autocorrelation function $K_{\tilde{W}_1 \tilde{W}_1}$ on time τ for a trajectory with initial conditions

$\tilde{W}_1(0) = 1.31$, $\tilde{W}_2(0) = 1.31$, $H_1(0) = 1.8$, $H_2(0) = 1.8$ (chaotic motion) on condition $\overline{B} = 0.1$.
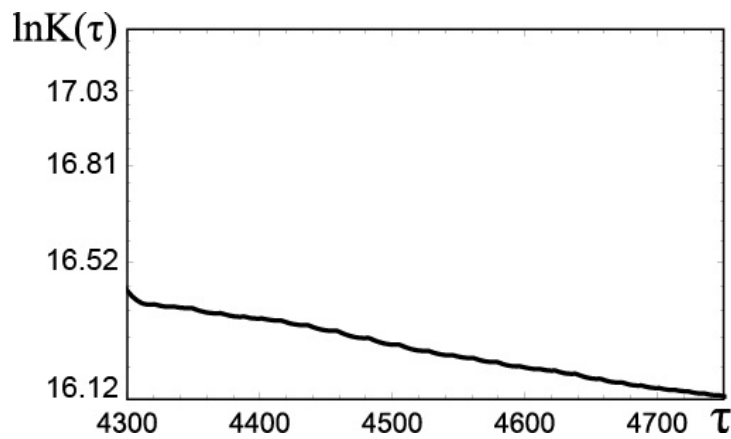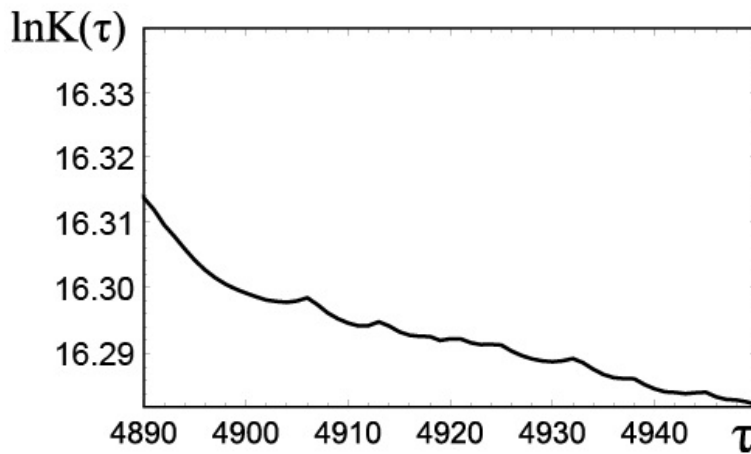
Fig. 17. A rectilinear dependence of the autocorrelation function $K_{\tilde{W}_1 \tilde{W}_1}$ in logarithmic scales from the time interval τ for strongly

chaotic motion on condition $\overline{B} = 0.1$.

CONCLUSION

In this work we have obtained the closed system of nonlinear equations for vortex and magnetic large-scale perturbations (magneto-vortex dynamo) in an obliquely rotating stratified electroconductive fluid in external uniformly magnetic field. At the initial stage small amplitudes of large-scale perturbations increase due to the average helicity

$\overline{\vec{v}_0 rot \vec{v}_0} \neq 0$ of small-scale motion in a rotating stratified electroconductive fluid excited by the external non-helical

force $\vec{F}_0 rot \vec{F}_0 = 0$. The mechanism of amplification of the large-scale perturbations is associated with the

development of large-scale instability of α -effect type. In the absence of external magnetic field $(\overline{\vec{B}} = 0)$ the linear equations of magneto-vortex dynamo are split into two subsystems: vortex and magnetic ones. In this case the large-scale vortex and magnetic perturbations are generated du to the development of the instability of HD α -effect and

MHD α -effect, respectively. Both instabilities occur when the vector of angular rotation velocity $\vec{\Omega}$ is deflected from the vertical axis OZ . Unlike the case of a homogeneous medium [46-47], the combined effects of rotarion and stratification of the medium (at heating from below) give rise to an essential amplification of the large-scale perturbations.This phenomenon becomes especially noticeable at the parameters of the medium $D \to 3$ and $Ra \to 5$ (see Fig. 3). In this case arises the mode of the maximal generation of the small-scale helical motion caused by the

action of the Coriolis force and temperature inhomogeneity. With the external magnetic field $(\overline{\vec{B}} \neq 0)$ the evolution of the vortex and magnetic perturbations is characterized by a positive feedback due to which the growth rate of the vortex and magnetic large-scale perturbations coincide. The «weak» external magnetic field favours generation of the perturbations, whereas «strong» field suppresses them (see Fig. 8c). Generation of the large-scale vortex and magnetic

perturbations also depends on the angle of deflection of the vector of angular rotation velocity $\vec{\Omega}$. It is minimal at $\theta \to 0$ or $\theta \to \pi$ (nearby the poles) and maximal at $\theta \to \pi/2$ (nearby the equator) (see the left part of Fig. 9). The performed analysis of the influence of rotation on the growth of the vortex and magnetic perturbations shows that at «fast» rotation they are suppressed. With the rise of the perturbation amplitude the instability is stabilized and then becomes stationary. With these conditions arise the nonlinear stationary vortex and magnetic structures. The dynamic system of equations which describes these structures is a Hamiltonian system in a four-dimensional phase space. The possibility of the existence of the large-scale chaotic vortex and magnetic fields in stationary mode is proved by

numerical methods. In the absence of external magnetic field $(\overline{\vec{B}} = 0)$ stationary chaotic structures arise in a rotating

stratified electroconductive fluid at the increase of the initial velocity of perturbations $\tilde{W}_{1,2}(0)$. With the external

magnetic field $(\overline{\vec{B}} \neq 0)$ these structures are formed at the rise of the initial values of the perturbed field $H_{1,2}(0)$.

APPENDIX
A. MULTI-SCALE ASYMPTOTIC EXPANSIONS

Let us consider the algebraic structure of the asymptotic expansion of eqs.(10)-(13) in different orders in R starting with the lowest of them. In the order R^{-3} we have only one equation:

$$\partial_i P_{-3} = 0 \quad \Rightarrow \quad P_{-3} = P_{-3}(X) \tag{58}$$

In the order R^{-2} there is the following equation:

$$\partial_i P_{-2} = 0 \quad \Rightarrow \quad P_{-2} = P_{-2}(X) \tag{59}$$

Eqs. (58) and (59) are satisfied automatically, since P_{-3} and P_{-2} are the functions of «slow» variables only. In the order R^{-1} we obtain the system of equations :

$$\partial_t W_{-1}^i + W_{-1}^k \partial_k W_{-1}^i = -\partial_i P_{-1} - \nabla_i P_{-3} + \partial_k^2 W_{-1}^i + \varepsilon_{ijk} W_j D_k +$$

$$+ \tilde{Q} \varepsilon_{ijk} \varepsilon_{jml} \partial_m B_{-1}^l B_{-1}^k + \tilde{Q} \varepsilon_{ijk} \varepsilon_{jml} \partial_m B_{-1}^l \overline{B_k} + e_i \widetilde{Ra} T_{-1}$$

$$\partial_t B_{-1}^i - Pm^{-1} \partial_k^2 B_{-1}^i = \varepsilon_{ijk} \varepsilon_{knp} \partial_j W_{-1}^n B_{-1}^p + \varepsilon_{ijk} \varepsilon_{knp} \partial_j W_{-1}^n \overline{B_p} \tag{60}$$

$$\partial_t T_{-1} - Pr^{-1} \partial_k^2 T_{-1} = -W_{-1}^k \partial_k T_{-1} + W_{-1}^z$$

$$\partial_i W_{-1}^i = 0, \qquad \partial_i B_{-1}^i = 0$$

The averaging of eqs. (60) over the «fast» variables gives the secular equation :

$$-\nabla_i P_{-3} + \varepsilon_{ijk} W_j D_k + e_i \widetilde{Ra} T_{-1} = 0, \quad W_{-1}^z = 0, \tag{61}$$

which corresponds to geostrophic equilibrium. In the zero order in R we have the following system of equations:

$$\partial_t v_0^i + W_{-1}^k \partial_k v_0^i + v_0^k \partial_k W_{-1}^i = -\partial_i P_0 - \nabla_i P_{-2} + \partial_k^2 v_0^i +$$

$$+ \varepsilon_{ijk} v_0^j D_k + \tilde{Q} \varepsilon_{ijk} \varepsilon_{jml} \left(\partial_m B_{-1}^l B_0^k + \partial_m B_0^l B_{-1}^k \right) + \tilde{Q} \varepsilon_{ijk} \varepsilon_{jml} \partial_m B_0^l \overline{B_k} + e_i \widetilde{Ra} T_0 + F_0^i$$

$$\partial_t B_0^i - Pm^{-1} \partial_k^2 B_0^i = \varepsilon_{ijk} \varepsilon_{knp} \left(\partial_j W_{-1}^n B_0^p + \partial_j v_0^n B_{-1}^p \right) + \varepsilon_{ijk} \varepsilon_{knp} \partial_j v_0^n \overline{B_p} \tag{62}$$

$$\partial_t T_0 - Pr^{-1} \partial_k^2 T_0 = -W_{-1}^k \partial_k T_0 - \partial_k (v_0^k T_{-1}) + v_0^z$$

$$\partial_i v_0^i = 0, \quad \partial_i B_0^i = 0$$

These equations give only one secular term:

$$\nabla P_{-2} = 0 \quad \Rightarrow \quad P_{-2} = const$$

Now consider the first-order approximation R^1 :

$$\partial_t v_1^i + W_{-1}^k \partial_k v_1^i + v_0^k \partial_k v_0^i + v_1^k \partial_k W_{-1}^i + W_{-1}^k \nabla_k W_{-1}^i = -\nabla_i P_{-1} - \partial_i \left(P_1 + \overline{P_1} \right) + \partial_k^2 v_1^i + 2 \partial_k \nabla_k W_{-1}^i + \varepsilon_{ijk} v_1^j D_k +$$

$$+ \tilde{Q} \varepsilon_{ijk} \varepsilon_{jml} \left(\partial_m B_{-1}^l B_1^k + \partial_m B_0^l B_0^k + \partial_m B_1^l B_{-1}^k + \nabla_m B_{-1}^l B_{-1}^k \right) + \tilde{Q} \varepsilon_{ijk} \varepsilon_{jml} \left(\partial_m B_1^l \overline{B_k} + \nabla_m B_{-1}^l \overline{B_k} \right) + e_i \widetilde{Ra} T_1$$

$$\partial_i B_1^i - Pm^{-1} \partial_k^2 B_1^i - Pm^{-1} 2 \partial_k \nabla_k B_{-1}^i = \varepsilon_{ijk} \varepsilon_{knp} \left(\partial_j W_{-1}^n B_1^p + \partial_j v_0^n B_0^p + \partial_j v_1^n B_{-1}^p + \nabla_j W_{-1}^n B_{-1}^p \right) + \tag{63}$$

$$+ \varepsilon_{ijk} \varepsilon_{knp} \left(\partial_j v_1^n \overline{B_p} + \nabla_j W_{-1}^n \overline{B_p} \right)$$

$$\partial_t T_1 - Pr^{-1} \partial_k^2 T_1 - Pr^{-1} 2 \partial_k \nabla_k T_{-1} = -W_{-1}^k \partial_k T_1 - W_{-1}^k \nabla_k T_{-1} - v_0^k \partial_k T_0 - v_1^k \partial_k T_{-1} + v_1^z$$

$$\partial_i v_1^i + \nabla_i W_{-1}^i = 0, \quad \partial_i B_1^i + \nabla_i B_{-1}^i = 0$$

This system yields the following secular equations:

$$W_{-1}^k \nabla_k W_{-1}^i = -\nabla_i P_{-1} + \tilde{Q} \varepsilon_{ijk} \varepsilon_{jml} \left(\nabla_m B_{-1}^l B_{-1}^k + \nabla_m B_{-1}^l \overline{B_k} \right) \tag{64}$$

$$\varepsilon_{ijk}\varepsilon_{knp}\left(\nabla_j W_{-1}^n B_{-1}^p + \nabla_j W_{-1}^n \overline{B_p}\right) = 0 \tag{65}$$

$$W_{-1}^k \nabla_k T_{-1} = 0, \quad \nabla_i W_{-1}^i = 0, \quad \nabla_i B_{-1}^i = 0 \tag{66}$$

For the second order R^2 we obtain the equations:

$$\partial_t v_2^i + W_{-1}^k \partial_k v_2^i + v_0^k \partial_k v_1^i + W_{-1}^k \nabla_k v_0^i + v_0^k \nabla_k W_{-1}^i + v_1^i \partial_k v_0^i + v_2^k \partial_k W_{-1}^i =$$

$$= -\nabla_i P_2 - \nabla_i P_0 + \partial_k^2 v_2^i + 2\partial_k \nabla_k v_0^i + \varepsilon_{ijk} v_2^j D_k +$$

$$+\tilde{Q}\varepsilon_{ijk}\varepsilon_{jml}\left(\partial_m B_{-1}^l B_2^k + \partial_m B_0^l B_1^k + \partial_m B_1^l B_0^k + \partial_m B_2^l B_{-1}^k + \nabla_m B_{-1}^l B_0^k + \nabla_m B_0^l B_{-1}^k\right) +$$

$$+\tilde{Q}\varepsilon_{ijk}\varepsilon_{jml}\left(\partial_m B_2^l \overline{B_k} + \nabla_m B_0^l \overline{B_k}\right) + e_i \tilde{Ra}\, T_2$$

$$\partial_t B_2^i - Pm^{-1}\partial_k^2 B_2^i - Pm^{-1}2\partial_k \nabla_k B_0^i = \varepsilon_{ijk}\varepsilon_{knp}\left(\partial_j W_{-1}^n B_2^p + \partial_j v_0^n B_1^p + \partial_j v_1^n B_0^p +\right.$$

$$= \varepsilon_{ijk}\varepsilon_{knp}\left(\partial_j W_{-1}^n B_2^p + \partial_j v_0^n B_1^p + \partial_j v_1^n B_0^p + \partial_j v_2^n B_{-1}^p + \nabla_j W_{-1}^n B_0^p + \nabla_j v_0^n B_{-1}^p\right) +$$

$$+ \varepsilon_{ijk}\varepsilon_{knp}\left(\partial_j v_2^n \overline{B_p} + \nabla_j v_0^n \overline{B_p}\right) \tag{67}$$

$$\partial_t T_2 - Pr^{-1}\partial_k^2 T_2 - Pr^{-1}2\partial_k \nabla_k T_0 = -W_{-1}^k \partial_k T_2 - W_{-1}^k \nabla_k T_0 -$$

$$- v_0^k \partial_k T_1 - v_0^k \nabla_k T_{-1} - v_1^k \partial_k T_0 - v_2^k \partial_k T_{-1} + v_2^z$$

$$\partial_i v_2^i + \nabla_i v_0^i = 0, \quad \partial_i B_2^i + \nabla_i B_0^i = 0$$

As seen after the averaging of the system of eqs. (67) over the «fast» variables, in the order R^2 secular terms are absent. Finally, let us consider the most significant order R^3. Here the equations have the following form:

$$\partial_t v_3^i + \partial_T W_{-1}^i + W_{-1}^k \partial_k v_3^i + v_0^k \partial_k v_2^i + W_{-1}^k \nabla_k v_1^i + v_0^k \nabla_k v_0^i + v_1^k \partial_k v_1^i + v_1^k \nabla_k W_{-1}^i +$$

$$+ v_2^k \partial_k W_{-1}^i = -\partial_i P_3 - \nabla_i\left(P_1 + \overline{P_1}\right) + \partial_k^2 v_3^i + 2\partial_k \nabla_k v_1^i + \Delta W_{-1}^i +$$

$$+\varepsilon_{ijk} v_3^j D_k + \tilde{Q}\varepsilon_{ijk}\varepsilon_{jml}\left(\partial_m B_{-1}^l B_3^k + \partial_m B_0^l B_2^k + \partial_m B_1^l B_1^k + \partial_m B_2^l B_0^k +\right.$$

$$+ \partial_m B_3^l B_{-1}^k + +\nabla_m B_{-1}^l B_1^k + \nabla_m B_0^l B_0^k + \nabla_m B_1^l B_{-1}^k\right) +$$

$$+\tilde{Q}\varepsilon_{ijk}\varepsilon_{jml}\left(\nabla_m B_3^l \overline{B_k} + \nabla_m B_1^l \overline{B_k}\right) + e_i \tilde{Ra}\, T_3$$

$$\partial_t B_3^i + \partial_T B_{-1}^i - Pm^{-1}\partial_k^2 B_3^i - 2Pm^{-1}\partial_k \nabla_k B_1^i - Pm^{-1}\Delta B_{-1}^i =$$

$$= \varepsilon_{ijk}\varepsilon_{knp}\left(\partial_j W_{-1}^n B_3^p + \partial_j v_0^n B_2^p + \partial_j v_1^n B_1^p + \partial_j v_2^n B_0^p + \partial_j v_3^n B_{-1}^p +\right.$$

$$+ \nabla_j W_{-1}^n B_1^p + \nabla_j v_0^n B_0^p + \nabla_j v_1^n B_{-1}^p\right) + \varepsilon_{ijk}\varepsilon_{knp}\left(\partial_j v_3^n \overline{B_p} + \nabla_j v_1^n \overline{B_p}\right) \tag{68}$$

$$\partial_t T_3 + \partial_T T_{-1} - Pr^{-1}\partial_k^2 T_3 - Pr^{-1}2\partial_k \nabla_k T_1 - Pr^{-1}\Delta T_{-1} =$$

$$- W_{-1}^k \partial_k T_3 - W_{-1}^k \nabla_k T_1 - v_0^k \partial_k T_2 - v_0^k \nabla_k T_0 -$$

$$- v_1^k \nabla_k T_1 - v_1^k \nabla_k T_{-1} - v_2^k \partial_k T_0 - v_3^k \partial_k T_{-1} + v_3^z$$

$$\partial_i v_3^i + \nabla_i v_1^i = 0, \quad \partial_i B_3^i + \nabla_i B_1^i = 0$$

By averaging this system of equations over the «fast» variables we obtain the basic secular equations which describe the evolution of the large-scale perturbations:

$$\partial_T W_{-1}^i - \Delta W_{-1}^i + \nabla_k \left(\overline{v_0^k v_0^i} \right) = -\nabla_i \overline{P}_1 + \tilde{Q} \varepsilon_{ijk} \varepsilon_{jml} \nabla_m \left(\overline{B_0^l B_0^k} \right) \tag{69}$$

$$\partial_T B_{-1}^i - Pm^{-1} \Delta B_{-1}^i = \varepsilon_{ijk} \varepsilon_{knp} \nabla_j \left(\overline{v_0^n B_0^p} \right) \tag{70}$$

$$\partial_T T_{-1} - Pr^{-1} \Delta T_{-1} = -\nabla_k \left(\overline{v_0^k T_0} \right) \tag{71}$$

B. SMALL-SCALE FIELDS IN THE ZERO ORDER WITH RESPECT TO R

In Appendix A we obtain the equations of asymptotic expansion in the zero-order approximation. Taking into account the new denotations $\vec{W} = \vec{W}_{-1}, \vec{H} = \vec{B}_{-1}$ we write them down in the following form:

$$\widehat{D}_W v_0^i = -\partial_i P_0 + \varepsilon_{ijk} v_0^j D_k + \tilde{Q} H_k \left(\partial_k B_0^i - \partial_i B_0^k \right) + \tilde{Q} \overline{B}_k \left(\partial_k B_0^i - \partial_i B_0^k \right) + e_i \widetilde{Ra} T_0 + F_0^i \tag{72}$$

$$\widehat{D}_H B_0^i = \left(H_p \partial_p + \overline{B}_k \partial_k \right) v_0^i \tag{73}$$

$$\widehat{D}_\theta T_0 = e_k v_0^k \tag{74}$$

$$\partial_i v_0^i = \partial_k B_0^k = \partial_i F_0^i = 0 \tag{75}$$

where the operators are denoted as :

$$\widehat{D}_W = \partial_t - \partial_k^2 + W_k \partial_k, \widehat{D}_H = \partial_t - Pm^{-1} \partial_k^2 + W_k \partial_k, \widehat{D}_\theta = \partial_t - Pr^{-1} \partial^2 + W_k \partial_k.$$

The small-scale oscillations of the magnetic field and the temperature are easily found from Eqs. (73)-(74):

$$B_0^i = \frac{\left(H_p + \overline{B}_p \right) \partial_p v_0^i}{\widehat{D}_H}, \quad T_0 = \frac{v_0^z}{\widehat{D}_\theta} \tag{76}$$

Now we substitute (76) into (72) and find the pressure P_0 using the condition of field solenoidality (75) :

$$P_0 = \varepsilon_{ijk} \frac{\partial_i v_0^j}{\partial^2} D_k + e_i e_k \widetilde{Ra} \frac{\partial_i v_0^k}{\partial^2 \widehat{D}_\theta} - \frac{\tilde{Q}(H_p + \overline{B}_p)}{\partial^2 \widehat{D}_H} \partial_p (H_k \partial^2 v_0^k) \tag{77}$$

Using the (77) we exclude the pressure from eq. (72) and obtain the equation for the velocity field of the zero-order approximation:

$$\left[\left(\widehat{D}_W - \frac{\tilde{Q}((H_k \partial_k)^2 + H_k \overline{B}_l \partial_k \partial_l)}{\widehat{D}_H} \right) \delta_{ij} - \left(\widetilde{Ra} \frac{e_j e_p}{\widehat{D}_\theta} + \varepsilon_{ijk} D_k \right) \widehat{P}_{ip} \right] v_0^j = F_0^i, \tag{78}$$

Where $\widehat{P}_{ip} = \delta_{ip} - \dfrac{\partial_i \partial_p}{\partial^2}$ is the projection operator. In order to find the small-scale field $\vec{v}_0$ it is convenient to present eq. (78) in the coordinate form:

$$\begin{cases} \hat{d}_{11} v_0^x + \hat{d}_{12} v_0^y + \hat{d}_{13} v_0^z = \widehat{F}_0^x \\ \hat{d}_{21} v_0^x + \hat{d}_{22} v_0^y + \hat{d}_{23} v_0^z = \widehat{F}_0^y \\ \hat{d}_{31} v_0^x + \hat{d}_{32} v_0^y + \hat{d}_{33} v_0^z = \widehat{F}_0^z \end{cases} \tag{79}$$

The components of the tensor $\hat{d}_{ij}$ have the following form:

$$\hat{d}_{11} = \widehat{D}_W - \frac{\tilde{Q}((H_k \partial_k)^2 + H_k \overline{B}_l \partial_k \partial_l)}{\widehat{D}_H} + \frac{D_2 \partial_x \partial_z - D_3 \partial_x \partial_y}{\partial^2}, \hat{d}_{12} = \frac{D_3 \partial_x^2 - D_1 \partial_x \partial_z}{\partial^2} - D_3,$$

$$\hat{d}_{13} = D_2 + \frac{D_1 \partial_x \partial_y - D_2 \partial_x^2}{\partial^2} + \widehat{Ra} \frac{\partial_x \partial_z}{\partial^2 \widehat{D}_\theta}, \hat{d}_{21} = D_3 + \frac{D_2 \partial_y \partial_z - D_3 \partial_y^2}{\partial^2},$$

$$\hat{d}_{22} = \widehat{D}_W - \frac{\widetilde{Q}((H_k \partial_k)^2 + H_k \overline{B}_l \partial_k \partial_l)}{\widehat{D}_H} + \frac{D_3 \partial_y \partial_x - D_1 \partial_y \partial_z}{\partial^2},$$

$$\hat{d}_{23} = \widehat{Ra} \frac{\partial_y \partial_z}{\partial^2 \widehat{D}_\theta} + \frac{D_1 \partial_y^2 - D_2 \partial_y \partial_x}{\partial^2} - D_1, \hat{d}_{31} = \frac{D_2 \partial_z^2 - D_3 \partial_z \partial_y}{\partial^2} - D_2,$$

$$\hat{d}_{32} = \frac{D_3 \partial_z \partial_x - D_1 \partial_z^2}{\partial^2} + D_1, \hat{d}_{33} = \widehat{D}_W - \frac{\widetilde{Q}((H_k \partial_k)^2 + H_k \overline{B}_l \partial_k \partial_l)}{\widehat{D}_H} +$$

$$+ \frac{D_1 \partial_z \partial_y - D_2 \partial_z \partial_x}{\partial^2} - \frac{\widetilde{Ra}}{\widehat{D}_\theta} + \widetilde{Ra} \frac{\partial_z^2}{\partial^2 \widehat{D}_\theta}.$$

It is obvious that the solution for the system (79) can be found using the Cramer rule:

$$v_0^x = u_0 = \frac{1}{\Delta} \left\{ \left(\hat{d}_{22} \hat{d}_{33} - \hat{d}_{32} \hat{d}_{23} \right) F_0^x + \left(\hat{d}_{13} \hat{d}_{32} - \hat{d}_{12} \hat{d}_{33} \right) F_0^y + \left(\hat{d}_{12} \hat{d}_{23} - \hat{d}_{13} \hat{d}_{22} \right) F_0^z \right\} \quad (80)$$

$$v_0^y = v_0 = \frac{1}{\Delta} \left\{ \left(\hat{d}_{23} \hat{d}_{31} - \hat{d}_{21} \hat{d}_{33} \right) F_0^x + \left(\hat{d}_{11} \hat{d}_{33} - \hat{d}_{13} \hat{d}_{31} \right) F_0^y + \left(\hat{d}_{13} \hat{d}_{21} - \hat{d}_{11} \hat{d}_{23} \right) F_0^z \right\} \quad (81)$$

$$v_0^z = w_0 = \frac{1}{\Delta} \left\{ \left(\hat{d}_{21} \hat{d}_{32} - \hat{d}_{22} \hat{d}_{31} \right) F_0^x + \left(\hat{d}_{12} \hat{d}_{31} - \hat{d}_{11} \hat{d}_{32} \right) F_0^y + \left(\hat{d}_{11} \hat{d}_{22} - \hat{d}_{12} \hat{d}_{21} \right) F_0^z \right\} \quad (82)$$

Here Δ is the determinant of the system of equations (79), which in the open form is:

$$\Delta = \hat{d}_{11} \hat{d}_{22} \hat{d}_{33} + \hat{d}_{21} \hat{d}_{32} \hat{d}_{13} + \hat{d}_{12} \hat{d}_{23} \hat{d}_{31} - \hat{d}_{13} \hat{d}_{22} \hat{d}_{31} - \hat{d}_{32} \hat{d}_{23} \hat{d}_{11} - \hat{d}_{21} \hat{d}_{12} \hat{d}_{33} \quad (83)$$

Now let us present the external force $\vec{F}_0$ in the complex form:

$$\vec{F}_0 = \vec{i} \frac{f_0}{2} e^{i\phi_2} + \vec{j} \frac{f_0}{2} e^{i\phi_1} + c.c. \quad (84)$$

Then all the operators contained in (80)-(83) act on the eigenfunctions from the left:

$$\widehat{D}_{W,H,\theta} e^{i\phi_1} = e^{i\phi_1} \widehat{D}_{W,H,\theta} \left(\vec{\kappa}_1, -\omega_0 \right), \quad \widehat{D}_{W,H,\theta} e^{i\phi_2} = e^{i\phi_2} \widehat{D}_{W,H,\theta} \left(\vec{\kappa}_2, -\omega_0 \right),$$

$$\Delta e^{i\phi_1} = e^{i\phi_1} \Delta \left(\vec{\kappa}_1, -\omega_0 \right), \quad \Delta e^{i\phi_2} = e^{i\phi_2} \Delta \left(\vec{\kappa}_2, -\omega_0 \right) \quad (85)$$

To simplify the formulae, assume that $\kappa_0 = 1$, $\omega_0 = 1$ and introduce the new denotations :

$$\widehat{D}_W \left(\vec{\kappa}_1, -\omega_0 \right) = \widehat{D}_{W_1}^* = 1 - i \left(1 - W_1 \right), \quad \widehat{D}_W \left(\vec{\kappa}_2, -\omega_0 \right) = \widehat{D}_{W_2}^* = 1 - i \left(1 - W_2 \right)$$

$$\widehat{D}_H \left(\vec{\kappa}_1, -\omega_0 \right) = \widehat{D}_{H_1}^* = Pm^{-1} - i \left(1 - W_1 \right), \quad \widehat{D}_H \left(\vec{\kappa}_2, -\omega_0 \right) = \widehat{D}_{H_2}^* = Pm^{-1} - i \left(1 - W_2 \right) \quad (86)$$

$$\widehat{D}_\theta \left(\vec{\kappa}_1, -\omega_0 \right) = \widehat{D}_{\theta_1}^* = Pr^{-1} - i \left(1 - W_1 \right), \quad \widehat{D}_\theta \left(\vec{\kappa}_2, -\omega_0 \right) = \widehat{D}_{\theta_2}^* = Pr^{-1} - i \left(1 - W_2 \right)$$

Note that the complex-conjugate terms are marked by asterisk. Further in the calculations some components in the tensors $\hat{d}_{ij} \left(\vec{\kappa}_1, -\omega_0 \right)$ and $\hat{d}_{ij} \left(\vec{\kappa}_2, -\omega_0 \right)$ vanish, and there remain the non-zero components:

$$\hat{d}_{11} \left(\vec{\kappa}_1, -\omega_0 \right) = \widehat{D}_{W_1}^* + \frac{\widetilde{Q} H_1 (H_1 + \overline{B}_1)}{\widehat{D}_{H_1}^*}, \hat{d}_{12} \left(\vec{\kappa}_1, -\omega_0 \right) = 0, \hat{d}_{13} \left(\vec{\kappa}_1, -\omega_0 \right) = 0,$$

$$\hat{d}_{21}\left(\vec{\kappa}_1, -\omega_0\right) = D_3, \ \hat{d}_{22}\left(\vec{\kappa}_1, -\omega_0\right) = \hat{d}_{11}\left(\vec{\kappa}_1, -\omega_0\right), \ \hat{d}_{23}\left(\vec{\kappa}_1, -\omega_0\right) = -D_1, \tag{87}$$

$$\hat{d}_{31}\left(\vec{\kappa}_1, -\omega_0\right) = -D_2, \ \hat{d}_{32}\left(\vec{\kappa}_1, -\omega_0\right) = D_1, \ \hat{d}_{33}\left(\vec{\kappa}_1, -\omega_0\right) = \tilde{d}_{22}\left(\vec{\kappa}_1, -\omega_0\right) - \frac{\widetilde{Ra}}{\widehat{D}_{\theta_1}^*}$$

$$\hat{d}_{11}\left(\vec{\kappa}_2, -\omega_0\right) = \widehat{D}_{W_2}^* + \frac{\widetilde{Q}H_2(H_2 + \overline{B}_2)}{\widehat{D}_{H_2}^*}, \ \hat{d}_{12}\left(\vec{\kappa}_2, -\omega_0\right) = -D_3, \ \hat{d}_{13}\left(\vec{\kappa}_2, -\omega_0\right) = D_2,$$

$$\hat{d}_{21}\left(\vec{\kappa}_2, -\omega_0\right) = 0, \ \hat{d}_{22}\left(\vec{\kappa}_2, -\omega_0\right) = \hat{d}_{11}\left(\vec{\kappa}_2, -\omega_0\right), \ \hat{d}_{23}\left(\vec{\kappa}_2, -\omega_0\right) = 0, \tag{88}$$

$$\hat{d}_{31}\left(\vec{\kappa}_2, -\omega_0\right) = -D_2, \ \hat{d}_{32}\left(\vec{\kappa}_1, -\omega_0\right) = D_1, \ \hat{d}_{33}\left(\vec{\kappa}_2, -\omega_0\right) = \hat{d}_{22}\left(\vec{\kappa}_2, -\omega_0\right) - \frac{\widetilde{Ra}}{\widehat{D}_{\theta_2}^*}$$

Taking into account the expressions (87)-(88) we find the velocity fields in the zero-order approximation:

$$u_0 = \frac{f_0}{2} \frac{\widehat{B}_2^*}{\widehat{A}_2^* \widehat{B}_2^* + D_2^2} e^{i\phi_2} + c.c. = u_{03} + u_{04} \tag{89}$$

$$v_0 = \frac{f_0}{2} \frac{\widehat{B}_1}{\widehat{A}_1^* \widehat{B}_1^* + D_1^2} e^{i\phi_1} + c.c. = v_{01} + v_{02} \tag{90}$$

$$w_0 = -\frac{f_0}{2} \frac{D_1}{\widehat{A}_1^* \widehat{B}_1^* + D_1^2} e^{i\phi_1} + \frac{f_0}{2} \frac{D_2}{\widehat{A}_2^* \widehat{B}_2^* + D_2^2} e^{i\phi_2} + c.c. = w_{01} + w_{02} + w_{03} + w_{04} \tag{91}$$

where

$$\widehat{A}_{1,2}^* = \widehat{D}_{W_{1,2}}^* + \frac{\widetilde{Q}H_{1,2}}{\widehat{D}_{H_{1,2}}^*}(H_{1,2} + \overline{B}_{1,2}), \ \widehat{B}_{1,2}^* = \widehat{A}_{1,2}^* - \frac{\widetilde{Ra}}{\widehat{D}_{\theta_{1,2}}^*}. \tag{92}$$

The velocity components satisfy the following relations: $w_{02} = \left(w_{01}\right)^*$, $w_{04} = \left(w_{03}\right)^*$, $v_{02} = \left(v_{01}\right)^*, v_{04} = \left(v_{03}\right)^*$, $u_{02} = \left(u_{01}\right)^*$, $u_{04} = \left(u_{03}\right)^*$. In the limiting case of non-electroconductive fluid $(\sigma = 0)$, without temperature gradient $(\nabla \overline{T} = 0)$ and external magnetic field $(\overline{B}_{1,2} = 0)$ the formulae (89)-(91) coincide with the results obtained in [41]. Now we calculate the small-scale oscillations of the magnetic field $\vec{B}_0$ using the expressions (76) and (89)-(91):

$$B_0^x = \tilde{u}_0 = \frac{f_0}{2} \frac{i(H_2 + \overline{B}_2)\widehat{B}_2^*}{\widehat{D}_{H_2}^* (\widehat{A}_2^* \widehat{B}_2^* + D_2^2)} e^{i\phi_2} + c.c. = \tilde{u}_{03} + \tilde{u}_{04} \tag{93}$$

$$B_0^y = \tilde{v}_0 = \frac{f_0}{2} \frac{i(H_1 + \overline{B}_1)\widehat{B}_1^*}{\widehat{D}_{H_1}^* (\widehat{A}_1^* \widehat{B}_1^* + D_1^2)} e^{i\phi_1} + c.c. = \tilde{u}_{03} + \tilde{u}_{04} \tag{94}$$

$$B_0^z = \widetilde{w}_0 = -\frac{f_0}{2} \frac{i(H_1 + \overline{B}_1)D_1}{\widehat{D}_{H_1}^* (\widehat{A}_1^* \widehat{B}_1^* + D_1^2)} e^{i\phi_1} + \frac{f_0}{2} \frac{i(H_2 + \overline{B}_2)D_2}{\widehat{D}_{H_2}^* (\widehat{A}_2^* \widehat{B}_2^* + D_2^2)} e^{i\phi_2} + c.c. = \tag{95}$$

$$= w_{01} + w_{02} + w_{03} + w_{04}$$

In the expressions for the small-scale oscillations $(\vec{v}_0, \vec{B}_0, T_0)$ the component of the angular velocity D_3 is absent due to the choice of the external force. Further Eqs. (89)-(95) will be used while calculating the correlation functions.

C. CALCULATION OF REYNOLDS AND MAXWELL STRESSES AND TURBULENT E.M.F.

To close the system of eqs. (17)-(20) which describe the evolution of the large-scale fields, it is necessary to calculate the following correlators:

$$T^{31} = \overline{w_0 u_0} = \overline{w_{03}\left(u_{03}\right)^*} + \overline{\left(w_{03}\right)^* u_{03}} \tag{96}$$

$$T^{32} = \overline{w_0 v_0} = \overline{w_{01}\left(v_{01}\right)^*} + \overline{\left(w_{01}\right)^* v_{01}} \tag{97}$$

$$S^{31} = \overline{\widetilde{w_0}\widetilde{u_0}} = \overline{\widetilde{w}_{03}\left(\widetilde{u}_{03}\right)^*} + \overline{\left(\widetilde{w}_{03}\right)^* \widetilde{u}_{03}} \tag{98}$$

$$S^{32} = \overline{\widetilde{w_0}\widetilde{v_0}} = \overline{\widetilde{w}_{01}\left(\widetilde{v}_{01}\right)^*} + \overline{\left(\widetilde{w}_{01}\right)^* \widetilde{v}_{01}} \tag{99}$$

$$G^{13} = \overline{u_0 \widetilde{w_0}} = \overline{u_{03}\left(\widetilde{w}_{03}\right)^*} + \overline{\left(u_{03}\right)^* \widetilde{w}_{03}} \tag{100}$$

$$G^{31} = \overline{w_0 \widetilde{u_0}} = \overline{w_{03}\left(\widetilde{u}_{03}\right)^*} + \overline{\left(w_{03}\right)^* \widetilde{u}_{03}} \tag{101}$$

$$G^{23} = \overline{v_0 \widetilde{w_0}} = \overline{v_{01}\left(\widetilde{w}_{01}\right)^*} + \overline{\left(v_{01}\right)^* \widetilde{w}_{01}} \tag{102}$$

$$G^{32} = \overline{w_0 \widetilde{v_0}} = \overline{w_{01}\left(\widetilde{v}_{01}\right)^*} + \overline{\left(w_{01}\right)^* \widetilde{v}_{01}} \tag{103}$$

At first let us calculate the Reynolds stresses (96)-(97). For this purpose we use the expressions for the small-scale velocity fields (89)-(91). Their substitution into (96)-(97) gives:

$$T^{31} = \frac{f_0^2}{2} \frac{D_2 q_2}{\left|\widehat{A}_2 \widehat{B}_2 + D_2^2\right|^2}, \tag{104}$$

$$T^{32} = -\frac{f_0^2}{2} \frac{D_1 q_1}{\left|\widehat{A}_1 \widehat{B}_1 + D_1^2\right|^2}, \tag{105}$$

where

$$q_{1,2} = 1 + \frac{QH_{1,2}(H_{1,2} + \overline{B}_{1,2})}{1 + Pm^2\left(1 - W_{1,2}\right)^2} - \frac{Ra}{1 + Pr^2\left(1 - W_{1,2}\right)^2}.$$

To calculate the correlators of the magnetic field or the Maxwell stresses S^{31} and S^{32}, we use the expressions (92)-(94). By substituting (92)-(94) into (98)-(99) we obtain :

$$S^{31} = \frac{H_2^2}{\left|\widehat{D}_{H_2}\right|^2} T^{31}, \quad S^{32} = \frac{H_1^2}{\left|\widehat{D}_{H_1}\right|^2} T^{32} \tag{106}$$

The differences $T^{31} - \widetilde{Q}S^{31}$ and $T^{32} - \widetilde{Q}S^{32}$ contained in the right sides of Eqs. (17)-(18) can be easily found using the expressions (105)-(106):

$$T^{31} - \widetilde{Q}S^{31} = T^{31}\left(1 - \frac{Q(H_2 + \overline{B}_2)^2}{Pm\left|\widehat{D}_{H_2}\right|^2}\right) = T^{31}Q_2 \tag{107}$$

$$T^{32} - \widetilde{Q}S^{32} = T^{32}\left(1 - \frac{Q(H_1 + \overline{B}_1)^2}{Pm\left|\widehat{D}_{H_1}\right|^2}\right) = T^{32}Q_1 \tag{108}$$

To calculate the group of oscillators (100)-(103) we will use the expressions for the small-scale velocity field (89)-(91) and the magnetic field (92)-(94) . Simple mathematical operations yield:

$$G^{13} = \frac{f_0^2}{4} \frac{i(H_2 + \overline{B}_2)D_2}{\left|\widehat{A}_2\widehat{B}_2 + D_2^2\right|^2} \cdot \left(\frac{\widehat{B}_2}{\widehat{D}_{H_2}^*} - \frac{\widehat{B}_2^*}{\widehat{D}_{H_2}}\right) \tag{109}$$

$$G^{31} = \frac{f_0^2}{4} \frac{i(H_2 + \overline{B}_2)D_2}{\left|\widehat{A}_2\widehat{B}_2 + D_2^2\right|^2} \cdot \left(\frac{\widehat{B}_2^*}{\widehat{D}_{H_2}^*} - \frac{\widehat{B}_2}{\widehat{D}_{H_2}}\right) \tag{110}$$

$$G^{23} = \frac{f_0^2}{4} \frac{i(H_1 + \overline{B}_1)D_1}{\left|\widehat{A}_1\widehat{B}_1 + D_1^2\right|^2} \cdot \left(\frac{\widehat{B}_1^*}{\widehat{D}_{H_1}} - \frac{\widehat{B}_1}{\widehat{D}_{H_1}^*}\right) \tag{111}$$

$$G^{32} = \frac{f_0^2}{4} \frac{i(H_1 + \overline{B}_1)D_1}{\left|\widehat{A}_1\widehat{B}_1 + D_1^2\right|^2} \cdot \left(\frac{\widehat{B}_1}{\widehat{D}_{H_1}} - \frac{\widehat{B}_1^*}{\widehat{D}_{H_1}^*}\right) \tag{112}$$

To close the equations for the large-scale magnetic field (24)-(25) , it is necessary to calculate the differences $G^{13} - G^{31}$ and $G^{23} - G^{32}$ corresponding to the turbulent e.m.f. components $\mathcal{E}_2 = \mathcal{E}_y$ and $\mathcal{E}_1 = \mathcal{E}_x$. Taking into account the expressions (109)-(112) we obtain:

$$\mathcal{E}_2 = G^{13} - G^{31} = \frac{f_0^2}{4} \frac{i(H_2 + \overline{B}_2)D_2}{\left|\widehat{A}_2\widehat{B}_2 + D_2^2\right|^2} \cdot \frac{(\widehat{B}_2 - \widehat{B}_2^*)}{\left|\widehat{D}_{H_2}\right|^2} \cdot \left(\widehat{D}_{H_2}^* + \widehat{D}_{H_2}\right) \tag{113}$$

$$\mathcal{E}_1 = G^{23} - G^{32} = -\frac{f_0^2}{4} \frac{i(H_1 + \overline{B}_1)D_1}{\left|\widehat{A}_1\widehat{B}_1 + D_1^2\right|^2} \cdot \frac{(\widehat{B}_1 - \widehat{B}_1^*)}{\left|\widehat{D}_{H_1}\right|^2} \cdot \left(\widehat{D}_{H_1}^* + \widehat{D}_{H_1}\right) \tag{114}$$

Using the expressions (86) and (92) let us write down some useful formulas:

$$\left|\widehat{A}_{1,2}\widehat{B}_{1,2} + D_{1,2}^2\right|^2 = \left|\widehat{A}_{1,2}\right|^2 \cdot \left|\widehat{B}_{1,2}\right|^2 + D_{1,2}^2 \cdot (\widehat{A}_{1,2}^*\widehat{B}_{1,2}^* + \widehat{A}_{1,2}\widehat{B}_{1,2}) + D_{1,2}^4,$$

$$\left|\widehat{A}_{1,2}\right|^2 = \left|\widehat{D}_{W_{1,2}}\right|^2 + \widetilde{Q}H_{1,2}(H_{1,2} + \overline{B}_{1,2})\left(\frac{\widehat{D}_{W_{1,2}}}{\widehat{D}_{H_{1,2}}^*} + \frac{\widehat{D}_{W_{1,2}}^*}{\widehat{D}_{H_{1,2}}}\right) + \frac{\widetilde{Q}^2 H_{1,2}^2 (H_{1,2} + \overline{B}_{1,2})^2}{\left|\widehat{D}_{H_{1,2}}\right|^2},$$

$$\left|\widehat{B}_{1,2}\right|^2 = \left|\widehat{A}_{1,2}\right|^2 - \widetilde{Ra}\left(\frac{\widehat{A}_{1,2}}{\widehat{D}_{\theta_{1,2}}^*} + \frac{\widehat{A}_{1,2}^*}{\widehat{D}_{\theta_{1,2}}}\right) + \frac{\widetilde{Ra}^2}{\left|\widehat{D}_{\theta_{1,2}}\right|^2},$$

$$\widehat{A}_{1,2}^*\widehat{B}_{1,2}^* + \widehat{A}_{1,2}\widehat{B}_{1,2} = \left(\widehat{A}_{1,2}^*\right)^2 + \left(\widehat{A}_{1,2}\right)^2 - \widetilde{Ra}\left(\frac{\widehat{A}_{1,2}^*}{\widehat{D}_{\theta_{1,2}}^*} + \frac{\widehat{A}_{1,2}}{\widehat{D}_{\theta_{1,2}}}\right), \tag{115}$$

$$\left|\widehat{D}_{W_{1,2}}\right|^2 = 1 + (1 - W_{1,2})^2, \left|\widehat{D}_{H_{1,2}}\right|^2 = Pm^{-2} + (1 - W_{1,2})^2, \left|\widehat{D}_{\theta_{1,2}}\right|^2 = Pr^{-2} + (1 - W_{1,2})^2,$$

$$\widehat{D}_{H_{1,2}} + \widehat{D}_{H_{1,2}}^* = 2Pm^{-1}, \widehat{D}_{W_{1,2}}\widehat{D}_{H_{1,2}} + \widehat{D}_{W_{1,2}}^*\widehat{D}_{H_{1,2}}^* = 2(Pm^{-1} - (1 - W_{1,2})^2),$$

$$\widehat{D}_{\theta_{1,2}}\widehat{D}_{H_{1,2}}^* + \widehat{D}_{H_{1,2}}\widehat{D}_{\theta_{1,2}}^* = 2(Pm^{-1}Pr^{-1} + (1 - W_{1,2})^2), \left(\widehat{D}_{W_{1,2}}\right)^2 + \left(\widehat{D}_{W_{1,2}}^*\right)^2 = 2(1 - (1 - W_{1,2})^2),$$

$$\widehat{D}^{*}_{W_{1,2}}\widehat{D}_{\theta_{1,2}} + \widehat{D}_{W_{1,2}}\widehat{D}^{*}_{\theta_{1,2}} = 2(Pr^{-1} + (1-W_{1,2})^2), \quad \widehat{D}^{*}_{W_{1,2}}\widehat{D}_{H_{1,2}} + \widehat{D}_{W_{1,2}}\widehat{D}^{*}_{H_{1,2}} = 2(Pm^{-1} + (1-W_{1,2})^2).$$

Let us substitute these relations into (107)-(108). So, we can find the difference of the Reynolds and Maxwell stresses:

$$T^{31} - \widetilde{Q}S^{31} = \frac{f_0^2}{2} \cdot \frac{D_2 q_2 Q_2}{4(1-W_2)^2 q_2^2 \widetilde{Q}_2^2 + \left[D_2^2 + W_2(2-W_2) + \mu_2\right]^2 + \xi_2}, \tag{116}$$

$$T^{32} - \widetilde{Q}S^{32} = \frac{f_0^2}{2} \cdot \frac{D_1 q_1 Q_1}{4(1-W_1)^2 q_1^2 \widetilde{Q}_1^2 + \left[D_1^2 + W_1(2-W_1) + \mu_1\right]^2 + \xi_1},$$

with the following denotations:

$$q_{1,2} = 1 + \frac{QH_{1,2}(H_{1,2}+\overline{B}_{1,2})}{1+Pm^2(1-W_{1,2})^2} - \frac{Ra}{1+Pr^2(1-W_{1,2})^2}, \quad Q_{1,2} = 1 - \frac{QPm(H_{1,2}+\overline{B}_{1,2})^2}{1+Pm^2\left(1-W_{1,2}\right)^2},$$

$$\widetilde{Q}_{1,2} = 1 - \frac{QPmH_{1,2}(H_{1,2}+\overline{B}_{1,2})}{1+Pm^2\left(1-W_{1,2}\right)^2} + \frac{RaPr}{1+Pr^2(1-W_{1,2})^2},$$

$$\mu_{1,2} = 2QH_{1,2}(H_{1,2}+\overline{B}_{1,2}) \cdot \frac{1+Pm\left(1-W_{1,2}\right)^2}{1+Pm^2\left(1-W_{1,2}\right)^2} + Q^2 H_{1,2}^2 (H_{1,2}+\overline{B}_{1,2})^2 \cdot \frac{1-Pm^2\left(1-W_{1,2}\right)^2}{\left(1+Pm^2\left(1-W_{1,2}\right)^2\right)^2} -$$

$$-Ra \cdot \frac{1+Pr(1-W_{1,2})^2 + 2QH_{1,2}(H_{1,2}+\overline{B}_{1,2}) \cdot \dfrac{1-PrPm\left(1-W_{1,2}\right)^2}{1+Pm^2\left(1-W_{1,2}\right)^2}}{1+Pr^2(1-W_{1,2})^2},$$

$$\xi_{1,2} = 2\Xi_{1,2} + 2\left(1-W_{1,2}\right)^2 \Pi_{1,2} - 2\left(1-W_{1,2}\right)^2 (1-\widetilde{Q}_{1,2}^2)\Pi_{1,2} - 2(1-q_{1,2}^2)\Xi_{1,2} + \Xi_{1,2}\Pi_{1,2} +$$

$$+ \chi_{1,2}\left(1-W_{1,2}\right)^2 + \chi_{1,2}(1+\sigma_{1,2}),$$

$$\Xi_{1,2} = -\frac{4\left(1-W_{1,2}\right)^2 \widetilde{Q}_{1,2} RaPr}{1+Pr^2\left(1-W_{1,2}\right)^2} + \frac{2\left(1-W_{1,2}\right)^2 Ra^2 Pr^2}{\left(1+Pr^2\left(1-W_{1,2}\right)^2\right)^2} +$$

$$+ Ra \cdot \frac{1+Pr(1-W_{1,2})^2 + 2QH_{1,2}(H_{1,2}+\overline{B}_{1,2}) \cdot \dfrac{1-PrPm\left(1-W_{1,2}\right)^2}{1+Pm^2\left(1-W_{1,2}\right)^2}}{1+Pr^2(1-W_{1,2})^2},$$

$$\Pi_{1,2} = \frac{4q_{1,2}Ra}{1+Pr^2\left(1-W_{1,2}\right)^2} + \frac{2Ra^2}{\left(1+Pr^2\left(1-W_{1,2}\right)^2\right)^2} -$$

$$-Ra \cdot \frac{1+Pr(1-W_{1,2})^2 + 2QH_{1,2}(H_{1,2}+\overline{B}_{1,2}) \cdot \dfrac{1-PrPm\left(1-W_{1,2}\right)^2}{1+Pm^2\left(1-W_{1,2}\right)^2}}{1+Pr^2(1-W_{1,2})^2},$$

$$\sigma_{1,2} = \frac{QH_{1,2}(H_{1,2}+\overline{B}_{1,2})}{1+Pm^2\left(1-W_{1,2}\right)^2} \cdot \left[2\left(1+Pm^2\left(1-W_{1,2}\right)^2\right) + QH_{1,2}(H_{1,2}+\overline{B}_{1,2}) \right],$$

$$\chi_{1,2} = \frac{2Ra}{1+Pr^2\left(1-W_{1,2}\right)^2} \cdot \left[\frac{Ra}{2} - \left(1-Pr\left(1-W_{1,2}\right)^2 + \right.\right.$$

$$\left.\left. + \frac{QH_{1,2}(H_{1,2}+\overline{B}_{1,2})(1+PrPm\left(1-W_{1,2}\right)^2)}{1+Pm^2\left(1-W_{1,2}\right)^2} \right) \right].$$

By substituting the relations (115) into (113)-(114) we find the expressions for a turbulent e.m.f. $\mathcal{E}_{1,2}$ in the explicit form:

$$\mathcal{E}_1 = f_0^2 \cdot \frac{D_1\left(1-W_1\right)Pm\widetilde{Q}_1(H_1+\overline{B}_1)}{\left(1+Pm^2\left(1-W_1\right)^2\right)\left[4\left(1-W_1\right)^2 q_1^2\widetilde{Q}_1^2 + \left[D_1^2+W_1\left(2-W_1\right)+\mu_1\right]^2 + \xi_1\right]}, \tag{117}$$

$$\mathcal{E}_2 = f_0^2 \cdot \frac{D_2\left(1-W_2\right)Pm\widetilde{Q}_2(H_2+\overline{B}_2)}{\left(1+Pm^2\left(1-W_2\right)^2\right)\left[4\left(1-W_2\right)^2 q_2^2\widetilde{Q}_2^2 + \left[D_2^2+W_2\left(2-W_2\right)+\mu_2\right]^2 + \xi_2\right]}.$$

ORCID IDs

Michael I. Kopp https://orcid.org/0000-0001-7457-3272, **Anatoly V. Tur** https://orcid.org/0000-0002-3889-8130,
Volodymyr V. Yanovsky https://orcid.org/0000-0003-0461-749X

REFERENCES

[1] J. Larmor, Rep. Brit. Assoc. Adv. Sc., 159-160 (1919).
[2] G. Moffat, *Возбуждение магнитного поля в проводящей среде [Magnetic Field Generation in Electrically Conducting Fluids]*, (Mir, Moscow, 1980), 343 p. (in Russian)
[3] Ya. Zeldovich, A. Ruzmaikin and D. Sokoloff, *Magnetic Fields in Astrophysics,* (Gordon and Breach, New York, 1983), pp. 265.
[4] G. Rüdiger, R. Hollerbach, *The magnetic universe. Geophysical and astrophysical dynamo theory,* (Wiley-VCH Verlag GmbH, Weinheim, 2004), pp. 338.
[5] Chris A. Jones, *Dynamo theory* (University of Leeds, UK, 2007), pp. 90.
[6] J. Parker, *Conversations on Electric and Magnetic Fields in the Cosmos,* (Princeton University Press, Princeton, 2007), pp. 200.
[7] F. Krauze and K.H. Redler, *Магнитная гидродинамика средних полей и теория динамо [Mean-Field Magnetohydrodynamics and Dynamo Theory]*, (Mir, Moscow, 1984), 314 p. (in Russian)
[8] A. Ruzmaikin, A. Shukurov and D. Sokoloff, *Magnetic Fields of Galaxies,* (Kluwer, Dordrecht, 1988).
[9] D.D. Sokoloff, R.A. Stepanov, P.G. Frick, Physics-Uspekhi **184** (3), 313-335 (2014), https://doi.org/10.3367/UFNr.0184.201403g.0313.
[10] V.I. Arnold, Ya.B. Zeldovich, A.A. Ruzmalkin, D.D. Sokolov, Sov. Phys. JETP **54**(6), 1083-1085 (1981).
[11] V.I. Arnold and B.A. Khesin, *Topological Methods in Hydrodynamics,* (Springer-Verlag, New York, 1998), pp. 374.
[12] H.P. Greenspan, *The theory of Rotating Fluids,* (Cambridge At the University Press, 1968), pp. 328.
[13] P.H. Roberts and A.M. Soward, *Rotating Fluids in Geophysics,* (Academic Press, 1978).
[14] J. Pedlosky, *Geophysical Fluid Dynamics* (Springer-Verlag, New York, 1987).
[15] V.I. Petviashvili and O.A. Pokhotelov, *Solitary Waves in Plasma and Atmosphere,* (Gordon&Breach Science Publishers, 1992).
[16] G.D. Aburjania, Kh.Z. Chargazia and O.A. Kharshiladze, Journal of Atmospheric and Solar-Terrestrial Physics, **72**, 971-981 (2010), https://doi.org/10.1016/j.jastp.2010.05.008.2010.
[17] M.Ya. Marov and A.V. Kolesnichenko, *Mechanics of Turbulence of Multicomponent Gases* (Astrophys. and Space Sci. Library, Vol. 269), (Kluwer Acad. Publ., Dordrecht, 2001), pp. 375.
[18] O.G. Onishchenko, O.A. Pokhotelov and N.M. Astafieva, Physics-Uspekhi, **51**(6), 577-590 (2008), http://dx.doi.org/10.1070/PU2008v051n06ABEH006588.
[19] M.V. Nezlin and E.N. Snezhkin, *Rossby Vortices and Solitons in Free Motion,* (Springer, Berlin, Heidelberg, 1993), pp. 223.
[20] H.K. Moffatt, J. Fluid Mech. **35**, 117-129 (1969), https://doi.org/10.1017/S0022112069000991.
[21] M. Steenbeck, F. Krause and K.H. Rädler, Z. Naturforsch, **21a**, 369-376 (1966).
[22] H.K. Moffatt, J. Fluid Mech. **106**, 27-47 (1981), https://doi.org/10.1017/S002211208100150X.
[23] F. Krause and G. Rüdiger, Astron. Nachr. **295**, 93-99 (1974).
[24] S.S. Moiseev, R.Z. Sagdeev, A.V. Tur, G.A. Khomenko and V.V. Yanovsky, Sov. Phys. JETP, **58**, 1149-1153 (1983).
[25] S.S. Moiseev, P.B. Rutkevitch, A.V. Tur and V.V. Yanovsky, Sov. Phys. JETP, **67**, 294-299 (1988).
[26] E.A. Lypyan, A.A. Mazurov, P.B. Rutkevitch and A.V. Tur, Sov. Phys. JETP, **75**, 838-841 (1992).
[27] S.S. Moiseev, R.Z. Sagdeev, A.V. Tur, G.A. Khomenko and A.M. Shukurov, Sov. Phys. Dokl. **28**, 925-928 (1983).

[28] G.V. Levina, S.S. Moiseev and P. B. Rutkevitch, Advances in Fluid Mechanics, **25**, 111-161 (2000).

[29] G.V. Levina, M.V. Starkov, S.E. Startsev, V.D. Zimin and S.S. Moiseev, Nonlinear Processes in Geophysics, **7**, 49-58 (2000), https://doi.org/10.5194/npg-7-49-2000.

[30] A.V. Tur, V.V. Yanovsky, e-print arXiv: https://arxiv.org/abs/1204.5024v1.

[31] A.V. Tur and V.V. Yanovsky, Open Journal of Fluid Dynamics, **3**, 64-74 (2013), https://doi.org/10.4236/ojfd.2013.32009.

[32] P.B. Rutkevich, JETP, **77**, 933-938 (1993).

[33] L.M. Smith and F. Waleffe, Physics of Fluids, **11**(6), 1608-1622 (1999), https://doi.org/10.1063/1.870022.

[34] L.M. Smith and F. Waleffe, Journal of Fluid Mechanics, **451**, 145-168 (2002).

[35] Yu.A. Berezin, V.P. Zhukov, G.V. Levina, S.S. Moiseev, P.B. Rutkevich and A.V. Tur, Heat Transfer-Soviet Research, **21**(2), 181-188 (1989).

[36] L.L. Kitchatinov, G. Rüdiger and G. Khomenko, Astron. Astrophys. **287**, 320-324 (1994).

[37] N. Kleeorin, I. Rogachevskii, https://arxiv.org/abs/1801.00493v1.

[38] U. Frishe, Z.S. She and P.L. Sulem, Physica D, **28**, 382-392 (1987), https://doi.org/10.1016/0167-2789(87)90026-1.

[39] V.V. Pipin, G. Rüdiger and L.L. Kitchatinov, Geophys. Astrophys. Fluid Dyn. **83**(1), 119-133 (1996), https://doi.org/10.1080/03091929608213644.

[40] O.A. Druzhinin and G.A. Khomenko, in: *Nonlinear World*, edited by V.G. Baryakhtar (World Scientific, Singapore, 1989), pp. 470.

[41] P.B. Rutkevitch, R.Z. Sagdeev, A.V. Tur and V.V. Yanovsky, in: *Proceeding of the IV Intern. Workshop on Nonlinear and Turb. Pros. in Physics* (Naukova dumka, Kiev, 1989).

[42] M.I. Kopp, A.V. Tur and V.V. Yanovsky, JETP, **120**(4), 733-750 (2015), https://doi.org/10.1134/S1063776115040081.

[43] M.I. Kopp, A.V. Tur and V.V. Yanovsky, https://arxiv.org/abs/1612.08860v1.

[44] P.N. Brandt, G.B. Scharmert, S. Ferguson, R.A. Shine, T.D. Tarbell and A.M. Title, Nature, **335**, 238-240 (1988).

[45] O.G. Chkhetiani, S.S. Moiseev and E. Golbraikh, JETP, **87**(3), 513-517 (1998), https://doi.org/10.1134/1.558688.

[46] M.I. Kopp, A.V. Tur and V.V Yanovsky, Open Journal of Fluid Dynamics, **05**(04), 311-321 (2015), https://doi.org/10.4236/ojfd.2015.54032.

[47] M.I. Kopp, A.V. Tur and V.V Yanovsky, https://arxiv.org/abs/1711.08623v1.

[48] G.Z. Gershuni and E.M. Zhukhovitckii, *Convective Stability of Incompressible Fluids* (Nauka, Moscow, 1972), pp. 392 (in Russian)

[49] S. Chandrasekhar, *Hydrodynamics and Hydromagnetic Stability* (Oxford Uni. Press, London, 1961), pp. 652.

[50] M.I. Kopp, A.V. Tur and V.V. Yanovsky, https://arxiv.org/abs/1706.00223v1.

[51] G. Rüdiger, Astron. Nachr. **299**(4), 217-222 (1978).

[52] Yu.L. Bolotin, A.V. Tur and V.V. Yanovsky, *Chaos: Concepts, Control and Constructive Use* (Series: Understanding Complex Systems, Springer, 2016).

**НЕЛІНІЙНЕ ДИНАМО В СТРАТИФІКОВАНІЙ ЕЛЕКТРОПРОВІДНІЙ РІДИНІ,
ЩО ПОХИЛО ОБЕРТАЄТЬСЯ В ОДНОРІДНОМУ МАГНІТНОМУ ПОЛІ**
Михайло Й. Копп[a], **Анатолій В. Тур**[c], **Костянтин М. Кулик**[a], **Володимир В. Яновський**[a,b]
*[a]Інститут монокристалів, Національна Академія Наук України
пр. Науки 60, 61001 Харків, Україна
[b]Харківський національний університет імені В.Н. Каразина
майдан Свободи, 4, 61022, Харків, Україна
[c] Університет Тулузи, Інститут астрофізичних досліджень та планетології
проспект полковника Роше 9, ВР 44346, 31028, Тулуза Cedex 4, Франція*

В роботі ми досліджували нову великомасштабну нестійкість, яка виникає в конвективній електропровідній рідині, що похило обертається в зовнішньому однорідному магнітному полі з дрібномасштабною зовнішньою силою, яка має нульову спіральність. Ця сила збуджує дрібномасштабні осциляції швидкості з малим числом Рейнольдса. За допомогою методу багатомасштабних асимптотичних розкладів отримані нелінійні рівняння для вихрових і магнітних збурень в третьому порядку за числом Рейнольдса. Показано, що в результаті спільної дії сили Коріоліса і дрібномасштабної зовнішньої сили в електропровідній рідині, що обертається, можлива великомасштабна нестійкість. Досліджена лінійна стадія магніто-вихрового динамо, що виникає в результаті нестійкостей типу α -ефекту. Вивчено механізм посилення великомасштабних вихрових збурень внаслідок розвитку гідродинамічного α - ефекту з урахуванням температурної стратифікації середовища. Показано, що «слабке» зовнішнє магнітне поле сприяє генерації вихрових та магнітних великомасштабних збурень, а «сильне» зовнішнє магнітне поле пригнічує генерацію магніто-вихрових збурень. Чисельними методами знайдені стаціонарні рішення рівнянь нелінійного магніто-вихрового динамо у вигляді локалізованих хаотичних структур у двох випадках, коли немає зовнішнього однорідного магнітного поля і коли воно присутнє.
КЛЮЧОВІ СЛОВА: рівняння магнітної гідродинаміки в наближенні Буссінеска, сила Коріоліса, багатомасштабні асимптотичні розкладання, дрібномасштабна неспіральна турбулентність, α -ефект, хаотичні структури.

**НЕЛИНЕЙНОЕ ДИНАМО В НАКЛОННО ВРАЩАЮЩЕЙСЯ СТРАТИФИЦИРОВАННОЙ
ЭЛЕКТРОПРОВОДЯЩЕЙ ЖИДКОСТИ В ОДНОРОДНОМ МАГНИТНОМ ПОЛЕ**
Михаил И. Копп[a], **Анатолий В. Тур**[c], **Константин Н. Кулик**[a], **Владимир В. Яновский**[a,b]
*[a]Институт монокристаллов, Национальная Академия Наук Украины
пр. Науки 60, 61001 Харьков, Украина
[b]Харьковский национальный университет имени В.Н. Каразина
пл. Свободы, 4, 61022, Харьков, Украина
[c] Университет Тулузы, Институт астрофизических исследований и планетологии
проспект полковника Роше 9, ВР 44346, 31028, Тулуза Cedex 4, Франция*

В работе мы исследовали новую крупномасштабную неустойчивость, которая возникает в наклонно вращающейся конвективной электропроводящей жидкости во внешнем однородном магнитном поле с мелкомасштабной внешней силой, имеющей нулевую спиральность. Эта сила возбуждает мелкомасштабные осцилляции скорости с малым числом Рейнольдса. С помощью метода многомасштабных асимптотических разложений получены нелинейные уравнения для вихревых и магнитных возмущений в третьем порядке по числу Рейнольдса. Показано, что в результате совместного действия силы Кориолиса и мелкомасштабной внешней силы во вращающейся электропроводящей жидкости возможна крупномасштабная неустойчивость. Исследована линейная стадия магнито-вихревого динамо, возникающего в результате неустойчивостей типа α-эффекта. Изучен механизм усиления крупномасштабных вихревых возмущений, вследствии развития гидродинамического α-эффекта с учетом температурной стратификации среды. Показано, что «слабое» внешнее магнитное поле способствует генерации вихревых и магнитных крупномасштабных возмущений, а «сильное» внешнее магнитное поле подавляет генерацию магнито-вихревых возмущений. Численными методами найдены стационарные решения уравнений нелинейного магнито-вихревого динамо в виде локализованных хаотических структур в двух случаях, когда нет внешнего однородного магнитного поля и когда оно присутствует.

КЛЮЧЕВЫЕ СЛОВА: уравнения магнитной гидродинамики в приближении Буссинеска, сила Кориолиса, многомасштабные асимптотические разложения, мелкомасштабная неспиральная турбулентность, α-эффект, хаотические структуры.

ON THE ATTENUATION OF A WAVE PACKET IN LIMITED SYSTEMS FILLED WITH AN ACTIVE MEDIUM AND PLASMA

🆔**Volodymyr M. Kuklin***, 🆔**Eugen V. Poklonskiy**, 🆔**Sergey M. Sevidov**

V.N. Karazin Kharkiv National University, Kharkiv, Ukraine
Svobody Sq. 4, Kharkiv, Ukraine, 61022
*Corresponding Author: kuklinvm1@gmail.com

In the article, for limited system conditions that form the spatial structure of the field, the attenuation processes of wave packets of finite amplitude are considered. The line width of the wave field may be the result of the dissipative processes (in a quantum system it is inverse of the lifetime of energy levels) or the result of reactive processes (in classical waveguide systems this is the spectral width of the packet). In the case of filling the waveguide with an active two-level medium, a description is possible using a quasiclassical model of the interaction of the field and particles. In this case, the quantum-mechanical description of the medium is combined with the classical representation of the field. Here, the Rabi frequency plays an important role, which determines the probabilities of induced radiation or absorption of field quanta and the oscillatory change in population inversion (nutation). Depending on the relationship between the Rabi frequency and the line width of the wave packet, the process can change the nature of the field behavior. In strong fields or with a significant population inversion, the line width can be neglected, while the field energy density is quite high. In this case, one should expect noticeable nutations of population inversions with different frequencies corresponding to the local Rabi frequency in different regions of the waveguide, the interference of which will determine the oscillatory behavior of the wave field. At a low level of electric field intensity or a slight population inversion, the mode of changing the field amplitude becomes monotonic. Plasma field damping (Landau damping) is considered. The role of population inversion is assumed by a quantity proportional to the derivative with respect to velocity of the electron distribution function. If the spectral width of the packet is small, the process of wave attenuation acquires a characteristic oscillatory form due to the exchange of energy between the wave and the plasma electrons captured by its field. The attenuation of wide packets is almost monotonic with the formation of a characteristic "plateau" in the vicinity of the phase velocity of the wave on the electron velocity distribution function.

KEYWORDS: attenuation of a wave pacadge, two-level active medium, interference of oscillations of population inversion, Landau damping

Let us consider the attenuation processes of wave packets of finite amplitude in bounded systems that impose a possible set of mode wavelengths in such a package and form the spatial field structure in the waveguides. If the waveguide is filled with an active two-level medium (a system of dipoles), a description is possible using a quasiclassical model of the interaction of the field and particles (see, for example, [1]). In this case, the quantum-mechanical description of the medium is combined with the classical representation of the field. In this approach, the Rabi frequency plays an important role, which determines the probabilities of induced radiation or absorption of field quanta [2,3] and the oscillatory change in population inversion (nutation).

Depending on the relationship between the Rabi frequency $\Omega = |d_{ab}| |E(t)| / \hbar$ (where d_{ab} the dipole moment of the particle and E the amplitude of the electric field, respectively) and γ_{12} the line width of the wave packet, the process can change the nature of the field behavior. Here, the line width is inversely proportional to the lifetime of states (the lifetime of energy levels), which is due to relaxation processes.

The population inversion $\mu = \rho_a - \rho_b$ (where ρ_a, ρ_b are the numbers of particles at the upper and lower energy levels, respectively) is related to the energy conservation law with the number of field quanta $N = |E(t)|^2 / 4\pi\hbar\omega \approx \mu = \rho_a - \rho_b$. In strong fields or with a significant population inversion the line width can be neglected, while the field energy density is quite high $\gamma_{12} < \Omega = |d_{ab}| |E(t)| / \hbar$ (similar ratio can be given for population inversion $\mu >> \gamma_{12}^2 \cdot \hbar / (\omega | d_{ab} |^2)$). In this case, one should expect noticeable nutations of population inversions with different frequencies corresponding to the local Rabi frequency Ω in different regions of the waveguide, the interference of which determines the behavior of the wave field [4].

If the opposite inequality holds $\gamma_{12} > \Omega$, this case corresponds to rather low levels of electric field intensity or small values of population inversion, which describes the behavior of a two-level system, first formulated in [5]. The mode of changing the field amplitude becomes monotonic, the characteristic time of the field change is proportional $\tau_\gamma \approx \gamma_{12} / \Omega^2$ while the population inversion tends to zero.

However, the wave field line width can be defined as dissipative processes (in a quantum system this is the reciprocal of the lifetime of energy levels) or reactive processes of wave packet formation (in classical waveguide systems this is the spectral packet width).

When considering the field damping in a plasma (Landau damping [6, 7] on electrons), the role of population inversion is taken by the quantity $\mu = n_2 - n_1 = f(v_0 + \hbar k / m) - f(v_0) = (\hbar k / m) \cdot \partial f(v) / \partial v |_{v=v_0}$, where $f(v)$ is the velocity distribution function of electrons, n_2, n_1 is the number of electrons whose velocity is less than and greater than the wave phase velocity [8,9]. In this case, it is the final spectral width of the wave packet that can affect the character of the velocity distribution of particles. With a large packet width, as is known [10], one can observe the process of so-called quasilinear relaxation, which leads to the formation of a "plateau" on the particle distribution function in the velocity space. By the way, the role of the Rabi frequency here is played by the oscillation frequency of the trapped particles in the potential well of the field $\Omega_{tr} = \sqrt{ekE / m_e}$ (here e, m_e is the charge and mass of the electron, and k is the wave number of oscillations, $v_{ph} = \omega / k$ the phase velocity of the wave).

If the spectral width of the packet is small $\Delta k \cdot v_{ph} \approx \Delta \omega \ll \Omega_{tr}$, the process of wave attenuation acquires a characteristic oscillatory form associated with the exchange of energy between the wave and plasma electrons captured by its field. In the case of the opposite inequality, the field attenuation is almost monotonous with the formation of a characteristic "plateau" in the vicinity of the phase velocity of the wave on the electron velocity distribution function corresponding to the state with zero population inversion, which is represented in this case $\mu = (\hbar k / m) \cdot \partial f(v) / \partial v |_{v=v_0} = 0$. Note that in the case of simultaneous filling of the waveguide with plasma and an active medium [11], both mechanisms of expansion of the spectral generation width should be taken into account.

And in the quantum case of field attenuation at a finite line width (finite lifetime of inverted states) and at attenuation of a wave packet of finite spectral width in the classical case, one can observe a transition from an oscillatory energy exchange between particles and a wave to a regime of monotonic change in the field amplitude, with the inversion $(\mu = \rho_a - \rho_b)$ or the value corresponding to it $(\mu = (\hbar k / m) \cdot \partial f(v) / \partial v |_{v=v_0})$ tends to zero, although the nature of these changes is different. Since the real processes of propagation of oscillations in limited systems are accompanied by the formation of wave packets, the dynamics of which have not been studied enough, their evolution should be considered in more detail.

The aim of the work is to elucidate the influence of the spectral line width of the wave packet on the wave attenuation pattern in waveguides filled with active medium and plasma.

MODEL OF A RESONATOR FILLED WITH AN ACTIVE TWO-LEVEL ENVIRONMENT

Let us discuss a one-dimensional model describing the attenuation of a wave with a finite spectral line width in limited space, filled with an active medium. Generally speaking, this process can also be considered as the transition of the nonequilibrium state of the system to a stable equilibrium state, which is accompanied by the exchange of energy between the wave and the active medium. We restrict ourselves to a two-level system. For perturbations of the electric field, polarization, and population inversion slowly varying over time, describing the excitation of electromagnetic waves in an active medium, the equations can be represented in the form [1].

$$\frac{\partial^2 E}{\partial t^2} + \delta \frac{\partial E}{\partial t} - c^2 \frac{\partial^2 E}{\partial x^2} = -4\pi \frac{\partial^2 P}{\partial t^2} , \tag{1}$$

$$\frac{\partial^2 P}{\partial t^2} + \gamma_{12} \frac{\partial P}{\partial t} + \omega^2 \cdot P = -\frac{2\omega |d_{ab}|^2}{\hbar} \mu E , \tag{2}$$

$$\frac{\partial \mu}{\partial t} = \frac{2}{\hbar \omega} < E \frac{\partial P}{\partial t} >, \tag{3}$$

moreover, the transition frequency ω between the levels corresponds to the field frequency, we neglect the relaxation of the inversion due to external reasons. We define δ - the decrement of field absorption in the medium, d_{ab} - the matrix element of the dipole moment of the fixed dipoles (more precisely, its projection onto the direction of the electric field), and write the population difference per unit volume as $\mu = n \cdot (\rho_a - \rho_b)$. Here, ρ_a and ρ_b the relative population of levels in the absence of a field γ_{12} is the inverse relaxation time of states, which in this case determines the width of the spectral line, n is the density of the dipoles of the active medium. Fields will be represented as $E = [E(t) \cdot \exp\{-i\omega t\} + E^*(t) \cdot \exp\{i\omega t\}]$ and $P = [P(t) \cdot \exp\{-i\omega t\} + P^*(t) \cdot \exp\{i\omega t\}]$. Note that in doing so $< E^2 > = 2 | E(t) |^2$. The number of field quanta is then equal $< E^2 > / 4\pi\hbar\omega = 2 | E |^2 / 4\pi\hbar\omega = N$.

For slowly varying quantities, the equations

$$\frac{\partial E(t)}{\partial t} + \delta \cdot E(t) = 2i\pi\omega P(t) , \tag{4}$$

$$\frac{\partial P(t)}{\partial t} + \gamma_{12} P(t) = \frac{|d_{ab}|^2}{i\hbar} \mu E , \tag{5}$$

$$\frac{\partial \mu}{\partial t} = \frac{2i}{\hbar} [E(t)P^*(t) - E^*(t)P(t)] . \tag{6}$$

From equation (6), by simple transformations we find

$$\frac{\partial N}{\partial t} + 2\delta N = \frac{i}{\hbar} \cdot [P(t)E^*(t) - P^*(t)E(t)],$$

where can one get the conservation law

$$\frac{\partial N}{\partial t} + 2\delta N + \frac{\partial \mu}{2\partial t} = 0.$$

To transform the above system of equations, we can use the notation $\mu/\mu_0 = M$, $\Omega_0 = |d_{ab}| \cdot |E_0| /\hbar = |d_{ab}| \cdot [4\pi\omega\mu_0 /\hbar]^{1/2}$ – the Rabi frequency corresponding to the value of the amplitude of the electric field $|E_0| = [4\pi\hbar\omega\mu_0]^{1/2}$, $E = \frac{E(t)}{[4\pi\hbar\omega\mu_0]^{1/2}}$, $P = \frac{P(t)}{[4\pi\hbar\omega\mu_0]^{1/2}} \cdot \frac{4\pi\omega}{\Omega_0}$, $\tau = \Omega_0 t$, $\Gamma_{12} = \gamma_{12} /\Omega_0$, $\Theta = \delta /\Omega_0$. Note that the absence of time derivatives in equations (4)-(6) is associated both with the immobility of the dipoles and with the formation of a standing wave in a limited resonator system, the shape of which does not change during the development of the process. Using these notations, we rewrite equations (4) - (6) in complex form

$$\frac{\partial E}{\partial \tau} + \Theta E = \frac{i}{2} P , \tag{7}$$

$$\frac{\partial P}{\partial \tau} + \Gamma_{12} P = -iM E , \tag{8}$$

$$\frac{\partial M}{\partial \tau} = -2i[E^*P - EP^*] . \tag{9}$$

The generation cases described by equations (10) - (12), when the natural line width is much less than the Rabi frequency $\Gamma_{12} << 1$, under the conditions of the formation of a standing electromagnetic wave due to reflections from its boundaries, were considered in [4]. If the conditions $\Gamma_{12} >> 1$ are satisfied, the oscillatory character (nutations) of the population inversions can be neglected and equations (7-9) can be written in the form

$$\frac{\partial N}{\partial \tau} + 2\Theta N = \frac{N \cdot M}{\Gamma_{12}} \tag{10}$$

$$\frac{\partial M}{\partial \tau} = -2\frac{N \cdot M}{\Gamma_{12}} . \tag{11}$$

Note that the transition from equation (7) to equation (10) is similar to the transition to the case noticeable spectral field width, when the spectral line width is greater than the inverse characteristic time of the change in the amplitude of perturbations [12, 13]. In dimensionless variables, this condition can be written as $\Gamma_{12} >> \frac{\partial P}{P \cdot \partial \tau}$, or something the same $\gamma_{12} >> \Omega = |d_{ab}||E(t)|/\hbar$. Obviously, the line width noticeably exceeds the Rabi frequency, while the characteristic time of the field change is proportional $\tau_\gamma \approx \gamma_{12} /\Omega^2$. This case corresponds to rather low levels of electric field intensity or small values of population inversion $\gamma_{12} >> [4\pi\omega]^{1/2} |d_{ab}| \mu /\hbar^{1/2}$.

That is, the system of (balanced) equations (9) - (10) describes the behavior of a two-level system in the presence of an electric field, first formulated in [5].

It should also be noted that the interval of variation of the inversion is determined by the choice μ_0 and the initial conditions, that is, the inversion at the initial moment can be both equal $\mu(0) = \mu_{max} = \rho_a$ and much smaller.

ATTENUATION OF A WAVE PACKAGE IN A RESONATOR FILLED WITH AN ACTIVE MEDIUM

In the resonator, the electromagnetic field is established due to reflection from the ends of the system partially or completely, as in the case under consideration. However, the inversion and polarization of the quantities localized in space, which allows us to determine these variables in individual spatial sectors. That is, the electromagnetic field can be represented as a standing wave, and in each of the spatial sectors $1 < j < S$ the field intensity can be represented in the form

$$| E_j (\tau = 0) |^2 = 2 \frac{1}{S} \cdot | E(\tau = 0) |^2 \cdot Sin^2 \{2\pi \frac{j}{S} + \alpha\} , \tag{12}$$

where α is an almost constant phase associated with the absorption of field energy δ. In the general case $\delta \approx \frac{c}{4\pi} | E |^2 (x = 0) / (\frac{<| E |^2>}{4\pi} b)$, where $b = m\lambda$ is the waveguide length.

It is easy to see that $| E |^2 (x = 0) = <| E |^2 > Sin^2 \alpha$ and $\delta \approx c(Sin^2 \alpha) / 2b$ where c is the group velocity of the wave outside the waveguide. However, we neglect the radiation from the waveguide below $\alpha = 0$. We can verify that $\sum_j 2 \frac{1}{S} Sin^2 \{2\pi \frac{j}{S}\} = m$ in the case under consideration, when a countable number of waves m fit along the length of the waveguide $b = m\lambda$. The total (relative) number of field quanta can be written in the form

$$N(\tau) = 2 \sum_{j=1}^{S} | E_j (\tau) |^2 = 2 | E(\tau) |^2 . \tag{13}$$

It is clear that without violating generality we can consider the case $m = 1$. The system of equations (7) - (9) in this case is transformed as follows.

$$\frac{\partial P_j}{\partial \tau} + \Gamma_{12} P_j = -i M_j E_j , \tag{14}$$

$$\frac{\partial M_j}{\partial \tau} = 2i[E_j P_j * - E_j * P_j] , \tag{15}$$

where $E_j(\tau) = (\sqrt{\frac{2}{S}}) \cdot | E(\tau) | \cdot Sin\{2\pi \frac{j}{S}\}$, $\frac{1}{2} \sum_{j=1}^{S} (M_j + M_j *) = M$.

We can also write down the conservation law, a consequence of equations (7) and (9)

$$\frac{1}{2} \frac{\partial M}{\partial \tau} + \frac{\partial N}{\partial \tau} = 0 . \tag{16}$$

Note that the time scale in this description is related to the scale of a simple model [4], as follows $\tau \to \tau \sqrt{S}$. A remarkable circumstance is the quality identity of the calculation results for the case of a simple model [4] and the more complicated description given below for the case of a narrow spectral line ($\Gamma_{12} = 0$), which indicates a rather simple mechanism of energy exchange between the wave and the active medium. It demonstrates the importance of interference of oscillations (nutations) population inversions to describe changes in the amplitude of the field of a steady form in a waveguide.

Results of numerical simulation. For calculations, we use equations (13)- (15), as well as the following quantities $N(\tau) = \frac{1}{S} \sum N_j (\tau)$, $M(\tau) = \frac{1}{S} \sum M_j (\tau)$, $E_j (\tau) = \sqrt{2N(\tau)} \cdot Sin \left(2\pi \frac{j}{S} \right)$. Below we used the initial conditions $N_0 = 1.45$, $M_0 = -1$, $S = 100$, $\Theta = 0$. Attention should be paid to the oscillations caused by the interference of the processes of induced radiation and absorption of field quanta in different parts of the waveguide (Fig. 1.). This phenomenon is discussed in detail in [4].

Fig. 1. The behavior of the relative number of quanta (bold line) and relative population inversion (thin line) over time with a negligible line width $\Gamma_{12} = 0$.

The population inversion oscillation frequency corresponds to the Rabi frequency and is proportional to the electric field in this local region. From the equations of a simple model presented in [4] for the same initial conditions it follows $N + 0.5M = N_0 + 0.5M_0 = 0.95$. It turns out in our case with different line widths over time $N \to 0.95$, moreover

$M \to 0$. With an increase in the width of the oscillation line of the field intensity (the number of quanta) and population inversions weaken (Fig. 2.)
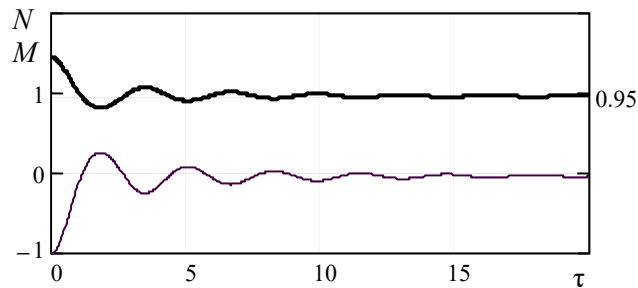
Fig. 2. The behavior of the relative number of quanta (bold line) and the relative population inversion (thin line) over time with a small line width $\Gamma_{12} = 0.25$.

With a sufficiently large line width, the mode of changing the field intensity (number of quanta) and population inversion becomes monotonic (Fig. 3.)
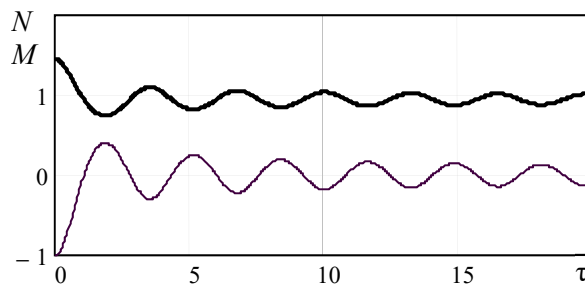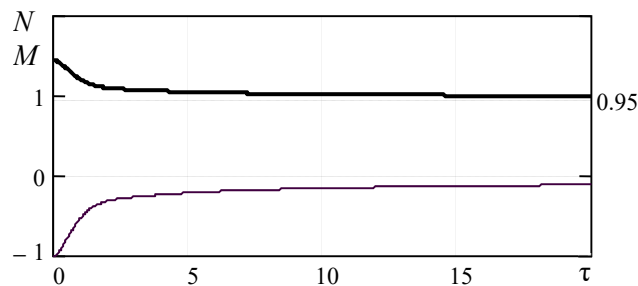

Fig. 3. The behavior of the relative number of quanta (bold line) and relative population inversion (thin line) over time with a line width $\Gamma_{12} = 3$.

This behavior of the number of quanta and the population inversion of a two-level system in the presence of an electric field is characteristic of the case when the process is described by balance equations, first presented in [5]. It is important to note that the finite width of the wave packet is able to suppress the interference of population inversion sections oscillating with different local Rabi frequencies in the field of a standing wave.

In conclusion of the section, we note that the broadening of the vibrational spectrum can occur not only due to relaxation of states (i.e., changes in the number of particles at the upper and lower energy levels) of the quantum system at small (or, which is one and the same, polarization attenuation, which can be seen from the equation (16)). In the case of a long waveguide, the field in the waveguide may exist in the form of a wave packet, the spectral width of which $\Delta k \cdot c = (2\pi / \lambda)[m^{-1} - (m-1)^{-1}] = \omega / m^2$. When $\omega / m^2 > \gamma_{12}$ the dynamics of the field attenuation in the waveguide can determine the spectral width of the wave packet. We consider this case below, where the processes of changing the number of particles at the upper and lower energy levels in the absence of a field are not significant.

ATTENUATION OF THE LANDAU WAVE PACKAGE IN A HOT PLASMA

Consider the process of attenuation of plasma (Langmuir) waves on plasma electrons. Electrons effectively interact with the wave, moving at a speed close to the phase velocity of the wave packet. For simplicity, we restrict ourselves to the one-dimensional case [6] (see also [7]). In this one-dimensional representation, plasma electrons emit and absorb quanta of longitudinal (Langmuir) waves - plasmons whose energy is equal $\hbar\omega(k)$. According to [8, 9], we determine the number of longitudinal wave quanta emitted per unit time in the range of wave numbers dk in cases of spontaneous and induced processes $n_m u_{mn} dk$ and $n_m w_{mn} N_k dk$, accordingly.

In this case, the particles emitting the quantum of the field — the plasmon, pass from state m to state n. In the same wavelength range, we similarly determine the plasmon absorption rate $n_n w_{nm} N_k dk$, where n_m is the number of particles in the state m, and N_k is the number of field quanta, u_{mn}, w_{mn}, w_{nm} are the coefficients in A. Einstein's equations which are equal to each other in the onedimensional case, considered below [14].

$$\partial n_m / \partial t = -(u_{mn} + w_{mn} \cdot N_k) \cdot n_m + w_{nm} \cdot N_k \cdot n_n, \tag{17}$$

$$\partial n_n / \partial t = -w_{nm} \cdot N_k \cdot n_n + (u_{mn} + w_{mn} \cdot N_k) \cdot n_m \quad \tag{18}$$

To describe the dynamics of the number of plasmons, we obtain the equation

$$dN_k / dt = u_{mn} \cdot n_m \{(1 - n_n / n_m) \cdot N_k + 1\} . \tag{19}$$

Note that the change in the plasmon energy density $d\mathrm{E}_k / dt = \hbar\omega(k) \cdot u_{mn} \cdot n_m$ due to spontaneous emission of particles per unit time is equal $w(k)$. With this in mind, the complete equation for the plasmon energy density takes the form:

$$d\mathrm{E}_k / dt = w(k) \cdot \{(1 - n_n / n_m) \cdot N_k + 1\} . \tag{20}$$

The change in the momentum of the particles upon plasmon emission $m \cdot (v_m - v_n) = \hbar k$, whence it follows $v_m = v_n + \hbar \cdot k / m$, which is also the case if the velocity interval over which the particle distribution function changes significantly exceeds $\hbar k / m$

$$\mu = n_m - n_n = f(v_n + \hbar k / m) - f(v_n) = (\hbar k / m) \cdot \partial f(v) / \partial v |_{v=v_n} \tag{21}$$

moreover, the value μ has the meaning of population inversion. For the spectral intensity of spontaneous emission of plasma particles $w(k)$, one can obtain the expression [9]

$$w(k) = 2e^2 \int_{-\infty}^{\infty} dv \cdot v \cdot f(v) \cdot \mathrm{Im}[k\varepsilon(kv,k)]^{-1} = 2\pi^2 e^2 [\omega_{pe}^2 / k^3] \cdot f[\omega(k) / k], \tag{22}$$

and equation (19) describing the spontaneous (first term of the right-hand side) and induced radiation (second term of the right-hand side) of Langmuir waves by plasma particles takes the form

$$d\mathrm{E}_k / dt = 2\pi^2 e^2 [\omega^2(k) / k^2] \cdot \{f[\omega(k) / k] + \mathrm{E}_k \cdot (k / \omega(k) \cdot m) \cdot \partial f(v) / \partial v |_{v=\omega(k)/k}\} . \tag{23}$$

If the velocity distribution function has the form $f(v) = (n_0 / v_T \sqrt{\pi}) \cdot \exp\{-\dfrac{v^2}{v_T^2}\}$, then the second term determines the linear decrement of the Landau damping of the Langmuir wave δ_L whose phase velocity ω / k is on plasma particles (we neglect spontaneous emission)

$$d\mathrm{E}_k / dt = -2\delta_L \mathrm{E}_k = \pi[\omega^3(k) / n_0 k] \frac{\partial f(v)}{\partial v} \cdot \mathrm{E}_k = \sqrt{\pi} \frac{\omega^3(kv - \omega)}{k^3 v_T^3} \exp\{-\frac{(v - \omega/k)^2}{v_T^2}\} \cdot \mathrm{E}_k . \tag{24}$$

The complex equation for the field, which describes the process of induced absorption of the plasma wave field by plasma electrons, can be written as

$$\frac{\partial(\omega\varepsilon)}{\partial\omega} \frac{\partial E_n}{\partial t} + i\omega\varepsilon \cdot E_n = \frac{4\pi e\omega}{k} \frac{\partial f}{\partial v}|_0 \cdot \int_{-\pi/k}^{\pi/k} d\xi_0 \int_{-v_m}^{v_m} v_0 dv_0 \exp(ik_n\xi + i\varphi_n) , \tag{25}$$

where $\xi = x - v_0 t$, $\Delta v = v - v_0$, $n_{b0} = \int f_0(v) dv$, $\Delta v_m \propto 6\pi |\gamma| / k_0$, and the initial conditions $\xi_0 = \xi(t=0) \subset (-\pi/k_0, \pi/k_0)$ and $\Delta v_0 = \Delta v(t=0) \subset (-\Delta v_m, \Delta v_m)$.

Results of numerical simulation. For calculations we use the equations

$$\frac{\partial A_n}{\partial \tau} + i(n - n_0) A_n = -8\pi \int_{-0.5}^{0.5} d\xi \int_{-\eta}^{+\eta} d\eta \cdot \eta \cdot \exp\{-2\pi n i\xi\} , \tag{26}$$

$$2\pi \cdot \frac{\partial^2 \xi}{\partial \tau^2} = -\mathrm{Re}[\sum_{3}^{6} A_n \cdot \exp\{2n\pi i\xi\}] , \tag{27}$$

where are the modes of the wave packet $A_n = |A_n| \exp\{i\varphi_n\}$, the main wave of $n_0 = 5$, the satellite $n = 3; 4; 6; 7$, under the following initial conditions: $A_5 = 1.0$ - the amplitude of the main wave, the amplitudes of the satellites - $A_3 = A_7 = 0.2$; $A_4 = A_6 = 0.7$; the number of particles is 5000, $\xi \subset (0,1)$ and $\eta = \dfrac{1}{2\pi} \cdot \dfrac{d\xi}{d\tau}, \xi = \dfrac{kx}{2\pi}$.

The behavior of the wave packet over time is investigated by changing the sum of squares of modules of all amplitudes $|A_n|^2$. This value determines the intensity of the resulting wave of our package: $I = \sum_{n=3}^{7} |A_n|^2$. We observe the decrease of the intensity of the wave packet, associated with the energy exchange between the field and the captured wave plasma electrons (Fig. 4).
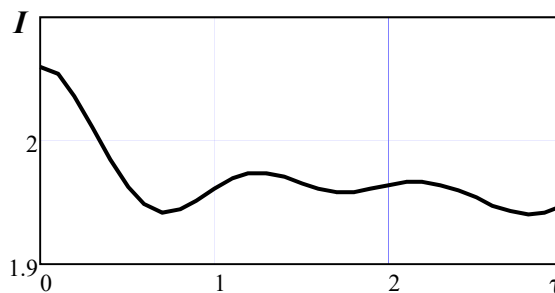
Fig. 4. The behavior of the intensity of wave I over time for the wave packet

In single-mode mode (the case of a narrow line width of the wave packet) oscillation of the wave intensity is observed. This mode of wave attenuation at the initial stage is known as Landau attenuation. In the calculated scheme, the intensity of the monochromatic wave is equal to $I = |A_5|^2$. In the developed mode the process becomes nonlinear [9, 10] with weak fading oscillations of the field (see Fig. 5).
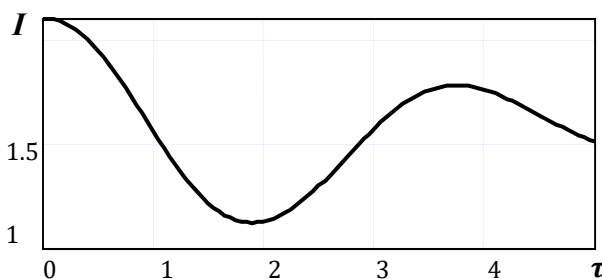
Fig. 5. The behavior over time of the intensity of wave I in single mode.

The electron distribution function in the vicinity of the phase wave velocity for different time instants for wave packets with different line widths is shown in Fig. 6,7.

We can cite the change in the distribution function of plasma electrons with time. In the single-mode the distribution function has a large change in oscillations of the wave amplitude (Fig. 6)
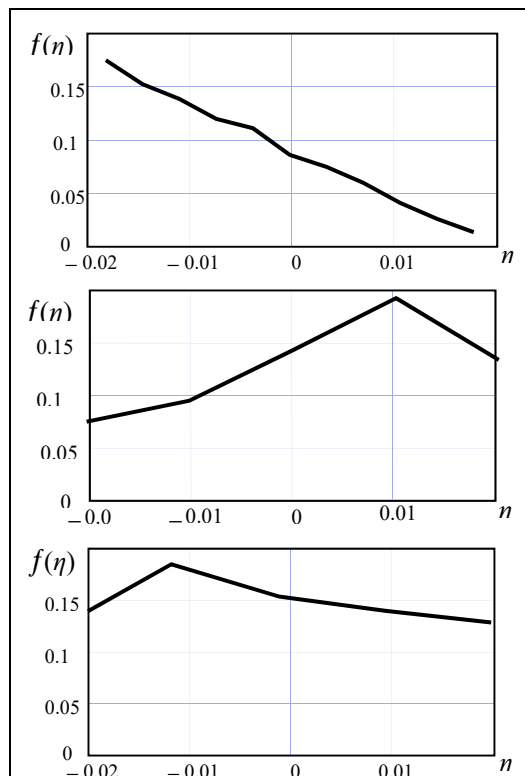
Fig. 6. Function of electron distribution in vicinity of phase velocity of the wave for time moments $\tau = 0; 3; 4$ in single-mode mode.

The attenuation of the packet leads to the formation of a stable state of the electron velocity distribution function with a practically zero velocity derivative near the phase velocity of the packet (Fig. 7)
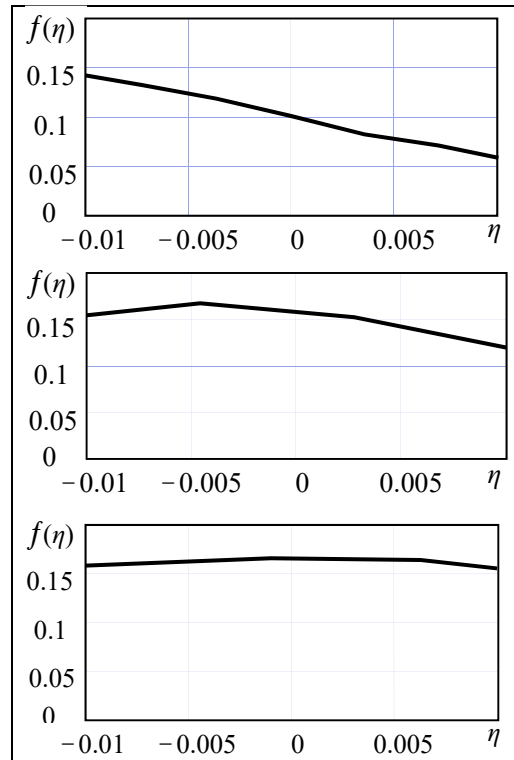
Fig. 7. The function of distribution of electrons in vicinity of phase velocity of the wave for time moments τ = 0; 2; 5 in case of attenuation of the wave packet.

CONCLUSIONS

When considering the processes of wave attenuation in a resonator filled with an active medium and in a plasma with a finite electron temperature, there is the reason for the transition of the nature of the change in the field amplitude from oscillatory to monotonic with increasing line width of the wave packet.

The nature of the oscillations in a resonator filled with an active medium is associated with the interference of oscillations of the population inversion in local regions. Inversion changes occur with the Rabi frequency, which depends on the electric field of a standing wave formed as a result of reflections from the ends of the resonator. In this case, strong fields or with a significant population inversion, the line width can be neglected. In this case, the field energy density is quite high $|E(t)|^2/4\pi >> \gamma_{12}^2\hbar^2/|d_{ab}|^2$ (a similar relation can be given for population inversion $\mu >> \gamma_{12}^2 \cdot \hbar/(\omega|d_{ab}|^2)$). At low levels of electric field intensity or a small population inversion, the inverse inequalities are satisfied and the line width should be taken into account, which leads to suppression of the interference of individual local inversion regions along the waveguide. This mode corresponds to the behavior of the system discussed for the first time in [5]. The nature of the change in the field amplitude becomes monotonic.

In a similar way, the width of the spectrum of the wave packet affects the character of the Landau damping [6] on plasma electrons. In this case, the role of population inversion is played by the quantity $\mu = n_2 - n_1 = f(v_0 + \hbar k/m) - f(v_0) = (\hbar k/m) \cdot \partial f(v)/\partial v|_{v=v_0}$, where $f(v)$ is the velocity distribution function of the electrons, n_2, n_1 are the numbers of electrons whose velocity is less than and greater than the phase velocity of the wave.

The role of the Rabi frequency here is played by the oscillation frequency of the trapped particles in the potential well of the field $\Omega_{tr} = \sqrt{ekE/m_e}$ (here e, m_e the charge and mass of the electron, a k is the wave number of oscillations, and $v_{ph} = \omega/k$ is the phase velocity of the wave).

In the case of a small spectral width of the packet $\Delta k \cdot v_{ph} \approx \Delta\omega << \Omega_{tr}$, the process of wave attenuation acquires a characteristic oscillatory form associated with the exchange of energy between the wave and plasma electrons captured by its field. In the case of the reverse inequality, the monotonic character of the field attenuation is observed with the formation of a characteristic "plateau" in the vicinity of the phase velocity of the wave on the electron velocity distribution function corresponding to the state with zero population inversion, which is presented in this case as $\mu = (\hbar k/m) \cdot \partial f(v)/\partial v|_{v=v_0} = 0$.

ORCID IDs
Volodymyr M. Kuklin http://orcid.org/0000-0002-0310-1582, **Eugen V. Poklonskiy** https://orcid.org/0000-0001-5682-6694
Sergey M. Sevidov https://orcid.org/0000-0002-9927-9237

REFERENCES
[1] P.S. Landa *Auto-oscillations in distributed systems*, (Nauka, Moscow, 1983), pp. 320. (in Russian)
[2] A.S. Davydov *Quantum mechanics*, (Fizmatgiz, Moscow, 1963), pp. 748. (in Russian)
[3] L. Allen and J. Eberly, *Optical resonance and two-level atoms*, (Witey-lnterscicitce Publication John Witty and Sons, New York-London-Sydney-Toronto, 1975), pp. 222.
[4] V.M. Kuklin and E.V. Poklonskiy, East Eur. J. Phys. **3**, 46-53 (2019), https://doi.org/10.26565/2312-4334-2019-3-06.
[5] A. Einstein, Phys. Zs. **18**, 121 (1917), http://web.ihep.su/dbserv/compas/src/einstein17/eng.pdf
[6] L.D. Landau, JETP, **16**, 574-586 (1946).
[7] A.A. Rukhadze and V.P. Silin, in: *Problems of Theoretical Physics. Scientific works. Issue 2*, edited by A.G. Zagorodny, N.F. Shulga and V.M. Kuklin, (KhNU, Kharkiv, 2016), pp. 376. (in Russian)
[8] A.A. Andronov, Izv. Vuz. Radiophysics, **4**(5), 861–866 (1961). (in Russian)
[9] A.N .Kondratenko and V.M. Kuklin, *Fundamentals of Plasma Electronics*, (Energoatomizdat, Moscow, 1988), pp. 320. (in Russian).
[10] A.I. Akhiezer, I.A. Akhiezer, A.G. Sitenko, K.M. Stepanov and R.V. Polovin, *Plasma Electrodynamics*, (Pergamon, N.Y., 1975), pp. 431.
[11] M.B. Bondarenko, A.N. Kondratenko and V.I. Tkachenko, Izv. Vuz. Radiophysics, **27**(11), 962-967 (1984), (in Russian).
[12] E.J. Valeo and C.R. Olerman, Phys. Rev. Lett. **30**(21), 1035-1038 (1973), https://doi.org/10.1103/PhysRevLett.30.1035
[13] J.J. Thomson and J.I. Karush, The Physics of Fluids, **17**(8), 1608-1613 (1974), https://doi.org/10.1063/1.1694940.
[14] V.M. Kuklin, *Selected chapters (theoretical physics)*, (KhNU, Kharkiv, 2018), pp. 224. (in Russian).

ЗАТУХАНИЕ ВОЛНОВОГО ПАКЕТА В ЗАПОЛНЕННЫХ АКТИВНОЙ СРЕДОЙ И ПЛАЗМОЙ В ОГРАНИЧЕННЫХ СИСТЕМАХ

В.М. Куклин, Е.В. Поклонский, С.М. Севидов
Харьковский национальный университет имени В. Н. Каразина, Харьков, Украина
пл. Свободы 4, г. Харьков, Украина, 61022

В работе для условий ограниченных систем, которые формируют пространственную структуру поля, рассмотрены процессы затухания волновых пакетов конечной амплитуды. Ширина линии волнового поля определяется как диссипативными процессами (в квантовой системе это величина, обратная времени жизни энергетических уровней) или реактивными процессами (в классических волноводных системах это спектральная ширина пакета). В случае заполнения волновода активной двухуровневой средой описание возможно с помощью квазиклассической модели взаимодействия поля и частиц. При этом квантовомеханическое описание среды объединяется с классическим представлением поля. Здесь существенную роль играет частота Раби, определяющая вероятности индуцированного излучения или поглощения квантов поля и осцилляторное изменение инверсии населенностей (нутацию). В зависимости от соотношения между значениями частоты Раби и ширины линии волнового пакета процесс может менять характер поведения поля. В сильных полях или при значительной инверсии населенностей шириной линии можно пренебречь, при этом плотность энергии поля достаточно велика. В этом случае следует ожидать заметных нутаций инверсии населенностей с разной частотой, отвечающей локальной частоте Раби в разных областях волновода, интерференция которых определит осцилляторное поведение поля волны. При низком уровне интенсивности электрического поля или небольшой инверсии населенностей, режим изменения амплитуды поля становится монотонным. Рассмотрено затухание поля в плазме (затухание Ландау). Роль инверсии населенностей берет на себя величина, пропорциональная производной по скорости от функции распределения электронов. Если спектральная ширина пакета мала, процесс затухания волны приобретает характерный осцилляторный вид, обусловленный обменом энергией между волной и захваченными ее полем электронами плазмы. Затухание широких пакетов практически монотонное с формированием в окрестности фазовой скорости волны характерного «плато» на функции распределения электронов по скоростям.

КЛЮЧЕВЫЕ СЛОВА: затухание волнового пакета, двухуровневая активная среда, интерференция осцилляций инверсии населенностей, затухание Ландау.

ПРО ЗАГАСАННЯ ХВИЛЬОВОГО ПАКЕТУ У ЗАПОВНЕНИХ АКТИВНИМ СЕРЕДОВИЩЕМ ТА ПЛАЗМОЮ У ОБМЕЖЕНИХ СИСТЕМАХ

В.М. Куклін, Є.В. Поклонський, С.М. Севідов
Харківський національний університет імені В.Н. Каразіна, Харків, Україна
м. Свободи 4, м. Харків, Україна, 61022

В роботі для умов обмежених систем, які формують просторову структуру поля, розглянуті процеси загасання хвильових пакетів кінцевої амплітуди. Ширина лінії хвильового поля визначається як диссипативними процесами (в квантовій системі це величина, зворотна часу життя енергетичних рівнів) або реактивними процесами (в класичних хвилеводних системах це спектральна ширина пакета). У разі заповнення хвилеводу активним дворівневим середовищем опис є можливим за допомогою квазікласичної моделі взаємодії поля і частинок. При цьому квантовомеханічний опис середовища об'єднується з класичним уявленням поля. Тут істотну роль грає частота Рабі, що визначає ймовірність індукованого випромінювання або поглинання квантів поля і осциляторну зміну (нутацію) інверсії заселеності. Залежно від співвідношення між значеннями

частоти Рабі і ширини лінії хвильового пакету може змінюватись характер поведінки поля. У сильних полях або при значній інверсії заселеності шириною лінії можна знехтувати, при цьому щільність енергії поля досить велика. В цьому випадку слід очікувати помітних нутацій інверсії заселеності з різною частотою, що відповідає локальній частоті Рабі в різних областях хвилеводу, інтерференція яких визначить осциляторну поведінку поля хвилі. При низькому рівні інтенсивності електричного поля або невеликий інверсії заселеності, режим зміни амплітуди поля стає монотонним. Розглянуто загасання поля в плазмі (загасання Ландау). Роль інверсії заселеності бере на себе величина, пропорційна похідній по швидкісті від функції розподілу електронів. Якщо спектральна ширина пакета мала, процес загасання хвилі набуває характерного осциляторного вигляду, обумовленого обміном енергією між хвилею і захопленими її полем електронами плазми. Загасання широких пакетів практично монотонне з формуванням в околиці фазової швидкості хвилі характерного «плато» на функції розподілу електронів за швидкостями.

КЛЮЧОВІ СЛОВА: загасання хвильового пакету, дворівневе активне середовище, інтерференція осциляцій інверсії заселеності, загасання Ландау.

THEORETICAL INVESTIGATION OF FUNDAMENTAL INHERENT PHYSICAL AND OPTOELECTRONIC PROPERTIES OF ZnSnSb₂ CHALCOPYRITE SEMICONDUCTOR

Shalini Tomar[a], Shiv Raj Bhardwaj[b], Saral Kumar Gupta[a], Ajay Singh Verma[a]*

[a]Department of Physics, Banasthali Vidyapith, Rajasthan, (India) 304022
[b]Department of Physics, B S A College Mathura, (India) 281004
*Corresponding Author: ajay_phy@rediffmail.com, Mobile: +91 9412884655
Received November 18, 2019; revised November 22, 2019; accepted December 18, 2019

Here in, we have investigated fundamental inherent physical properties like as structural, electronic, optical, elastic, thermal etc of the ZnSnSb₂ by using the accurate full potential linearized augmented plane wave (FP-LAPW) method. These materials have higher energy gaps and lower melting points as compared to their binary analogues, because of which they are considered to be important in crystal growth studies and device applications. For structural properties, the minimization has been done in two steps, first parameter u is minimized by the calculation of the internal forces acting on the atoms within the unit cell until the forces become negligible, for this MINI task is used, which is included in the WIEN2K code. Second, the total energy of crystal is calculated for a grid of volume of the unit cell (V) and c/a values. Five values of c/a are used for each volume and a polynomial is fitted to the calculated energies to calculate the best c/a ratio. We have presented the electronic and optical properties with the recently developed density functional of Tran and Blaha. Furthermore, optical features such as dielectric functions, refractive indices, extinction coefficient, optical reflectivity, absorption coefficients, optical conductivities, were calculated for photon energies up to 40 eV. We have used WC and TB-mBJ exchange correlation potential for these properties and yield a direct band gap of 0.46 eV for this material and the obtained electronic band gap matches well with the experimental data. The TB-mBJ potential gives results in good agreement with experimental values that are similar to those produced by more sophisticated methods, but at much lower computational costs. The main peaks of real part of the electronic dielectric function $\varepsilon_1(\omega)$ which is mainly generated by electronic transition from the top of the valence band to the bottom of conduction band, occurs at 1.59 eV and $\varepsilon_1(\omega)$ spectra further decreases up to 4.99 eV. The imaginary part of the electronic dielectric constant $\varepsilon_2(\omega)$ is the fundamental factor of the optical properties of a material. The proposed study shows that the critical point of the $\varepsilon_2(\omega)$ occurs at 0.42 eV, which is closely related to the obtained band gap value 0.46 eV. The maximum reflectivity occurs in region 3.74-11.33 eV. This material has non-vanishing conductivity in the visible light region (1.65 eV-3.1 eV), the main peak occurs at 3.80 eV, which fall in the UV region. The elastic constants at equilibrium in BCT structure have also determined. The elastic stiffness tensor of chalcopyrite compounds has six independent components, because of the symmetry properties of the space group, namely C_{11}, C_{12}, C_{13}, C_{33}, C_{44} and C_{66} in Young notation. The thermal properties such as thermal expansion, heat capacity, Debye temperature, entropy, Grüneisen parameter and bulk modulus were calculated employing the quasi-harmonic Debye model at different temperatures and pressures and the silent results were interpreted. To determine the thermodynamic properties through the quasi-harmonic Debye model, a temperature range 0 K 500 K has been taken. The pressure effects are studied in the 0–7 GPa range. Similar trends have been observed in the considered temperature range, but above 600 K trends get disturbed which may be due to melting of material. Based on the semi-empirical relation, we have determined the hardness of the materials, which attributed to different covalent bonding strengths. Most of the investigated parameters are reported for the first time.
KEYWORDS: Ab-initio calculations; electronic properties; optical properties; elastic constants; thermal properties

The $A^{II} B^{IV} C_2^{V}$ semiconductors have recently received attention due to their potential usage in various nonlinear laser devices [1-3], i.e. second harmonic generation, sum mixing, difference frequency generation and parametric oscillation covering a broad part of the electromagnetic spectrum from ultraviolet to the infrared through the visible region. These materials have higher energy gaps and lower melting points as compared to their binary analogues, because of which they are considered to be important in crystal growth studies and device applications. Apart from it, the other important technological applications of these materials are in light emitting diodes, infrared detectors, infrared oscillations, etc [4-8].

A considerable amount of experimental and theoretical work related to the prediction of crystal structures, lattice constants, phase diagrams and related properties has been done during the last few years [9-13]. But comparatively, less attention, however, has been paid to the ZnSnSb₂ which adopts a chalcopyrite structure [14,15]. Tenga et al [16] have studied the high temperature form of ZnSnSb₂ which adopted a disordered cubic sphalerite structure where Zn and Sn atoms are randomly distributed over the same crystallographic position. A first principles investigation by the same group suggests that the tetragonal low-temperature form of ZnSnSb₂ has a narrow band gap of about 0.2 eV in agreement with the semimetal behavior of the material. Very recently, Mishra et al [17] have demonstrated the effect of the p–d hybridization, structural distortion and cation electronegativity on the band gap of the ZnSnSb₂ by using Tight binding Linear Muffin-Tin orbital method.

In the paper we present the structural, electronic, optical, elastic and thermal properties of ZnSnSb₂ in chalcopyrite phase. We have presented the theoretical study of expansion coefficient (α), heat capacities (C_v and C_p), bulk modulus (B and B_s), Debye temperature (θ_D), hardness (H) and Gruneisen parameter (γ) of ZnSnSb₂ which are nevertheless scarce in literature. The outline of the paper is as follows. In section II we have given a brief review of the computational scheme

used. The calculations of the structural, electronic and optical properties along with the computed elastic and thermal properties are described in section III; while the summary and conclusions are drawn in section VI.

COMPUTATIONAL METHODS

The calculations were done using FP-LAPW computational scheme [18,19] as implemented in the WIEN2K code [20]. The FP-LAPW method expands the Kohn-Sham orbitals in atomic like orbitals inside the muffin-tin (MT) atomic spheres and plane waves in the interstitial region. The Kohn-Sham equations were solved using the recently developed Wu-Cohen generalized gradient approximation (WC-GGA) [21,22] for the exchange-correlation (XC) potential. It has been shown that this new functional is more accurate for solids than any existing GGA and meta-GGA forms. For a variety of materials, it improves the equilibrium lattice constants and bulk moduli significantly over local-density approximation [23] and Perdew-Burke-Ernzerhof (PBE) [24] and therefore is a better choice. For this reason we adopted the new WC approximation for the XC potential in studying the present systems. Further for electronic structure calculations modified Becke–Johnson potential (TB-mBJ) [25] as coupled with WC-GGA is used.

The valence wave functions inside the atomic spheres were expanded up to $l=10$ partial waves. In the interstitial region, a plane wave expansion with $R_{MT}K_{max}$ equal to seven was used for all the investigated systems, where R_{MT} is the minimum radius of the muffin-tin spheres and K_{max} gives the magnitude of the largest K vector in the plane wave expansion. The potential and the charge density were Fourier expanded up to $G_{max} = 10$. We carried out convergence tests for the charge-density Fourier expansion using higher G_{max} values. The R_{MT} (muffin-tin radii) are taken to be 2.2, 2.22 and 2.15 (in atomic unit) for Zn, Sn ans Sb respectively. The modified tetrahedron method [26] was applied to integrate inside the Brillouin zone (BZ) with a dense mesh of 5000 uniformly distributed k-points (equivalent to 405 in irreducible BZ) where the total energy converges to less than 10^{-6} Ry.

RESULTS AND DISSCUSSION
Structural Properties

The ternary chalcopyrite semiconductor crystallizes in the chalcopyrite structure with sapce group $I-\overline{42}d$ (D_{2d}^{12}). The Zn atom is located at (0,0,0); (0,1/2,1/4), Sn at (1/2,1/2,0); (1/2,0,1/4) and Sb at (u,1/4,1/8); (-u,3/4,1/8); (3/4,u,7/8); (1/4,-u,7/8). Two unequal bond lengths d_{Zn-Sb} and d_{Sn-Sb} result in two structural deformations, first is characterized by u parameter defined as $u=0.25+ (d_{Zn-Sb}^2 − d_{Sn-Sb}^2)/a^2$ where a is the lattice parameter in x and y direction, and the second parameter $\eta=c/a$, where c is lattice parameter in z direction which is generally different from 2a.

To determine the best energy as a function of volume, we minimized the total energy of the system with respect to the other geometrical parameters. The minimization is done in two steps, first parameter u is minimized by the calculation of the internal forces acting on the atoms within the unit cell until the forces become negligible, for this MINI task is used which is included in the WIEN2K code. Second, the total energy of crystal is calculated for a grid of volume of the unit cell (V) and c/a values, where each point in the grid involves the minimization with respect to u. Five values of c/a are used for each volume and a polynomial is then fitted to the calculated energies to calculate the best c/a ratio. The result is an optimal curve (c/a, u) as a function of volume. Further a final optimal curve of total energy is obtained by minimizing the energy verses [V, c/a (V), u (V)] by FP-LAPW calculations and Murnaghan equation of state [27].

Further we have used the calculated lattice constants for determination of inter atomic distance for A – C and B – C bonds by the following relations [15].

$$x = 0.5 - (c^2 / 32\ a^2\ -\ 1/16\ )^{1/2}; \qquad d_{A-C} = [a^2x^2 + (4a^2 + c^2)\ /\ 64]^{1/2};$$

$$d_{B-C} = [a^2(1/2 - x)^2 + (4a^2 + c^2)\ /\ 64]^{1/2}; \ d\ (in\ Å) = (d_{A-C} + d_{B-C})/2. \qquad (1)$$

We have also calculated the bulk modulus (B in GPa) by using the semi-empirical equations developed by Verma and co-authors [28, 29] for chalcopyrite semiconductors as follows,

$$B = A + S \times \sqrt[4]{Z_1 Z_2 Z_3} \times \left(\frac{k_B T_m}{\Omega} \right), \qquad (2)$$

$$B = 4056\ (Z_1 Z_2 Z_3)^{0.15}\ d^{-5}, \qquad (3)$$

where k_B, T_m, Ω and d is the Boltzman's constant, melting temperature, bond volume and inter atomic distance respectively; $Z_1 Z_2 Z_3$ (product of ionic charges)48 for $A^{II}B^{IV}C_2^V$ semiconductors. A and S are constants and the values are 9.09042 and 38.47051 respectively for the chalcopyrite semiconductors. Table 1 presents the lattice constants and obtained along with the bulk modulus and its pressure derivative (B'). The calculated total energy per ZnSnSb$_2$ unit as a function of volume is shown in Fig. 1.
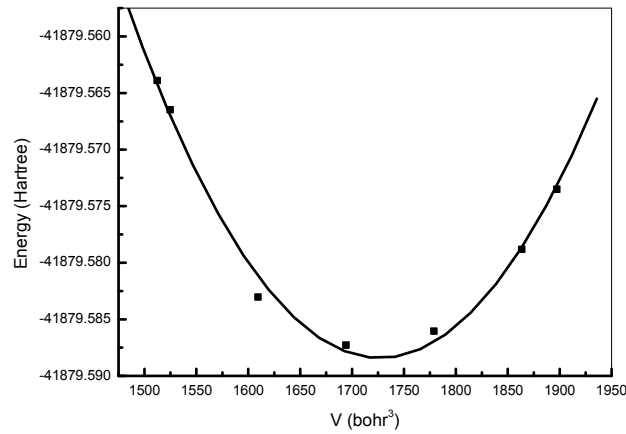
Fig. 1. Calculated total energies as a function of volume of ZnSnSb$_2$

Table 1

The various obtained parameters of ZnSnSb$_2$ calculated in WC-GGA

a (Å)	c (Å)	u	d (Å)^C	B (GPa)	B′
6.259$^\#$	12.901$^\#$	0.235$^\#$	2.739$^\$$	46$^\#$	7.978$^\#$
6.273$^{\$\$}$	12.546$^{\$\$}$		2.716$^{\$\$}$	35*, 47**, 49***	
Ω$^\#$(10^{-30}m^3)	T$_m$ (K)$^\#$	n$^\#$	n^D	ε$_\infty$$^\#$	ε$_\infty$^{E}
32.2122	600 K	3.693	4.157	13.64	13.0
$^\#$this work; $^{\$\$}$Reference [15]; ^{C}Calculated from equation (1); ^{D}Calculated from equation (8); ^{E}Calculated from equation (7); Ω is bond volume, *Calculated from equation (2); **Calculated from equation (3); ***Calculated from equation (3) data taken from Reference [15].					

Electronic and optical properties

The present calculations using the WC and TB-mBJ method yields a direct band gap of 0.46 eV for ZnSnSb$_2$, as shown in Fig. 2(a).

(a)

(b)
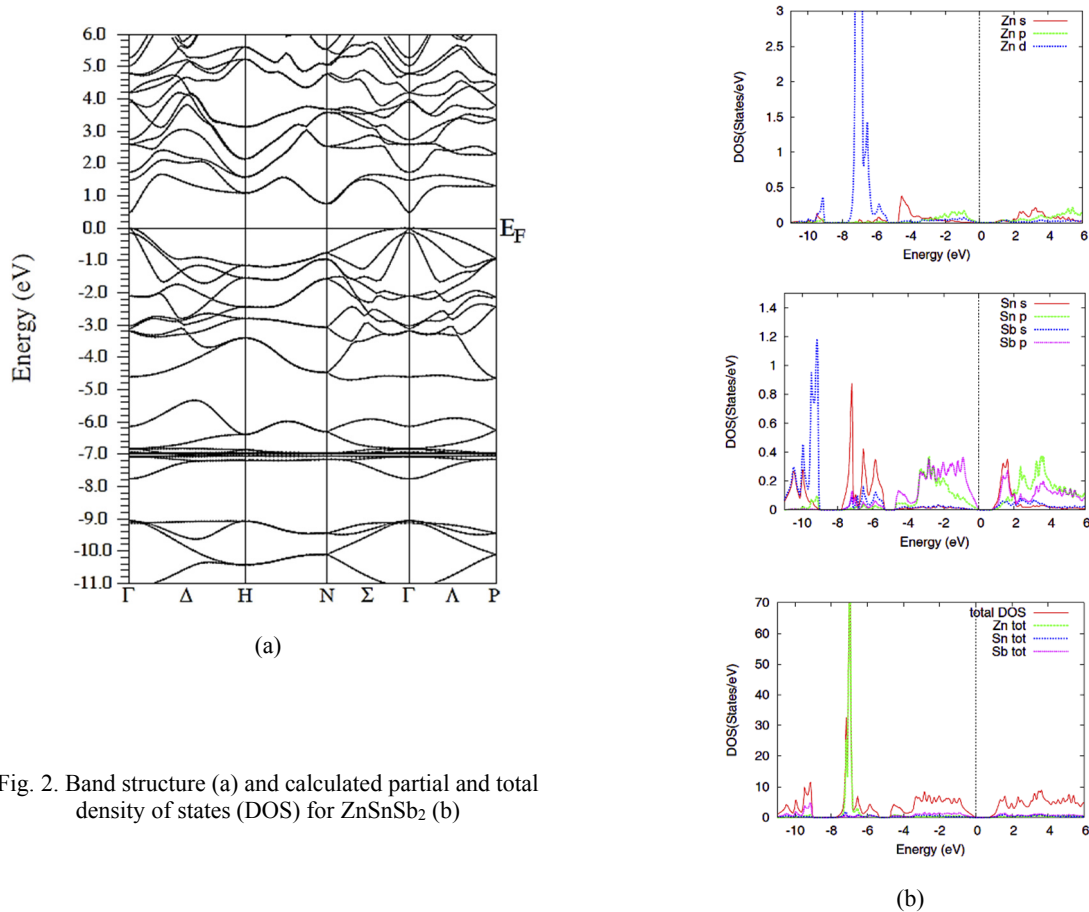
Fig. 2. Band structure (a) and calculated partial and total density of states (DOS) for ZnSnSb$_2$ (b)

As clear from the Fig. 2 that the obtained electronic band gap matches well with the experimental data (0.4 eV) predicted by Kiselyova et al [30]. Mishra et al, [17] and Bhosale et al [31] have been reported an estimate of the theoretical band gap of ZnSnSb$_2$ as 0.19 eV and 0.46 eV respectively. The total and partial density of state (TDOS and PDOS) corresponding to the band structures shown in Fig. 2(b) along with the Fermi energy level for 0 GPa pressure. The position of the Fermi level is at 0 eV. The PDOS are very useful as they give information on hybridization and the orbital character of the states. It can be seen that in Fig. 2(b), the lowest valence bands are essentially dominated by Sb-s states, with minor presence Sn-p and Sn-s states. The intermediate valence band is essentially dominated by Zn-d states. The other valence bands are essentially dominated by Sb-s states. The conduction band consists essentially of Sn-s and Sb-p with a minor presence Sn-p and Sb-s states. The comparison of the theoretical band gaps with available experimental data shows that TB-mBJ correlation potential allows the prediction of band gap values much closer to the experimental values. The TB-mBJ potential gives results in good agreement with experimental values that are similar to those produced by more sophisticated methods, but at much lower computational costs [25].

The linear response to an external electromagnetic field with a small wave vector is measured through the complex dielectric function,

$$\varepsilon(\omega) = \varepsilon_1(\omega) + i\varepsilon_2(\omega), \tag{4}$$

which is related to the interaction of photons with electrons[32]. The imaginary part $\varepsilon_2(\omega)$ of the dielectric function could be obtained from the momentum matrix elements between the occupied and unoccupied wave functions and is given by [33]

$$\varepsilon_2(\omega) = \frac{2\pi^2 e^2}{\Omega \varepsilon_0} \sum_{i \in c. f \in v} \sum_k \left| \left\langle \Psi_k^c \left| \hat{\mu} . r \right| \Psi_k^v \right\rangle \right|^2 \delta \left[E_k^c - E_k^v - \hbar\omega \right]. \tag{5}$$

The real part $\varepsilon_1(\omega)$ can be evaluated from $\varepsilon_2(\omega)$ using the Kramer-Kronig relations and is given by[34]

$$\varepsilon_1(\omega) = 1 + \left(\frac{2}{\pi} \right) \int_0^\infty \frac{\omega'^2 \varepsilon_2(\omega')}{\omega'^2 - \omega^2} d\omega'. \tag{6}$$

All of the other optical properties, including the absorption coefficient α(x), the refractive index n(x), the extinction coefficient k(x), and the energy-loss spectrum L(x), can be directly calculated from $\varepsilon_1(\omega)$ and $\varepsilon_2(\omega)$ [33,35].
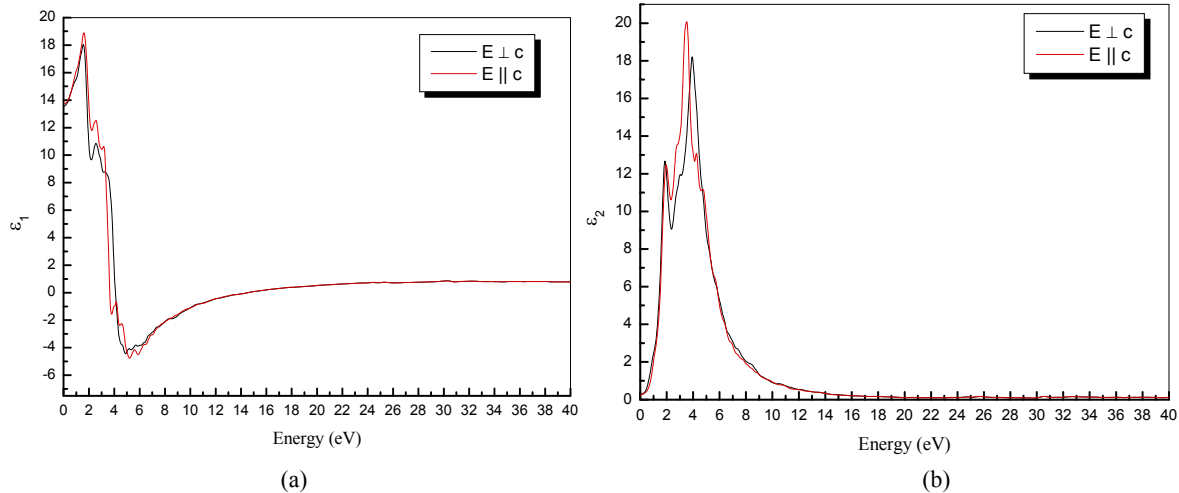
Fig. 3. The calculated (a) real $\varepsilon_1(\omega)$ and (b) imaginary $\varepsilon_2(\omega)$ parts of complex dielectric constant for ZnSnSb$_2$

Fig. 3(a) and 3(b) displays the real and imaginary parts respectively of the electronic dielectric functions ε(ω) spectrum for the photon energy ranging up to 40 eV. The main peaks of real part of the electronic dielectric function $\varepsilon_1(\omega)$ which is mainly generated by electronic transition from the top of the valence band to the bottom of conduction band, occurs at 1.59 eV and $\varepsilon_1(\omega)$ spectra further decreases up to 4.99 eV. Optical spectra exhibit anisotropy in two directions (along basal-plane and z-axis) with a very small difference (0.01517) in the static limit. The imaginary part of the electronic dielectric constant $\varepsilon_2(\omega)$ is the fundamental factor of the optical properties of a material. The proposed study shows that the critical point of the $\varepsilon_2(\omega)$ occurs at 0.42 eV, which is closely related to the obtained band gap value 0.46 eV. This point corresponds to the Γ_c—Γ_v splitting which gives the threshold for the direct optical transitions between the absolute valence band maximum and the first conduction band minimum and is known as fundamental adsorption edge. An estimation of dielectric constant for the comparison can be given by the relation developed by Verma et al [13] for chalcopyrites as follows,

$$\varepsilon_{XY} = S \left(Z_X Z_Y \right)^A d_{XY}^2, \tag{7}$$

where d_{XY} is the inter atomic distance of (A-C and B-C bond). $Z_X Z_Y$ is product of ionic charges of A-C and B-C bond and the values are 6 and 12 respectively. A and S are constants with the values 0.83 and 0.27 respectively for $A^{II}B^{IV}C_2^V$ semiconductors.

Fig. 4(a),(b) present the refractive index n (ω) and the extinction coefficient k (ω) respectively. The refractive index spectrum shows an anisotropic behavior (Δn (0eV)=0.02052), hence only the average value is listed in Table 1.
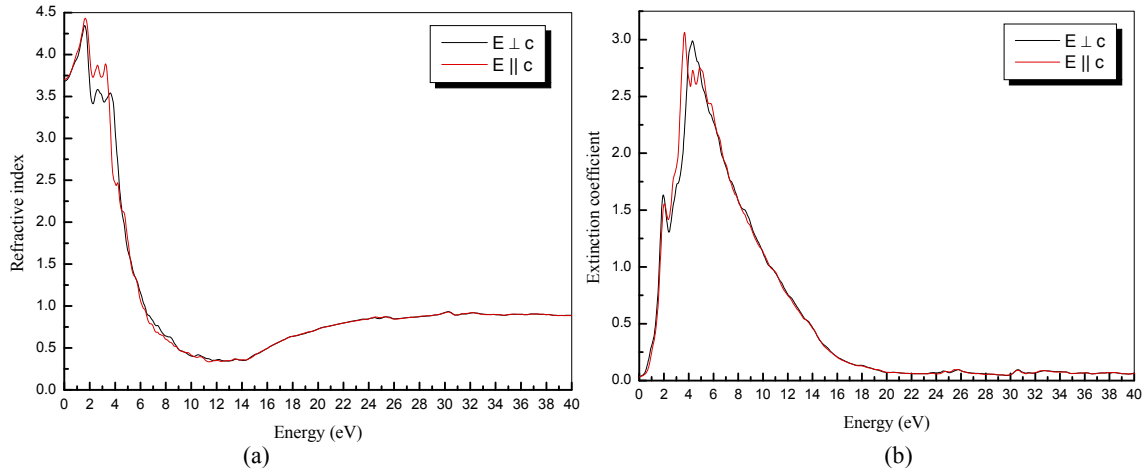
Fig. 4. The calculated (a) refractive index and (b) extinction coefficient for ZnSnSb$_2$

The refractive index increases with energy reaching a maximum value in the visible region for all compounds. The peak values the refractive index has a value of 4.39 at 1.61 eV. The extinction coefficient k (ω) is related to the decay or damping of the oscillation amplitude of the incident electric field, the extinction coefficient k (ω) decreases with increasing the incident photon energy. The peak value obtained for the extinction coefficient occurs at the point where the dispersive part of dielectric constant (ε_1 (ω)) has a zero value (Fig. 4(a)) for all the compounds. The extinction coefficient k (ω) decreases with increasing the incident photon energy.

The refractive index (n) of these compounds can also be evaluated by using the relation given by Verma et al[36] for chalcopyrites as follows,

$$n = 0.31(Z_1 Z_2 Z_3)^{0.15} d^2 , \tag{8}$$

Where d is the inter atomic distance and $Z_1 Z_2 Z_3$ (product of ionic charges) = 48 for $A^{II}B^{IV}C_2^V$ semiconductors.

The calculated optical reflectivity R (ω) and absorption coefficient are α (ω) displayed in Fig. 5(a),(b) respectively. The maximum reflectivity occurs in region 3.74 eV - 11.33 eV. The absorption coefficient indicates the fraction of light lost by the electromagnetic wave when it passes through a unit thickness of the material. It is clear that polarization has a minor influence on the spectrum. From the absorption spectrum, we can easily find the absorption edge at 0.45 eV. When the photon energy is more than the absorption edge value, then adsorption coefficient increases. The absorption coefficients further decrease rapidly in the high energy region, which is the typical characteristic of semiconductors. Optical conductivity parameters are closely related to the photo-electric conversion efficiency and mainly used to measure the change caused by the illumination. Fig. 6 shows the optical conductivity of ZnSnSb$_2$. It's clear that the material has non-vanishing conductivity in the visible light region (1.65 eV - 3.1 eV), the main peak occurs at 3.80 eV, which fall in the UV region.
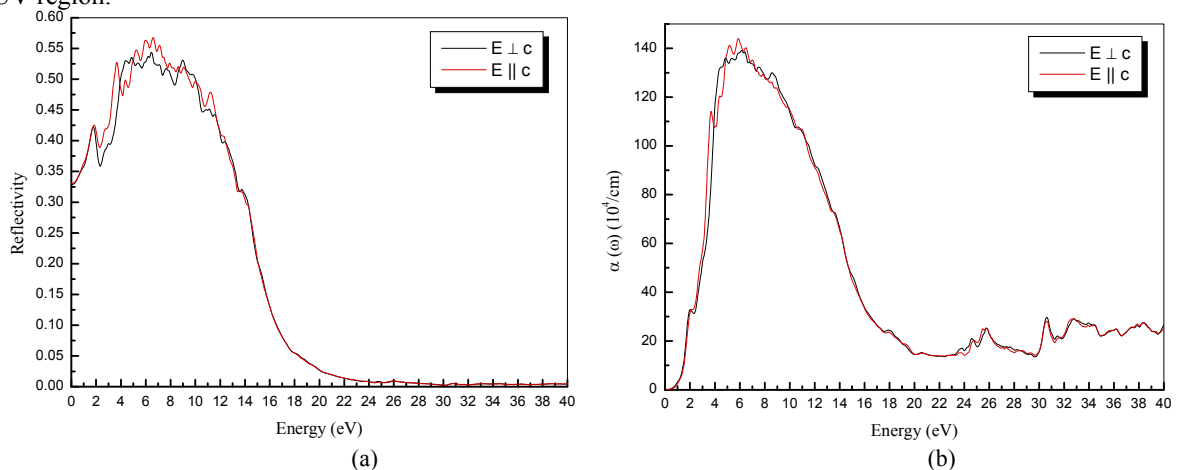
Fig. 5. The calculated (a) reflectivity (R (ω)) and (b) absorption coefficient ($\alpha(\omega)$) for ZnSnSb$_2$
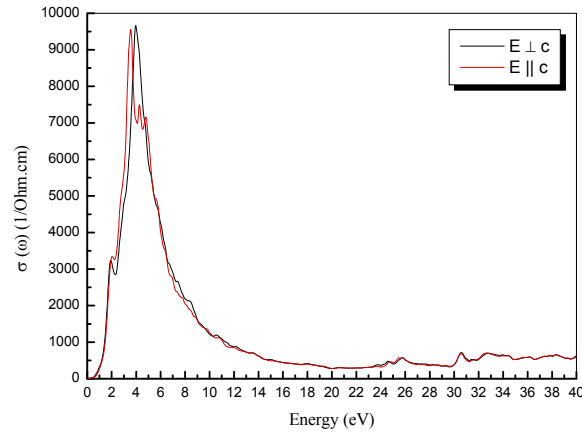
Fig. 6. The calculated photoconductivity ($\sigma(\omega)$) for ZnSnSb$_2$

Elastic Properties

The determination of the elastic constants requires knowledge of the curvature of the energy curve as a function of strain for selected deformations of the unit cell. The deformations [37] are shown in Table 2 and chosen such that the strained systems have the maximum possible symmetry. The WIEN2K package [20] facilitates this task by providing a force-driven optimization of the internal cell geometry. The elastic stiffness tensor of chalcopyrite compounds has six independent components, because of the symmetry properties of the D_{2d}^{12} space group, namely C$_{11}$, C$_{12}$, C$_{13}$, C$_{33}$, C$_{44}$ and C$_{66}$ in Young notation. The calculated elastic constant for the tetragonal phase of ZnSnSb$_2$ are listed in Table 3. The calculated elastic constants fulfill the mechanical stability criteria for the tetragonal systems:

$$C_{11} > |C_{12}|, (C_{11}+C_{12}) C_{33} > 2C_{13}^2, C_{44} > 0, \text{ and } C_{66} > 0.$$

In order to check the internal consistency of calculated elastic constants we can compare the bulk modulus reported on Table 1&3 with an equivalent combination of the C$_{ij}$'s.

Table 2.

The lattice parameters of the deformed tetragonal unit cell, the expression relating the δ and ε variables, the finite Lagrangian strain tensor (Voigt notation) and the value of the second derivative, $(1/2V)(d^2E/d\varepsilon^2)$, in terms of the elastic constants (ε being deformation coordinate and E the energy)

Strained cell	ε	Strain (η)	dE^2/d ε^2
$(a+\delta, a+\delta, \frac{c+c\delta}{a}, 90,90,90)$	$\frac{(a+\delta)^2}{a^2}-1$	$(\frac{\varepsilon}{2}, \frac{\varepsilon}{2}, \frac{c\varepsilon}{2a}, 0,0,0)$	$\frac{1}{4}(C_{11}+C_{12}) + \frac{1}{8}C_{33} + \frac{1}{2}C_{13}$
$(a+\delta, a+\delta, c, 90,90,90)$	$\frac{(a+\delta)^2}{a^2}-1$	$(\frac{\varepsilon}{2}, \frac{\varepsilon}{2}, 0,0,0,0)$	$\frac{1}{4}(C_{11}+C_{12})$
$(a, a, \frac{c+c\delta}{a}, 90,90,90)$	$\frac{(c+\delta)^2}{c^2}-1$	$(0,0,\frac{\varepsilon}{2},0,0,0)$	$\frac{1}{8}C_{33}$
$(a, a+\delta, c, 90,90,90)$	$\frac{(a+\delta)^2}{a^2}-1$	$(0,\frac{\varepsilon}{2},0,0,0,0)$	$\frac{1}{8}C_{11}$
$(a, a, c, 90, 90+\delta, 90)$	$\sin\delta$	$(0,0,0,0,\varepsilon,0)$	C_{44}
$(a, a, c, 90, 90, 90+\delta)$	$\sin\delta$	$(0,0,0,0,0,\varepsilon)$	C_{66}

Table 3.

Elastic constants C$_{ij}$ (in GPa) of ZnSnSb$_2$ compared with available data

C$_{11}$	C$_{12}$	C$_{13}$	C$_{33}$	C$_{44}$	C$_{66}$
63.4[#], 78.7*	39.2[#], 49.2*	33.1[#], 46.7*	65.6[#], 73.8*	49.9[#], 27.1*	74.4[#], 24.6*
B (GPa)[#]	G (GPa)[#]	Y (GPa)[#]	ν[#]	κ_a (GPa^{-1})[#]	κ_c (GPa^{-1})[#]
45	33	80	0.20	0.0072	0.0080
*Calculated from equation (29); [#]this work					

Bulk modulus should be found from above by the Voigt approximation (uniform strain assumption) [38-40]:

$$B_V = \frac{1}{9}\left(2C_{11} + C_{33} + 2C_{12} + 4C_{13}\right), \tag{9}$$

$$B_R = \frac{(C_{11} + C_{12})C_{33} - 2C_{13}^2}{C_{11} + C_{12} + 2C_{33} - 4C_{13}}. \tag{10}$$

Voigt and Reuss approximations provide, in fact, an estimation of the elastic behaviour of an isotopic material, for instance a polycrystalline sample. Such a medium would have a single shear constant, G, upper bounded (G_v) and lower bounded (G_R) by

$$G_V = \frac{1}{30}\left(M + 3C_{11} - 3C_{12} + 12C_{44} + 6C_{66}\right), \tag{11}$$

$$G_R = 15\left\{\frac{18B_V}{C^2} + \frac{6}{(C_{11} - C_{12})} + \frac{6}{C_{44}} + \frac{3}{C_{66}}\right\}^{-1}; \quad C^2 = (C_{11} + C_{12})C_{33} - 2C_{13}^2. \tag{12}$$

In the Voigt-Reuss-Hill approximation [41], the B and G of the polycrystalline material are approximated as the arithmetic mean of the Voigt and Reuss limits:

$$B = \frac{B_V + B_R}{2}, \tag{13}$$

$$G = \frac{G_V + G_R}{2}. \tag{14}$$

Finally the Poisson ratio and the Young modulus are obtained as

$$\upsilon = \frac{3B - 2G}{2(3B + G)}, \tag{15}$$

$$Y = \frac{9BG}{3B + G}. \tag{16}$$

Using the single crystal C_{ij} data, one can evaluate the linear compressibilities along the principles axis of the lattice. For the tetragonal structure, the linear compressibilities κ_a and κ_c along the a- and c-axis respectively are given in term of elastic constants by the following relations;

$$\kappa_a = -\frac{1}{a}\frac{\partial a}{\partial p} = \frac{C_{33} - C_{13}}{C_{33}(C_{11} + C_{12}) - 2C_{13}^2}, \tag{17}$$

$$\kappa_c = -\frac{1}{c}\frac{\partial c}{\partial p} = \frac{C_{11} + C_{12} - 2C_{13}}{C_{33}(C_{11} + C_{12}) - 2C_{13}^2}. \tag{18}$$

Pugh [42] proposed that the resistance to plastic deformation is related to the product Gb, where 'b' is the Burgers vector, and that the fracture strength is proportional to the product Ba, where 'a' corresponds to the lattice parameter. As b and a are constants for specific materials, the Ba/Gb can be simplified into B/G. This formula was recently exploited in the study of brittle vs ductile transition in intermetallic compounds from first-principles calculations [43, 44]. A high B/G ratio is associated with ductility, whereas a low value corresponds to the brittle nature. The critical value which separates ductile and brittle material is around 1.75, i.e., if B/G > 1.75, the material behaves in a ductile manner otherwise the material behaves in a brittle manner. We have found that B/G ratio is 1.35, classifying the material as brittle. The c/a ratio is ~ 2.06, indicates the behavior similar to its binary analog.

Thermal Properties

To investigate the thermodynamic properties of Zn-chalcopyrite, we have used Gibbs program. The obtained set of total energy versus primitive cell volume determined in previous section has been used to derive the macroscopic properties as a function of temperature and pressure from the standard thermodynamic relations. Gibbs program is based on the quasi-harmonic Debye model [45], in which the non-equilibrium Gibbs function $G^*(V; P, T)$ can be written in the form of:

$$G^*(V; P, T) = E(V) + PV + A_{vib}[\theta_D; T] \tag{19}$$

where E(V) is the total energy per unit cell, PV corresponds to the constant hydrostatic pressure condition, θ_D is the Debye temperature, and A_{vib} is the vibrational term, which can be written using the Debye model of the phonon density of states as [46, 47]:

$$A_{vib}[\theta_D; T] = nkT\left[\frac{9\theta}{8T} + 3\ln(1 - e^{-\theta/T}) - D\left(\frac{\theta}{T}\right)\right] \tag{20}$$

where n is the number of atoms per formula unit, D(θ/T) represents the Debye integral, and for an isotropic solid, θ is expressed as [46]:

$$\theta_D = \frac{\hbar}{k}\left[6\pi^2 V^{1/2} n\right]^{1/3} f(\sigma)\sqrt{\frac{B_S}{M}} \tag{21}$$

M being the molecular mass per unit cell and B_S the adiabatic bulk modulus, approximated by the static compressibility [45]:

$$B_S \cong B(V) = V \frac{d^2 E(V)}{dV^2} \tag{22}$$

$f(\sigma)$ is given by Refs. [45,48, 49]; where σ is the Poisson ratio.

Therefore, the non-equilibrium Gibbs function G*(V; P, T) as a function of (V; P, T) can be minimized with respect to volume V,

$$\left(\frac{\partial G^*(V;P,T)}{\partial V} \right)_{P,T} = 0. \tag{23}$$

By solving Eq. (23), one can obtain the thermal equation of state (EOS) V(P, T). The heat capacity C_V and the thermal expansion coefficient α are given by [41],

$$C_V = 3nk \left[4D\left(\frac{\theta}{T}\right) - \frac{3\theta/T}{e^{\theta/T} - 1} \right] \tag{24}$$

$$S = nk \left[4D\left(\frac{\theta}{T}\right) - 3\ln(1 - e^{-\theta/T}) \right] \tag{25}$$

$$\alpha = \frac{\gamma C_V}{B_T V} \tag{26}$$

where γ is the Grüneisen parameter, which is defined as:

$$\gamma = -\frac{d \ln \theta(V)}{d \ln V} \tag{27}$$

Through the quasi-harmonic Debye model, one could calculate the thermodynamic quantities of any temperatures and pressures of compounds from the calculated E–V data at T = 0 and P = 0.

We have also provided a prediction of the hardness (H in GPa) and six independent elastic constants (C_{ij} in GPa) by using the semi-empirical equations developed by Verma and co-authors[50, 51],

$$H = K B^{K+1} \tag{28}$$

B = Bulk modulus; K = 0.59for $A^{II}B^{IV}C_2^V$

$$C_{ij} = A_{ij} \times \left(\frac{k_B T_m}{(Z_1 Z_2 Z_3)\Omega} \right)^{0.15} \quad (i = 1, 3, 4, 6 \text{ and } j = 1, 2, 3, 4, 6) \tag{29}$$

$A_{11} = 160, A_{12} = 100, A_{13} = 95, A_{33} = 150, A_{44} = 55, A_{66} = 50$

where $Z_1 Z_2$ and Z_3 are the ionic charges on the A, B and C elements respectively and the value of product of ionic charge is 48 for $A^{II}B^{IV}C_2^V$ [50]. The calculated values are presented in Table 3.
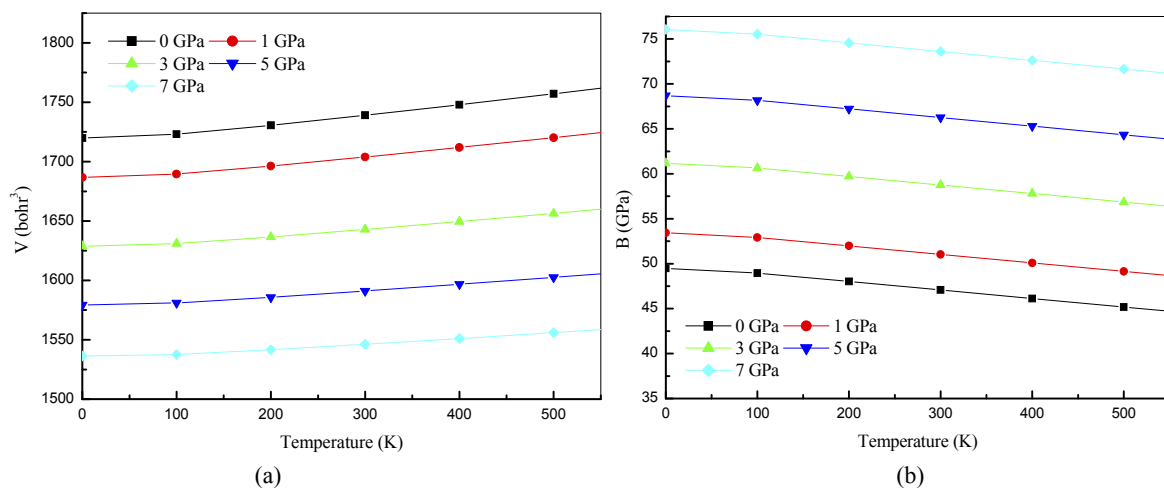
Fig. 7. The calculated values of (a) Volume (V) and (b) Bulk modulus (B) at different temperature and pressure for ZnSnSb$_2$.

To determine the thermodynamic properties through the quasi-harmonic Debye model, a temperature range 0 K-500 K has been taken. The pressure effects are studied in the 0–7 GPa range. Similar trends have been observed in the considered temperature range, but above 600 K trends get disturbed which may be due to melting of material. Hence for convenience we have taken 600 K as the melting temperature (T_m) in the proposed study. Fig. 7(a) presents relationships between the equilibrium volume V (bohr^3) and pressure at various temperatures. Meanwhile, V increases

slightly as the temperature increases, whereas the equilibrium volume V decreases dramatically as the pressure P increases at a given temperature. This account suggests that the $ZnSnSb_2$ under loads turns to be more compressible with increasing pressure than decreasing temperature. Fig. 7(b) presents the bulk modulus slightly which decreases with increasing temperature at a given pressure and increases with increasing pressure at a given temperature.

(a)

(b)
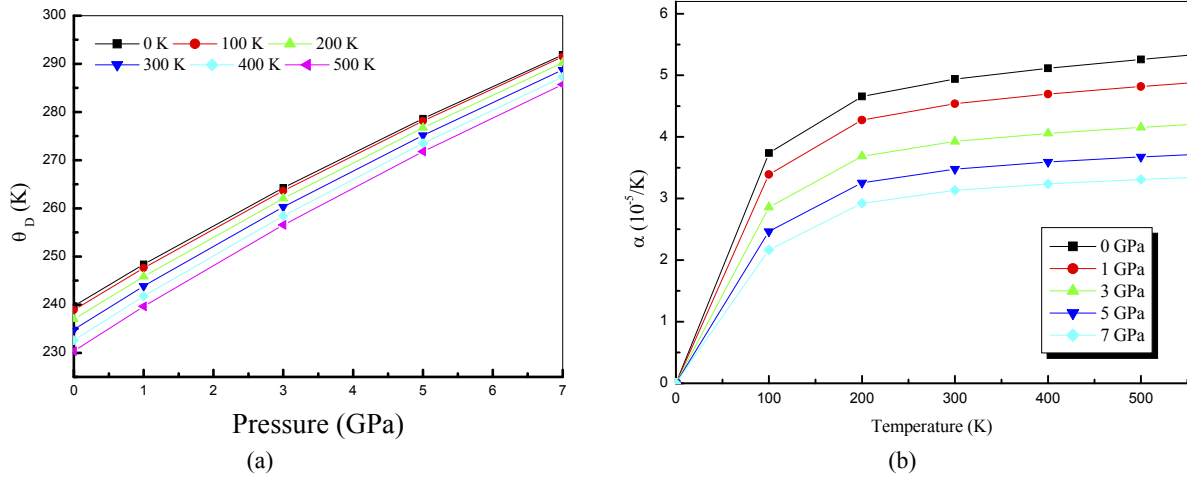
Fig. 8. (a) Debye temperature and (b) Thermal expansion coefficients at various temperature and pressure for $ZnSnSb_2$.

The variation of the Debye temperature θ_D (K) as a function of pressure and temperature illustrated by proposed results is displayed in Fig. 8(a). With the applied pressure increasing, the Debye temperatures are almost linearly increasing. Fig. 8 (b) shows the volume thermal expansion coefficient $\alpha(10^{-5}/K)$ of $ZnSnSb_2$ at various pressures, from which it can be seen that the volume thermal expansion coefficient α increases quickly at a given temperature particularly at zero pressure below the temperature of 300 K. After a sharp increase, the volume thermal expansion coefficient of the $ZnSnSb_2$ is nearly insensitive to the temperature above 300 K due to the electronic contributions.
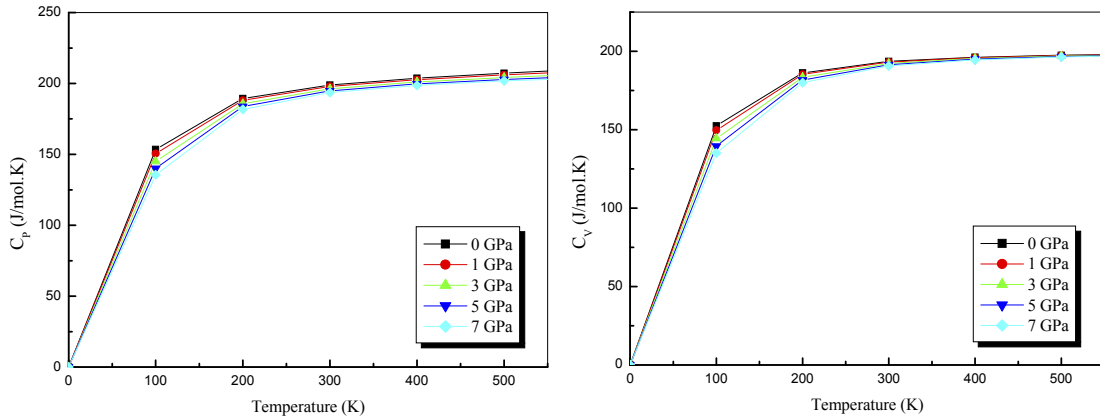
Fig. 9. Heat capacity vs temperature at various pressures for $ZnSnSb_2$.

As very important parameters, the heat capacities of a substance not only provide essential insight into the vibrational properties but are also mandatory for many applications. The proposed calculation of the heat capacities C_P and C_V of $ZnSnSb_2$ verses temperature at pressure range 0-7 GPa are shown in the following Fig. 9. From this figure, we can see that the constant volume heat capacity C_V and the constant pressure capacity C_P are very similar in appearance and both of them are proportional to T^3 at low temperatures. At high temperatures, the anharmonic effect on heat capacity is suppressed; which is called Dulong-Petit limit, with the increasing of the temperature, whereas C_P increases monotonically with the temperature. Fig. 10(a) shows the entropy vs temperature at various pressures for $ZnSnSb_2$. The entropies are variable by power exponent with increasing temperature but the entropies are higher at low pressure than that at high pressure at same temperature. The Grüneisen parameter γ is another important quantity for the materials. In Fig. 10(b), we have shown the values of Grüneisen parameter γ at different temperatures and pressures. It shows the value γ increases as the temperature increases at a given pressure and decreases as the pressure increases at a given temperature.

Table 4.

Selection of thermal properties of $ZnSnSb_2$ at 300 K; isothermal and adiabatic bulk moduli (B and B_S in GPa), Hardness (H in GPa), Gruneisen parameter (γ), Debye temperature (θ_D in K) and thermal expansion coefficient (α in 10^{-5}/K),

B (GPa)	B_S (GPa)	H (GPa)	γ	θ_D (K)	α (10^{-5}/K)
47.1	48.4	2.64	1.86	235	4.94

In Fig. 11, we have shown the values of hardness (H in GPa) at different temperatures and pressures. It shows the hardness decreases as the temperature increases at a given pressure and increases as the pressure increases at a given temperature. The values of hardness are reported for the first time at different pressure and temperature. Table 4 present the thermal properties such as isothermal bulk modulus, hardness, Grüneisen parameter, Debye temperature and thermal expansion coefficient at 300 K.

(a)   (b)
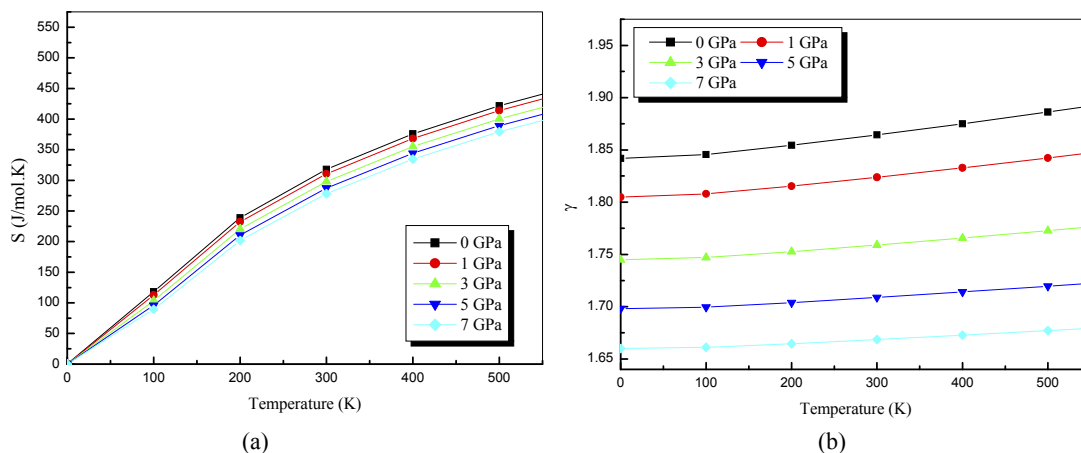
Fig. 10. Entropy (a) and Gruneisen parameter (b) at various pressures and temperatures for ZnSnSb$_2$
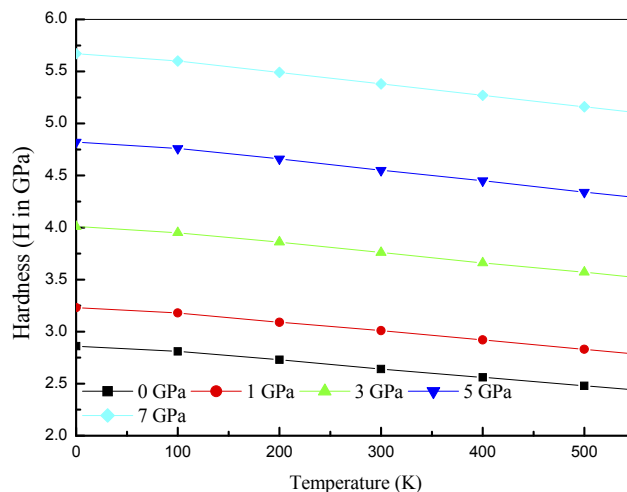
Fig. 11. Hardness vs temperature at various pressures for ZnSnSb$_2$.

SUMMARY AND CONCLUSION

We have successfully simulated the ZnSnSb$_2$ compound based on the DFT method using the full potential linear augmented plane waves (FP-LAPW), as embodied in the WIEN2k code, and applied the TB-mBJ exchange potential on this system to predict its band gap more precisely. Besides, the calculated partial DOSs indicated that majority of the valence electronic bands correspond to the p orbitals of antimony atoms which are consistent with those of the other semiconductors of the same group. The proposed result shows that TB-mBJ has significantly improved the electronic structure of the system. A direct band gap of 0.46 eV, which is very close to the experimentally measured value of 0.40 eV, was obtained. We have compared electronic, optical and elastic properties with the calculated values of theoretical models [13, 28, 29, 36, 50, 51]. The values are in good agreement with the proposed method and theoretical models. Thermal properties such as Grüneisen parameter, volume expansion coefficient, bulk modulus, specific heat, entropy, Debye temperature and hardness are calculated successfully at various temperatures and pressures, and trends are discussed. To the best of our knowledge, most of the investigated parameters are reported for the first time and hoped to stimulate the succeeding studies.

ORCID IDs

Shalini Tomar https://orcid.org/0000-0001-7385-3061, **Shiv Raj Bhardwaj** https://orcid.org/0000-0002-1895-158X,
Saral Kumar Gupta https://orcid.org/0000-0002-0446-8984, **Ajay Singh Verma** https://orcid.org/0000-0001-8223-7658

REFERENCES
[1]   A.S. Verma, Solid State Communications, **149**(29-30), 1236-1239 (2009), https://doi.org/10.1016/j.ssc.2009.04.011.
[2]   G. Murtaza, Sibghat-Ullah, R. Khenata, A.H. Reshak and S.S. Hayat, J. Optoelectronics and Advanced Materials, **16**(1-2),
       110-116 (2014), https://old.joam.inoe.ro/index.php?option=magazine&op=view&idu=3402&catid=82.

[3]   Y. You, B. Zhao, S. Zhu, T. Gao, H. Hou and Z. He, J. Solid State Chem. **185**, 264-270 (2012), https://doi.org/10.1016/j.jssc.2011.10.014.
[4]   A.S. Verma, Phil. Mag. **89**(2), 183-193 (2009), https://doi.org/10.1080/14786430802593814.
[5]   S. Kamran, K. Chen and L. Chen, Phys. Rev. B, **77**(9), 094109 (2008). https://doi.org/10.1103/PhysRevB.77.094109.
[6]   B. Derby, Phys. Rev. B, **76**(5), 054126 (2007). https://doi.org/10.1103/PhysRevB.76.054126.
[7]   S.Q. Wang and H.Q. Ye, J. Phys. Condens. Matter. **17**(28), 4475 (2005). http://dx.doi.org/10.1088/0953-8984/17/28/007.
[8]   X. Jiang and W.R.L. Lambrecht, Phys. Rev. B, **69**(3), 035201 (2004), https://doi.org/10.1103/PhysRevB.69.035201.
[9]   S. Ozakia and S. Adachi, J. App. Phys. **100**(11), 113526 (2006). https://doi.org/10.1063/1.2400804.
[10] A. Kosuga, T. Plirdpring, R. Higashine, M.Matsuzawa, K. Kurosaki and S. Yamanaka, App. Phy. Letts. **100**(4), 042108 (2012), https://doi.org/10.1063/1.3678044.
[11] J. Łazewski, H. Neumann, P.T. Jochym and K. Parlinski, J. App. Phys. **93**(7), 3789-3795 (2003), https://doi.org/10.1063/1.1556179.
[12] S. Limpijumnong, W.R.L. Lambrecht, Phys. Rev. B, **65**(16), 165204 (2002),https://doi.org/10.1103/PhysRevB.65.165204.
[13] A.S. Verma and D. Sharma, Phys. Scr. **76**(1), 22-24 (2007), https://doi.org/10.1088/0031-8949/76/1/004.
[14] W. Scott, J. Appl. Phys. **44**(11), 5165-5166 (1973), https://doi.org/10.1063/1.1662110.
[15] J.L. Shay and J.H. Wernick, *Ternary Chalcopyrite Semi-conductors: Growth Electronic Properties and Applications*, (Pergamon Press, Oxford, 1975), pp. 11,12,73.
[16] A. Tengå, F.J. Garcıa-Garcıa, A.S. Mikhaylushkin, B. Espinosa-Arronte, M. Andersson and U.Haussermann, Chem. Mater. **17**(24), 6080-6085 (2005), https://doi.org/10.1021/cm0516053.
[17] S. Mishra and B. Ganguli, J. Solid State Chemistry, **200**, 279-286 (2013), https://doi.org/10.1016/j.jssc.2013.01.007.
[18] G.K.H. Madsen, P. Blaha, K. Schwarz, E. Sjöstedt and L. Nordström, Phys. Rev. B **64**(19), 195134 (2001), https://doi.org/10.1103/PhysRevB.64.195134.
[19] K. Schwarz, P. Blaha and G.K.H Madsen, Comput. Phys. Commun. **147**(1-2), 71-76 (2002), https://doi.org/10.1016/S0010-4655(02)00206-0.
[20] P. Blaha, K. Schwarz, G.K.H. Madsen, D. Kvasnicka, and J. Luitz, *WIEN2k: An Augmented Plane Wave+Local Orbitals Program for Calculating Crystal Properties*(Karlheinz Schwarz/Techn. Universität, Wien, Austria, 2001).
[21] Z. Wu and R. E. Cohen, Phys. Rev. B **73**(23), 235116 (2006), https://doi.org/10.1103/PhysRevB.73.235116.
[22] F. Tran, R. Laskowski, P. Blaha, and K. Schwarz, Phys. Rev. B, **75**(11), 115131 (2007), https://doi.org/10.1103/PhysRevB.75.115131.
[23] W. Kohn and L.J. Sham, Phys. Rev. **140**, A1133 (1965),https://doi.org/10.1103/PhysRev.140.A1133.
[24] J.P. Perdew, K. Burke, and M. Ernzerhof, Phys. Rev. Lett. **77**(4), 3865 (1996), https://doi.org/10.1103/PhysRevLett.77.3865.
[25] F. Tran and P. Blaha, Phys. Rev. Lett. **102**(22), 226401 (2009), https://doi.org/10.1103/PhysRevLett.102.226401.
[26] P.E. Blochl, O. Jepsen, O.K. Andersen, Phys. Rev. B **49**(23), 16223 (1994), https://doi.org/10.1103/PhysRevB.49.16223.
[27] F.D. Murnaghan, Proc. Natl. Acad. Sci. USA, **30**, 244 (1947), https://dx.doi.org/10.1073%2Fpnas.30.9.244.
[28] A.S. Verma, Mat. Chem. Phys. **139**(1), 256-261 (2013), https://doi.org/10.1016/j.matchemphys.2013.01.032.
[29] A.S. Verma and S.R. Bhardwaj, J. Phys: Condensed Matter, **19**(2), 026213 (2007), https://doi.org/10.1088/0953-8984/19/2/026213.
[30] N.N. Kiselyova, A.V. Stolyarenko, T. Gu, W. Lu and A.A. Baikov, (2007), http://lab11.imet-db.ru/publ/pdf/44CD-Kiselyova.pdf
[31] J. Bhosale, A. K. Ramdas, A. Burger, A. Munoz, A. H. Romero, M. Cardona, R. Lauck and R. K. Kremer, Phys. Rev. B, **86**(19), 195208 (2012), https://doi.org/10.1103/PhysRevB.86.195208.
[32] J. Sun, H. T. Wang, N.B. Ming, J. He and Y. Tian, Appl. Phys. Letts. **84**(22), 4544-4546 (2004), https://doi.org/10.1063/1.1758781.
[33] S. Saha and T.P. Sinha and A. Mookerjee, Phys. Rev. B **62**(13), 8828 (2000), https://doi.org/10.1103/PhysRevB.62.8828.
[34] P.Y.Yu and M. Cardona, *Fundamentals of Semiconductors*, (Springer-Verlag, Berlin, 1996).
[35] M.Q. Cai, Z. Yin and M.S. Zhang, Appl. Phys. Letts, **83**(14), 2805-2807 (2003), https://doi.org/10.1063/1.1616631.
[36] A.S. Verma, Phys. Status Solidi B, **246**(1), 192-199 (2008), https://doi.org/10.1002/pssb.200844242.
[37] J.F. Nye, *Physical Properties of Crystals, Their Representation by Tensors andMatrices*, (Oxford Univ.Press, Oxford, USA, 1985).
[38] W. Voigt, *Lehrbuch der Kristallphysik*, (Teubner, Leipzig, 1928).
[39] I.R. Shein, A.L. Ivanovskii, Scripta Materiali, **59**(10), 1099-1102 (2008), https://doi.org/10.1016/j.scriptamat.2008.07.028.
[40] A. Reuss, Z. Angew, ZAMM, **9**, 49-58 (1929), https://doi.org/10.1002/zamm.19290090104.
[41] R. Hill, Proc. Phys. Soc. Lond. A, **65**, 349 (1952), https://doi.org/10.1088/0370-1298/65/5/307.
[42] S.F. Pugh, Philos. Mag. **45**, 823 (1953), https://doi.org/10.1080/14786440808520496.
[43] K. Chen and L. Zhao, J. Appl. Phys. **93**(5), 2414-2417 (2003), https://doi.org/10.1063/1.1540742.
[44] K. Chen, L. Zhao, J.S. Tse andJ.R. Rodgers, Phys. Lett. A, **331**(6), 400-403 (2004), https://doi.org/10.1016/j.physleta.2004.09.034.
[45] M.A. Blanco, E. Francisco and V. Luaña, Comput. Phys. Commun. **158**(1), 57-72 (2004), https://doi.org/10.1016/j.comphy.2003.12.001.
[46] M.A. Blanco, A. Martín Pendás, E. Francisco, J.M. Recio and R. Franco, J. Mol. Struct. Theochem. **368**, 245-255 (1996), https://doi.org/10.1016/S0166-1280(96)90571-0.
[47] M. Flórez, J.M. Recio, E. Francisco, M.A. Blanco and A. Martín Pendás, Phys. Rev. B, **66**(14), 144112 (2002), https://doi.org/10.1103/PhysRevB.66.144112.
[48] E. Francisco, M.A. Blanco and G. Sanjurjo, Phys. Rev. B,**63**(9), 094107 (2001), https://doi.org/10.1103/PhysRevB.63.094107.
[49] J.P. Poirier, *Introduction to the Physics of Earth's Interior*, (Cambridge University Press, Oxford, 2000), pp. 39.
[50] A.S. Verma and S.R. Bhardwaj, J. Phys: Condensed Matter. **19**(2), 026213 (2007), https://doi.org/10.1088/0953-8984/19/2/026213.
[51] A.S. Verma, S. Sharma, R. Bhandari, B.K. Sarkar and V.K. Jindal, Mat. Chem. and Phys. **132**(2-3), 416-420 (2012), https://doi.org/10.1016/j.matchemphys.2011.11.047.

ТЕОРЕТИЧНЕ ДОСЛІДЖЕННЯ ФУНДАМЕНТАЛЬНИХ ФІЗИЧНИХ ТА ОПТОЕЛЕКТРОННИХ ВЛАСТИВОСТЕЙ НАПІВПРОВІДНИКОВОГО ХАЛКОПІРИТУ ZnSnSb2

Ш. Томар[a], Ш.Р. Бхардвай[b], С.К. Гупта[a], А.С. Верма[a]
[a]Фізичний факультет, Банастхалі Від'япіт, Раджастан, (Індія) 304022
[b]Фізичний факультет, BSA Коледж Матура, (Індія) 281004

В статті досліджено невід'ємні фундаментальні фізичні властивості, такі як структурні, електронні, оптичні, пружні, теплові тощо для ZnSnSb2, використовуючи точний повний потенціал лінеаризованої розширеної плоскої хвилі (FP-LAPW). Ці матеріали мають більш високі енергетичні щілини та нижчі температури плавлення порівняно з їх бінарними аналогами, через що вони вважаються важливими в дослідженнях росту кристалів та в застосуванні для пристроїв. Для структурних властивостей мінімізація проводиться в два етапи, перший параметр u мінімізується шляхом обчислення внутрішніх сил, що діють на атоми всередині одиничної чарунки, поки сили не стануть незначними, для цього використовується завдання MINI, що входить до коду WIEN2K. По-друге, загальна енергія кристала обчислюється для сітки об'єму одиничної чарунки (V) та співвідношення c/a. Для кожного об'єму використовуються п'ять значень c/a, і застосовується поліноміальна підгонка до обчислених енергій, щоб отримання найкращого співвідношення c/a. Ми представили електронні та оптичні властивості з нещодавно розробленим функціоналом щільності Tran і Blaha. Крім того, оптичні характеристики, такі як діелектричні функції, показники заломлення, коефіцієнт згасання, оптична відбивна здатність, коефіцієнти поглинання, оптична провідність, розрахували для енергій фотона до 40 еВ. Для цих властивостей ми використовували WC і TB-mBJ обмінний кореляційний потенціал і отримали величину забороненої зони у діапазоні 0,46 еВ для цього матеріалу, і отримана заборонена зони діапазону добре відповідає експериментальним даним. Потенціал TB-mBJ дає хорошу згоду з експериментальними значеннями, подібними до тих, що отримуються більш досконалими методами, але за значно менших обчислювальних витрат. Основні піки реальної частини електронної діелектричної функції $\varepsilon_1(\omega)$, яка в основному генерується електронним переходом від вершини валентної зони до нижньої зони провідності, наступає при 1,59 еВ, а спектри $\varepsilon_1(\omega)$ далі зменшуються до 4,99 еВ. Уявна частина електронної діелектричної постійної $\varepsilon_2(\omega)$ є основним фактором оптичних властивостей матеріалу. Пропоноване дослідження показує, що критична точка $\varepsilon_2(\omega)$ виникає при 0,42 еВ, що тісно пов'язане з отриманим значенням щілини в діапазоні 0,46 еВ. Максимальна відбивна здатність виникає в області 3,74-11,33 еВ. Цей матеріал має не зникаючу провідність у зоні видимого світла (1,65 еВ – 3,1 еВ), основний пік настає при 3,80 еВ, який потрапляє у УФ область. Визначено також пружні константи при рівновазі в структурі BCT. Тензор пружної жорсткості сполук халкопіриту має шість незалежних компонентів через властивості симетрії просторової групи, а саме: C_{11}, C_{12}, C_{13}, C_{33}, C_{44} та C_{66} у нотації Юнга. Теплові властивості, такі як теплове розширення, теплоємність, температура Дебая, ентропія, параметр Грюнайзена та об'ємний модуль, були обчислені за допомогою квазігармонічної моделі Дебая при різних температурах і тиску. Для визначення термодинамічних властивостей за допомогою квазігармонічної моделі Дебая було взято температурний діапазон 0 K-500 K. Ефекти тиску досліджено в діапазоні 0 – 7 ГПа. Подібні тенденції спостерігаються і в розглянутому діапазоні температур, але вище 600 K тренди порушуються, що може бути пов'язано з плавленням матеріалу. Виходячи з напівемпіричного відношення, ми визначили твердість матеріалів, що пов'язано з різною силою ковалентного зв'язку. Про більшість досліджуваних параметрів повідомляється вперше.

КЛЮЧОВІ СЛОВА: обчислення Ab-initio; електронні властивості; оптичні властивості; пружні константи; теплові властивості

ТЕОРЕТИЧЕСКИЕ ИССЛЕДОВАНИЯ ФУНДАМЕНТАЛЬНЫХ ФИЗИЧЕСКИХ И ОПТОЭЛЕКТРОННЫХ СВОЙСТВ ПОЛУПРОВОДНИКОВОГО ХАЛКОПИРИТА ZnSnSb2

Ш. Томар[a], Ш.Р. Бхардвай[b], С.К. Гупта[a], А.С. Верма[a]
[a]Физический факультет, Банастхали Видьяпит, Раджастан, Индия, 304022
[b]Физический факультет, BSA Колледж Матур, Индия, 281004

В статье исследованы неотъемлемые фундаментальные физические свойства, такие как структурные, электронные, оптические, упругие, тепловые и т.д. для ZnSnSb2, используя точный полный потенциал линеаризованной расширенной плоской волны (FP-LAPW). Эти материалы имеют более высокие энергетические щели и низкие температуры плавления по сравнению с их бинарными аналогами, поэтому они считаются важными в исследованиях роста кристаллов и в применении для устройств. Для структурных свойств минимизация проводилась в два этапа, первый параметр «u» минимизируется путем вычисления внутренних сил, действующих на атомы внутри единичной ячейки, пока силы не станут незначительными, для этого используется задача MINI, которая входит в код WIEN2K. Во-вторых, общая энергия кристалла исчисляется для сетки объема единичной ячейки (V) и соотношения «c/a». Для каждого объема используются пять значений «c/a», и применяется полиномиальная подгонка вычисленных энергий, для получения наилучшего соотношения «c/a». Мы представили электронные и оптические свойства недавно разработанным функционалом плотности Tran и Blaha. Кроме того, оптические характеристики, такие как диэлектрические функции, показатели преломления, коэффициент затухания, оптическая отражательная способность, коэффициенты поглощения, оптическая проводимость, рассчитаны для энергий фотонов до 40 эВ. Для этих свойств мы использовали WC и TB-mBJ обменный корреляционный потенциал и получили величину запрещенной зоны в диапазоне 0,46 эВ для этого материала, и полученная ширина запрещенной зоны хорошо соответствует экспериментальным данным. Потенциал TB-mBJ дает хорошее согласие с экспериментальными значениями, подобные тем, что получаются более совершенными методами, но при значительно меньших вычислительных затратах. Основные пики реальной части электронной диэлектрической функции $\varepsilon_1(\omega)$, которая в основном генерируется электронным переходом от вершины валентной зоны до нижней зоны проводимости, наступает при 1,59 эВ, а спектры $\varepsilon_1(\omega)$ дальше уменьшаются до 4,99 эВ. Мнимая часть электронной диэлектрической постоянной $\varepsilon_2(\omega)$ является основным фактором оптических свойств материала. Предлагаемое исследование показывает, что критическая точка $\varepsilon_2(\omega)$ возникает при 0,42 эВ, что тесно связано с полученным значением щели в диапазоне 0,46 эВ. Максимальная отражательная способность возникает в области 3,74 - 11,33 эВ. Этот материал имеет не исчезающую проводимость в зоне видимого света (1,65 эВ – 3,1 эВ), основной пик наступает при 3,80 эВ, который попадает в УФ область. Определены упругие константы при равновесии в структуре BCT. Тензор упругой жесткости соединений халкопирита имеет шесть независимых компонентов через свойства симметрии

пространственной группы, а именно: C_{11}, C_{12}, C_{13}, C_{33}, C_{44} и C_{66} в нотации Юнга. Тепловые свойства, такие как тепловое расширение, теплоемкость, температура Дебая, энтропия, параметр Грюнайзена и объемный модуль, были вычислены с помощью квазигармонических модели Дебая при различных температурах и давлениях. Для определения термодинамических свойств с помощью квазигармонических модели Дебая было взято температурный диапазон 0 K-500 K. Эффекты давления исследованы в диапазоне 0-7 ГПа. Подобные тенденции наблюдаются и в рассматриваемом диапазоне температур, но выше 600 K тренды нарушаются, что может быть связано с плавлением материала. Исходя из полуэмпирического отношения, мы определили твердость материала, что связано с разной силой ковалентной связи. О большинстве исследуемых параметров сообщается впервые.

КЛЮЧЕВЫЕ СЛОВА: расчеты Ab-initio; электронные свойства; оптические свойства; упругие постоянные; тепловые свойства

MACROPARTICLE REFLECTION FROM A BIASED SUBSTRTATE IN PLASMA ION IMPLANTATION SYSTEMS

Elena V. Romashchenko*, Aleksander A. Bizyukov, Igor O. Girka

V. N. Karazin Kharkiv National University
Svobody sq., 4, 61022, Kharkiv, Ukraine
Corresponding Author: ev.romashchenko@gmail.com
Received December 18, 2019; accepted January 20, 2020

Generation of metal plasma in vacuum arc discharge is always accompanied by a production of macroparticles (MPs). The MP contamination in coatings is the most important technological problem in plasma immersion ion implantation (PIII). For the case of PIII with long pulse duration, the results of theoretical study of MP charging and dynamics in the plasma sheath are presented. To describe the MP charging in the sheath the sheath model is combined with orbital motion limited (OML) theory. The MP charging in the sheath is studied with taking into account emission processes from MP surface as well as kinetic electron emission (KEE) from the high voltage substrate. The charge and dynamics of MP are governed by local parameters of counter fluxes of ions and secondary electrons from the substrate. The MP charge depends on the MP local position within the sheath. The dominant role in MP charging is shown to be played by KEE from the substrate, which is an important feature of PIII. KEE from the substrate changes the potential profile within the sheath, the sheath thickness, and current balance on MP surface. MP charge is obtained to be negative because it is caused by higher current density of secondary electrons from the substrate than that of ions. The latter is possible for KEE yield larger than a unit. The substrate biasing influences both the release of secondary electrons from the substrate under ion impact and their acceleration in the sheath. The increasing of negative substrate bias is demonstrated to result in the increasing of absolute value of negative MP charge, and, thereby, the increasing of electrostatic reflection of MP from the substrate. The negative substrate biasing is shown to be the effective alternative method to reduce MP contaminations in coatings without applying any magnetic filters.
KEY WORDS: plasma immersion ion implantation, macroparticle, kinetic electron emission

Vacuum arc is known to provide a means for producing metal plasma for thin film deposition and ion implantation [1, 2]. The favorable characteristic features of the vacuum arc metal plasma are the high ion flux, high ionization degree, and multiple ion charge [3-5]. Ion bombardment of a substrate surface changes its physical, electrical, and chemical properties. Substrate biasing is an established technique to control the ion bombardment energy. The amplitude of the bias is a key parameter, which results in a qualitatively different kind of surface modification. Low-energy ion bombardment with energies from several tens of electronvolts to several hundreds of electronvolts is used for thin film deposition. Plasma immersion ion implantation (PIII) is an effective surface modification technique. The typical bias in PIII belongs to the range from 1 to 100 kV, with the lower values for semiconductor applications and higher values for metallurgical applications [2]. Besides, the bias is usually pulsed to allow the plasma to replace depleted ions between the pulses.

The macroparticles (MPs) contamination in many PIII applications, particularly semiconductor applications, is the most important technological problem [6]. The MP size occurs in the range from fraction to tens microns. The incorporation of MPs into the coating degrades the quality of the films, e.g. produces surface roughening, protuberances, bumps and pinholes. The experimental observations reveal that the number of MPs can be reduced by substrate biasing [7]. We have recently considered the effect of negative substrate biasing on MP contamination in vacuum arc deposition (VAD) [8]. The energy of multiply charged ions at the substrate is increased by applying a negative bias. The multiply charged ions may cause a release of secondary electrons from the substrate surface. Secondary electron emission (SEE) occurs through two general processes, known as kinetic electron emission (KEE) and potential electron emission (PEE). Because of the relatively low kinetic energy of the ions (below 1 keV), only PEE is of importance in the VAD. In contrary to VAD, KEE is an important feature of PIII [9].

The aim of this work to study the effect of substrate biasing on MP contamination in ion implantation system with taking KEE into account.

SHEATH MODEL FOR ION IMPLANTATION

In PIII, the substrate is immersed into a vacuum arc produced plasma, and series of negative high-voltage pulses are applied to the substrate. Applying a high voltage negative bias to the substrate accelerates and implants the ions. A collisionless dynamic sheath model for implantation of singly charged ions has been introduced by Lieberman [10]. Later, this model has been extended to take the multiple charge state into account [11]. According to Lieberman model [10], when a high voltage pulse of amplitude $-V_0$ is applied, the electrons are driven away from the substrate region on a time scale of inverse electron plasma frequency ω_{pe}^{-1}. This time is very short, of about few nanoseconds. This leads, in turn, to production of a region of positive space charge known as the ion matrix sheath. Then, on the slower time scale of the order of inverse ion plasma frequency ω_{pi}^{-1}, the ions are accelerated toward the substrate by the electric field

inside the sheath and the ion current density reaches a maximum. Subsequently, the sheath edge expands outwards uncovering more ions until the end of the voltage pulse. The ion matrix sheath evolves into a quasi-static Child law sheath with time-varying current density [10]

$$J_C = \frac{4}{9}\varepsilon_0 \left(\frac{2Ze}{m_i}\right)^{1/2} \frac{V_0^{3/2}}{s(t)^2},$$ (1)

where s is the sheath thickness, m_i is the ion mass, ε_0 is the permittivity constant, e is the elementary charge, Z is the ion charge state.

The sheath expansion velocity $s(t)$ is given by

$$s(t) = s_0\left(1 + \frac{2}{3}\omega_{pi}t\right)^{1/3},$$ (2)

where

$$\omega_{pi} = \left(\frac{Z^2 e^2 n_0}{\varepsilon_0 m_i}\right)^{1/2}$$ (3)

is the ion plasma frequency, and

$$s_0 = \left(\frac{2\varepsilon_0 V_0}{Zen_0}\right)^{1/2}$$ (4)

is the matrix sheath thickness.

In metal plasma produced by a vacuum arc, an equilibrium steady-state ion sheath can be formed [13,14].

The steady-state Child law thickness, which is the maximum sheath thickness that can be reached, is [12]

$$s_{\max} = s_0\left(\frac{2u_0}{9u_B}\right)^{1/2},$$ (6)

where the characteristic ion velocity u_0 is

$$u_0 = \left(\frac{2ZeV_0}{m_i}\right)^{1/2},$$ (5)

the Bohm velocity u_B is

$$u_B = \left(\frac{Zk_BT_e}{m_i}\right)^{1/2},$$ (6)

k_B is the Boltzman constant, T_e is the electron temperature.

The stationary Child law sheath is established for the time [6]

$$t_C = \left(\frac{3}{2}\left(\frac{s_{\max}}{s_0}\right)^3 - \frac{3}{2}\right)\omega_{pi}^{-1},$$ (7)

and approximate expression for this time is

$$t_C \approx \frac{\sqrt{2}}{9}\omega_{pi}^{-1}\left(\frac{2ZeV_0}{k_BT_e}\right)^{3/4}.$$ (8)

For example, for the magnitude -2 kV of the substrate bias, the sheath reaches its quasi-stationary position in metal plasma during about few μs. Therefore, in the case of application of low implantation voltage and long pulse duration (in limiting case: DC), the steady-state sheath model can be considered.

The ions accelerated by electric field of the sheath deliver significant kinetic and potential energy to the substrate. The high kinetic energies make it possible for them to penetrate deeply into the surface, to change the atomic composition and structure in near-surface region of the target material, and, thereby, to change the properties of the surface material [12]. When ions impact the substrate with high energies, they cause the PEE and KEE from the substrate. The implantation current density is the sum of the ion current density j_i and secondary electron current density j_{se}

$$j = j_i + j_{se} = \left(1 + \frac{\gamma}{Z}\right)j_i.$$ (9)

Recognizing that there are two contributing process we can write the total SEE yield γ as

$$\gamma = \gamma_p + \gamma_k,$$ (10)

where γ_p is the potential SEE yield, and γ_k is the potential SEE yield.

At high sheath voltages (>1kV), the electron emission mechanism is mainly determined by the kinetic energy of the arriving ions, and KEE becomes dominant. Therefore, the contribution to the total SEE yield by KEE is much larger than that by PEE, $\gamma \approx \gamma_k$. The KEE yield γ_k is proportional to the square root of the kinetic ion energy, which is, in turn, determined by the applied voltage V_0, $\gamma \sim (V_0)^{1/2}$.

In the coordinate system applied in the present paper, a plasma-sheath interface is taken to be the origin, $x=0$, and the position of the substrate is determined by the sheath thickness. The flux of secondary electrons is accelerated away from the substrate in the sheath electric field that accelerates the ion flux towards the substrate. To obtain the potential distribution $\Phi(x)$ within the sheath one has to consider both particle fluxes in Poisson's equation - to and from the substrate:

$$\frac{d^2\Phi}{dx^2} = -\frac{e}{\varepsilon_0}\left[Zn_i - n_{se}\right],$$ (11)

where n_i and n_e are the ion and electron density, respectively.

The expressions for the densities of ions and secondary electrons can be obtained from the equations of continuity and energy conservation

$$n_i = \frac{j_i}{e}\sqrt{\frac{m_i}{2(\varepsilon_{io} - Ze\Phi)}},$$ (12)

and

$$n_{se} = \frac{j_{se}}{e}\sqrt{\frac{m_e}{2e(\Phi - V_0)}},$$ (13)

where m_e is the electron mass, ε_{io} is the initial energy of ions.

The quasi-neutrality condition at the sheath edge is

$$n_0 = Zn_i(0) + n_{se}(0),$$ (14)

where n_0 is the bulk plasma density.

The Bohm criterion is oversatisfied at the sheath edge because of supersonic velocity of implanted metal ions. The boundary conditions for integration of Poisson's equation (11) are: $\Phi(0)=0$; $d\Phi/dx=0$. The potential variation in the sheath can be found numerically by integrating the Eq. (11). The MPs are assumed to have no effect on the sheath structure.

MP CHARGING

We consider the MP with the radius a as a spherical probe immersed into the counter fluxes of ions and secondary electrons from the substrate. In addition, secondary electrons from MP surface can be produced by electron and by ion impacts.

The MP charge Q is one of the most important characteristics for the MP dynamics. The MP charge Q is determined by the MP potential V_d with respect to the local sheath potential:

$$Q(x) = CV_d(x),$$ (15)

where C is the capacitance of the MP. If the MP radius is much smaller than the Debye length $\lambda_D = (\varepsilon_0 T_e /n_0 e^2)^{1/2}$ then the capacitance is

$$C = 4\pi\varepsilon_0\left(1 + a/\lambda_D\right) \approx 4\pi\varepsilon_0 a.$$ (16)

The MP charging time depends on competition of different currents onto and from the MP surface. The steady-state potential to which a MP is charged is determined from the balance of particle currents to the grain:

$$I_i(V_d) + I_{se}(V_d) + I_{i-e}(V_d) + I_{e-e}(V_d) = 0,$$ (17)

where I_i is the ion current, I_{se} is the current of fast secondary electrons emitted from the substrate, I_{i-e} is the secondary electron current from the MP surface caused by the impact of ions, I_{e-e} is the current of secondary electrons emitted from the MP surface due to fast electron bombardment.

We calculate the currents I_i and I_e to the MP surface by using the orbital motion limited (OML) approach [15]. For $V_d < 0$,

$$I_i = \pi a^2 j_i\left(1 - \frac{2ZeV_d}{m_i u_i^2}\right),$$ (18)

$$I_{se} = \pi a^2 j_{se}\left(1 + \frac{2eV_d}{m_e u_e^2}\right),$$ (19)

$$I_{i-e} = \left(\gamma/Z\right)I_i,$$ (20)

$$I_{e-e} = \delta I_e,$$ (21)

where u_i is the ion velocity, u_e is the velocity of secondary electrons; $I_i = 0$, if $2ZeV_d /m_iu_i^2 > 1$; and $I_e = 0$, if $2eV_d/m_eu_e^2 < 1$.

The secondary electron yield δ is described by Sternglass's universal curve [16]

$$\delta = 7.4 \cdot \delta_m \cdot \frac{\varepsilon_e}{\varepsilon_{em}} Exp\left(-2\sqrt{\frac{\varepsilon_e}{\varepsilon_{em}}}\right), \tag{22}$$

where ε_e is the primary electron energy, and ε_{em} is the energy for which the secondary yield δ_m is maximum.

In the case of PIII, the value of the SEE yield δ is comparable with value of the SEE yield γ.

RESULTS AND DISCUSSION

The model described above is applied to the case of titanium cathodic arc plasma used for PIII. The specific plasma parameters are taken as typical values from experiments: the electron temperature is $T_e = 1$ eV, the plasma bulk density is $n=10^{16}$ m^{-3}, mean initial kinetic energy of ions is $\varepsilon_i = 54$ eV, mean ion charge is $Z=2$.

Using substrate bias of about -1kV, the energy of titanium ions with $Z=2$ at the substrate surface is of at least 2 keV. The resulting ion energy for substrate bias $V_0 = -2$ kV is of at least 4 keV. For these values of substrate bias KEE is dominant.
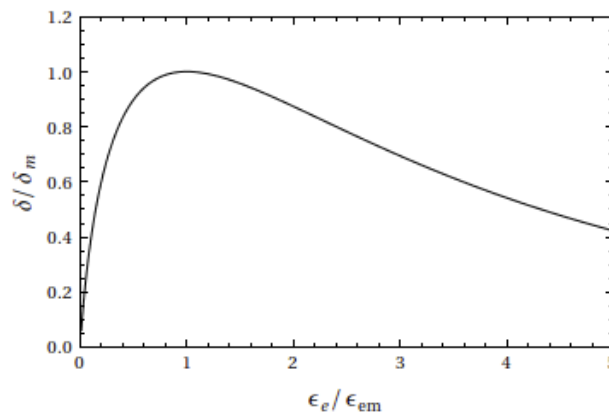
Fig.1. The secondary electron emission yield δ
The secondary electron emission yield δ for electron impact on a solid as a function of primary electron energy

To begin with, one needs to know the SEE coefficients. The expression (22) makes it possible to find the SEE yield δ as a function of the energy of incident electrons ε_e (Fig. 1). Titanium has $\delta_m = 0.83$ and $\varepsilon_{em} = 300$ eV. The SEE yield δ depends strongly on the electron energy, which reaches a maximum value at the sheath edge and a minimum value at the substrate. The substrate voltage bias provides the upper limit to the coefficient δ. The measured total SEE yield γ is presented in Ref. [9]. For an accelerating substrate bias $V_0 = -6$ kV, SEE yield γ is about 2.7. Therefore, knowing that $\gamma \sim (V_0)^{1/2}$, the corresponding SEE yields γ for substrate bias $V_0 = -1$ kV, and -2 kV, are equal 1.1, and 1.6, respectively.

Equation (11) is numerically integrated to give the dependence of the potential distribution $\Phi(x)$ within the sheath on the normalized coordinate $z = x/\lambda_D$. Numerical solutions of (11) with (18)-(21) allow to determine the MP charge as a function of the MP position z for given sheath potential profile $\Phi(x)$. The profile of MP charge for different values of substrate bias is shown in Fig. 2.

The negative MP charge is caused by higher current density of secondary electrons from the substrate than that of ions. An increase in substrate bias leads to larger absolute values of negative MP charge. The negatively charged MP is decelerated by electric field of the sheath. That is why for large repulsive field, MP cannot reach the substrate.
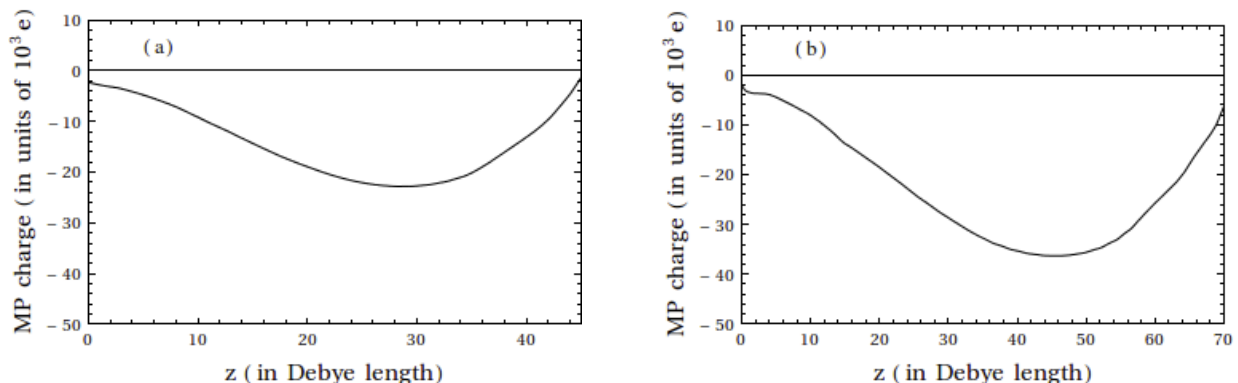
Fig. 2. The profile of MP charge in the sheath
The dependence of the charge of the MP of radius 0.25 μm, on the MP position z for different substrate biases: (a)−1kV, (b) −2kV

CONCLUSION

SEE is relevant for charging of MP in the near-substrate plasma. The substrate biasing directly influences the release of secondary electrons from the substrate because the KEE is dependent on the kinetic energy of the incident ions. In implantation sheath, KEE from the substrate contributes to the MP charging more significantly as compared with emission from MP surface due to high voltage bias of the substrate. The obtained results are in good agreement with the experimental data. PIII is demonstrated to be controllable technique for modification of surface without MPs.

ORCID IDS

Elena V. Romashchenko https://orcid.org/0000-0001-7815-8172,
Aleksander A. Bizyukov https://orcid.org/0000-0003-0192-5219
Igor O. Girka https://orcid.org/0000-0001-6662-8683

REFERENCES

[1] R.L. Boxman, P.I. Martin and D.M. Sanders, editors, *Handbook of vacuum arcs science and technology: fundamentals and applications* (Noyes Publications, New Jersey, 1995), pp. 737.

[2] A. Anders, editor, *Handbook of plasma immersion ion implantation and deposition* (John Wiley & Sons, New York, 2000), pp. 736.

[3] I.I. Beilis, IEEE Trans. Plasma Sci. **29**(5), 657-670 (2001), https://doi.org/10.1109/27.964451.

[4] G.Yu. Yushkov, A.Anders, E.M. Oks and I.G. Brown, J. Appl. Phys. **88**(10), 5618-5622 (2000), https://doi.org/10.1063/1.1321789.

[5] E.M. Oks, IEEE Trans. Plasma Sci. **30**(1), P. 202-207 (2002), https://doi.org/10.1109/TPS.2002.1003861.

[6] R.L. Boxman and S. Goldsmith, Surf. Coat. Technol. **52**, 39-50 (1992), https://doi.org/10.1016/0257-8972(92)90369-L.

[**7**] C.N. Tai, E.S. Koh and K. Akari, Surf. Coat. Technol. **43/44**, 324-335 (1990), https://doi.org/10.1016/0257-8972(90)90085-Q.

[8] A.A. Bizyukov, I.O. Girka and E.V. Romashchenko, IEEE Trans. Plasma Sci. **44**(7), 1050-1056 (2016), https://doi.org/10.1109/TPS.2016.2573284.

[9] A. Anders, *Cathodic arcs: from fractal spots to energetic condensation*, (Springer, New York, 2008), pp. 540.

[10] M.A. Lieberman, J. Appl. Phys. **66**(7), 2926-2929 (1989), https://doi.org/10.1063/1.344172.

[11] S. Qin, C. Chan and Z. Jin, J. Appl. Phys. **79**(7), 3432-3437 (1996), https://doi.org/10.1063/1.360640.

[12] M.A. Lieberman and A.J. Lichtenberg, *Principles of plasma discharge and material processing*, (John Wiley&Sons, New York, 2000), pp. 299.

[13] A. Anders, Surf. Coat. Technol. **136**(1-3), 85-92 (2001), https://doi.org/10.1016/S0257-8972(00)01017-3.

[14] I.G. Brown, O.R. Monteiro and M.M.M. Bilek, Appl. Phys. Lett. **74**(17), 2426-2428 (1999), https://doi.org/10.1063/1.123869.

[15] I. Langmuir, in: *Collected Works of Irving Langmuir*, edited by G. Suits (Pergamon, New York, 1961).

[16] E.J. Sternglass, *The theory of secondary electron emission*, (Westinghouse Res. Lab. Sci. Pap,Pittsburgh, 1954).

**ВІДБИТТЯ МАКРОЧАСТИНКИ ВІД ЗАРЯДЖЕНОЇ ПІДКЛАДКИ
У ПЛАЗМОВИХ СИСТЕМАХ ІОННОЇ ІМПЛАНТАЦІЇ**
О.В. Ромащенко, О.А. Бізюков, І.О. Гірка
Харківський національний університет імені В. Н. Каразіна
м. Свободи, 4, 61022, Харків, Україна

Генерація металевої плазми у вакуумно-дуговому розряді завжди супроводжується виробництвом макрочастинок (МЧ). Забруднення поверхонь МЧ є найбільш важливою технологічною проблемою при плазмовій імерсійній імплантації іонів (ПІІІ). Результати теоретичного дослідження заряджання та динаміки МЧ у плазмовому шарі представлено для випадку ПІІІ з імпульсами довгої тривалості. Для опису заряджання МЧ у шарі теоретичну модель шару поєднано з теорією обмеженого орбітального руху (ООР). Заряджання МЧ у шарі досліджено з урахуванням як емісійних процесів з поверхні МЧ, так і кінетичної електронної емісії (КЕЕ) з підкладки з високим потенціалом зсуву. Заряд і динаміка МЧ визначаються локальними параметрами протилежних потоків іонів та вторинних електронів з підкладки. Заряд МЧ залежить від положення МЧ усередині шару. Показано, що домінуючу роль у заряджанні МЧ відіграє КЕЕ з підкладки, яка є важливою властивістю ПІІІ. КЕЕ з підкладки змінює профіль потенціалу усередині шару, товщину шару та баланс струмів на поверхню МЧ. Отримано, що МЧ заряджається негативно внаслідок того, що густина струму вторинних електронів з підкладки є більшою за густину струму іонів. Це можливо, коли коефіцієнт КЕЕ більший за одиницю. Застосування негативного потенціалу зсуву до підкладки впливає на виривання вторинних електронів з підкладки іонами та на їх прискорення у шарі. Отримано, що збільшення негативного зсуву потенціалу підкладки призводить до збільшення абсолютної величини негативного заряду МЧ, та таким чином, до збільшення електростатичного відбиття МЧ від підкладки. Показано, що застосування негативного потенціалу зсуву до підкладки є ефективним альтернативним засобом зменшення забруднень МЧ покриттів без застосування магнітних фільтрів.

КЛЮЧОВІ СЛОВА: плазмова імерсійна імплантація іонів, макрочастинка, кінетична електронна емісія

**ОТРАЖЕНИЕ МАКРОЧАСТИЦЫ ОТ ЗАРЯЖЕННОЙ ПОДЛОЖКИ
В ПЛАЗМЕННЫХ СИСТЕМАХ ИОННОЙ ИМПЛАНТАЦИИ**
Е.В. Ромащенко, А.А. Бизюков, И.А. Гирка
Харьковский национальный университет имени В. Н. Каразина
пл. Свободы, 4, 61022, Харьков, Украина

Генерация металлической плазмы в вакуумно-дуговом разряде всегда сопровождается производством макрочастиц (МЧ). Загрязнение покрытий МЧ является наиболее важной технологической проблемой при плазменной иммерсионной имплантации ионов (ПИИИ). Результаты теоретического исследования зарядки и динамики МЧ в плазменном слое

представлены для случая ПИИ с импульсами большой длительности. Для исследования зарядки МЧ в слое теоретическая модель слоя скомбинирована с теорией ограниченного орбитального движения (ООД). Зарядка МЧ в слое изучена с учетом как эмиссионных процессов с поверхности МЧ, так и с учетом кинетической электронной эмиссии (КЭЭ) с подложки с высоким потенциалом смещения. Заряд и динамика МЧ определяются локальными параметрами встречных потоков ионов и вторичных электронов с подложки. Заряд МЧ зависит от положения МЧ в слое. Показано, что доминирующую роль в зарядке МЧ играет КЭЭ, которая является важной особенностью ПИИИ. КЭЭ с положки изменяет профиль потенциала внутри слоя, толщину слоя и баланс токов на поверхность МЧ. Получено, что МЧ заряжается отрицательно вследствие того, что плотность тока вторичных электронов с подложки больше, чем плотность тока ионов. Это возможно, когда коэффициент КЕЕ больше единицы. Приложение отрицательного потенциала смещения к подложке влияет на вырывание вторичных электронов из подложки ионами и на их ускорение в слое. Получено, что увеличение отрицательного потенциала смещения подложки приводит к увеличению абсолютной величины отрицательного заряда МЧ, и тем самым, к увеличению электростатического отражения МЧ от подложки. Показано, что применение отрицательного потенциала смещения к подложке является эффективным альтернативным методом уменьшения загрязнения покрытий МЧ без применения магнитных фильтров.

КЛЮЧЕВЫЕ СЛОВА: плазменная иммерсионная имплантация ионов, макрочастица, кинетическая электронная эмиссия

FIRST PRINCIPLES CALCULATIONS OF CARBON-NANOTUBE AND BORON-NANOTUBE BASED SINGLE ELECTRON TRANSISTORS

Sraja Chauhan, Ajay Singh Verma*

Department of Physics, Banasthali Vidyapith, Rajasthan, 304022, India
*Corresponding author: ajay_phy@rediffmail.com
Received November 26, 2019; revised February 11, 2020; accepted February 13, 2020

Low power consumption, small device size and better controlled onto the charge carriers are the factors, that made Single-electron transistor (SET) a suitable candidate for molecular electronics; yet there are some improvements that can be done in order to use it practically. The single electron transistor (SET) operates through the tunnelling of electron via two tunnel junctions. Choosing a suitable island material plays a key role in the tunnelling of electron through the tunnel junctions. In the present work, the First principle calculations of carbon-nanotube and boron-nanotube based Single-Electron Transistors have been performed. The three types of configurations of nanotubes i.e. zigzag (5,0), armchair (3,3) and chiral (4,2), of the smallest possible diameter (approximately 4A°), have been used. The calculations have been carried out using Atomistic toolkit (ATK-VNL) simulation package which is a density functional theory (DFT) based package. In the present work, local density approximations (LDA) as well as generalized gradient approximation(GGA) have been used to demonstrate the properties of nanotubes-based SET. These approaches have been implemented for a nanotube that is lying just above the gate dielectric. On the either side of the dielectric the electrodes are present, source in the left and drain in the right. The metallic electrodes made of gold (W=5.28eV) and the dielectric material of the dielectric constant $10\epsilon o$ have been used. The charging energies and additional energies of both types of nanotubes-based SET in the isolated as well as in the electrostatic environment have been calculated using the approximations. The calculated values of the charging energies in the electrostatic environment have been found to be less than the charging energies in isolated configuration that shows the renormalization of molecular energy levels. Variations of total energies against gate voltages and Charge stability diagrams (CSD) have been discussed.
KEYWORDS: Carbon Nanotube, Boron Nanotube, Single-Electron Transistor (SET), Electron Affinity, Ionization Energy, Addition Energy, Charge stability diagram (CSD)

Recent developments in the semiconductor electronics industry depict that Moore's law has become realistic as the size of storage devices decreasing day by day since past decades. Now, one can have billions of information in a small pocket, which has become possible only due to the advancement in molecular electronics. After reaching to the ultimate limit of microelectronics, for a device size of 10 nm or less, single-electron effects came into the existence [1-3]. Single-electron transistors are based on the very simple Coulomb blockade principle and can control the flow of even a single electron i.e. the elementary charge.

A Single-electron transistor (SETs) is a technique by which the flow of single electron can be controlled and hence it requires very less amount of power consumption [4-11]. This device, in general, consists of three metallic electrodes i.e. source, drain and gate. In between the two electrodes, source and drain, an island (metal/semiconductor) is placed just above to the gate electrode and isolated from the gate by a thin dielectric slab. In SETs, a free electron is trapped onto the nano-meter sized island and can tunnel through it by quantum mechanical tunnelling which is known as Coulomb blockade [12-16]. Island is capacitively coupled to the electrodes by two small junctions and electron will be trapped onto the island until the energy supplied by the voltage source is greater than the coulomb energy ($e^2/2C$) of the system. Gate works as a key controller in the device because by changing the gate voltage, charge on the island can be controlled. Figure 1(a) is the schematic representation of a conventional SET device while fig 1(b) represents the electrostatic model of a conventional SET device.
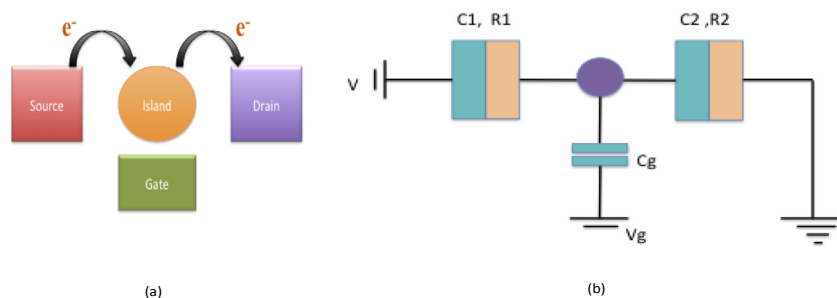

Fig. 1. (a) Schematic representation of a Single-electron transistor (SET) device.
(b)The electrostatic model of a conventional SET device.

Nanotubes, one of the most important nano materials, have been generously studied and can be categorized into two types i.e. organic and inorganic. Organic nanotubes such as Carbon nanotubes, which were discovered by Iijima, show astonishing electrical properties and these properties depend upon the diameter and chirality [17,18], while the inorganic nanotubes similarly include boron-nitride, Si, gold etc. [19,20,21]. Pure boron nanotubes were discovered later, and it has been predicted that all boron nanotubes are found to be metallic in nature [22-27]. In this study we have used carbon and boron nanotubes of (5,0), (3,3) and (4,2), i.e. zigzag, armchair and chiral configuration respectively, as island in SET. It is found that these configurations are the smallest possible nanotubes (that can be experimentally synthesized) with a diameter of about 0.4 nm [28]. We have used two approximations i.e. Local Density Approximation (LDA) and Generalized Gradient Approximation (GGA) to compare the carbon nanotube and boron nanotube-based transistors. Further, CNT based SET and BNT based SET has been used to study in isolated and SET configurations. Additional energies, charge stability diagrams and variations of total energies to that of the gate voltages have been calculated.

COMPUTATIONAL METHODOLOGY
Computational details

In order to model Single-electron transistor (SET), the basic requirement is an optimized structure, for which Density Functional Theory (DFT) based Atomistic Toolkit-Virtual Nanolab (ATK-VNL) [29] package has been used. After optimization, the modeling of SET and all calculations have been executed by using the same in which the double zeta polarized basis set are used to expand the wave functions while local density approximation (LDA) as well as Generalized Gradient Approximation (GGA) have been used [30].To design SET, parameters are chosen to be 1Å, 3.4Å and 3Å, which are gate electrode thickness, gate-oxide thickness, and source-drain thickness widths respectively. Dielectric material of dielectric constant $10\epsilon o$ [31] has been used. Source-drain and gate electrodes in SET are supposed to be of metallic type and here metal with work function 5.28 eV [32-33] i.e. gold is considered. In device analysis, perpendicular components of electric field at the boundaries are made zero by using Neumann boundary conditions. In molecular energy spectrum, energy zero is set to absolute energy.

Basic theoretical details

Density functional theory (DFT) [34-36] is normally utilized to analyze the electronic structure of multifarious systems, holding a lot of atoms for example huge molecules or solids. It is established on electron density rather than wave functions and handles both exchange and correlation. The chief purpose of this theory is to substitute the many-body (MB) wave function with the electronic density as the essential measure. While the MB wave function is based on 3N erratic, three spatial erratic for every of the N electrons, the density is simply a function of three erratic and is a straightforward measure to deal with both conceptually and practically. This theory has a widespread application to quantum mechanical many body problems (QMMBP), where the system of interacting electrons is mapped in an exclusive mode onto an effective non-interactive system with the same total density. Every property is therefore a functional of density. Because density decides potential; which determine Hamiltonian, energy and wave functions; from which all the properties can be determined.

The chief difficulty with DFT is that the precise functional for exchange and correlation are not recognized apart from for the free electron gas. However, approximations survive which allow the calculation of definite physical quantities fairly exactly. In physics, the majority broadly used approximation is LDA, where the functional depends only on the density at the coordinate where the functional is evaluated:

$$E_{XC}[n] = \int \varepsilon_{XC}(n)d^3r$$

Generalized gradient approximations (GGA) are immobile local but also obtain into account the gradient of the density at the similar coordinate:

$$E_{XC}[n_\uparrow, n_\downarrow] = \int \varepsilon_{XC}(n_\uparrow, n_\downarrow, \nabla_{n_\uparrow}, \nabla_{n_\downarrow})d^3r$$

RESULTS AND DISCUSSION

At first, we did the optimization of the nanotubes and then all six configurations [CNT (5,0), CNT (3,3), CNT (4,2), BNT(5,0), BNT(3,3) and BNT(4,2)] have been modeled in SET configuration using the DFT based ATK-VNL software. All calculations have been carried out using two approximations LDA and GGA. Idea behind using the two approximations was to compare the results from both the methods. In order to expand the wave functions, double zeta polarized (DZP) basis set has been used. Neumann boundary conditions, i.e. the value of electric field set to zero, have been applied. The modeled SET configuration for CNT (5,0) is shown in Fig. 2, in which it can be seen that the nanotube has been placed just above the dielectric slab connected to the third i.e. gate electrode and the complete system is surrounded by the metallic electrodes. Within the metallic region, on each electrode the potential is fixed to applied bias.

After the completion of modeling, the SET configurations have been used to analyze the charge stability diagram (CSD) and variation of total energies with respect to the gate voltages. The total energies for the neutral state in SET

environment for carbon nanotube of (5,0), (3,3) and (4,2) configurations are found to be -3118.49721 eV, -1859.83117 eV, and -8783.33288 eV respectively, while for boron nanotube of (5,0), (3,3) and (4,2) configurations are found to be -1540.39202 eV, -925.66558 eV, -4319.81442 eV respectively by using LDA approximations. On the other hand, when GGA approximations are used then the total energies for the same are found to be -3112.89942 eV, -1858.27950 eV, -8763.08354 eV, -1535.00817 eV, -924.07263 eV and -4301.51111 eV respectively. To calculate charging energies i.e. affinity energies and ionization energies, it is required to calculate total energies of distinct charge states (-1, -2, 0, 1, 2). Affinity energy, E_A, is the energy emitted/absorbed by adding one electron to the molecule on the other hand, ionization energy, E_I, is the energy emitted/absorbed by deducting one electron from the molecule. In equation form these may be written as follows:

$$E_A = E^{-1} - E^0$$

$$E_I = E^{+1} - E^0$$

where E^0 is the energy of the molecule at neutral state, E^{+1} is the energy of positively charged molecule and E^{-1} is the energy of negatively charged molecule.
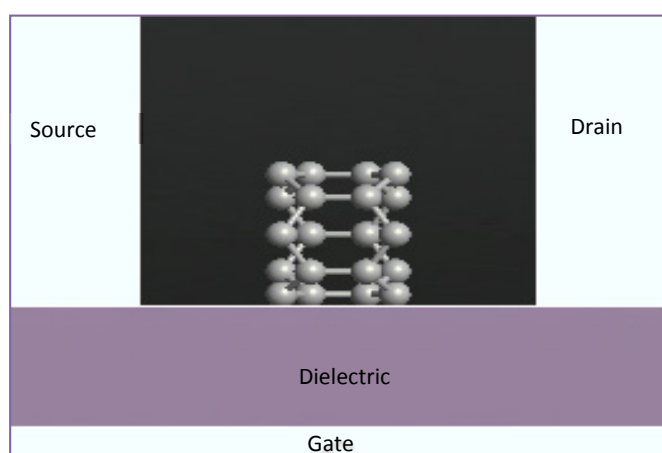
Fig. 2. SET configurations of CNT (5,0)

For all configurations of CNT and BNT, the calculated values of charging energies by LDA and GGA approximations are shown in the tabular form. In the table below, Table, charging energies have been calculated by using both the approximation methods for isolated configuration and for SET configuration respectively. As it is clear from the table that the value of charging energies is decreasing for most of the structures of CNT as well as for BNT from isolated to SET environment. This decrease in charging energies shows the stabilization of the charge by electrostatic surroundings.

Table.

Charging and additional energies for CNT and BNT in isolated and electrostatic surroundings by using both the approximation.

			LDA			GGA		
			E_I(eV)	E_A(eV)	$E_{ADD}=E_A-E_I$(eV)	E_I(eV)	E_A(eV)	$E_{ADD}=E_A-E_I$(eV)
ISO	CNT	(5,0)	5.59236	-2.96275	-8.55511	5.51546	-2.93499	-8.45045
		(3,3)	7.35366	-0.86581	-8.21947	7.29691	-0.8811	-8.17801
		(4,2)	4.92968	-2.79152	-7.7212	4.8809	-2.74619	-7.62709
	BNT	(5,0)	6.30343	-3.79847	-10.1019	6.23544	-3.73954	-9.97498
		(3,3)	8.86497	-5.02667	-13.89164	8.75737	-5.00505	-13.76242
		(4,2)	5.88888	-5.02643	-10.91531	5.77556	-4.9287	-10.70426
SET	CNT	(5,0)	6.47731	-4.93234	-11.40965	6.50309	-4.55857	-11.06166
		(3,3)	6.26139	-4.35388	-10.61527	6.29442	-4.37368	-10.6681
		(4,2)	5.35121	-5.02946	-10.75916	5.44697	-5.14483	-10.5918
	BNT	(5,0)	5.87573	-4.5	-10.37573	5.87078	-4.43984	-10.31062
		(3,3)	7.19601	-2.14373	-9.33974	6.86654	-3.14544	-10.01198
		(4,2)	5.43252	-4.50399	-10.35896	5.4218	-4.89782	-10.31962

Improvement in the conductance can be observed by calculating the additional energy, which is the difference of affinity energy (E_A) and ionization energy (E_I),

$$E_{Add} = E_A - E_I$$

From the Table it can be seen that there is a remarkable decrease of the additional energies for SET environment of CNT (5,0), CNT (3,3) and CNT (4,2) structures for both the approximations used. Decrease in additional energy shows the stabilization of the charges in the structures. A very small reduction is seen for the BNT (5,0), while for BNT (3,3) and BNT (4,2) values of energies are not decreasing. This may happen due to the instability of the structures. From the table it is also clear that CNT (5,0) has the lowest additional energy among all the configurations. Also, it is clear that by using LDA, we are obtaining the lowest energy for the same. On the other hand, by using GGA, we are obtaining the lowest energy for armchair type CNT i.e. (3,3). While in the case of boron nanotube [20-22], we are obtaining good results for BNT (5,0) by using GGA method.

Fig. 3. Variation of total energies against gate voltage by using LDA
(a) – CNT (5,0), (b) – CNT(3,3), (c) – CNT(4,2), (d) – BNT(5,0), (e) – BNT(3,3), (f) – BNT4,2)

Fig. 3 and 4 show the variation of total energies [by considering LDA (Fig.3) and by GGA (Fig.4)] with respect to gate voltages for distinct charge states in which different color map is used i.e. blue (-2), green (-1), red (0), turquoise (1), and violet (2). Different color map depicts different charge state. From the fig. 3 it is clear that for CNT (5,0), CNT (3,3), BNT (5,0), and BNT (3,3) configurations, the system has minimum energy in the neutral state i.e. 0 charge state. Since 0 charge state represents the stability of any system therefore the system is stable in zero charge state. One more thing that can be noted from the Fig. 3 is that when a negative bias is applied then positive states are getting stable. This indicates

the fact that on applying negative biasing, gate will be negatively biased, and an electron will be eliminated from the CNT/BNT and making it positively charged.

As a result, the HOMO level of CNT/BNT appears to be above the electrode's Fermi level. At the same time, when positive bias is applied then negative charge states are getting stable. This indicates that when positive bias is applied, gate will be positively charged then an electron is attracted towards CNT/BNT and making it negatively charged. As a result, the LUMO level of CNT/BNT appears to be above the electrode's Fermi level. Configuration (4,2) is not showing that much promising stabilization properties as from both the Fig. 3 and Fig. 4 it is clear that system is not so stable in their neutral state as the minimum energy of the system is not for the zero-charge state.
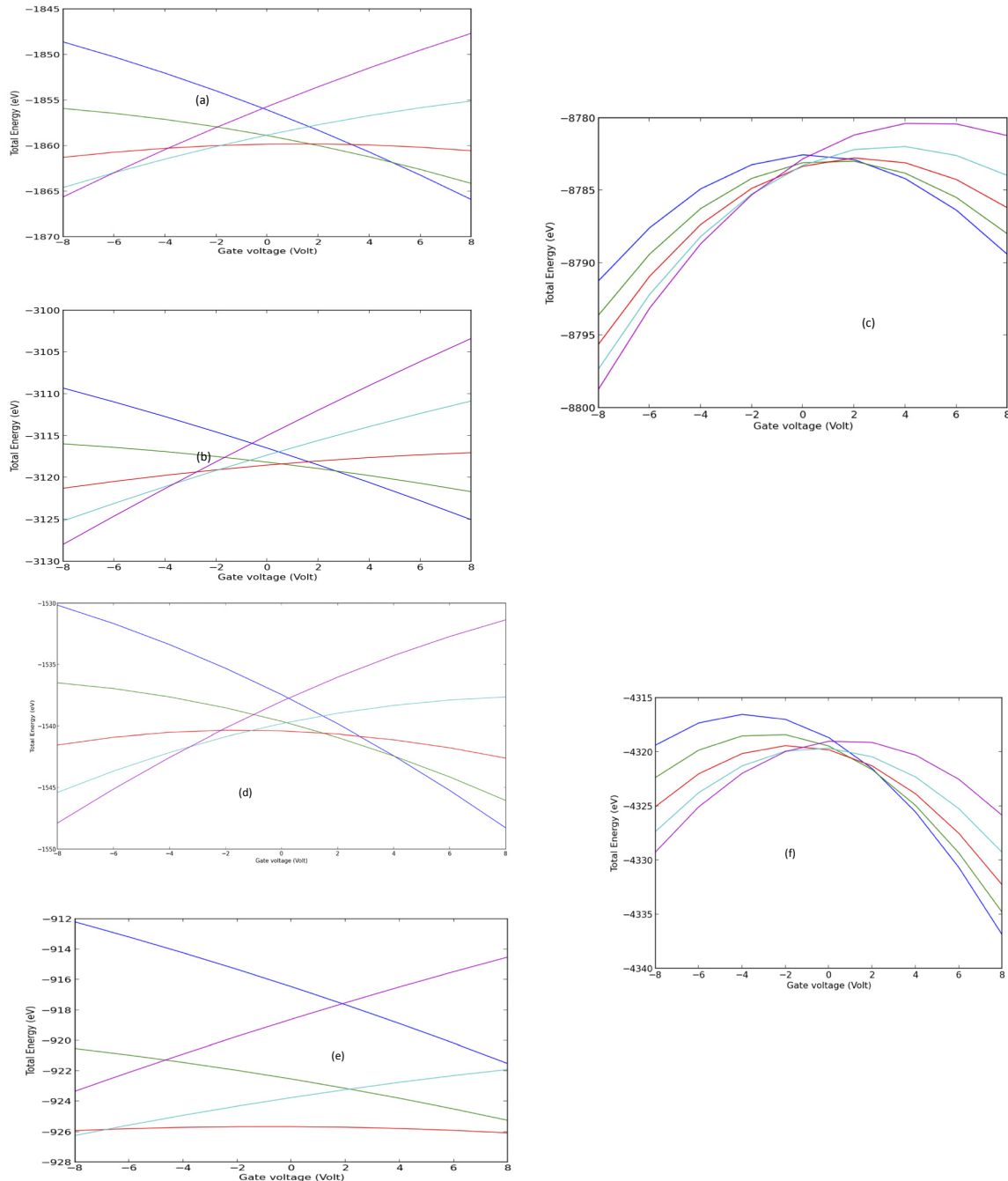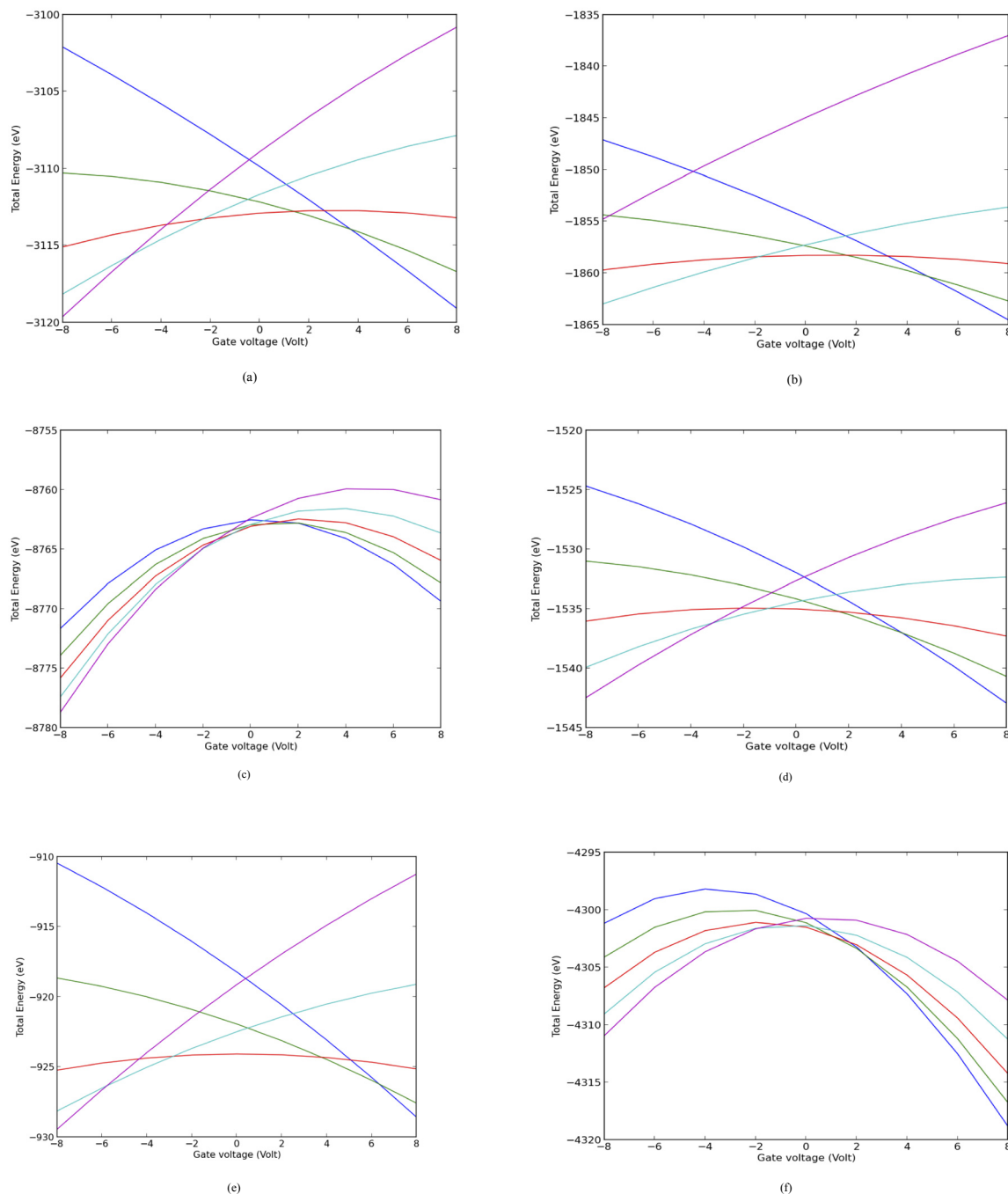

Fig. 4. Variation of total energies against gate voltage by using GGA
(a) – CNT(5,0), (b) – CNT(3,3), (c) – CNT(4,2), (d) – BNT(5,0), (e) – BNT (3,3), (f) – BNT (4,2)

Charge stability diagrams (CSD) have been plotted for the investigation of conductance and are shown in Fig. 5 and Fig. 6 [by using LDA and GGA respectively]. CSD explains the dependence of conductance on the source-drain and voltage. In this diagram, for different gate voltages the charging energies of CNT/BNT in SET surroundings have been plotted. A certain number of energy levels i.e. charge states are present for a fixed value of source-drain and gate voltage. Different colors represent the different energy levels i.e. blue (0), light blue (1), green (2), orange (3) and red (4) in CSD

and conductance depends upon the number of charge states in bias window. As much as the width of the central dark region decreases, less the charging energy will be needed to bring SET into conduction state.

Fig. 5. Charge stability diagram (CSD) for CNT_SET (a,b,c) and BNT_SET (d,e,f)
CSD shows different number of charge states for different bias with blue (0), light blue (1), green (2), orange (3) and red (4)
[by considering LDA]

From the Fig. 5 and Fig. 6 it can be shown that central dark blue region is minimum for CNT (5,0) when calculations are done using LDA. On the other hand, when GGA method has been used to calculate total energies, BNT (5,0) is showing the minimum dark blue region. As much as the width of the central dark region decreases, less the charging energy will be needed to bring SET into conduction state. If we compare all the devices structures, calculating by using LDA as well as GGA, then we can state that CNT (5,0) by calculating LDA is showing better results because it has the minimum charging energy and the smaller coulomb blockade region among all other candidates, i.e. for this configuration electron is trapped in the coulomb diamond for a less time as compared to other configurations. Since the charging energy is the amount of energy that is required for an electron to tunnel through the tunnel junction, so it can increase the amount of the current flow and can make the SET operation fast.
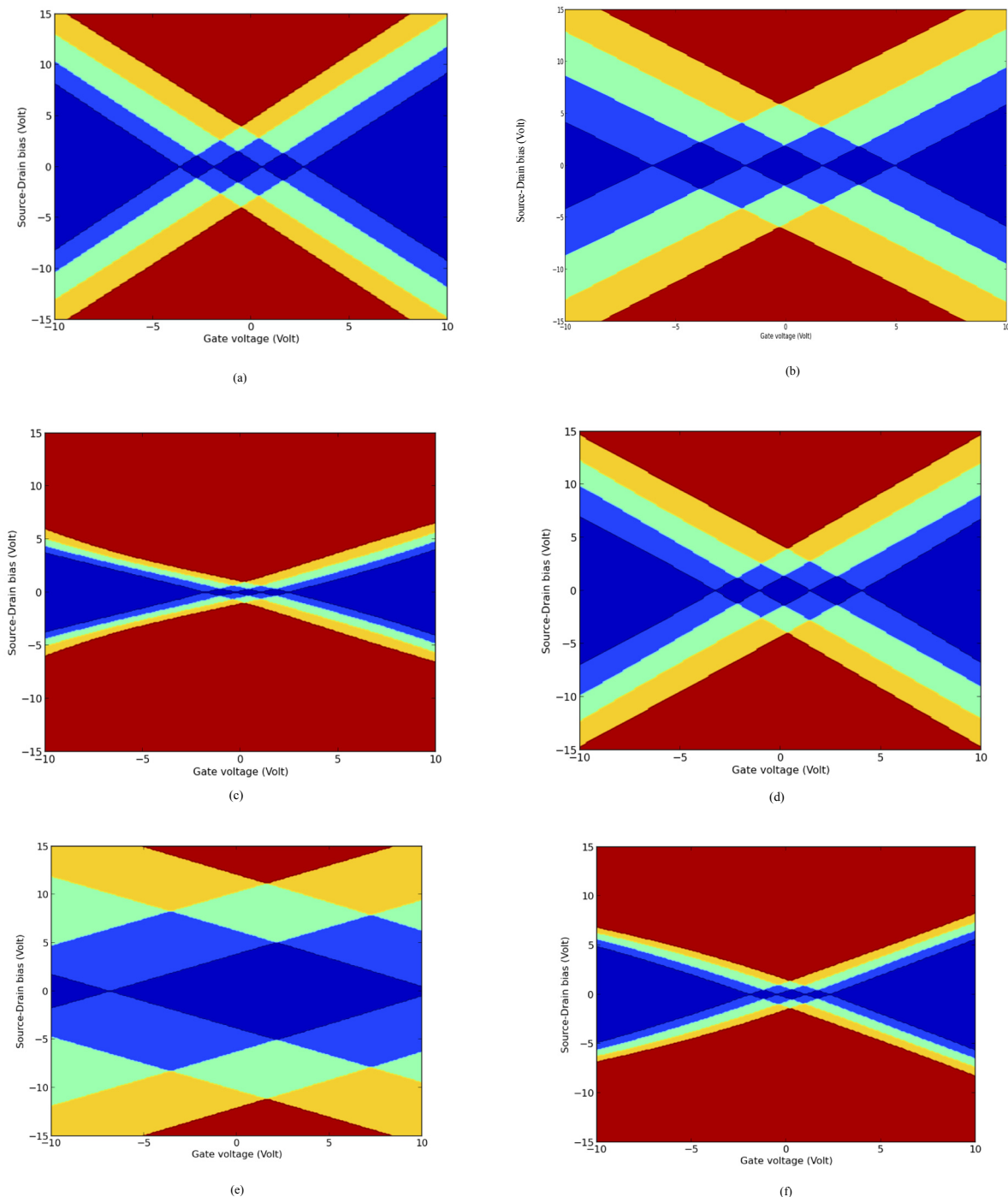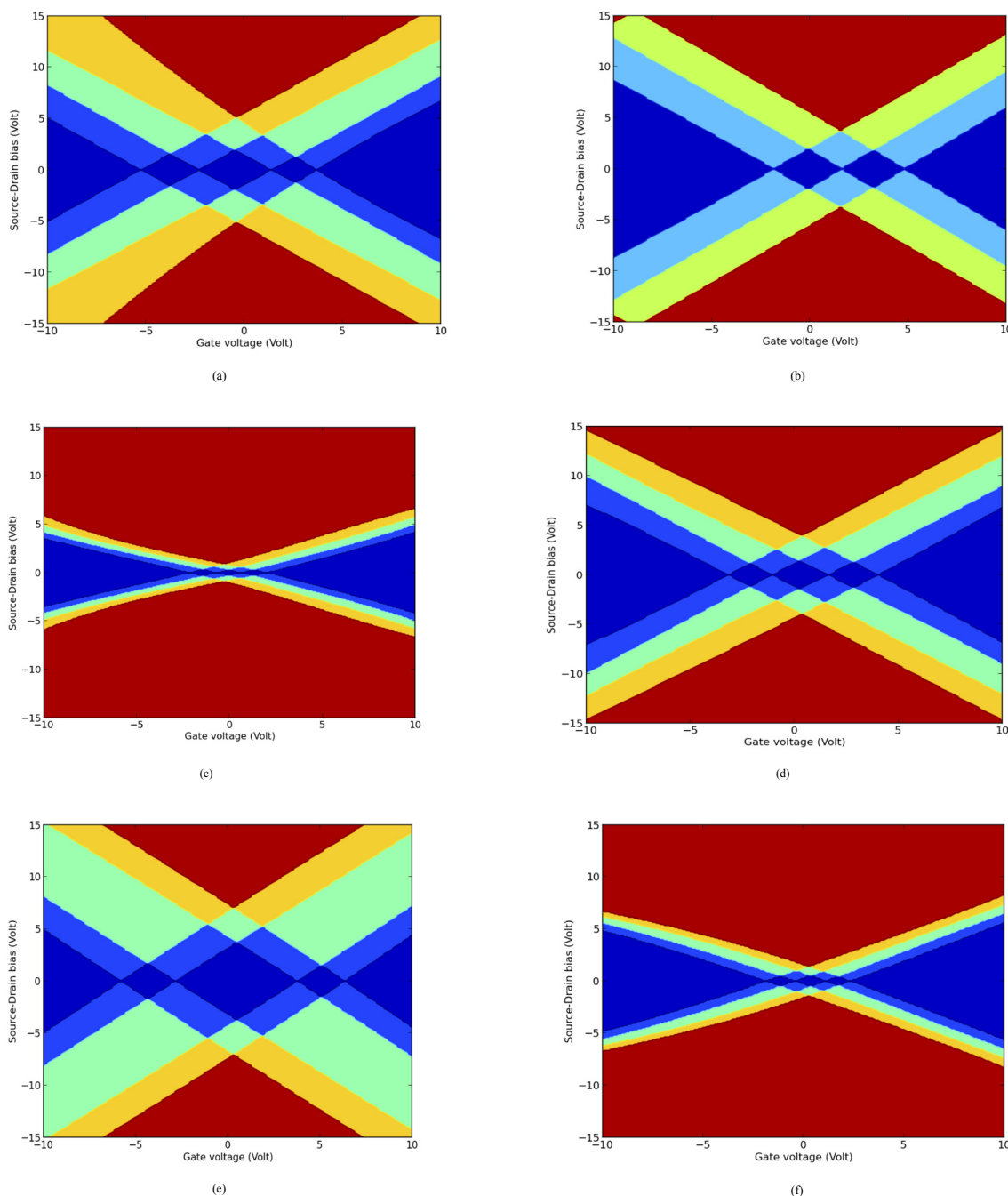
Fig. 6. Charge stability diagram (CSD)for CNT_SET (a,b,c) and BNT_SET (d,e,f)
CSD shows different number of charge states for different bias with blue (0), light blue (1), green (2), orange (3) and red (4)
[by considering GGA]

CONCLUSIONS

In the present work, the calculations exhibit the application of DFT to obtain the perceptivities into the different properties of nanotubes based Single-Electron Transistor working in a Coulomb blockade regime. SETs with the different islands i.e. carbon nanotube and boron nanotube have been modelled and compared for their conductivity and fast switching property with the help of charge stability diagram (CSD) and the variation of the total energies against gate voltage for different states of charges. Due to the stabilization of the charges, the charging energies have decreased for electrostatic surroundings. Addition energy for the island CNT(5,0) has been found to be the lowest for electrostatic environment. Charge stability diagrams (CSD) have been compared and suggest CNT(5,0) for better performance and fast switching properties for the area of the coulomb blockade region is reduced as compared to other islands, therefore for this island less amount of energy is needed to bring SET in the ON state. Therefore, nanotubes-based SETs have been successfully modelled and studied by both the approximation methods and we found the good results from LDA for the island CNT (5,0).

ORCID IDs

Sraja Chauhan https://orcid.org/0000-0002-7055-8574, **Ajay Singh Verma** https://orcid.org/0000-0001-8223-7658

REFERENCES

[1] D. Darau, G. Begemann, A. Donarini, M. Grifoni, M. Grifoni, Physics Review B, **79**(23), 235404 (2009), https://doi.org/10.1103/PhysRevB.79.235404.

[2] T.A. Gschneidtner, Y.A. Diaz Fernandez and K. Moth-Poulsen, Progress in self-assembled single-molecule electronic devices, J. Materials Chemistry C, **1**(43), 7127 (2013), https://doi.org/10.1039/C3TC31483A.

[3] *The Chip that Jack Built*, Texas Instruments, accessed May 29, 2008.

[4] G. Fiori, M. Pala and G. Iannaccone, IEEE Transactions on Nanotechnology, **4**(4), 415-421 (2005), https://doi.org/10.1109/TNANO.2005.851284.

[5] A. Chen, J. Hutchby, V. Zhirnov and G. Bourianoff, *Emerging Nanoelectronics Devices*, (John Wiley & Sons, 2015), pp. 540.

[6] J. Wu, J. Min and Y. Taur, IEEE Transactions on Electron Devices", **62**(9), 3019–3024 (2015), https://doi.org/10.1109/TED.2015.2458977.

[7] C. Bäuerle, D.C. Glattli, T. Meunier, F. Portier, P. Roche, P. Roulleau and X. Waintal, Reports on Progress in Physics, **81**(5), 056503 (2018), https://doi.org/10.1088/1361-6633/aaa98a.

[8] J. Jalil, Y. Zhu, C. Ekanayake and Y. Ruan, Nanotechnology, **28**(14), 142002 (2017), https://doi.org/10.1088/1361-6528/aa57aa.

[9] S.I. Garduño, A. Cerdeira, M. Estrada, J. Alvarado, V. Kilchystka and D. Flandre, J. Applied Physics, **109**, 084524 (2011), https://doi.org/10.1063/1.3575324.

[10] K.K. Likharev, Proceedings of the IEEE, **87**, 606-632 (1999), https://doi.org/10.1109/5.752518.

[11] M.L. Perrin, B. Enrique and H.S.J. van der Zant, Chemical Society Reviews **44**, 902- 919 (2015), https://doi.org/10.1039/C4CS00231H.

[12] Y. Takahashi, Y. Ono, A. Fujiwara and H. Inokawa, J. Physics. Condensed Matter, **14**, 995-1033 (2002), https://doi.org/10.1088/0953-8984/14/39/201.

[13] V.K. Hosseini, M.T. Ahmadi, S. Afrang and R. Ismail, J. Electron. Mater. **46**(7), 4294–4298 (2017), https://doi.org/10.1007/s11664-017-5354-7.

[14] V.V. Shorokhov, D.E. Presnov, S.V. Amitonov, Y.A. Pashkin and V.A. Krupenin, Nanoscale, **9**, 613-620 (2017) https://doi.org/10.1039/C6NR07258E.

[15] F. Wang, J. Fang, Sh. Chang, Sh. Qin, X. Zhang, H. Xu, Physics Letters A, **381**, 476-480 (2017), https://doi.org/10.1016/j.physleta.2016.11.015.

[16] V. Khadem Hosseini, M T. Ahmadi, S. Afrang and R. Ismail, J. Electron. Mater. **46**, 4294-4298 (2017), https://doi.org/10.1007/s11664-017-5354-7.

[17] Z.A.K. Durrani, *Single-electron devices and circuits in silicon*, (Imperial College Press, London, 2010).

[18] F. Willy and Y. Darma, J. Physics: Conference Series, **739**, 012048 (2016), https://doi.org/10.1088/1742-6596/739/1/012048.

[19] K. Seike, Y. Kanai, Y. Ohno, K. Maehashi, K. Inoue and K. Matsumoto, Japanese Journal of Applied Physics, **54**, 06FF05 (2015), https://doi.org/10.7567/JJAP.54.06FF05.

[20] X. Yang, Y Ding and J. Ni, Physics Review B, **77**, 041402(R), (2008), https://doi.org/10.1103/PhysRevB.77.041402.

[21] D. Zhang, R. Zhu and C. Liu, J. Mater. Chem., **16**, 2429-2433, (2006), https://doi.org/10.1039/B517480E.

[22] A. Quandt and A.Y. Liu and I. Boustani, Physical Review B, **64**, 125422 (2001), https://doi.org/10.1103/PhysRevB.64.125422.

[23] D. Ciuparu, R.F. Klie, Y. Zhu and L. Pfefferle, J. Physical Chemistry B, **108**, 3967-3969 (2004), https://doi.org/10.1021/jp049301b.

[24] A. Quandt and I. Boustani, Chem. Phys. Chem. **6***,* 2001-2008 (2005), https://doi.org/10.1002/cphc.200500205.

[25] V. Bezugly, J. Kunstmann, B. Grundkotter-Stock, T Frauenheim, T. Niehaus and G. Cuniberti, ACS Nano **5**, 4997-5005 (2011), https://doi.org/10.1021/nn201099a.

[26] F. Liu, C. Shen, Z. Su, X. Ding, S. Deng, J. Chen, N. Xuand and H. Gao, Jour. Mater. Chem. **20**, 2197–2205 (2010), https://doi.org/10.1039/B919260C.

[27] V. Bezugly, J. Kunstmann, B. Grundkotter-Stock, T. Frauenheim, T. Niehaus and G. Cuniberti, ACS Nano, **5**, 4997-5005 (2011), https://doi.org/10.1021/nn201099a.

[28] L.C. Qin, X. Zhao, K. Hirahara, Y. Miyamoto, Y. Ando and S. Iijima, Nature, **408**, 50 (2000), https://doi.org/10.1038/35040699.

[29] Atomistic Toolkit-Virtual Nanolab. Quantum wise A/S, http://quantumwise.com/

[30] M. Brandbyge, J.L. Mozos, P. Ordejón, J. Taylor and K. Stokbro, Physical Review B*,* **65**, 165401 (2002), https://doi.org/10.1103/PhysRevB.65.165401.

[31] J. Robertson, The European Physical Journal-Applied Physics*,* **28,** 265-291 (2004), https://doi.org/10.1051/epjap:2004206.

[32] Synopsys Inc. Mountain, CA94043, http://docs.quantumwise.com/tutorials/work_function_ag_100/work_function_ag_100.html.

[33] K.I. Hashim, J. Applied Mathematics and Physics, **6**, 1324-1331 (2018), https://doi.org/10.4236/jamp.2018.66111.

[34] K. Capelle, Brazillian Journal of Physics, **36**, 1318-1343 (2006), http://dx.doi.org/10.1590/S0103-97332006000700035.

[35] R. Nityananda, J. Science Education, **22**(8), 809-811 (2017), https://doi.org/10.1007/s12045-017-0529-3.

[36] U. Mordovina, T. E. Reinhard, I. Theophilou, H. Appel and A. Rubio, J. Chemical Theory and Computation, **15**, 5209-5220 (2019), https://doi.org/10.1021/acs.jctc.9b00063.

**ПЕРШОПРИНЦИПИ РОЗРАХУНОКУ ОДНОЕЛЕКТРОННИХ ТРАНЗИСТОРІВ
НА НАНОТУБКАХ ВУГЛЕЦЮ ТА БОРУ**

Сраджа Чаухан, Аджай Сінгх Верма
Кафедра фізики, Банасталі Від'япіт, Раджастан, 304022, Індія.

Низьке споживання енергії, невеликий розмір пристрою та краща керованість носіїв заряду – це фактори, які зробили одноелектронний транзистор (SET) придатним кандидатом для молекулярної електроніки, але є деякі вдосконалення, які можна зробити для його практичного використання. Одноелектронний транзистор (SET) працює на основі тунелювання електронів через два тунельних переходи. Вибір відповідного острівного матеріалу відіграє ключову роль у тунелюванні електронів через тунельні переходи. В даній роботі виконані розрахунки першопринципів одноелектронних транзисторів на основі вуглецевих та нанотрубок на основі бору. Використовували три типи конфігурацій нанотрубок, тобто зигзаг (5,0), крісло (3,3) та хіральний тип (4,2), з найменшим можливим діаметром (приблизно 4A°). Розрахунки проводилися за допомогою пакету моделювання Atomistic Toolkit (ATK-VNL), який є пакетом на основі теорії функціональної щільності (DFT). У цій роботі для демонстрації властивостей SET на основі нанотрубок використовується наближення локальної щільності (LDA), а також узагальнене наближення градієнта (GGA). Ці підходи були реалізовані для нанотрубок, що лежать трохи вище діелектричного затвору. По обидва боки діелектрика присутні електроди, джерело ліворуч і стік справа. Використовувались металеві електроди із золота (W = 5,28eB) та діелектричного матеріалу з діелектричною сталою $10\epsilon o$. Енергії зарядки та додаткові енергії обох типів SET на основі нанотрубок як в ізольованому, так і в електростатичному середовищі були розраховані за допомогою наближень. Обчислені значення енергій заряджання в електростатичному середовищі виявились меншими, ніж енергії заряджання в ізольованій конфігурації, що показує перенормування рівнів молекулярної енергії. Обговорено варіації загальної енергії від напруги на затвору та діаграми стійкості заряду (CSD).

КЛЮЧОВІ СЛОВА: нанотрубка вуглецю, нанотрубка бору, одноелектронний транзистор (SET), спорідненість електронів, енергія іонізації, енергія додавання, діаграма стійкості заряду (CSD)

ПЕРВОПРИНЦИПЫ РАСЧЕТА ЭЛЕКТРОННЫХ ТРАНЗИСТОРОВ НА НОТРУБКАХ ИЗ УГЛЕРОДА И БОРА

Сраджа Чаухан, Аджай Сингх Верма
Физический факультет, Banasthali Vidyapith, Раджастхан, 304022, Индия

Низкое потребление энергии, небольшой размер устройства и лучшая управляемость носителей заряда – это факторы, которые сделали одноэлектронный транзистор (SET) пригодным кандидатом для молекулярной электроники, но есть некоторые усовершенствования, которые можно сделать для его практического использования. Одноэлектронный транзистор (SET) работает на основе туннелирования электронов через два туннельных перехода. Выбор соответствующего островного материала играет ключевую роль в туннелировании электронов через туннельные переходы. В данной работе выполнены расчеты первопринципов одноэлектронных транзисторов на основе нанотрубок углерода и бора. Использовали три типа конфигураций нанотрубок, то есть зигзаг (5,0), кресло (3,3) и хиральный тип (4,2), с наименьшим возможным диаметром (примерно 4A°). Расчеты проводились с помощью пакета моделирования Atomistic Toolkit (ATK-VNL), который является пакетом на основе теории функциональной плотности (DFT). В этой работе для демонстрации свойств SET на основе нанотрубок используется приближение локальной плотности (LDA), а также обобщенное приближение градиента (GGA). Эти подходы были реализованы для нанотрубок, лежащих чуть выше диэлектрического затвора. По обе стороны диэлектрика присутствуют электроды, источник слева и сток дело. Использовались металлические электроды из золота (W = 5,28 эВ) и диэлектрического материала с диэлектрической постоянной $10\epsilon o$. Энергии зарядки и дополнительные энергии обоих типов SET на основе нанотрубок как в изолированном, так и в электростатическом среде были рассчитаны с помощью приближений. Вычисленные значения энергий подзарядки в электростатической среде оказались меньшими, чем энергии подзарядки в изолированной конфигурации, что показывает перенормировку уровней молекулярной энергии. Обсуждены вариации общей энергии от напряжения на затворе и диаграммы устойчивости заряда (CSD).

КЛЮЧЕВЫЕ СЛОВА: углеродная нанотрубка, нанотрубка бора, одноэлектронный транзистор (SET), сродство к электрону, энергия ионизации, добавочная энергия, диаграмма стабильности заряда (CSD).

LIQUIDUS SURFACE AND SPINODAL OF Fe-B-C ALLOYS

Natalia Yu. Filonenko[a,b]*, Alexandra N. Galdina[c]

[a]State Institution "Dnipropetrovsk Medical Academy of the Ministry of Health of Ukraine"
9, Vernadsky Str., Dnipro,49044, Ukraine
[b]Z.I. Nekrasov Iron and Steel Institute of National Academy of Sciences of Ukraine
1, Akademika Starodubova Square, Dnipro, 49107, Ukraine
[c]Oles Honchar Dnipro National University
72, Haharina Ave., Dnipro, 49010, Ukraine
*Corresponding Author: natph2016@gmail.com
Received 24 November 2019; revised December 4, 2019; accepted December 23, 2019

In this work the study is performed for the specimens of Fe-B-C alloys with boron content of 0.005–7.0 wt. % and carbon content of 0.4–6.67 wt. %, the rest is iron. According to the findings of microstructure analysis, XRD and differential thermal analyses, the primary phases and the temperatures of their formation are determined. Depending on boron content (in the range of 1.5–8.80 wt. %) and carbon content (0.5–6.67 wt. %) in the Fe-B-C alloys, the primary phases in the process of crystallization are γ-Fe, boron cementite $Fe_3(CB)$ and boride Fe_2B. The outcomes of the experiment carried out in this work determine the phase composition and phase transformations occurring in the alloys and the liquidus surface is constructed. The findings show that the liquidus temperature for Fe-B-C system alloys is low compared to binary Fe-B and Fe-C alloys. At the liquidus surface of the Fe-B-C alloys, there is a point at boron content of 2.9 wt. % and carbon content of 1.3 wt. % with the lowest temperature of 1375 K and it is the point of intersection of monovariant eutectics. This fact is in a good agreement with the results of other authors. The microstructure of alloys located at the curves of monovariant eutectics is represented by the $γ–Fe+Fe_2B$ and $γ–Fe+Fe_3(CB)$ eutectics and the primary crystals of Fe_2B iron boride in the shell of $Fe_3(BC)$ boron cementite. In this paper it is shown experimentally the existence of a quasi-binary section and the coordinates of the peritectic point are fixed: the boron content is 5.0 wt. %, carbon content is 3.0 wt. % and the temperature is 1515 K. The free energy of the Fe-B-C melt is calculated for the first time by the quasi-chemical method and the surface of thermodynamic stability of the Fe-B-C melt is plotted, depending on temperature and boron and carbon content in the alloy. The results obtained in the paper show that in order to obtain a homogeneous Fe-B-C melt, which does not contain any microheterogeneous structure in the form of short-order microregions, it is necessary to perform the overheating more than to 180 K for the region where the primary phase is iron, and no less than to 200 K for the regions with boron cementite and boride.

KEY WORDS: Fe-B-C system alloys, Fe_2B boride, $Fe_3(CB)$ boron cementite, eutectics, thermodynamic stability of a melt.

The Fe-B-C system alloys have good physical properties, such as hardness and wear resistance, corrosion resistance [1-4].

The processes occurring in the melts of alloys are known to affect the phase composition of the alloys after crystallization. To predict these processes, the thermodynamic stability of the melt should be determined.

The study of the phase composition of Fe-B-C alloys is paid much attention [4-8]. Investigation of $Fe_{0.68}B_{0.16}C_{0.6}$ (at. %) and $Fe_{0.76}B_{0.06}C_{0.18}$ (at. %) alloys shows that formation of cubic boron carbide $Fe_{23}(BC)_6$ occurs after annealing at 1073 K. After annealing of these specimens at 1273 K, the formation of $Fe_3(BC)$ boron cementite is observed, and by means of DTA (differential thermal analysis) it is determined that the solid state is formed at 1400 K [5, 9].

The authors of [4] note that when boron content is 1.0–3.0 wt. % in the Fe-B-C alloy after crystallization the formation of γ-iron primary phase occurs at the temperature of 1422 K. This is in agreement with the results of the authors [6]. With increase in boron content in the alloy up to 3.8 wt. %, the primary phase after crystallization is Fe_2B boride.

The liquidus surface of the Fe-B-C alloys was first obtained by G. Tammann, the ternary eutectic point is represented at this surface at boron content of 2.9 wt. % and carbon content of 1.5 wt. %, and at the temperature of 1383 K. The authors of [8] points out that the eutectic point occurs at boron content of 2.6 wt. % and carbon content of 1.5 wt. %, at the temperature of 1339 K, and in Ref. [10] it is stated that there is a minimum of boron and carbon content and the temperature at 1.5 wt. % boron and 2.5 wt. % carbon at 1402 K on the liquidus surface.

Thus, currently the temperature of liquidus surface as a function of boron and carbon content for the $Fe-Fe_2B-Fe_3(CB)$ alloys is not unanimous. For the moment there are no data available on the homogeneity and thermodynamic stability of Fe-B-C melts.

The purpose of this study is to derive of the liquidus temperature dependence on boron and carbon content in the alloy and to determine the homogeneity limit of the $Fe-Fe_2B-Fe_3(CB)$ melt.

MATERIALS AND METHODS

The investigation was carried out for the specimens with boron content of 0.005–7.0 wt. % and carbon content of 0.4–6.67 wt. %, the rest was iron. To obtain the Fe-B-C alloys, we used such constituents: carbonyl iron (with iron content of 99.95 wt. %), amorphous boron (with boron content of 97.5 wt. %), graphite (with carbon content of 99.96 wt. %). The smelting of specimens was performed in a Tammann furnace in the alundum crucibles in argon

atmosphere. The cooling rate of the alloys was 20 K/min. To determine the chemical composition of alloys, chemical and spectral analyses were used [11]. To reveal the peculiarities of phase transformations in the Fe-B-C system alloys, differential thermal analysis (DTA) of 72 specimens was performed by means of derivatograph.

The phase composition of alloys was studied by method of X-ray microanalysis by means of JSM-6490 microscope with ASID-4D scanning head and "Link Systems 860" software energy-dispersive X-ray microanalyser, and by means of optical microscope "Neophot-21". The X-ray electron probe analysis was carried out using internal standards. The X-ray and X-ray diffraction analyses were performed with DRON-3 diffractometer in monochromated Fe-K$_\alpha$ radiation.

RESULTS AND DISCUSSION

Study of the liquidus temperature in the Fe-B-C system alloys and the primary phases in relation to boron and carbon content, shows that at 3.0 wt. % boron and 0.65 wt. % carbon the formation of γ-Fe primary crystals occurs while crystallization in the temperature range of 1417–1420 K. In the temperature range of 1397–1403 K the γ-Fe+Fe$_2$B eutectics formation occurs, and at 1393–1396 K the γ-Fe+Fe$_3$(CB) eutectics appears. The γ-Fe↔α-Fe transformation takes place at the temperature of 996 K (Fig. 1).
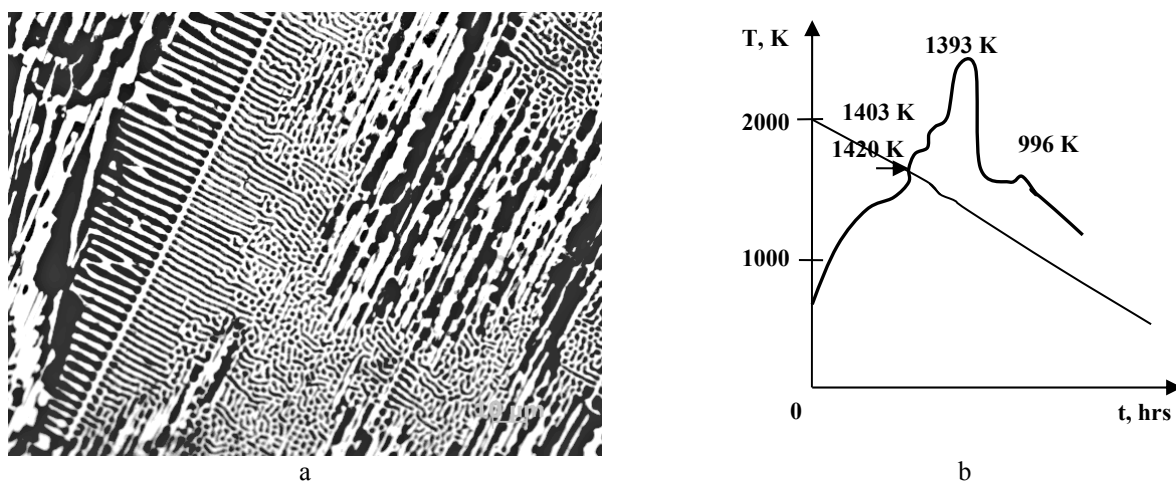
Fig. 1. The microstructure, ×800 (a), DTA curve (b) of the alloy with boron content of 3.0 wt. % and carbon content of 0.65 wt. %

The microhardness for iron is 389.5 GPa, for the γ-Fe+Fe$_2$B eutectics – 897.2 GPa, and for the γ-Fe+Fe$_3$(CB) eutectics – 755.4 GPa.
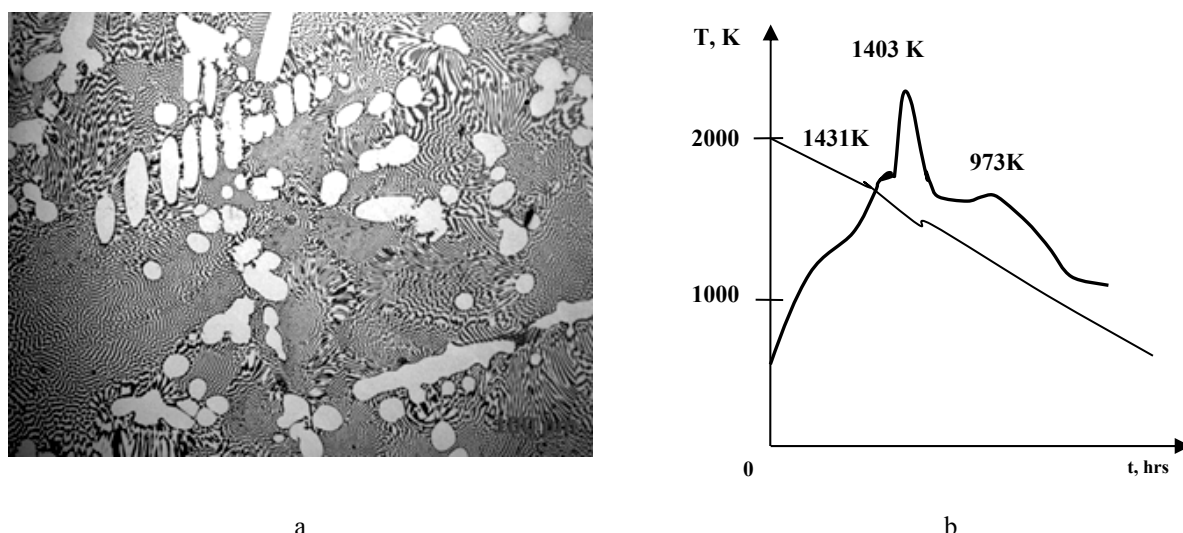
Fig. 2. The microstructure, ×500 (a), DTA curve (b) of the alloy with boron content of 3.43 wt. % and carbon content of 2.25 wt. %

Investigation of the alloys with 0.3–5.5 wt. % boron and 2.1–6.6 wt. % carbon shows that the primary crystals in the process of crystallization are Fe$_3$(CB) boron cementite formed within the temperature range of 1427–1431K. At further cooling the formation of the γ-Fe+Fe$_3$(CB) eutectics with lamellar morphology is observes in the temperature range of 1387–1403 K (Fig. 2). The γ-Fe↔α-Fe transformation is detected at the temperature of 973 K.

The results of durometric analysis reveals that the microhardness of boron cementite is 723.1 GPa, and that for the γ-Fe+Fe$_3$(CB) eutectics is 675.8 GPa.

For the alloys with 2.2–8.8 wt. % boron and 0.5–2.1 wt. % carbon during the crystallization the formation of primary crystals of Fe₂B iron boride occurs. In certain parts of the structure the primary borides are observed surrounded with the shell consisting of Fe₃(BC) boron cementite and the α-Fe+Fe₃(BC) eutectics with morphology similar to that of the boride eutectics (α-Fe+Fe₂B) (Fig. 3a).

The results of differential thermal analysis indicates that the primary crystals of boride are formed from the melt in the temperature range of 1498–1533 K and surrounded with boron cementite shell appeared during the peritectic transformation $L + Fe_2B \rightarrow Fe_3(CB)$ at 1388–1433 K; the γ-Fe+Fe₃(CB) eutectics is formed at the constant temperature of 1399 K, which implies the possibility of the four-phase transformation $L + Fe_2B \rightarrow \gamma - Fe + Fe_3(CB)$ and the transformation γ-Fe↔α-Fe at 925 K (Fig. 3c). The microhardness for iron boride is 1123.6 GPa, for boron cementite – 789.1 GPa, and for eutectics – 863.2 GPa.
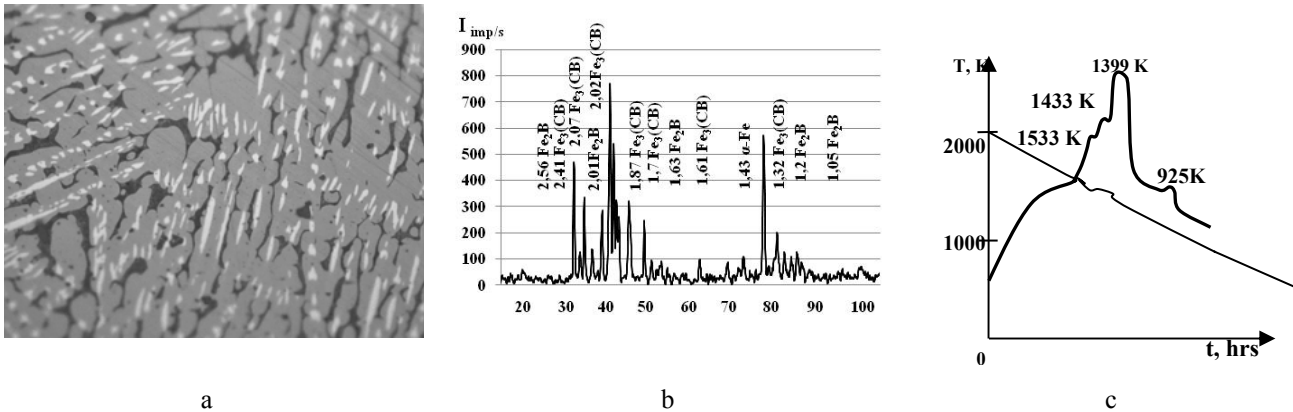
Fig. 3. The microstructure (a), diffractogram (b), DTA curve (c) of the alloy with 2.5 wt. % boron and 4.0 wt. % carbon

The findings show that the liquidus temperature for Fe-B-C system alloys is low compared to binary Fe-B and Fe-C alloys. This is in agreement with the results of other authors [12].

The study of microstructure, XRD and DTA for 72 specimens allows us to construct the liquidus surface for the alloys of Fe-B-C system (Fig. 4).

One of the important factors affecting the formation of the alloys structure under cooling is determination of the liquid stability, i.e. the temperature when the homogeneity of the liquid is observed and there are no any microcrystalline formations.

The Helmholtz free energy is known to be a function of independent variables $F = F(V, T, x_i)$, where V is a volume, T is a temperature, x_i is a weight content of elements, i=1, 2, 3, 4 (x_1=x_{Fe}, x_2=x_B, x_3=x_C, x_4=$x_{V (vacancy)}$). Provided that there are no any external force and change in volume ($V = $ const, $p = $ const) the total differential of Helmholtz free energy is written in a form

$$dF = dU - d(TS) + d(pV) = -SdT + \sum_{i=1}^{4} \mu_i dx_i,$$

where U is the internal energy. Correspondingly, the thermodynamic forces are the entropy $S = -\left(\dfrac{\partial F}{\partial T}\right)_{x_i}$, and the

chemical potential of the constituent in compound $\mu_i = \left(\dfrac{\partial F}{\partial x_i}\right)_T$.

To determine the phase stability, let us find the variation of Helmholtz free energy:

$$\delta F = \sum_{n=1}^{\infty} \frac{1}{n!}\left[\delta T \frac{\partial}{\partial T} + \delta x_1 \frac{\partial}{\partial x_1} + \delta x_2 \frac{\partial}{\partial x_2} + \delta x_3 \frac{\partial}{\partial x_3} + \delta x_4 \frac{\partial}{\partial x_4}\right]^n F . \qquad (1)$$

The general condition of the phase stability by Gibbs is that arbitrary variations of the internal energy and external parameters of the system should not cause both reversible and irreversible processes in the system (to keep the system in equilibrium), so they must be such that [13]:

$$\delta U - T\delta S + p\,\delta V - \mu_1\delta x_1 - \mu_2\delta x_2 - \mu_3\delta x_3 - \mu_4\delta x_4 > 0 . \qquad (2)$$

So, to determine the thermodynamic stability of the Fe-B-C system melt, we use the approach proposed by the author of [14].

The determinant of stability for the melt is:

$$D = \begin{vmatrix} \left(\dfrac{\partial S}{\partial T}\right)_{x_1 x_2 x_3} & \left(\dfrac{\partial \mu_1}{\partial T}\right)_{x_1 x_2 x_3 x_4} & \left(\dfrac{\partial \mu_2}{\partial T}\right)_{x_1 x_2 x_3 x_4} & \left(\dfrac{\partial \mu_3}{\partial T}\right)_{x_1 x_2 x_3 x_4} & \left(\dfrac{\partial \mu_4}{\partial T}\right)_{x_1 x_2 x_3 x_4} \\[2mm] \left(\dfrac{\partial \mu_1}{\partial T}\right)_{x_1 x_2 x_3 x_4} & \left(\dfrac{\partial \mu_1}{\partial x_1}\right)_{T x_2 x_3 x_4} & \left(\dfrac{\partial \mu_1}{\partial x_2}\right)_{T x_3 x_1 x_4} & \left(\dfrac{\partial \mu_1}{\partial x_3}\right)_{T x_2 x_1 x_4} & \left(\dfrac{\partial \mu_1}{\partial x_4}\right)_{T x_3 x_1 x_3} \\[2mm] \left(\dfrac{\partial \mu_2}{\partial T}\right)_{x_1 x_2 x_3 x_4} & \left(\dfrac{\partial \mu_1}{\partial x_2}\right)_{T x_3 x_1 x_4} & \left(\dfrac{\partial \mu_2}{\partial x_2}\right)_{T x_1 x_3 x_4} & \left(\dfrac{\partial \mu_2}{\partial x_3}\right)_{T x_2 x_1 x_4} & \left(\dfrac{\partial \mu_2}{\partial x_4}\right)_{T x_3 x_1 x_2} \\[2mm] \left(\dfrac{\partial \mu_3}{\partial T}\right)_{x_1 x_2 x_3 x_4} & \left(\dfrac{\partial \mu_1}{\partial x_3}\right)_{T x_2 x_1 x_4} & \left(\dfrac{\partial \mu_2}{\partial x_3}\right)_{T x_2 x_1 x_4} & \left(\dfrac{\partial \mu_3}{\partial x_3}\right)_{T x_1 x_2 x_4} & \left(\dfrac{\partial \mu_3}{\partial x_4}\right)_{T x_2 x_1 x_3} \\[2mm] \left(\dfrac{\partial \mu_4}{\partial T}\right)_{x_1 x_2 x_3 x_4} & \left(\dfrac{\partial \mu_1}{\partial x_4}\right)_{T x_3 x_1 x_2} & \left(\dfrac{\partial \mu_2}{\partial x_4}\right)_{T x_3 x_1 x_2} & \left(\dfrac{\partial \mu_3}{\partial x_4}\right)_{T x_2 x_1 x_2} & \left(\dfrac{\partial \mu_4}{\partial x_4}\right)_{T x_1 x_2 x_3} \end{vmatrix}. \tag{3}$$

The case of *D=0* was first defined by J. W. Gibbs as a critical state of matter [15]. During the supercritical transitions the determinant and coefficients of stability pass through finite minima that correspond to the growth of fluctuations. The locus of these minima is a low-stability curve. It should be noted that for different coefficients of stability, the curves of lowered stability may not be coinciding. For these reasons the curve of lowered stability for *D*, which includes all equilibrium characteristics of the system and therefore best describes its stability, is used as a basis. The threshold case of supercritical transitions when fluctuations in the system reach the maximum level, the determinant and coefficients of stability pass zero minima, is the critical state. So, let us find when *dD=0*.

The Helmholtz free energy we find by the quasi-chemical method as:

$$\begin{aligned} F = 11(&N_1 N_1 \nu_{11} + N_1 N_2 \nu_{12} + N_1 N_3 \nu_{13} + N_2 N_2 \nu_{22} + N_3 N_3 \nu_{33} + N_3 N_4 \nu_{34} + \\ &+ N_2 N_4 \nu_{24} + N_1 N_4 \nu_{14}) + 11 kT((N_1 + N_2 + N_3 + N_4) \ln(N_1 + N_2 + N_3 + N_4) - , \\ &- N_1 \ln N_1 - N_2 \ln N_2 - N_3 \ln N_3 - N_4 \ln N_4) \end{aligned} \tag{4}$$

where T is the temperature (K), ν_{ij} is the interaction energy of components (J/mol).

To calculate the free energy of the melt, we used the values of energies of interactions between the components from the works [15-20]. The sum is taken over all i and j provided $i \neq j$.

From Eq. (4) we obtain the thermodynamic functions of the melt:

$$S = -\left(\frac{\partial F}{\partial T}\right)_{x_i} = -k\left((x_1 + x_2 + x_3 + x_4) \ln(x_1 + x_2 + x_3 + x_4) - x_1 \ln(x_1) - x_2 \ln(x_2) - x_3 \ln(x_3) - x_4 \ln(x_4)\right)$$

$$\mu_1 = \left(\frac{\partial F}{\partial x_1}\right)_{T x_2 x_3 x_4} = 22 x_1 \nu_{11} + 11 x_2 \nu_{12} + 11 x_3 \nu_{13} + 11 x_4 \nu_{14} + kT(\ln(x_1 + x_2 + x_3 + x_4) - \ln(x_1))$$

$$\mu_2 = \left(\frac{\partial F}{\partial x_2}\right)_{T x_1 x_3 x_4} = 11 x_1 \nu_{12} + 22 x_2 \nu_{22} + 11 x_4 \nu_{24} + kT(\ln(x_1 + x_2 + x_3 + x_4) - \ln(x_2))$$

$$\mu_3 = \left(\frac{\partial F}{\partial x_3}\right)_{T x_1 x_2 x_4} = 11 x_1 \nu_{13} + 22 x_3 \nu_{33} + 11 x_4 \nu_{34} + kT(\ln(x_1 + x_2 + x_3 + x_4) - \ln(x_3))$$

$$\mu_4 = \left(\frac{\partial F}{\partial x_4}\right)_{T x_1 x_2 x_3} = 11 x_1 \nu_{14} + 11 x_2 \nu_{24} + 11 x_3 \nu_{34} + kT(\ln(x_1 + x_2 + x_3 + x_4) - \ln(x_4))$$

$$\left(\frac{\partial \mu_1}{\partial x_1}\right)_{T x_1 x_2 x_3} = 22 \nu_{11} + kT\left(1/(x_1 + x_2 + x_3 + x_4) - 1/x_1\right), \quad \left(\frac{\partial \mu_1}{\partial T}\right)_{x_1 x_2 x_3 x_4} = k\left(\ln(x_1 + x_2 + x_3 + x_4) - \ln(x_1)\right),$$

$$\left(\frac{\partial \mu_1}{\partial x_2}\right)_{T x_1 x_3 x_4} = 11 \nu_{12} + kT/(x_1 + x_2 + x_3 + x_4),$$

$$\left(\frac{\partial \mu_1}{\partial x_3}\right)_{T x_1 x_2 x_4} = 11 \nu_{13} + kT/(x_1 + x_2 + x_3 + x_4), \quad \left(\frac{\partial \mu_1}{\partial x_4}\right)_{T x_1 x_2 x_3} = 11 \nu_{14} + kT/(x_1 + x_2 + x_3 + x_4)$$

Liquidus Surface and Spinodal of Fe-B-C Alloys

$$\left(\frac{\partial \mu_2}{\partial x_2}\right)_{Tx_1x_3x_4} = 22v_{22} + kT(1/(x_1+x_2+x_3+x_4)-1/x_2), \quad \left(\frac{\partial \mu_2}{\partial T}\right)_{x_1x_2x_3x_4} = k(\ln(x_1+x_2+x_3+x_4)-\ln(x_2)),$$

$$\left(\frac{\partial \mu_2}{\partial x_1}\right)_{Tx_2x_3x_4} = 11v_{12} + kT/(x_1+x_2+x_3+x_4),$$

$$\left(\frac{\partial \mu_2}{\partial x_3}\right)_{Tx_1x_2x_4} = kT/(x_1+x_2+x_3+x_4), \quad \left(\frac{\partial \mu_2}{\partial x_4}\right)_{Tx_1x_2x_3} = 11v_{24} + kT/(x_1+x_2+x_3+x_4)$$

$$\left(\frac{\partial \mu_3}{\partial x_3}\right)_{Tx_1x_2x_4} = 22v_{33} + kT(1/(x_1+x_2+x_3+x_4)-1/x_3),$$

$$\left(\frac{\partial \mu_3}{\partial T}\right)_{x_1x_2x_3x_4} = k(\ln(x_1+x_2+x_3+x_4)-\ln(x_3)), \quad \left(\frac{\partial \mu_4}{\partial x_4}\right)_{Tx_1x_2x_3} = kT(1/(x_1+x_2+x_3+x_4)-1/x_4)$$

$$\left(\frac{\partial \mu_4}{\partial T}\right)_{x_1x_2x_3x_4} = k(\ln(x_1+x_2+x_3+x_4)-\ln(x_4)), \quad \left(\frac{\partial \mu_3}{\partial x_1}\right)_{Tx_2x_3x_4} = 11v_{13} + kT/(x_1+x_2+x_3+x_4),$$

$$\left(\frac{\partial \mu_3}{\partial x_2}\right)_{Tx_1x_3x_4} = kT/(x_1+x_2+x_3+x_4), \quad \left(\frac{\partial \mu_3}{\partial x_4}\right)_{Tx_1x_2x_3} = 11v_{34} + kT/(x_1+x_2+x_3+x_4),$$

$$\left(\frac{\partial \mu_4}{\partial x_1}\right)_{Tx_2x_3x_4} = 11v_{14} + kT/(x_1+x_2+x_3+x_4), \quad \left(\frac{\partial \mu_4}{\partial x_2}\right)_{Tx_1x_3x_4} = 11v_{24} + kT/(x_1+x_2+x_3+x_4),$$

$$\left(\frac{\partial \mu_4}{\partial x_3}\right)_{Tx_1x_2x_4} = 11v_{34} + kT/(x_1+x_2+x_3+x_4)$$

To determine the stability of the melt, the condition $dD = 0$ should be fulfilled:

$$dD = \left(\frac{\partial D}{\partial T}\right)_{x_1x_2x_3x_4} dT + \left(\frac{\partial D}{\partial x_1}\right)_{Tx_2x_3x_4} dx_1 + \left(\frac{\partial D}{\partial x_2}\right)_{Tx_1x_3x_4} dx_2 + \left(\frac{\partial D}{\partial x_3}\right)_{Tx_1x_2x_4} dx_3 + \left(\frac{\partial D}{\partial x_4}\right)_{Tx_1x_2x_3} dx_4 = 0. \tag{5}$$

The condition (5) holds when

$$\left(\frac{\partial D}{\partial T}\right)_{x_1x_2x_3x_4} = 0, \quad \left(\frac{\partial D}{\partial x_1}\right)_{Tx_2x_3x_4} = 0, \quad \left(\frac{\partial D}{\partial x_2}\right)_{Tx_1x_3x_4} = 0, \quad \left(\frac{\partial D}{\partial x_3}\right)_{Tx_1x_2x_4} = 0, \left(\frac{\partial D}{\partial x_4}\right)_{Tx_1x_2x_3} = 0. \tag{6}$$

The resulting system of equations (6) is solved numerically using the mathematical package Maple. The solution of system of equations (6) is shown in Fig. 4.

The experimental results obtained in this study enable to construct the liquidus surface, and calculated data allow plotting the surface of thermodynamic stability of the melt (Fig. 4). The liquidus surface of the Fe-B-C alloys was first obtained by G. Tammann; the ternary eutectic point with 2.9 wt. % boron and 1.5 wt. % carbon at 1383 K was mapped on this surface. The ternary eutectic point is the intersection of the curves of monovariant binary eutectics.

The liquidus surface study presented in [10] indicates that the ternary eutectic point occurs at boron content of 1.5 wt. % and carbon content of 2.5 wt. % and at the temperature of 1402 K.

The results obtained in this work reveal that at the liquidus surface in Fe-B-C alloys there is a minimum at boron content of 2.9 wt. % and carbon content of 1.3 wt. % at 1375 K. The findings are in good agreement with data given in [5], where it is pointed out that the solidus temperature is 1400 K. In this paper it is shown experimentally the existence of a quasi-binary section and the coordinates of the peritectic point are fixed: the boron content is 5.0 wt. %, carbon content is 3.0 wt. % and the temperature is 1515 K.

The process of the formation of the primary phases has a great effect on the structural state and phase transformations in the alloy. At the moment there are lack of data on determining and investigating the homogeneity of the melt of Fe-B-C alloys without any microcomplexes. According to the outcomes, to obtain the homogeneous Fe-B-C melt (without any microheterogeneous structure in the form of short-range microregions) where the primary crystals are γ-Fe phase, it is necessary to perform the overheating more than to 180–200 K. For the alloys with boron and carbon content close to the quasi-binary cross-section, to obtain the homogeneous melt it is necessary to perform the overheating of alloy more than to 220–250 K.
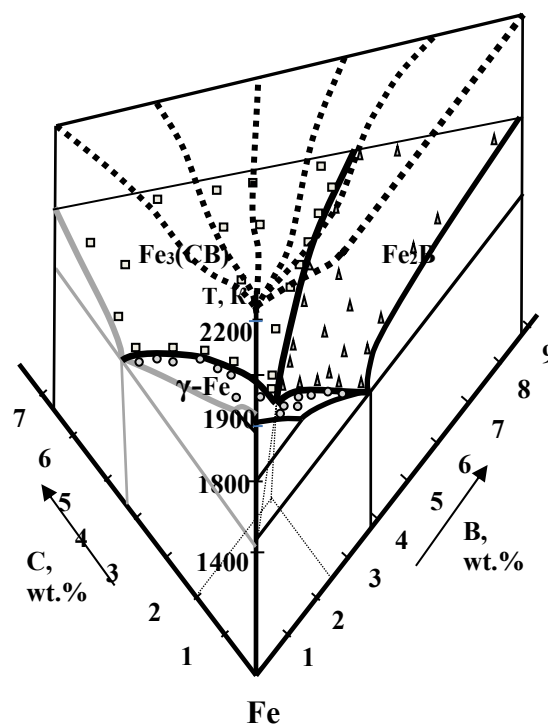
Fig. 4. The state diagram of the Fe-B-C system ($\square$ – Fe$_3$(CB), $\triangle$ – Fe$_2$B, $\circ$ – γ-Fe) and the surface of thermodynamic stability of the melt ($\blacksquare$ – the Fe-B diagram, $\blacksquare$ – the Fe-C diagram, $\blacksquare$ – the eutectics curves, $\bullet\bullet\bullet\bullet\bullet\bullet$ – the surface of thermodynamic stability of the Fe-B-C melt)

CONCLUSION

In the paper the phase composition and phase transformation occurring in the alloys with boron content of 0.005-7.0 wt. % and carbon content of 0.4–6.67 wt. % (the rest is iron) is studied. It is shown that formation of the primary phases γ-Fe, Fe$_2$B and Fe$_3$(CB) takes place depending on boron and carbon content in the alloys.

The liquidus surface is plotted experimentally for the Fe-B-C system alloys in the concentrarion range of 0-8.85 wt. % boron and 0–6.65 wt. % carbon and it is shown that the ternary eutectic point occurs at the liquidus surface in the alloys of Fe-B-C systems with boron content of 2.9 wt. % and carbon content of 1.3 wt. % at the temperature of 1375 K.

In this paper, using the quasi-chemical methos, we obtain for the first time the temperature dependence of the Helmholtz free energy of the Fe-B-C melt. We obtain the dependences of the temperature of thermodynamic stability of the melt on boron and carbon content in the alloy and plot the surface of concentration anomaly without any microcomplexes in the melt. According to the outcomes, it is necessary to perform the overheating more than to 180 K to obtain the homogeneous Fe-B-C melt, which does not contain the microheterogeneous structure in the form of short-order microregions.

The work was performed within the specific project "Resurs" KC063.18 "Development of chemical composition and technological decisions for the manufacture of railway wheels for different application and their maintainability" of the NAS of Ukraine.

ORCID IDs
Ⓓ**Natalia Yu. Filonenko** https://orcid.org/0000-0003-1219-348X, Ⓓ**Alexandra N. Galdina** https://orcid.org/0000-0003-2311-8506

REFERENCES
[1] Fu Han-guang, Nonferrous Metals. **9**, 113 (2005), http://en.cnki.com.cn/Article_en/CJFDTotal-ZZZZ200509006.htm.
[2] Zhao Guorong, Li Zhenhua, Liu Meihong, He Zhengyuan, Hot Working Technology. **15**, 113 (2011), http://en.cnki.com.cn/Article_en/CJFDTotal-SJGY201115001.htm.
[3] Song Xu, Fu Han, Yang Jun, Transactions of Materials and Heat Treatment. **10,** 164 (2008), http://en.cnki.com.cn/Article_en/CJFDTOTAL-JSCL200801010.htm.
[4] P. Sang, H. Fu, Y. Qu, C. Wang and Y. Lei, Materials Science & Engineering Technology. **46**(9), 962 (2015), https://doi.org/10.1002/mawe.201500397.
[5] Ayako Sudo, Tsuyoshi Nishi, Noriko Shirasu, Masahide Takano and Masaki Kurata, Journal of Nuclear Science and Technology. **52**(10), 1308 (2015), https://doi.org/10.1080/00223131.2015.1016465.

[6] Xiangyi Ren, Hanguang Fu, Jiandong Xing, Yongwei Yang and Shuli Tang, Journal of Materials Research. **32**(16), 3078 (2017), https://doi.org/10.1557/jmr.2017.304.

[7] Zhi Fu Huang, Jian Dong Xing, Sheng Qiang Ma, Yi Min Gao, Ming Zheng and Li Qiu Sun, Key Engineering Materials. **732**, 59 (2017), https://doi.org/10.4028/www.scientific.net/KEM.732.59.

[8] I.M. Spiridonova, S.B. Pilyaeva, E.B. Syxovaya, E.B. Zinkovskiy, Visnyk Dnipropetrovskogo nacionalnogo universytetu. Serija Fizyka. Radioelektronika, **8**, 32-44 (2002). (in Ukrainian)

[9] N.Yu. Filonenko, S.B. Pilyaeva, Journal of V.N. Karazin Kharkiv National University, series "Physics", **21**(1135), 49–51 (2014), https://periodicals.karazin.ua/physics/article/view/7817/7290. (in Ukrainian)

[10] Eberhard Schürmann, Clausthal, Shao-Xiong Li, Jilin Bor 37. Jahrgang,121-129 (1985).

[11] S.V. Tverdokhlebova, Visnyk Dnipropetrovskogo nacionalnogo universytetu. Serija Fizyka. Radioelektronika, **14**(12/1), 100-104 (2007), http://www.vdnu.narod.ru/v14/pdf/s26_14.pdf. (in Ukrainian)

[12] Takafumi Hibino, Teruo Bitoh, Journal of Alloys and Compounds. **707**(15), 82 (2017), https://doi.org/10.1016/j.jallcom.2016.12.060.

[13] E.D. Soldatova, Journal of Molecular Liquids. **127**(1-3), 99 (2006), https://doi.org/10.1016/j.molliq.2006.03.027.

[14] N.Yu. Filonenko, East. Eur. J. Phys. **5**(1), 55-60 (2018), https://doi.org/10.26565/2312-4334-2018-1-06.

[15] J.W. Gibbs, *Термодинамика. Статистическая механика* [*Thermodynamic. Statistical Mechanics*], (Moscow, Nauka, 1982), pp. 584. (in Russian)

[16] Tian Wei He, Ye Hua Jiang, Rong Zhou, Jing Feng, RSC Advances. **51**, 45250 (2016), https://doi.org/10.1039/C6RA05969D.

[17] D. Terentyev, K. Heinola, A. Bakaev and E. E. Zhurkin, Scripta Materialia. **86**, 9 (2014), https://doi.org/10.1016/j.scriptamat.2014.04.003.

[18] T. Ohnuma, N. Soneda and M. Iwasawa, Acta Materialia. **57**, 5947 (2009), https://doi.org/10.1016/j.actamat.2009.08.020.

[19] N.Yu. Filonenko, O.S. Baskevych and V.V. Soboliev, Journal Scientific Bulletin of National Mining University. **4**, 74 (2012), http://nv.nmu.org.ua/index.php/en/component/jdownloads/finish/34-04/528-2012-4-filonenko/0.

[20] O.Yu. Bereza, N.Yu. Filonenko, O.S. Baskevich, Physics and Chemistry of Solid State, **13**(3), 968-973 (2012), http://page.if.ua/uploads/pcss/vol13/1304-21.pdf. (in Ukrainian)

ПОВЕРХНЯ ЛІКВІДУСУ ТА СПІНОДАЛЬ СПЛАВІВ СИСТЕМИ Fe-B-C

Н.Ю. Філоненко[a,b], О.М. Галдіна[c]

[a]*ДЗ «Дніпропетровська державна медична академія МОЗ України»*
49044, Україна, м. Дніпро, вул. Володимира Вернадського, 9
[b]*Інститут чорної металургії ім. З.І. Некрасова НАН України (ІЧМ НАНУ)*
49107, Україна, м. Дніпро, пл. Ак. Стародубова К.Ф., 1
[c]*Дніпровський національний університет імені Олеся Гончара*
49010, Україна, м. Дніпро, просп. Гагаріна, 72

В даній роботі дослідження здійснювали на зразках сплавів системи Fe-B-C з вмістом бору 0,005–7,0% (мас.) та карбону 0,4–6,67% (мас.), інше – залізо. За результатами мікроструктурного, рентгеноструктурного та диференційного термічного аналізів визначені первинні фази та температури їх утворення. В залежності від вмісту бору (в інтервалі 1,5–8,80% (мас.)) та карбону (0,5–6,67% (мас.)) в сплавах системи Fe-B-C первинними фазами при кристалізації є γ–Fe, бороцементит $Fe_3(CB)$ та борид Fe_2B. За результатами експерименту, проведеного в даній роботі, досліджено фазовий склад та фазові перетворення, що відбуваються в сплавах, та побудована поверхня ліквідусу. Дослідження, проведені в даній роботі, показали, що сплави системи Fe-B-C мають низьку температуру ліквідусу у порівнянні з бінарними сплавами Fe-B та Fe-C. На поверхні ліквідусу сплавів системи Fe-B-C існує точка при вмісті бору 2,9% (мас.) та карбону 1,3% (мас.), яка має найменшу температуру 1375 K та є точкою перетину моноваріантних евтектик, що корелює з результатами інших авторів. Мікроструктура сплавів, розташованих на лініях моноваріантних евтектик, представлена: евтектиками γ–Fe+Fe_2B, γ–Fe+$Fe_3(CB)$ та первинними кристалами бориду заліза Fe_2B в оболонці з бороцементиту $Fe_3(BC)$. Експериментально в даній роботі показано існування квазібінарного перерізу та визначені координати точки перитектики: при вмісті бору 5,0 % (мас.) та карбону 3,0 % (мас.) та температурі 1515 K. Вперше квазіхімічним методом отримано вільну енергію та побудовано поверхню термодинамічної стійкості розплаву Fe-B-C в залежності від температури та вмісту бору й карбону в сплаві. Отримані в роботі результати показали, що для досягнення однорідного розплаву Fe-B-C, що не містить мікронеоднорідної структури у вигляді мікроділянок з ближнім порядком, необхідно виконати перегрів: для ділянки, де первинною фазою є залізо, більш ніж на 180 K, а для ділянок, що містять бороцементит та борид, – не менш ніж на 200 K.

КЛЮЧОВІ СЛОВА: сплави системи Fe-B-C, борид Fe_2B, бороцементит $Fe_3(CB)$, евтектика, термодинамічна стійкість розплаву.

ПОВЕРХНОСТЬ ЛИКВИДУСА И СПИНОДАЛЬ СПЛАВОВ СИСТЕМЫ Fe-B-C

Н.Ю. Филоненко[a,b], А.Н. Галдина[c]

[a]*ГУ «Днепропетровская государственная медицинская академия МОЗ Украины»*
49044, Украина, г. Днепр, ул. Владимира Вернадского, 9
[b]*Институт черной металлургии им. З.И. Некрасова НАН Украины (ИЧМ НАНУ)*
49107, Украина, г. Днепр, ул. Ак. Стародубова К.Ф., 1
[c]*Днепровский национальный университет имени Олеся Гончара*
49010, Украина, г. Днепр, просп. Гагарина, 72

В данной работе исследования осуществляли на образцах сплавов системы Fe-B-C с содержанием бора 0,005-7,0% (мас.) и углерода 0,4-6.67% (мас.), остальное – железо. По результатам микроструктурного, рентгеноструктурного и дифференциального термического анализов определены первичные фазы и температуры их образования. В зависимости от содержания бора и углерода (бора в интервале 1,5-8,80% (мас.) и углерода 0,5-6,67% (мас.)) в сплавах системы Fe-B-C при кристаллизации первичными фазами являются: γ-Fe, бороцементит $Fe_3(CB)$ и борид Fe_2B. По результатам эксперимента,

проведенного в данной работе, исследованы фазовый состав и фазовые превращения, которые происходят в сплавах, и построена поверхность ликвидуса. Исследования, проведенные в данной работе, показали, что сплавы системы Fe-B-C имеют более низкую температуру ликвидуса по сравнению с бинарными сплавами Fe-B и Fe-C. На поверхности ликвидуса сплавов системы Fe-B-C существует точка с содержанием бора 2,9% (мас.) и углерода 1,3% (мас.), которая имеет наименьшую температуру 1375 К и является точкой пересечения моновариантных эвтектик, что коррелирует с результатами других авторов. Микроструктура сплавов, расположенных на линиях моновариантних эвтектик, представлена: эвтектиками γ-Fe+Fe$_2$B, γ-Fe+Fe$_3$(CB) и первичными кристаллами боридов железа Fe$_2$B в оболочке из бороцементита Fe$_3$(BC). Экспериментально в данной работе показано существование квазибинарного сечения и определены координаты точки перитектики: при содержании бора 5,0% (мас.) и углерода 3,0% (мас.) и температуре 1515 К. Впервые с использованием квазихимического метода получена свободная энергия и построена поверхность термодинамической устойчивости расплава Fe-B-C в зависимости от температуры и содержания бора и углерода в сплаве. Полученные в работе результаты показали, что для достижения однородного расплава Fe-B-C, который не содержит микронеоднородной структуры в виде микроучастков с ближним порядком, необходимо выполнить перегрев: для участка, где первичной фазой является железо, более чем на 180 К, а где первичными фазами являются бороцементит и борид – не менее чем на 200 К.

КЛЮЧЕВЫЕ СЛОВА: сплавы системы Fe-B-C, борид Fe$_2$B, бороцементит Fe$_3$(CB), эвтектика, термодинамическая устойчивость расплава.

EFFECT OF KIND OF DEFORMATION ON YOUNG'S MODULUS, DAMAGE PARAMETER, TEXTURE AND STRUCTURE OF ALLOY Mg – 5% Li (wt)

Valentin Usov[a]*, Heinz-Günter Brokmeier[b,e], Nataliia Shkatulyak[c], Elena Savchuk[d], Norbert Schell[e]

[a]*South Ukrainian National Pedagogical University named after K. D. Ushinsky, Department of Technological and Professional Education, Staroportofrankovskaya Str. 26, 65020, Odessa, Ukraine,*
[b]*Institute for Materials Science and Engineering - Department of TEXMAT - University of Technology Clausthal*
Agricolastrasse, 6, D-38678, Clausthal-Zellerfeld, Germany
[c]*South Ukrainian National Pedagogical University named after K. D. Ushinsky, Department of Physics*
Staroportofrankovskaya Str. 26, 65020, Odessa, Ukraine
[d]*National University "Odessa Maritime Academy", Department of Physics*
Didrichson's street, 8, 65000 Odessa, Ukraine
[e]*German Engineering Materials Science Centre (GEMS), Helmholtz-Zentrum Geesthacht*
Max-Planck-Str. 1, D-21502 Geesthacht, Germany
*Corresponding Author: valentinusov67@gmail.com
Received December 14, 2019; revised December 24, 2019; revised January 13, 2020; accepted January 21, 2020

Effect of deformation by extrusion, rolling after extrusion (in combination with annealing and changing the rolling direction), and subsequent alternating bending (AB) with the number of cycles 0.5, 1, 3, and 5 on the elastic modulus (E), damage accumulation parameter (damage parameter ω), crystallographic texture, and substructure parameters of the binary Mg-5%Li alloy have been studied. The damage parameter ($0 \le \omega \le 1$), which is interpreted as the relative reduction in the effective load-bearing cross-sectional area due to damage accumulation, was found by the change in the elastic modulus after various above types of deformation. At this, we used to compare equivalent deformation and equivalent elastic energy models. The substructure parameters (crystalline domains sizes D, lattice distortion ε, dislocation density ρ) were estimated by analyzing the physical broadening of the lines diffraction on the crystal lattice of studied alloy of the penetrating hard X-ray synchrotron radiation. It was found that in the studied alloy, sheet forms a texture, at which the hexagonal prism axis is 90° deviated from the normal direction (ND) to the sheet up to transverse direction (TD) after extrusion of the ingot at 350°C in combination with its further rolling in the direction of extrusion axis (rolling direction RD) to a thickness of 4.5 mm and annealing at 350°C after each pass. At this the crystallographic directions ⟨11$\bar{2}$0⟩ and ⟨10$\bar{1}$0⟩ coincide with RD. The texture, at which the hexagonal prism axis is deviated from ND to TD by angles ranging from 15 to 70° (unlike from texture of basal type of the pure magnesium) is formed after further rolling of studied alloy to a thickness of 1 mm with the changing of the RD on 90° in combination with annealing at 350°C after each pass. The crystallographic direction ⟨21$\bar{3}$1⟩ coincides with RD. The anisotropy of above mentioned characteristics was found. Correlation and regression analysis showed that the anisotropy and the values of E, D, ε, and ρ, are decreased, and the values of ω are increased with an increase of alternating bend cycles' number. It is shown that changes in the above characteristics are mainly due to the crystallographic texture formed during thermomechanical processing and subsequent alternating bending of Mg-5%Li alloy sheets, which is confirmed by data of correlation and regression analysis.
KEYWORDS: extrusion, rolling, alternating bending, texture, anisotropy, Young's modulus, damage parameter, substructure.

Magnesium and its alloys have recently attracted scientific and practical interest due to the increased demand for weight loss in a number of industries such as automotive, aerospace. Low density and high specific strength are the basis for such interest [1]. However, pure magnesium and its usual alloys with aluminum and zinc of the AZ31 type exhibit insufficient formability during stamping and deep drawing [2]. It is known that magnesium shows a pronounced anisotropy of mechanical properties after deformation. Anisotropy of the mechanical properties arises mainly due to the pronounced texture, which develops during plastic deformation, which is typical for metals with a hexagonal crystal structure. Moreover, in the production of sheet material, texture can, in principle, affect the production process and the resulting mechanical properties. The deformation behavior of hexagonal metals as a whole significantly complicates the variety of possible deformation mechanisms, such as basic, prismatic, pyramidal sliding and a number of twinning modes. In addition, activation of deformation mechanisms depends on the *c/a* ratio [3]. Thus, there is a need for the development of new magnesium alloys with high corrosion resistance and good mechanical properties. It was shown that alloying magnesium with a small amount of lithium can significantly increase the ductility and corrosion resistance even in an alloy with a hexagonal lattice [4].

Usually, sheet and rolled metal would be straightened by roller straightening machines before use in order to reduce residual stresses and increase flatness [5]. In the process of straightening, sheet metal is subjected to alternating tensile deformation of the convex side and compression on the concave side of the sheet due to alternating bending (AB). Significant changes in the microstructure and texture occur during the AB process, despite a slight deformation [6]. The crystallographic texture formation in Mg – 5% Li (wt) alloy sheets was studied in [6], after the ingot extrusion and subsequent rolling at a change in direction, as well as the effect of the subsequent AB on the microstructure, texture and anisotropy of mechanical properties. It was found that the intensity and scattering of the texture depend on AB

cycles number. The most significant changes in texture were observed after 3…5 cycles of AB. Texture changes affected the anisotropy of mechanical properties. Regular changes in the anisotropy of both mechanical properties and the microstructure, represented by equiaxed grains containing twins, occur during alternating bending.

At the same time, it is not investigated the tendency to destruction of Mg-5%Li alloy sheets obtained as a result of deformation by extrusion and subsequent rolling with a change in direction and further alternating bending. As was mentioned above, the alternating bending is used to increase flatness and reduce of residual stresses in the sheet metal before its use. In this case, sub- and microdefects accumulate in the metal during deformation: point (vacancies and interstitial atoms), linear (dislocations), surface (submicrocracks), bulk (micropores). Association of these defects during the increase in deformation leads to formation of microcracks, which are combined into the main crack that can lead to failure [7, 8].

The damages accumulation concept of the continuum mechanics turned out to be promising for describing the macroscopic behavior of a material during deformation. To characterize the accumulation of damage, the so-called damage parameter ω is used, which was proposed already in the early works of Kachanov [7] and Rabotnov [8], and is also being developed in our time [9 - 11].The damage parameter $0 \leq \omega \leq 1$ characterizes the totality of microstructural changes in the material caused by the appearance and accumulation of microdefects under operational loads. The damage parameter is interpreted as the relative reduction in the effective load-bearing cross-sectional area due to the accumulation of damages. Material degradation is caused by a gradual decrease in the effective area, which actually bears tensile loads and determines the tensile strength of the sample. With this interpretation, the damage parameter can be represented as follows:

$$\omega = \frac{(S - S_0)}{S_0}, \qquad (1)$$

where S_0 and S is the cross-sectional area of the intact sample and the current cross-sectional area of the tested sample, respectively; $(S_0 - S)$ is the area occupied by microvoids and microcracks.

The damage parameter can be obtained by measuring of elastic modulus changes, with this interpretation. According to the hypothesis of equivalent deformation [9], the damage parameter ω can be found from the relation

$$\omega = \frac{1 - E}{E_0}, \qquad (2)$$

where E_0 and E are the elastic modulus of the intact sample and the current modulus value of the tested sample, respectively.

If we use the model of equivalent elastic energy [10], then we can define ω as a tensor of the fourth rang

$$\omega = 1 - \left(\frac{E}{E_0}\right)^{1/2} \qquad (3)$$

Only one component of the tensor in (3) is nonzero for uniaxial tension [11]. The damage parameter ω can be found at the uniaxial tension by changing the elastic characteristics, taking into account the representative element of the volume of orthotropic symmetry. It means that the most complex anisotropy that can be represented is orthotropic. The effective elastic properties remained orthotropic with good accuracy even with a high density of interacting cracks, as was shown by the micromechanical analysis [7]. As it was experimentally shown in [12], an assessment of the damage parameter based on the Lemaitre equivalent deformation model [9] gives higher values of the damage parameter compared to models based on the equivalent elastic energy pattern [10, 11] and which give very similar numerical values. Therefore, the assessment of the damage parameter ω according to (3) is the best in comparison with (2) when analyzing the anisotropy of damage to sheet material [12].

The crystallographic texture, which is formed in the process of plastic deformation, also has a significant effect on the accumulation of structural defects and, accordingly, damages [13].

At the same time, the lack of sufficient physical justification of the models (kinetic equations) gives rise to ambiguity in experimental estimates of the damage parameter ω, depending on the method of its determination for the same sample of the material under study [12]. The relationship between the damage parameter and the change in the structural state and texture under external influences can still be obtained only on the basis of the corresponding correlation and regression analysis.

Goal of this article is the study of the effect of extrusion processing with followed rolling and alternating bending as well as texture on elastic properties, damage parameter, crystalline domains sizes D, lattice distortion ε, and dislocation density ρ of Mg-5%Li alloy.

MATERIALS AND METHODS

The original cylindrical blanks of the Mg-5%Li alloy were subjected to processing in two successive modes (conditionally I and II).

Processing Mode I. The cylindrical Mg-5% Li ingots with a diameter of 60 mm and a length of 120 mm were extruded at 350°C. Thus slabs 60 mm wide and 6 mm thick were obtained. Then the slabs were rolled in the longitudinal direction to a thickness of 4.5 mm in two passes. Heating to 350°C was conducted after each pass.

Processing Mode II. The alloy strips of 4.5 mm thick obtained after processing in the first mode were rolled then in the transverse direction to a thickness of 2 mm in 10 passes with reduction of 10% per pass. The heating was conducted to 350°C after each pass. Then, the rolling direction changed by 90 ° each time, and thus the sheet was rolled to a thickness of 1 mm with a decrease of about 10% per pass.

The sheets of the investigated alloy, processed in accordance with mode II, were next subjected to straightening by means of the alternating bending. Process of sheets straightening by means of the alternating bending was modeled on a manual three-roller device. The diameter of the bending roller was 50 mm. The metal moving speed at the bending was approximately 150 mm/s. The one cycle consisted of bending in one direction (0.25 cycles), returning to a flat state (0.5 cycles), bending in the opposite direction (0.75 cycles) and straightening (1.0 cycle). Studies were performed after 0.5, 1.0, 3.0 5.0 of AB

Young's modulus was measured dynamically by the frequency of natural bending vibrations of flat rectangular samples 100 mm long and 10 mm wide. The measurement error of Young's modulus did not exceed 1%. [14]. Samples were cut out through every 15° from the rolling direction (RD) up to the transverse direction (TD) from the original sheets processed in accordance with mode II, as well as from the same sheets after 0.5, 1.0, 3.0, and 5.0 cycles of alternating bending. Samples for studying the texture and substructure parameters were also cut out.

We found the damage parameters using changes in the Young's modulus of the processed samples relative to original samples in the corresponding sheet directions according to relations (2) and (3).

Diffraction patterns were recorded to analyze line broadening for defect density description. The high energy materials science beamline HEMS@Petra III /Hasylab DESY (Hamburg-Germany) equipped with a Perkin-Elmer area detector was used to obtain two-dimensional pattern [15]. Synchrotron radiation with energy of 87 keV and a wavelength of 0.014235 nm a high penetration depth, similar to thermal neutrons [16], allowed the study in the transmission mode. Beam size was 0.5 mm. Calibration of the instrumental set-up, see figure 1, was performed by a LaB_6 standard. The calibration includes determination of the sample to detector distance (0.901m), the wavelength and the instrumental line broadening. The shooting scheme is shown in Fig. 1.
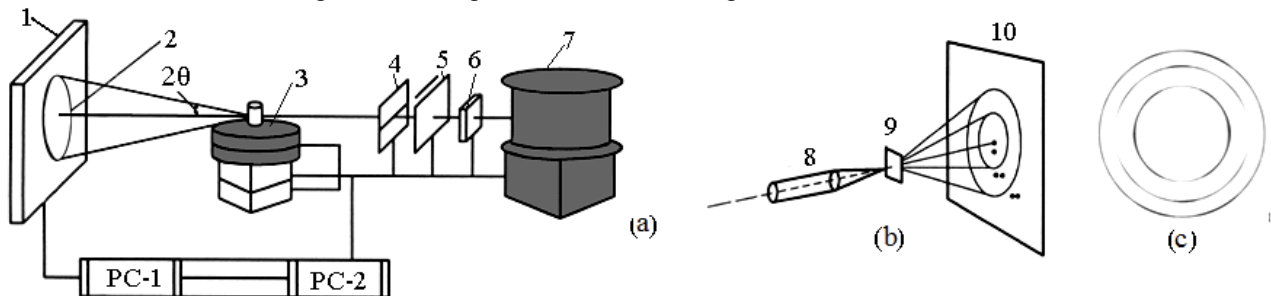

Fig. 1. Sketch of the set-up using synchrotron radiation beam; (a) diffraction pattern measurement; (b) (b) pin whole technique; (c). example of an area detector image; ((a): 2D detector (1); beam stopper (2); sample (3); vertical and horizontal slots, respectively, (4) and (5); a diode (6); monochromator (7); PC1 and PC2 are rotation and displacement devices, respectively. In scheme (b): a monochromatic beam (8); a sample (9), and a detector (10)).

The microstructure parameters (crystalline domains sizes D, values of crystal lattice distortion $\varepsilon = \Delta d_{hkl} / d_{hkl}$, and dislocation density ρ) were calculated using standard 1-dimensional diffraction pattern generated by Fit2D [17] from area detector pictures. The analysis of the line broadening was carried out using the Origin-6G computer program. Crystalline domains sizes D, values of crystalline lattice distortion and dislocation density ρ were estimated by means of Williamson-Hall methods [18, 19].

The texture analysis was performed using the method of inverse pole figures (IPF) on the measurements in the normal direction (ND) to the rolling plane (ND IPF) and the rolling direction (RD IPF) taken on a DRON-3M diffractometer by using of the MoKα radiation in reflection mode from two sides of sheets after the corresponding number cycles of AB. The pole densities of IPF were found from the integrated intensity of the diffraction lines with allowance for the sample without texture. A textureless sample was manufactured from small recrystallized sawdust of the investigated magnesium alloy. The Morris normalization was used, when constructing the IPFs [20].

EXPERIMENTAL RESULTS AND DISCUSSION

Inverse pole figures of the investigated alloy are presented in Fig. 2. The texture of the sheet processed according to I mode is characterized by the presence of a relatively weak basal component (pole density 1.14 in Fig. 2a) and a very strong component $\langle 10\bar{1}0 \rangle$ (pole density 6.64 in Fig. 2a). This corresponds to the texture, at which the normal to the basal plane (0001) is deflected by 90° to the TD. In this case, the rolling direction of such a sheet coincides mainly with the crystallographic directions $\langle 11\bar{2}0 \rangle$ with scattering up to $\langle 10\bar{1}0 \rangle$ (Fig. 2b). The addition of lithium to magnesium changes the balance of the deformation mechanisms, which in turn affects the texture.

Fig. 2c, d is showed the ND IPF and RD IPF of the alloy under study after treatment in the mode II. It can be seen that the hexagonal prism axis is deviated from ND on about 15 to 70^0 towards the TD, in contrast to the basal rolling texture of pure magnesium. The crystallographic direction $\langle 21\bar{3}1\rangle$ (pole density 3.70) coincides mainly with the RD (Fig. 2d). At the same time, it should be noted that the region of increased pole density on inverse pole figure of the rolling direction occupies a rather wide region between poles $\langle 30\bar{3}2\rangle$, $\langle 11\bar{2}0\rangle$ and $\langle 10\bar{1}0\rangle$.
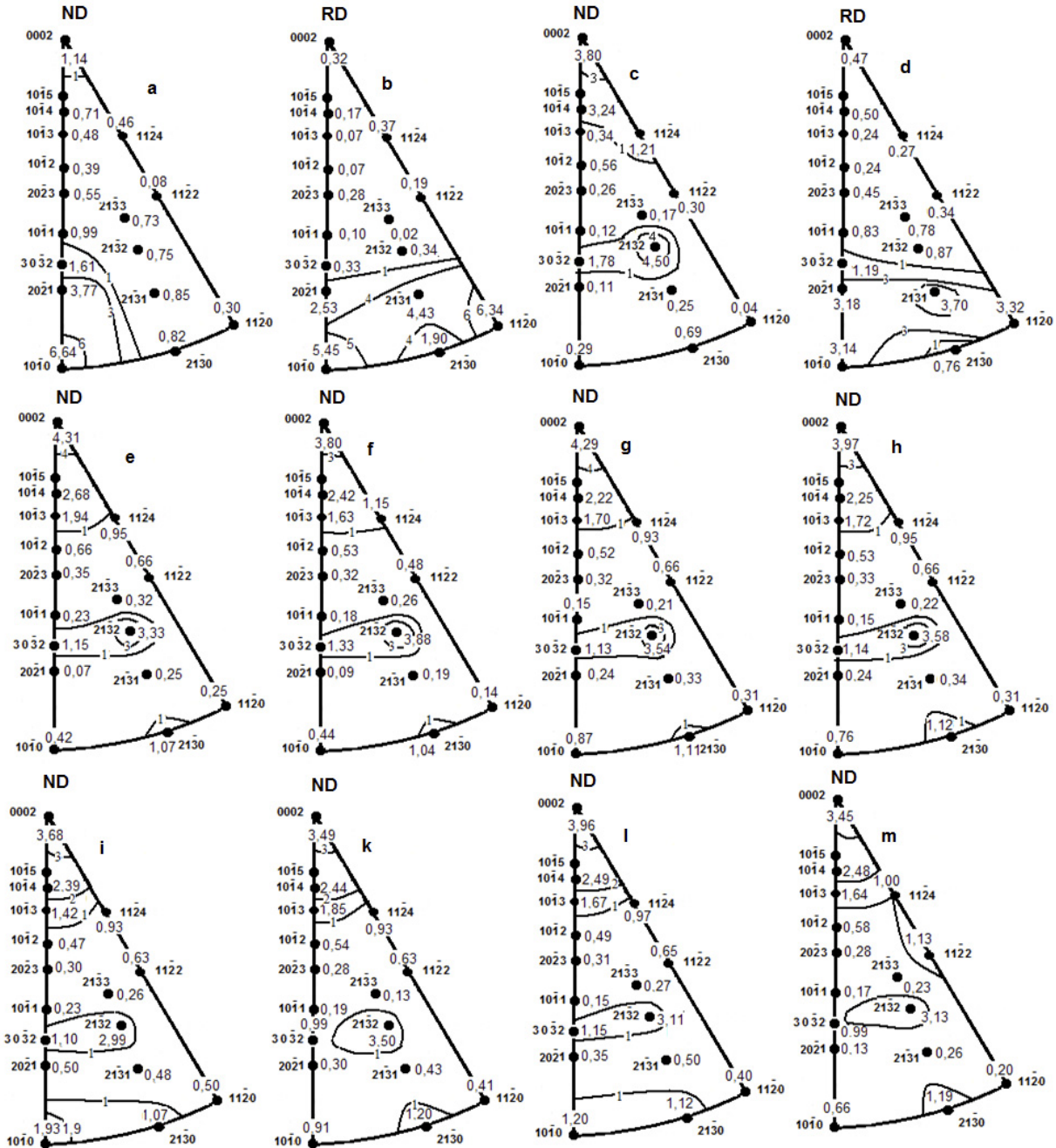
Fig. 2. Experimental inverse pole figures of alloy Mg-5% Li: (a, b) are after extrusion and rolling in longitudinal direction (Proceeding Mode I); (c, d) are extrusion and rolling with changing direction (Proceeding Mode II), (e–m) are after processing in accordance with the mode II and subsequent alternating bending using different number of cycles: 0.5 (e, f); 1.0 (g, h); 3.0 (i, k), and 5.0 (l, m) cycles. (f, h, k, m) correspond to the stretched side of the sheet; (e, g, i, l) correspond to the compressed side of sheets of alloy

Doping of magnesium with lithium reduces the *c/a* axis ratio and thereby activates not basal sliding mechanisms. In particular, at elevated temperatures, the role of the prismatic <*a*> slip of dislocations in Mg-Li alloys can be significant [4]. Formation of the texture components of the basal type deviated up to the TD is probably facilitated by activation of the prismatic <*a*> slip, as well as twinning (Fig. 3).

The type, nature and degree of texture scattering after alternating bending depends on the cycle's number of alternating bending, as mentioned above. A more detailed description of the texture and microstructure after the AB can be found in [6].

Fig. 3. Microstructure of Mg-5%Li alloy machined by Proceeding Mode I

The integrated diffraction spectra of the Mg-5% Li alloy treated in according with the processing mode II, as well as after a different number of cycles of alternating bending are shown in Fig. 4.
Lattice distortion is evaluated usually on the basis of the classical Williamson-Hall method [18]. This method gives good results in the absence of anisotropy of the broadening of diffraction lines.

Anisotropy of the physical broadening of the diffraction lines due to the crystallographic texture of the samples in the studied alloy (Fig's. 2, 4) was found. Therefore, further analysis was performed using the modified Williamson – Hall method [19]. The method for processing the width of diffraction peaks makes it possible to estimate the dislocations density. Assuming that the strain broadening of the lines is due to dislocations and that the average dislocation contrast factor $(\overline{C})$ is known, the full width at half maximum (FWHM) of the X-ray diffraction peak (XRD) with allowance for instrumental correction and correction for absorption can be represented using a modified equation Williamson – Hall as follows [19]:

$$\text{FWHM} = \frac{0{,}9}{D} + \frac{(\pi M^2 b^2)}{2}\rho^{1/2}\left(K\overline{C}^{1/2}\right)^2 + O\left(K\overline{C}^{1/2}\right)^4 \tag{6}$$

Here D, b, and ρ are, respectively, the crystalline domain size, the absolute value of the Burgers vector of the dislocation, and the dislocations density. So called dislocation arrangement parameter M is depended on the outer effective cut-off radius of dislocations, $K = (2\sin\theta)/\lambda$, θ is the diffraction angle, λ is the radiation wavelength, O is the highest order of the value $K\overline{C}^{1/2}$.

For the convenience of further analysis, we introduce the following notation:

$$\text{FWHM} = y; \ (0.9/D) = C; \ [\frac{(\pi M^2 b^2)}{2}\rho^{1/2}] = B; \ \left(K\overline{C}^{1/2}\right)^2 = x; \ O\left(K\overline{C}^{1/2}\right)^4 = Ax^2$$

The relation (6) takes such form at the new notation:

$$y = C + Bx + Ax^2 \tag{6a}$$

In metals and alloys with a hexagonal lattice, one should take into account the manifold of 11 different slip systems and the corresponding Burgers vectors [21]. They can be divided into three main slip systems with the following Burgers vectors: $b_1 = 1/3\langle 11\bar{2}0\rangle$ ($\langle a\rangle$ type), $b_2 = \langle 0001\rangle$ ($\langle c\rangle$ type) and $b_3 = \langle 11\bar{2}3\rangle$ ($\langle c + a\rangle$ type). The average dislocation contrast factor $(\overline{C})$ for various slip systems during deformation of pure magnesium can be determined from [21]. However, as mentioned above, alloying magnesium with lithium leads to the change as the c/a ratio as well the elastic constants magnitude. So for pure magnesium $(c/a) = 1.624$ [22]. For the studied alloy Mg-5%Li $c/a = 1.610$, according to our data.

The elastic constants of the Mg-5%Li alloy were calculated by us earlier [23]. The results are shown in Table 1.

Table 1

Elastic modules of single crystal of Mg-5%Li alloy

Elastic modules of single crystal of Mg (mass) 5 % Li alloy, GPa				
C11	C12	C13	C33	C44
51.2	20.1	17.1	64.7	19.8

The average values of the parameters of the dislocation contrast of the studied alloy were calculated using the freely distributed computer program ANIZC [24]. For this purpose, we used the elastic constants given in the Table 1.In this case, we took into account the influence of both edge and screw dislocations of the <a>, <a + c>, <c> type in the ratio of 0.6, 0.38, 0.02 respectively [25] for the diffraction lines shown in Fig. 4.
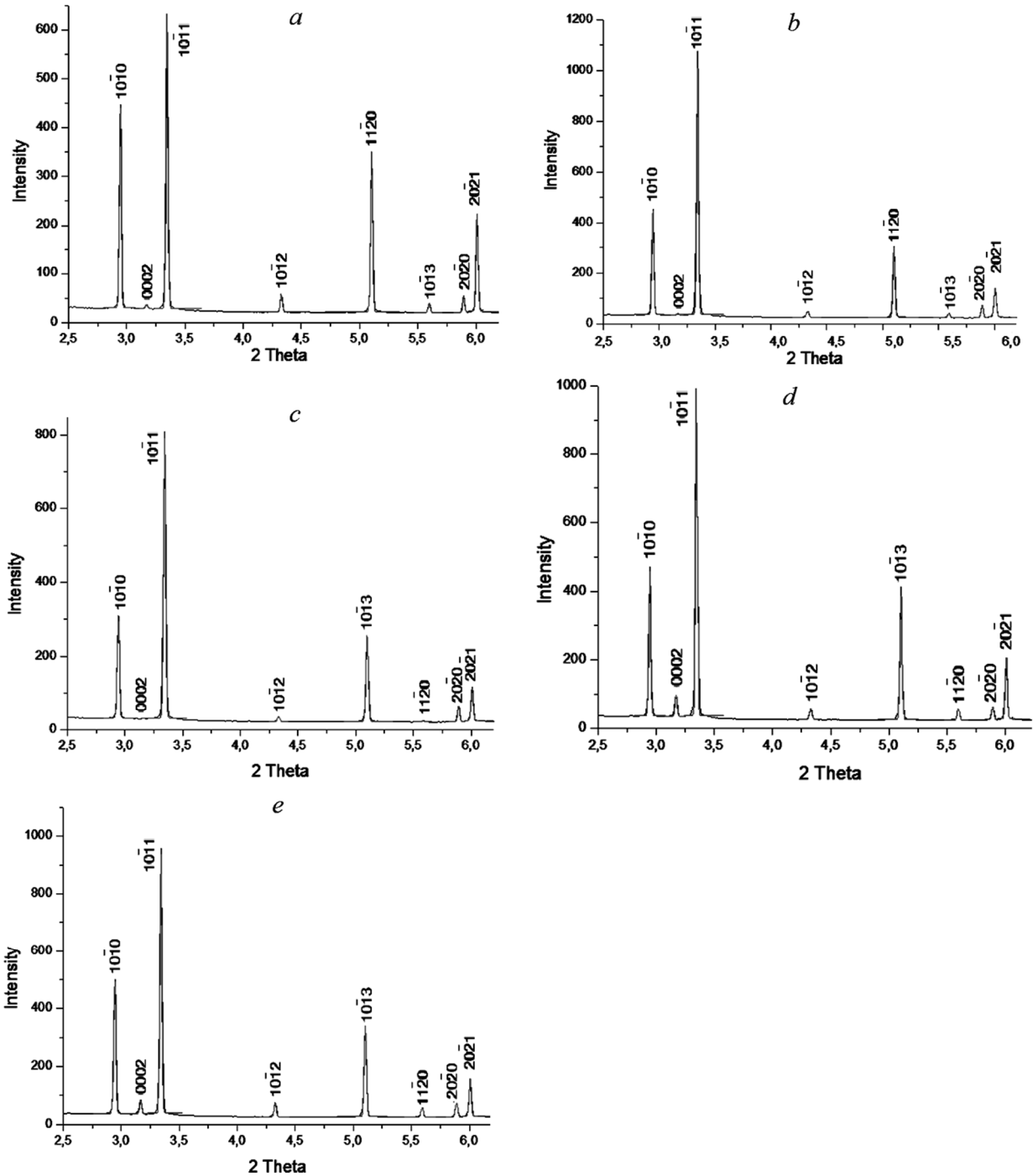

Fig. 4. Integral diffraction spectra of the alloy Mg-5%Li: (a) after treatment by proceeding mode II, extrusion and rolling with changing direction; (b– e) after subsequent alternating bending using various numbers of cycles: 0.5 (b); 1.0 (c); 3.0 (d), and 5.0 (e) cycles

The average value of the Burgers vector of dislocations turned out to be 0.151 nm. In [25] the influence of equal channel angular pressing (ECAP) on the crystalline domains sizes, lattice distortion, and the dislocation density of the AZ91 magnesium alloy were studied. It was shown that the parameter M (6) decreases from 2.5 to 1.6 during processing. We accepted the value of the parameter M equal to 2 to assess the dislocation density of studied alloy Mg - 5% Li (wt).

As a result of our calculations, we obtained the following relationships of type (6a) both for the original samples obtained by processing in modes I and II, and for samples after alternating bending (Table 2).

Table 2

Modified Williamson-Hall Equations for Mg-5%Li alloy

Processing mode	Cycles number of alternating bending	Equations (6a)	Approximation reliability factor R^2
I	0	$y = 0.02184 + 0.0006x + 0.00044x^2$	0.98
II	0	$y = 0.02282 + 0.0055x + 0.00007x^2$	0.98
II	0.5	$y = 0.02487 + 0.00062x + 0.00005x^2$	0.99
II	1.0	$y = 0.02360 + 0.00067x + 0.00001x^2$	0.98
II	3.0	$y = 0.02493 + 0.00074x + 0.00009x^2$	0.99
II	5.0	$y = 0.02554 + 0.00078x + 0.00003x^2$	0.99

If the magnitude of the coefficient B is known, then the dislocation density can be estimated, as this follows from equations (6) and (6a). The results of analysis of the substructure (distortion of the crystal lattice ε, crystallite domains sizes D and dislocation density $ρ$) after processing according to the I and II Modes, and also after different number n of AB cycles are presented in Table 3.

Table 3

Substructure parameters of the Mg-5%Li alloy after various processing

Structure Characteristics	Processing Mode I	Processing Mode II	Alternating bending				
		Cycles number, n					
		0	0,5	1	3	5	
D, nm	41	39	38	37	36	35	
$ε×10^{-4}$	5.86	2.03	2.31	2.39	2.91	3.15	
$ρ×10^{14}$, m^{-2}	2.19	2.11	2.51	3.13	3.82	4.25	

The sizes of the crystalline domains D decrease, while the lattice distortion ε and the dislocation density ρ increase with increasing of the cycle number of alternating bending (Table 3). Strong correlations take places between the value of the substructure parameters of the alloy processed according to mode II and the number n of AB cycles. The corresponding regression equations and approximation reliability coefficients have the form:

$$D = 0.014n^2 − 1.44n + 38.73; R^2 = 0.96, \tag{7}$$

$$ε × 10^{-4} = −0.034n^2 + 0.386n + 2.063; R^2 = 0.99; \tag{8}$$

$$ρ × 10^{14} = −0.087n^2 + 0.831n + 2.232; R^2 = 0.98 \tag{9}$$

Table 4 presents values of the elastic modulus E in different directions of the sheets of the alloy under study and the anisotropy coefficients η after processing according to mode II as well as after different number of cycles of the subsequent alternating bending. The value of anisotropy coefficients η can be found by the ratio:

$$η = [(F_{max} − F_{min})/F_{min}] · 100\%, \tag{10}$$

where F is the value of the corresponding property.

The directionally averaged values of the elastic modulus E decrease with an increase in the number of AB cycles (Table 4). The analysis showed that there is a strong correlation between the directionally averaged elastic modulus values E and the number n of AB cycles. The corresponding regression equation and approximation reliability coefficient have the form:

$$E_{av} = 0.29n^2 − 2.30n + 50.96; R^2 = 0.85 \tag{11}$$

To study the effect of alternating bending on the damage parameter ω, we assume that the samples of the studied alloy immediately after treatment in the mode II have not damages and are characterized by elastic modules E_0, and after the corresponding number of AB cycles, the samples are characterized by elastic modules E.

Valentin Usov, Heinz-Günter Brokmeier et al.

Table 4

Modules of elasticity (*E*) and coefficients of anisotropy (η) after various treatment of Mg-5%Li alloy sheets

Angle with rolling direction	Processing mode									
	Processing mode II (0)		Alternating bending cycles number							
			0.5		1.0		3.0		5.0	
	E, GPa	η, %	*E*, GPa	η, %	*E*, GPa	η, %	*E*, GPa	η, %	*E*, GPa	η, %
0	50.3		48.2		46.8		44.2		46.2	
15	50.6		48.1		46.8		45.3		46.1	
30	51.3		48.0		47.1		47.9		46.2	
45	52.1	5.2	48.2	3.3	49.5	10.9	49.4	11.8	46.2	3.3
60	52.6		48.7		51.0		49.1		46.7	
75	52.8		49.3		51.1		47.2		47.3	
90	52.9		49.6		51.9		46.2		47.6	
Average value	51.8	5.2	48.6	3.3	49.2	10.9	47.0	11.8	46.6	3.3

The values of the damage parameter ω according to relations (2) and (3) are presented in Tables 5 and 6.

The analysis showed that there are strong correlations between the damage parameters ω_1 and ω_2 averaged over the directions in sheets of the investigated alloy, on the one hand, and the number of AB cycles, on the other hand (Tables 5, 6).

Table 5

Damage parameters ω_1 and anisotropy coefficients after various processing of Mg-5%Li alloy sheets

Angle with rolling direction	Processing mode									
	Alternating bending cycles number									
	Processing mode II (0)		0.5		1.0		3.0		5.0	
	$\omega_1 = 1 - E/E_0$	η, %	ω_1,	η, %	ω_1	η, %	ω_1	η, %	ω_1	η, %
0			0.042		0.070		0.121		0.082	
15			0.049		0.075		0.105		0.089	
30			0.06.4		0.082		0.066		0.099	
45	0	0	0.07.5	79	0.050	332	0.052	144	0.113	38
60			0.074		0.030		0.067		0.112	
75			0.067		0.032		0.106		0.104	
90			0.062		0.019		0.127		0.100	
Average value ω_1	0	0	0.062	79	0.051	332	0.092	144	0.100	38

Table 6

Damage parameters ω_2 and anisotropy coefficients after various processing of Mg-5%Li alloy sheets

Angle with rolling direction	Processing mode									
	Alternating bending cycles number									
	Processing mode II (0)		0.5		1.0		3.0		5.0	
	$\omega_2 = 1 - \left(E/E_0\right)^{1/2}$	η, %	ω_2	η, %	ω_2	η, %	ω_2	η, %	ω_2	η, %
0			0.021		0.035		0.063		0.042	
15			0.025		0.038		0.054		0.046	
30			0.033		0.042		0.034		0.051	
45	0	0	0.038	81	0.025	340	0.026	149	0.058	40
60			0.038		0.015		0.034		0.058	
75			0.034		0.016		0.055		0.054	
90			0.032		0.009		0.065		0.051	
Average value ω_2	0	0	0.032	81	0.026	340	0.047	149	0.051	40

The corresponding regression equations and approximation reliability coefficients R^2 have the form:

$$\omega_1 = -0.005n^2 + 0.044n + 0.016; \ R^2 = 0.85, \tag{12}$$

$$\omega_2 = -0.002n^2 + 0.022n + 0.008; \ R^2 = 0.86. \tag{13}$$

The value of the damage parameter averaged over all directions in the sheets, increases with an increase in the number of AB cycles to 5 in accordance with relations (12) and (13). Anisotropy of the both elastic modulus and damage parameters takes place, both in the original sheet processed according to the mode II and after alternating bending (Tables 4-6).

The anisotropy of the elastic modulus reaches its maximum value after 3 cycles of AB. Anisotropy coefficients of the damage parameters are maximal after 1 cycle of AB. Minimum of the anisotropy is observed after 5 cycles of AB (Tables 4-6).

The effect of the crystallographic texture on the anisotropy of elastic properties, as well as of lattice distortion, crystalline domains sizes, dislocation density and damage parameters after the corresponding number of alternating bending cycles can be established by comparing the values of the above properties in different sheet directions with the pole density values at the corresponding inverse pole figures for the normal direction (ND IPFs). Changes in the texture can be described quantitatively by a change in the normalized values of the pole density exceeding 1 (which corresponds to a sample without texture) on the IPF ND (Fig. 2). We assume that only crystallite orientations whose normalized pole density is greater than unity contribute to the anisotropy of properties. In this case, it is necessary to renormalize the pole density taking into account only the above orientations.

For this purpose, first we average the values of the pole density (exceeding 1) on the ND IPF's obtained for two sides of the sheets after each number of cycles of alternating bending (Fig. 2). Sums of the average values of the above pole densities we use as normalization factors $\sum P_{hkil}^{av}$ for the corresponding number of cycles to determine the relative contribution to the texture of each of the above P_{hkil}^{av} for each number of cycles. For this, we find the relations $P_{hkil}^{av}/\sum P_{hkil}^{av}$ for the corresponding number of AB cycles. In principle, the last relation has the sense of the volume fraction of the corresponding texture component in the above approximation.

The contribution of each texture component to the corresponding properties we will taken into account in the form of sums of the products P_{hkil}^{av} on its volume fraction of $P_{hkil}^{av}/\sum P_{hkil}^{av}$, i.e. $\sum \left(P_{hkil}^{av} \times (P_{hkil}^{av}/\sum P_{hkil}^{av}) \right)$. We will call them "relative normalized values of the pole density" P_{rel}. These values are summarized in the Table 7.

Table 7

Normalized values of pole densities exceeding 1 on the IPF ND

Cycles number	0	0.5	1.0	3.0	5.0
P_{rel}	3.43	2.92	2.89	2.51	2.53

The analysis showed that there are significant correlations between the P_{rel} values (Table 7), on the one hand, the crystalline domains sizes D, the lattice distortion ε, the dislocation density ρ (Table 3), the elastic modulus E_{av} averaged over the direction in the sheets of the studied alloy (Table 4) and damage parameters ω_1, ω_2 (Tables 5, 6), on the other hand.

The corresponding regression equations and approximation reliability coefficients have the form:

$$D = -2.40P_{rel}^2 + 18.11P_{rel} + 5.08; \ R^2 = 0.90 \tag{14}$$

$$\varepsilon \cdot 10^{-4} = 1.22P_{rel}^2 - 8.37P_{rel} + 16.35; \ R^2 = 0.95 \tag{15}$$

$$\rho \cdot 10^{14} = 1.48P_{rel}^2 - 100.95 + 22.20; \ R^2 = 0.93 \tag{16}$$

$$E = -0.19P_{rel}^2 + 4.32P_{rel} - 34.70; \ R^2 = 0.98 \tag{17}$$

$$\omega_1 = -0.007P_{rel}^2 - 0.058P_{rel} + 0.293; \ R^2 = 0.98 \tag{18}$$

$$\omega_2 = -0.004P_{rel}^2 - 0.025P_{rel} + 0.142; \ R^2 = 0.97 \tag{19}$$

Kearns texture coefficients are often used to quantify the texture of hexagonal materials [26]. These coefficients f_j (the index j means the corresponding direction in the sample (ND, RD or TD) express the degree of directivity of the

c-axes of the crystalline HCP cell of grains with a given geometric direction in the polycrystalline material and can be found from the inverse pole figure by the ratio [27]:

$$f_j = \langle cos^2 \alpha_i \rangle_j = \sum_i A_i P_{ji} cos^2 \alpha_i \qquad (20)$$

Where $P_{ji} = \frac{I_i/I_R}{\sum_\Delta (A_i \cdot I_i/I_R)}$; I_i/I_R is the ratio of the integrated intensity I_i of *i*-th reflection at the *j*-th IPF to the corresponding value for the sample without texture I_R; A_i are the statistical weights of the *i* reflection $(\sum A_i P_{ji} = 1)$ [20]; α_i is the deviation angle of the *i*-th crystallographic direction of the c axis the *j* direction in the sample.

To find the Kearns texture coefficients by equation (20), we used the IPF in Fig. 2, the values of A_i taken from [28]. We calculated the angles α_i according to well-known formulas using the above mentioned $c/a = 1.61$ ratio for Mg-5% Li alloy.

The Kearns texture coefficients calculated by ND IPF (f_{ND}) and by RD IPF (f_{RD}) for the sheets obtained by processing in the Mode I were, respectively, 0.232 and 0.142. Kearns texture coefficients (f_{ND}) and (f_{RD}) of the original alloy sheet processed by mode II are shown in Table 8. In Table 8 are also shown the Kearns texture coefficients calculated by the ND IPF of both sheets sides ($f_{ND}^{(1)}$, $f_{ND}^{(2)}$), as well as after averaging by two sides sheets alloy ($f_{ND}^{(av)}$) after various number of alternating bending cycles.

Table 8

The Kearns texture coefficients calculated from the IPF data in Fig. 2.

Processing Mode II													
Alternating bending													
Cycles number													
0		0.5			1.0			3.0			5.0		
f_{ND}	f_{RD}	$f_{ND}^{(1)}$	$f_{ND}^{(2)}$	$f_{ND}^{(av)}$	$f_{ND}^{(1)}$	$f_{ND}^{(2)}$	$f_{ND}^{(av)}$	$f_{ND}^{(1)}$	$f_{ND}^{(2)}$	$f_{ND}^{(av)}$	$f_{ND}^{(1)}$	$f_{ND}^{(2)}$	$f_{ND}^{(av)}$
0.390	0.393	0.435	0.407	0.421	0.409	0.388	0.398	0.399	0,411	0.404	0.417	0.411	0.414

The mismatches in the distribution of pole density at the ND pole figures of the opposite sheets sides after the corresponding number of cycles of alternating bending were revealed, as can be seen in fig. 2 (e – m). This is due to the fact that on the convex side, the surface layers of the sample undergo tensile deformation (Fig. 2 f, h, k, m), while the layers on the opposite side of the sheet undergo compression deformation (Fig. 2, e, g, i, l). During extension, on the contrary, the metal layers on the convex side of the sheet undergo compression deformation, while the metal layers on the concave side of the sheet experience tensile deformation. Similar discrepancies were found earlier in the work [27] at the investigation of the crystallographic texture of Zr-2.5% Nb alloy strip. The strip was obtained by straightening part of the pipe after cut along axis. Discrepancies in the distribution of pole density on the ND IPFs of the opposite sides of the sheets of the alloy under study after a different number of alternating bending cycles naturally reflected on the values of the corresponding Kearns texture coefficients (Table 8).

The Kerns texture coefficient f_{ND} of the studied alloy original sheet processed according to Mode II, as well as the average Kerns texture coefficients f_{ND}^{av} after a different number of alternating bending cycles (Table 8), we used to further analyze their relationship with the sizes of the crystalline domains D, of the crystal lattice distortion ε, dislocation density ρ (Table 3), as well as with the averaged by the sheet directions Young's modulus E (Table 4) and damage parameters ω_1 and ω_2 after the corresponding number of alternate bending cycles (Table 5, 6).

The analysis showed that there are significant correlations between the f_{ND}^{av} values (Table 8), on the one hand, the crystalline domains sizes D, the lattice distortion ε, the dislocation density ρ (Table 3), the elastic modulus E_{av} averaged over the direction in the sheets of the studied alloy (Table 4) and damage parameters ω_1, ω_2 (Tables 5, 6), on the other hand.

The corresponding regression equations and approximation reliability coefficients have the form:

$$D = 10880 \left(f_{ND}^{(av)} \right)^2 - 8865,7 f_{ND}^{(av)} + 1841,5; \quad R^2 = 0.97 \qquad (21)$$

$$\varepsilon \cdot 10^{-4} = -3192,8 \left(f_{ND}^{(av)} \right)^2 + 2607,2 \, f_{ND}^{(av)} - 529,3; \quad R^2 = 0.79 \qquad (22)$$

$$\rho \cdot 10^{14} = -69045,5 \left(f_{ND}^{(av)} \right)^2 + 5024,4 \, f_{ND}^{(av)} - 1142; \quad R^2 = 0.85 \qquad (23)$$

$$E = 13430,0 \left(f_{ND}^{(av)} \right)^2 - 11010,0 + 2303,1 \quad R^2 = 0.97 \qquad (24)$$

$$\omega_1 = -257,6 \left(f_{ND}^{(av)} \right)^2 + 211,3 f_{ND}^{(av)} = 43,2; \quad R^2 = 0.97 \qquad (25)$$

$$\omega_2 = -130,8 \left(f_{ND}^{(av)} \right)^2 + 107,2 f_{ND}^{(av)} - 21,93; \quad R^2 = 0.97 \qquad (26)$$

CONCLUSION

It was studied the effect of the processing regime I (deformation by extrusion, rolling after extrusion in combination with annealing), as well as the effect of successive regime II (strips after processing in accordance with the regime I, were rolled further in combination with annealing and changing the direction of rolling) on the texture, .substructure characteristics (crystalline domains sizes, lattice distortions, and dislocation density) of the Mg-5 % Li (wt.) alloy sheets.

It was found that after the Mg-5% Li alloy treatment in accordance with regime I, a texture is formed in the sheets, at which the axis of the hexagonal prism is 90° deflected from ND to TD. The crystallographic directions $\langle 12\bar{2}0 \rangle$ and $\langle 10\bar{1}0 \rangle$ coincide with RD. In that case the crystalline domains size D = 41 nm, lattice distortions value ε =5.86 $\cdot$ 10^{-4}, and dislocation density ρ =2.19 $\cdot$ $10^{14} m^{-2}$.

After the Mg-5% Li alloy treatment in accordance with regime II, a texture is formed in the sheets, at which the axis hexagonal prism is deviated from ND to TD by angles ranging from 15 to 70^0, in contrast to the texture of basal type after rolling of the pure magnesium. The crystallographic direction $\langle 21\bar{3}1 \rangle$ coincides with RD. In that case the crystalline domains size D = 39 nm, lattice distortions value ε =2.03 $\cdot$ 10^{-4}, and dislocation density ρ =2.11 $\cdot$ $10^{14} m^{-2}$.

The effect of subsequent alternating bending of the Mg-5 % Li (wt.) alloy sheets processed in accordance with regime II on texture, substructure characteristics (crystalline domains sizes, lattice distortions, and dislocation density), elastic properties and damage parameters of sheets has been also studied. It was found that values of crystalline domains sizes D and elastic modulus E averaged over all directions in the sheets are decreased, and magnitudes of lattice distortion ε, dislocation density ρ, and damage parameters ω are increased with increasing numbers cycles of alternating bending. The character of changes can be described by the corresponding regression equations (7) - (9) and (11).

It is observed the anisotropy of the both elastic modulus and damage parameters, both in the original sheet processed according to the mode II and after alternating bending. The anisotropy of the elastic modulus reaches its maximum value after 3 cycles of the alternating bending. Anisotropy coefficients of damage parameters are maximal after 1 cycle of alternating bending. Anisotropy minimums of the elastic modulus and damage parameters are observed after 5 cycles of the alternating bending.

Changes in the values of crystalline domains sizes D, lattice distortion ε, dislocations density ρ, elastic modulus E, and damage parameters ω are mainly due to the crystallographic texture formed during thermomechanical processing and cycle's number of subsequent alternating bending of sheets. The corresponding regularities have been described by regression equations (14) - (19), as well as (21-26).

ORCID IDs
Valentin Usov https://orcid.org/0000-0001-7855-5370, **Heinz-Günter Brokmeier** https://orcid.org/0000-0002-8808-1313,
Nataliia Shkatulyak https://orcid.org/0000-0003-4905-001X, **Elena Savchuk** https://orcid.org/0000-0002-4249-6505

REFERENCES
[1] Z. Yang, J.P. Li, J.X. Zhang, G.W. Lorimer, and J. Robson, **21(**5) 313-326 (2008), https://doi.org/10.1016/S1006-7191(08)60054-X
[2] L. Ruihong, P. Fusheng, B. Jiang, D. Hanwu and Y. Qingshan, Materials Science & Engineering A, **562**, 33–38 (2013), http://dx.doi.org/10.1016/j.msea.2012.11.032
[3] K. Alaneme, and E. Okotete, Journal of Magnesium and Alloys, **5** (4), 460-475, (2017), https://doi.org/10.1016/j.jma.2017.11.001
[4] H. Hafekamp, M. Niemeyer, R. Bohem, U. Holzkamp, C. Jaschik and V. Kaese, Material Science Forum, **350-351**, 31-42 (2000). https://doi.org/10.4028/www.scientific.net/MSF.350-351.31
[5] Methods of leveling sheet metal https://blog.arku.com/us/methods-of-leveling-sheet-metal/
[6] N. Shkatulyak, S. Smirnova, and V. Usov, Hindawi Publishing Corporation, International Journal of Metals, Article ID 349810, 8 pages, (2015). http://dx.doi.org/10.1155/2015/349810.
[7] L.M. Kachanov, *Основы механики разрушения [Fundamentals of fracture mechanics]*, (Nauka, Moscow, 1974), 312 p. https://lib-bkm.ru/13776 [in Russian].
[8] Y.N. Rabotnov, *Избранные произведения. Проблемы механики деформируемого твердого тела* [*Selected works. Problems of the mechanics of a deformable solid*], (Nauka, Moslow, 1991, 196 p.) [in Russian].
[9] J. Lemaitre, R. Desmorat, and M. Sauzay,. *Eur. J. Mech. A,* **19 (**2), 187-208, (2000). https://www.sciencedirect.com/science/article/pii/S0997753800001613
[10] N.R. Hansen, and H. L. Schreyer, Int. J. Solid. Structures, **31** (3), 359-389, (1994). https://kopernio.com/viewer?doi=10.1016/0020-7683(94)90112-0&token=WzM3NTM2LCIxMC4xMDE2LzAwMjAtNzY4Myg5NCk5MDExMi0wIl0.IbXai4W6T9jPyaO_4p_S86QIzV8
[11] C.L Chow, and J. Wang, International Journal of Fracture, **33**, (1) 3-16, (1987), https://link.springer.com/article/10.1007/BF00034895.
[12] M. Bobyr, O. Khalimon, and O. Bondarets, Journal of Mechanical Engineering NTUU «Kyiv Polytechnic Institute», 67, 5-13, (2013). http://nbuv.gov.ua/UJRN/VKPI_mash_2013_67_3
[13] V.V. Usov, and N.M. Shkatulyak, Russian Physics Journal, **47**, (11), 1139-1146, (2004), https://www.researchgate.net/publication/226984093_Fractal_nature_of_the_dislocation_structure_of_low-alloyed_steel_after_controlled_rolling
[14] Technical Review ITC-ME/ATCP (2010). http://www.atcpndt.com/images/products/sonelastic/articles/RT03-ATCP.pdf.
[15] H.-G. Brokmeier, S. Yil, N. Park and J. Homeyer. Electron Resource, Solid State Phenomena **105**, 55–60, (2005), http://www.scientific.net/SSP.105.55

[16] H.-G. Brokmeier, Sangbong Yi, Textures in Engineering Materials: From Fundamentals to Applications, in Neutrons and Synchrotron Radiation in Engineering Materials Science, (2017) pp.55-72, Wiley-VCH

[17] FIT2D: An introduction Overview. http://www.esrf.eu/computing/scientific/FIT2D/FIT2D_INTRO/fit2d.html

[18] G. Williamson and W. Hall Acta metallurgica, **1**(1), 22-31 (1953). http://www.xray.cz/xray/csca/kol2011/kurs/Dalsi-cteni/clanky/Williamson-ActaMet-1953-1-22-WH-Plot.pdf

[19] T. Ungár, and J. Gubicza, Ultrafine Grained Materials II, 595–604, (2013), https://core.ac.uk/download/pdf/11856593.pdf

[20] P.R. Morris, Journal of Applied Physics, **30**, (4), 595-596, (1959), https://doi.org/10.1063/1.1702413

[21] C. Dragomir, and T. Unga´r, J. Appl. Cryst., **35**, 556–564, (2002). https://doi.org/10.1107/s0021889802009536

[22] H.B. Huntington, Solid State Physics, 213–351, (1958). https://doi.org/10.1016/S0081-1947(08)60553-6

[23] N. Shkatulyak, V. Usov and S. Smirnova, International Journal of Advances in Materials Science and Engineering, **4**(4), 1-11, (2015), https://www.researchgate.net/publication/283650995_Single_Crystal_Magnesium_Lithium_Alloy_Elastic_Constants

[24] A. Borbely, http://metal.elte.hu/anizc/.

[25] Gubicza, N.H. Nam, K. Mathis, and V.V. Stolyarov, Z. Kristallogr. Suppl., **23,** 93-98, (2006), http://gubicza.web.elte.hu/publikaciok/epdic9_sajat.pdf

[26] J.J. Kearns, Journal of Nuclear Materials, **299**(2), 171–174 (2001), https://doi.org/10.1016/S0022-3115(01)00686-9.

[27] V. Grytsyna, D. Malykhin, T. Yurkova et al. East Eur. J. Phys. **3**, 38-45 (2019), https://doi.org/10.26565/2312-4334-2019-3-05.

[28] N.V. Ageev, A.A. Babareko and S.Ya. Betsofen, Izv. Ross. Akad. Nauk, Ser. Met. **1**, 94–103 (1974).

ВПЛИВ ВИДУ ДЕФОРМАЦІЇ НА МОДУЛЬ ЮНГА, ПАРАМЕТР ПОШКОДЖЕНОСТІ, ТЕКСТУРУ І СТРУКТУРУ СПЛАВА Mg - 5% (ваг.) Li

Валентин Усов[a], Хайнц-Гюнтер Брокмеєр[b,e], Наталія Шкатуляк[c], Олена Савчук[d], Норберт Шелл[e]

[a]*Південноукраїнський національний педагогічний університет імені К. Д. Ушинського, кафедра технологічної і професійної освіти, вул. Старопортофранківська. 26, 65020, Одеса, Україна*

[b]*Інститут матеріалознавства та інженерії - факультет ТЕХМАТ - Технологічний університет Клаусталь Agricolastrasse, 6, D-38678, Клаусталь-Целлерфельд, Німеччина*

[c]*Південноукраїнський національний педагогічний університет імені К. Д. Ушинського, кафедра фізики вул. Старопортофранківська. 26, 65020, Одеса, Україна*

[d]*Національний університет "Одеська морська академія", фізичний факультет вул. Дідріхсона, 8, 65000, Одеса, Україна*

[e]*Німецький центр конструктивного матеріалознавства (GEMS), Центр імені Гельмгольца вул. Макса Планка, 1, D-21502 Гестхахт, Німеччина*

Вивчено вплив деформації екструзією, прокаткою після екструзії (в поєднанні з відпалом і зміною напрямку прокатки) і подальшого знакозмінного вигину (ЗІ) з числом циклів 0,5, 1, 3 і 5 на модуль пружності (E), параметр накопичення пошкоджень (параметр пошкоджуваності ω), кристалографічну текстуру і параметри субструктури бінарного сплаву Mg - 5% Li (ваг.). Параметр пошкоджуваності ($0 \leq \omega \leq 1$), який інтерпретується як відносне зменшення ефективної несучої площі поперечного перерізу через накопичення пошкоджень, був знайдений зі зміни модуля пружності після різних вищезазначених типів деформації. При цьому ми використовували для порівняння моделі еквівалентної деформації та еквівалентної пружної енергії. Параметри субструктури (розміри кристалічних доменів D (області когерентного розсіювання, мікродеформації кристалічної гратки ε, щільність дислокацій ρ) оцінювалися шляхом аналізу фізичного розширення ліній дифракції жорсткого проникаючого рентгенівського синхротронного випромінювання на кристалічній гратці досліджуваного сплаву. Було виявлено, що після екструзії злитка сплаву при 350°С і подальшої прокатки в напрямку осі екструзії (напрямок прокатки НП) до товщини 4,5 мм в поєднанні з відпалом при 350°С після кожного проходу утворюється текстура. При такій текстурі вісь шестигранної призми відхиляється на 90° від нормального напряму (НН) до поперечного напрямку (ПН). При цьому кристалографічні напрямки $\langle 11\bar{2}0 \rangle$ і $\langle 10\bar{1}0 \rangle$ збігаються з НП. Текстура, при якій вісь гексагональної призми відхиляється від НН до ПН на кути від 15 до 70° (на відміну від текстури базисного типу чистого магнію), формується після подальшої прокатки досліджуваного сплаву до товщини 1 мм зі зміною НП після кожного проходу на 90° в поєднанні з відпалом при 350°С. Кристалографічні напрямки $\langle 21\bar{3}1 \rangle$ збігаються з НП. Виявлена анізотропія вищевказаних характеристик. В результаті кореляційного і регресійного аналізу було встановлено, що анізотропія і значення *E* і *D* зменшуються, а значення ε, ρ і ω збільшуються зі збільшенням числа циклів знакозмінного вигину. Показано, що зміни вищевказаних характеристик обумовлені, в основному, кристалографічною текстурою, сформованою в процесі термомеханічної обробки і подальшого знакозмінного вигину листів сплаву Mg - 5% Li (ваг.), що підтверджується даними кореляційного і регресійного аналізу.

КЛЮЧОВІ СЛОВА: екструзія, прокатка, знакозмінний вигин, текстура, анізотропія, модуль Юнга, параметр пошкоджуваності, субструктура.

ВЛИЯНИЕ ВИДА ДЕФОРМАЦИИ НА МОДУЛЬ ЮНГА, ПАРАМЕТР ПОВРЕЖДЕННОСТИ, ТЕКСТУРУ И СТРУКТУРУ СПЛАВА Mg - 5% (вес.) Li

Валентин Усов[a], Хайнц-Гюнтер Брокмеєр[b,e], Наталья Шкатуляк[c], Елена Савчук[d], Норберт Шелл[e]

[a]*Южно-Украинский национальный педагогический университет им. К.Д. Ушинского, кафедра технологического и профессионального образования, ул. Старопортофранковская. 26, 65020, Одесса, Украина*

[b]*Институт материаловедения и инженерии - факультет ТЕХМАТ - Технологический университет Клаусталь, Agricolastrasse, 6, D-38678, Клаусталь-Целлерфельд, Германия*

[c]*Южно-Украинский национальный педагогический университет им. К. Д. Ушинского, физический факультет ул. Старопортофранковская. 26, 65020, Одесса, Украина*

[d]*Национальный университет "Одесская морская академия", физический факультет улица Дидрихсона, 8, 65000, Одесса, Украина*

[e]*Немецкий центр конструкционного материаловедения (GEMS), Центр имени Гельмгольца ул. Макса Планка, 1, D-21502, Гестахт, Германия*

Изучено влияние деформации экструзией, прокаткой после экструзии (в сочетании с отжигом и изменением направления прокатки) и последующего знакопеременного изгиба (ЗИ) с числом циклов 0,5, 1, 3 и 5 на модуль упругости (E), параметр накопления повреждений (параметр поврежденности ω), кристаллографическую текстуру и параметры субструктуры бинарного сплава Mg - 5% Li (вес.). Параметр поврежденности ($0 \leq \omega \leq 1$), который интерпретируется как относительное уменьшение эффективной несущей площади поперечного сечения из-за накопления повреждений, был найден по изменению модуля упругости после различных вышеупомянутых типов деформации. При этом мы использовали для сравнения модели эквивалентной деформации и эквивалентной упругой энергии. Параметры субструктуры (размеры кристаллических доменов D (области когерентного рассеяния), микроискажения решетки ε, плотность дислокаций ρ) оценивались путем анализа физического уширения линий дифракции на кристаллической решетке исследуемого сплава проникающего жесткого рентгеновского синхротронного излучения. Было обнаружено, что после экструзии слитка сплава при 350°С и последующей прокатки в направлении оси экструзии (направление прокатки НП) до толщины 4,5 мм в сочетании с отжигом при 350°С после каждого прохода образуется текстура. При такой текстуре ось шестигранной призмы отклоняется на 90° от нормального направления (НН) к поперечному направлению (ПН). При этом кристаллографические направления $\langle 11\bar{2}0 \rangle$ и $\langle 10\bar{1}0 \rangle$ совпадают с НП. Текстура, при которой ось гексагональной призмы отклоняется от НН до ПН на углы от 15 до 70° (в отличие от текстуры базисного типа чистого магния), формируется после дальнейшей прокатки исследуемого сплава до толщины 1 мм с изменение НП на 90 ° в сочетании с отжигом при 350°С после каждого прохода. Кристаллографические направления $\langle 21\bar{3}1 \rangle$ совпадают с НП. Обнаружена анизотропия вышеуказанных характеристик. В результате корреляционного и регрессионного анализа было установлено, что анизотропия и значения E и D уменьшаются, а значения ε, ρ и ω увеличиваются с увеличением числа циклов чередующегося изгиба. Показано, что изменения вышеуказанных характеристик обусловлены, в основном, кристаллографической текстурой, сформированной в процессе термомеханической обработки и последующего знакопеременного изгиба листов сплава Mg - 5% Li (вес.), что подтверждается данными корреляционного и регрессионного анализа.
КЛЮЧЕВЫЕ СЛОВА: экструзия, прокатка, знакопеременный изгиб, текстура, анизотропия, модуль Юнга, параметр поврежденности, субструктура

STUDY OF RADIATION-CHEMICAL STRUCTURING OF COMPOSITIONS BASED ON EPOXY OLIGOMERS

Lidiya F. Podhornaya, Vyacheslav L. Avramenko*, Oleh H. Karandashov

National Technical University "Kharkiv Politechnic Institute"
Kirpichova str., 2, 61002, Kharkiv, Ukraine
*Corresponding Author: avramenko@kpi.kharkov.ua

The processes of radiation-chemical structuring of modified epoxy acrylic compositions were studied depending on the nature of epoxy oligomers and modifiers. ED-20 and ED-22 grades epoxy oligomers were chosen as epoxidian oligomers; 3,4-epoxyhexahydrobenzal-3,4-epoxy-1,1-bis(hydroxymethyl)cyclohexane (UP-612 grade), 3,4-epoxycyclohexylmethyl-3,3-epoxycyclohexanecarboxylate (UP-632 grade) were chosen as cycloaliphatic oligomers; diethylene glycol diglycidyl ether (DEG) was chosen as aliphatic oligomer. To modify the epoxy oligomers, unsaturated acrylic monomers, such as acrylic acid and methyl acrylic acid ester; aromatic and aliphatic oligoester acrylates, such as α,ω-methacryl(bis-diethylene glycol)phthalate (MDP-1 grade), α,ω-methacryldi(diethyleneglycolphthalate) (MDP-2 grade), α,ω-methacryl(bis-triethyleneglycol)phthalate (MGP-9 grade) and atri-(oxyethylene)-α,ω-dimethacrylate (TGM-3 grade); condensation product of linseed oil dimerized fatty acids and polyethylenepolyamine, such as oligoamide L-20 grade; condensation product of ricinoleic acid, castor oil and maleic anhydride, such as unsaturated polyester PE-220, were used. The thermophysical and relaxation properties of cross-linked polymers, obtained under exposure to γ-radiation of Co^{60} and electrons accelerated by the absorbed radiation dose of 50–150 kGy at the beam current of 2-4 mA and electron energy of 240-300 keV, were studied. The distance from the exhaust window of the accelerator to the irradiated surface of the samples was 63-80 mm. The thermophysical properties of the cured polymers were evaluated using thermomechanical studies on a thermomechanograph with the temperature rise of 1°/min and the pressure of 0.54 MPa in the temperature range of 293-673 K, as well as the differential thermal and thermogravimetric analyzes on a system derivatograph by L. Paulik, R. Paulik, L. Erdei in the temperature range of 293–973 K with the rise rate of 7°/min. The relaxation properties and molecular mobility of the cross-linked polymers were studied by the dielectric method. The dielectric loss tangent was determined in the temperature range of 143-393K at the frequency of 1 kHz using a digital automatic bridge of alternating current R-589. The test sample temperature was measured using a potentiometer on a copper-constantan thermocouple, which was placed in the measuring cell along with the test sample. The samples were cooled by placing the cell in a vessel with liquid nitrogen. As a result of the studies, the influence of the chemical nature of epoxy oligomers and unsaturated modifiers on the processes of structure formation and molecular mobility of polymers, obtained under conditions of radiation-chemical curing, was established. It was determined, that when modifying epoxy oligomers with acrylic acid, methyl acrylic acid ester, oligoester acrylates of MGP-9 ((α,ω-methacryl(bis-triethyleneglycol)phthalate)) or TGM-3 ((tri-(oxyethyleneglicol)-α,ω-dimethacrylate)) grades, the structuring of compositions, based on the DEG-1 aliphatic epoxy oligomer and UP-612 cycloaliphatic oligomer, was more efficient than the compositions based on unsaturated ETO oligomers grade such as 2-ethylhexylepoxytallate oligomer and epoxidian oligomers of ED-20 and ED-22 grades. It was established, that the modifier oligoamide of L-20 grade, containing primary and secondary amino groups, increased the radiation sensitivity of the compositions, based on epoxidian and cycloaliphatic oligomers, and reduced the inhibitory effect of atmospheric oxygen. The optimal composition and the main technological parameters were determined, what allowed to obtain materials with high physical and mechanical properties and adhesive strength to various metals. The application of the developed materials under industrial conditions will make it possible to organize a continuous high-speed radiation-chemical process for producing polymer coatings on metals, providing improved working conditions, lower energy consumption, as compared to the thermochemical process of the coatings production, and will increase the corrosion resistance of metals.

KEY WORDS: radiation-chemical structuring, ionizing radiation, differential thermal analysis, macromolecule, epoxy oligomer

The operational properties of materials, as well as their physical and chemical characteristics, substantially depend on the structure of the cured polymer, the configuration and flexibility of macromolecules, their kinetic properties [1,2]. An important task of technological progress is still the development of technologies providing lower energy consumption and improved working conditions, what allows increasing the service life of products and equipment. One of the directions in the development of high-strength, heat-resistant, and chemically resistant protective materials for metal surfaces is the formation of cross-linked polymers under the thin-layer radiation-chemical structuring [3]. The properties of polymers, obtained under the radiation-chemical structuring, are studied insufficiently. Here, an important role is played by the choice of polymer compositions based on materials produced by industry, the possibility of their modification in order to increase the operational properties of the materials obtained on their basis. It is also important to establish the relationship of the service properties of the selected materials with the structure of the obtained cross-linked polymer, molecular characteristics and concentration of the starting components of the compositions under study. Besides, these properties have a significant impact on the strength and performance characteristics of products, obtained in mass production (hermetic sealing, mass production of protective coatings and products), where these structuring methods contribute to obtaining various types of products with the required set of properties. A special industry of widespread use of polymer composite material (PCM) is general instrument engineering, the manufacture of electronic equipment, where high adhesion, low residual stresses, fast curing speed in mass production, low shrinkage, and high

moisture protection are extremely important. Important indicators of a PCM, obtained under the ionizing radiation exposure, are its thermophysical properties, strength, adhesion to various substrates, and the level of residual stresses, arising at PCM quick structuring under the radiation-chemical curing [4].

The object of this study was to develop the compositions, based on epoxy oligomers, structured at low absorbed radiation doses under conditions of free access of atmospheric oxygen, which could be recommended as metal protective coatings with high adhesion and other operational properties. In this case, one of the effective ways to increase the radiation sensitivity of compositions based on epoxy oligomers, such as modification of them with various unsaturated reactive oligomers (RO) and monomers was used, and the relationship of the properties of the obtained cross-linked polymers with the chemical nature and composition of the starting components was established [5].

RESEARCH METHOD

The above mentioned set of properties was studied on the basis of thermo-mechanical research, differential-thermal and thermo-gravimetric analyzes, and of the research of macromolecules relaxation properties.

The thermophysical and relaxation properties of cross-linked polymers, obtained under exposure to γ-radiation of Co^{60} and electrons, accelerated by the absorbed radiation dose of 50-150 kGy at the beam current of 2-4 mA and the electron energy of 240-300 keV, were studied. The distance from the outlet window of the accelerator to the irradiated surface of the samples was 63-80 mm.

The thermophysical properties of the cured polymers were estimated using thermo-mechanical studies on a thermo-mechanograph with the temperature rise of 1 K/min and the pressure of 0.54 MPa in the temperature range of 293-673 K, as well as by the differential thermal and thermo-gravimetric analyzes using the derivatograph of the system by L. Paulik, R. Paulik, L. Erdei in the temperature range of 293–973 K with the rise rate of 7°/min [6].

The relaxation properties and molecular mobility of the cross-linked polymers were studied by the dielectric method. The dielectric loss tangent was determined in the temperature range of 143-393 K at the frequency of 1 kHz using a digital automatic bridge of alternating current R-589.

The temperature of the test sample was measured using a potentiometer connected to a copper-constantan thermocouple, which was placed in the measuring cell along with the test sample. The samples were cooled by placing the cell in a vessel with liquid nitrogen.

To study the properties of the obtained polymer coatings on metals, standard methods were used [7].

EXPERIMENTAL RESULTS AND DISCUSSION

Thermomechanical studies of compositions based on epoxy oligomers of various chemical nature, modified by unsaturated reactive oligomers (RO) and monomers, which are structured directly under exposure to the ionizing radiation, were carried out. The compositions were cured in bulk by γ-radiation of Co^{60} with the dose of 50-100 kGy.

The nature of the thermomechanical curves of the cured epoxy oligomer – acrylic acid (AA) compositions (the absorbed radiation dose was 63 kGy) (Fig.1) indicates, that the cured products have high rigidity, low deformation (8-15%) and sufficiently high heat resistance (the samples are destroyed at 593 K) [8,9].
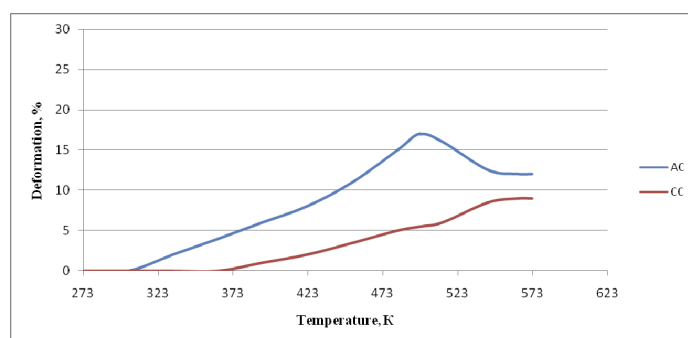

Fig. 1. Thermomechanical curves of polymers based on compositions AC, CC

The composition containing a cycloaliphatic epoxy oligomer CC (cycloaliphatic composition) is structured to form a more rigid structure (the glass transition temperature of the polymer based on this composition is 403 K, which is 80 K higher than that of the composition based on the aliphatic oligomer of DEG grade (AC - aliphatic composition), which is 323 K.

When heating the samples obtained under irradiation with the dose of 420 kGy, some decomposition of polymers with gas release is observed, what indicates to the polymer destruction.

The composition, containing the unsaturated aliphatic epoxy oligomer 2-ethylhexyl epoxytallate of the ETO grade and AA, is not cured with the dose of 100-150 kGy under the effect of both γ-radiation and accelerated electrons.

The compositions, containing the diane epoxy oligomer of ED–20 grade and AA, modified with the PE-220 oligoester, are cured at the dose of 100 kGy to form sufficiently brittle blocks, that are destroyed at mechanical treatment. It is impossible to obtain from them the samples for thermomechanical studies.

The thermomechanical studies of the cured compositions, containing an aliphatic oligomer as an epoxy oligomer, in the presence of modifying components (Fig. 2), showed that the presence of acrylic acid methyl ester (AM) in the composition provides a more elastic polymer composition AC-MM (aliphatic composition - acrylicacid methyl ester modified). The value of deformation in the highly elastic state of the cured composition, containing AM, is 5-7% higher than that of the cured compositions without it (AC-N – aliphatic composition - not modified). In this case the glass transition temperature remains unchanged.
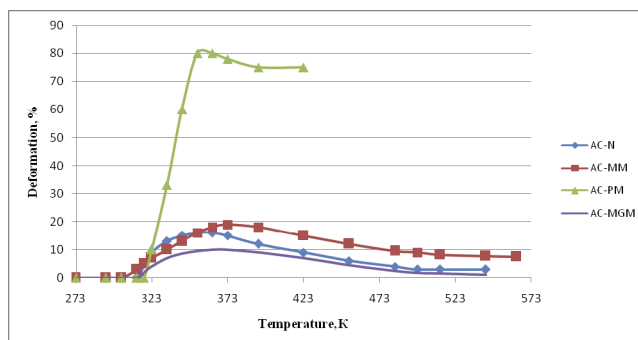
Fig. 2. Thermomechanical curves of polymers based on compositions AC-N, AC-MM, AC-PM

The heat resistance of the composition in the presence of AM is also higher. The destruction temperature is 613 K, while for the composition without it is 555 K.

Modification of the compositions with oligoester PE-220 (PE-220 – polyester) (AC-PM – aliphatic-polyester modified composition) provides samples with lower heat-resistant (destruction at 423 K), with the values of highly elastic deformations higher, than those, when modified with MGP-9 grade oligomer (Fig. 2, AC-MGM (aliphatic composition – methacryl glycol modified), what confirms the conclusion, that PE-220 does not participate in the formation of the cross-linked polymer, but plays the role of a plasticizing agent.

The polymers, obtained by curing the compositions with the participation of the cycloaliphatic epoxy oligomer of UP-612 grade and in the presence of modifying additives, are characterized by greater rigidity (Fig. 3, composition CC-P –cycloaliphatic composition-polymer, UP-612 grade oligomer not modified, CC-PM – cycloaliphatic composition – polymer, UP-612 grade oligomer modified by acrylic acid methyl ester). The presence of AM in the compositions causes a decrease in the glass transition temperature of the samples and an increase in highly elastic deformation (Fig. 3, compositions CC-P and CC-MP). The cured compositions with the participation of the diane epoxy oligomers and oligoamide of L-20 grade have a lower glass transition temperature than in the presence of PE-220 (Fig. 3, compositions DC-PM ((epoxydian (ED-20 grade oligomer) composition - with PE-220 grade oligomer modified by acrylic acid methyl ester)), DC-LM ((ED-20 grade oligomer) composition - with L-20 grade oligoamide (condensation product of linseed oil dimerized fatty acids)) modified by acrylic acid methyl ester).
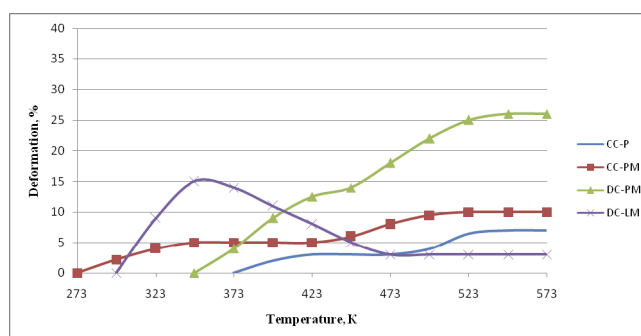

Fig. 3. Thermomechanical curves based on the compositions CC-P, CC-PM, DC-PM, DC-LM

For the polymers, based on compositions involving oligoamide L-20 (composition DC-LM), an additional cross linking of the polymer at the temperature increase is observed. On the thermomechanical curve this is indicated by a smooth decrease in highly elastic deformation.

The samples, obtained by structuring the composition based on ED-20 and UP-612, which is modified with MGP-9, are destroyed at 563–573 K and practically do not deform, what indicates the formation of rigid brittle structures.

Thus, the thermomechanical studies have shown, that during the radiation-chemical curing the epoxy compositions have the cross-linked structure and are characterized by a fairly high heat resistance (563–613 K). More rigid cross-linked polymers are formed at structuring the compositions, based on cycloaliphatic epoxy oligomers and the MGP-9 grade modifier, as compared to the compositions based on the aliphatic diane oligomer and unsaturated oligomer

PE-220. With inclusion of AM into the composition, the highly elastic deformation increases, the glass transition temperature decreases, and the heat resistance increases.

For the compositions containing the aliphatic DEG oligomer, as well as in the presence of L-20 grade oligoamide an increase in temperature causes intensification of the structuring process and a decrease in highly elastic deformation.

The behavior of the compositions cured under the impact of electrons, accelerated by the absorbed radiation dose of 120 kGy, and under exposure to high temperature and oxygen, as well as the polymers thermal stability were studied using DTA (differential thermal analysis) and TG (thermogravimetric) analysis [9,10].

The table presents the data on estimation of the thermal stability of compositions, which are cured by the absorbed radiation dose of 120 kGy and heat-treated at 393 K for 15 minutes.

Table

Thermal stability of polymers obtained when the compositions are irradiated by the absorbed radiation dose of 120 kGy and heat-treated at 393 K for 15 min

Composition	Temperature, K, at which the mass loss is, %					Temperature of maximum mass loss rate, K
	10	20	30	40	50	
DC-LMM	510	576	633	663	693	653
DC2-LMM	513	610	653	676	713	685
CC-LMM	553	590	616	653	700	615
DC-LMT	550	610	653	690	718	683

Modification of the compositions by oligoester acrylate of TGM-3 grade ((DC-LMT – epoxydian (ED-20 grade oligomer) composition – with L-20 grade oligoamide modified by acrylic acid methyl ester and tri-(oxyethyleneglicol)-α,ω-dimethacrylate)) promotes the formation of polymers with greater thermal stability than when they are modified by MGP-9 (DC-LMM composition – epoxydian ((ED-20 grade oligomer) composition – with L-20 grade oligoamide modified by acrylic acid methyl ester and α,ω-methacryl(bis-triethyleneglycol)phthalate)). The epoxy oligomers with lower molecular weight form polymers with higher thermal stability (DC2-LMM and DC-LMM).

The relaxation properties of the compositions cured by γ-radiation of Co^{60} and accelerated electrons were determined by the dielectric method, which is one of the most sensitive methods for studying molecular relaxation used to determine the physical properties of polymers [11].

The research of the processes of the compositions dielectric relaxation depending on the molecular weight and nature of the epoxy oligomer (Fig. 4) showed, that in the molecules, containing the epoxy-oligomer of ED-22 grade (ED – epoxy diane oligomer), the dipole-segmental relaxation process is very weak. Even a slight decrease in the molecular weight of the oligomer, as compared to the ED-20 grade epoxidian oligomer, is accompanied by a shift of the maximum of dipole-segmental relaxation processes toward higher temperatures and indicates the formation of more rigid structures in the cured compositions. In the compositions, based on the cycloaliphatic oligomer, the maximum of the dipole-segmental relaxation processes is in the region of lower temperatures as compared to the polymers, based on the epoxydian oligomer.
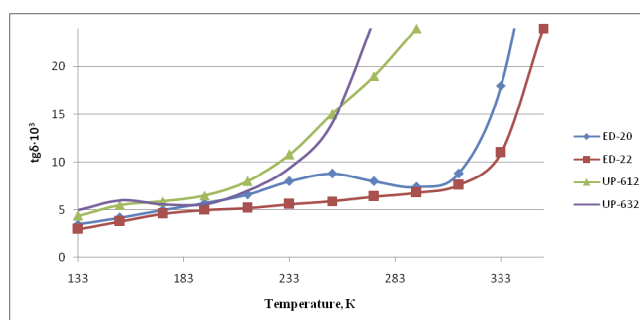

Fig.4. Temperature dependence of tgδ cured compositions based on ED-20, ED-22, UP-612, UP-632

On the whole, the dipole-segmental and dipole-radical relaxation processes in the cured compositions under study are observed in the temperature range of 223–283 K and 173–193 K, respectively.

In the compositions, containing the cycloaliphatic epoxy oligomer, in the process of radiation-chemical structuring the destruction processes also occur, resulting in an increase in the materials electrical conductivity at elevated temperatures, what leads to a distortion of the maximum position due to the segmental motion of macromolecules. However, according to the research data, it can be concluded, that the maximum dipole-segmental losses for these polymers are in the region of lower temperatures as compared to the cured compositions, containing Diane epoxy oligomers, what indicates the formation of a more micro-heterogeneous structure in the compositions, containing cycloaliphatic oligomers, and the structure imperfection of their spatial lattice.

The results of studying the influence of the nature of oligoesters with different length of the aliphatic chain and different content of aromatic nuclei on the relaxation properties during the radiation-chemical structuring (Fig. 5)

indicate, that the greatest plasticizing effect is observed when MDP-2, which has a greater amount of aliphatic and aromatic fragments in the molecule, as compared to other oligoester acrylates, is present in the compositions. The maximum dipole-segmental loss of the cured compositions with the participation of MDP-2 is shifted toward lower temperatures and makes 252K. The smallest plasticizing effect is made by MDP-1, which has a shorter aliphatic chain as compared to MGP-9, and a more compact molecule as compared to MDP-2. The maximum dipole-segmental loss in polymers with MDP-1 is shifted toward higher temperatures and makes 283K. MGP-9 and TGM-3 are in an intermediate position (the temperatures of the maxima of the dipole-segmental relaxation process are 254 K and 261 K, respectively).
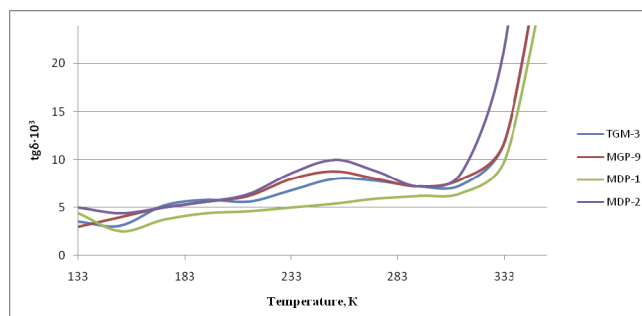

Fig. 5. Temperature dependence of the tgδ cured compositions based on TGM-3, MGP-9, MDP-1, and MDP-2

On the basis of the results of the research on the thermophysical and relaxation properties of radiation-curable epoxy composites, subject to the molecular characteristics and quantitative composition of the systems, the optimal compositions were chosen, allowing to obtain protective coatings on various metal surfaces (copper, aluminum, steel) with high adhesive strength (grade 1 by the method of lattice notches), bending strength = 1 mm, impact strength = 5 J, hardness = 0.900 rel. units, high chemical resistance, good dielectric properties (ρ_v = 5,3·10^{13} Ohm·m; $tg\ \delta$ at 1 kHz = 0.01 – 0.035; ε = 2.0 – 6.0). The highest hardness and glittering effect of the materials are provided by cycloaliphatic oligomer UP-612 and modifier MGP-9.

CONCLUSIONS

Thus, the processes of radiation-chemical structuring of modified epoxy acrylic compositions, subject to the nature of epoxy oligomers and modifiers, were investigated. The thermophysical and relaxation properties of cross-linked polymers, obtained under exposure to γ-radiation of Co^{60} and electrons, accelerated by the absorbed radiation dose of 50–150 kGy, were studied. The influence of the chemical nature of epoxy oligomers and unsaturated modifiers on the processes of structure formation and molecular mobility of polymers was established.

It was determined, that when modifying epoxy oligomers with acrylic acid, methyl acrylic acid ester, MGP-9 or TGM-3 oligoester acrylates, the structuring of compositions, based on the DEG-1 aliphatic epoxy oligomer and UP-612 cycloaliphatic oligomer, was more efficient than with the compositions based on unsaturated ETO grade oligomers such as 2-ethylhexylepoxytallate oligomer and epoxidian oligomers of ED-20 and ED-22 grades. It was established, that the modifier oligoamide of L-20 grade, containing primary and secondary amino groups, increased the radiation sensitivity of the compositions, based on epoxidian and cycloaliphatic oligomers, and reduced the inhibitory effect of atmospheric oxygen.

As a result of the research, the optimal composition and the main technological parameters were determined, what made it possible to obtain materials with high physical and mechanical properties and adhesive strength to various metals. The application of the developed materials under industrial conditions will make it possible to organize a continuous high-speed radiation-chemical process for deposition of polymer coatings on metals, which provides improved working conditions, lower energy consumption as compared to the thermo-chemical process of the coating production, and will increase the corrosion resistance of metals.

REFERENCES

[1] V.I. Irzhak, B.A. Rozenberh, N.S. Enikolopiyan, *Сетчатые полимеры* [*Cross-linked polymers*], (Moscow, Nauka, 1979) pp. 250. (in Russian)
[2] A.L. Volynskii and N.F. Bakeev, Surface Phenomena in the Structural and Mechanical Behaviour of Solid Polymers, New York: Taylor & Francis, 2016.
[3] A.I. Vilensky, Radiation-Chemical and Structural Changes in Polymers Irradiated with High-Energy Ions. J. Synch. Investig. **12**, 619–622 (2018).
[4] Sh.M. Mammadov and A.A. Garibov, *Radiation physics and chemistry of polymers*, (LAP Lambert Acad. Publishing, Germany, Saarbrucken, 2015), pp. 668.
[5] E.N. Mochalova, I.V. Lounev, M.F. Galikhanov, I.A. Gabrakhmanov, R.R. Fatikhova, Y.A. Gusev and R.Y. Deberdeev. Study of electret and dielectric properties of epoxiamine polymer materials. Butlerov Communications, **49**(1), 91-97 (2017). ROI: jbc-02/17-49-1-91
[6] Simultaneous Thermal Analyzer - STA 449 F5 Jupiter® Method, Technique and Applications, 2015, pp. 16.

[7] M.I. Karyakina, *Лабораторный практикум по испытанию лакокрасочных материалов и покрытий* [*Laboratory workshop for testing paints and coatings*], (Khimiya, Moscow, 1979), pp. 240. (in Russian)

[8] Y. Rabek, *Экспериментальные методы в химии полимеров* [*Experimental methods in polymer chemistry*], (Mir, Moscow, 1983), pp. 384. (in Russian)

[9] A.P. Belokurova, V.A. Burmistrov, T.A. Aheev, *Термомеханический метод исследования полимеров* [*Thermomechanical method for the study of polymers*], (Ivanovo, 2006), pp. 36. (in Russian)

[10] V.M. Sutyahin, A.A. Lyapkov, *Физико–химические методы исследования полимеров* [*Physico-chemical methods for the study of polymers*], (Tomsk, 2008), pp. 130. (in Russian).

[11] I.Y. Averko-Antonovich, R. T. Bikmullin, *Методы исследования структуры и свойств полимеров* [*Methods for studying the structure and properties of polymers*], (Kazan`, 2002), pp. 604. (in Russian)

ORCID IDs

Lidiya F. Podhornaya https://orcid.org/0000-0001-5549-6726,

Vyacheslav L. Avramenko https://orcid.org/0000-0002-6968-1321

Oleh H. Karandashov https://orcid.org/0000-0002-3192-6944

ДОСЛІДЖЕННЯ РАДІАЦІЙНО-ХІМІЧНОГО СТРУКТУРУВАННЯ КОМПОЗИЦІЙ НА ОСНОВІ ЕПОКСИДНИХ ОЛІГОМЕРІВ

Л.П. Підгорна, В.Л. Авраменко, О.Г. Карандашов

Національний технічний університет «Харківський політехнічний інститут»

вул. Кирпичова, 2, 61002, Харків, Україна

Досліджено процеси радіаційно-хімічного структурування модифікованих епоксіакрілових композицій в залежності від природи епоксидних олігомерів і модифікаторів. У якості епоксидних олігомерів були обрані епоксидіанові олігомери марок ЕД-20, ЕД-22; у якості циклоаліфатичних олігомерів були обрані 3,4-епоксигексагідробензаль-3,4-епокси 1,1-біс-(гідроксиметил) -ціклогексан, марки УП-612, а також 3,4-епоксициклогексілметил-3,3-епоксициклогексанкарбоксілат, марки УП-632; і дігліціділовий ефір діетиленгліколю ДЕГ був обраний в якості аліфатичного олігомера. Для модифікації епоксидних олігомерів використовували: ненасичені акрилові мономери, такі як акрилова кислота та складний ефір метілакрилової кислоти; ароматичні і аліфатичні олігоефірні акрилати, такі як α, ω-метакрил (біс-діетиленгліколь) фталат (марки MDP-1), α, ω-метакрілді (діетиленгліколь фталат) (марки MDP-2), α, ω-метакрил (біс-триетиленгліколь)) фталат (марки MGP-9), три- (оксіетиленгліколь) -α, ω-диметакрилат (марка TGM-3); продукт конденсації дімерізованних жирних кислот лляної олії і поліетиленполіамін, такого як олігоамід марки L-20; продукт конденсації рицинолевої кислоти, касторової олії і малеїнового ангідриду, такого як ненасичений поліефір PE-220. Вивчено теплофізичні і релаксаційні властивості сітчастих полімерів, отриманих під дією γ-випромінювання Co⁶⁰ і електронів, прискорених поглиненою дозою випромінювання 50-150 кГр при струмі в пучку 2-4 мА і енергії електронів 240-300 кеВ. Відстань від випускного вікна прискорювача до опромінюваної поверхні зразків становила 63-80 мм. Теплофізичні властивості затверділих полімерів оцінювали за допомогою термомеханічних досліджень на термомеханографі при підйомі температури 1º/хв і тиску 0,54 МПа в інтервалі температур 293-673K, а також методом диференціального термічного і термогравіметричного аналізів на дериватографі системи Л. Паулік, Р. Паулік, Л. Ердеі в інтервалі температур 293-973 К зі швидкістю підйому 7º/хв. Релаксаційні властивості і молекулярну рухливість сітчастих полімерів вивчали діелектричним методом. Визначення тангенса кута діелектричних втрат здійснювали в температурному інтервалі 143-393K при частоті 1 кГц цифровим автоматичним мостом змінного струму Р-589. Вимірювання температури досліджуваного зразка проводили за допомогою потенціометра від термопари мідь-константан, яка перебувала у вимірювальному відсіку разом із досліджуваним зразком. Охолодження зразків здійснювали шляхом розміщення відсіку в посудину з рідким азотом. В результаті досліджень встановлено вплив хімічної природи епоксидних олігомерів і ненасичених модифікаторів на процеси формування структури і молекулярну рухливість полімерів, отриманих в умовах радіаційно-хімічного затвердіння. Визначено, що при модифікації епоксидних олігомерів акриловою кислотою, метиловим ефіром акрилової кислоти, олігоефіракрилатом МГФ-9 або ТГМ-3 структурування композицій на основі аліфатичного епоксиолігомера ДЕГ-1 і циклоаліфатичного олігомера УП-612 здійснюється більш ефективно у порівнянні з композиціями на основі ненасиченого олігомеру ОЕТ і епоксидіанових олігомерів ЕД-20 і ЕД-22. Встановлено, що модифікатор олігоамід Л-20, що містить первинні і вторинні аміногрупи, підвищує радіаційну чутливість композицій на основі епоксидіанових і циклоаліфатичних олігомерів і зменшує інгібуючу дію кисню повітря. Визначено оптимальний склад композицій та основні технологічні параметри, що дозволяють отримувати матеріали з високими фізико-механічними властивостями і адгезійною міцністю до різних металів. Застосування розроблених матеріалів у промислових умовах дозволить організувати безперервний високошвидкісний радіаційно-хімічний процес отримання полімерних покриттів на металах з поліпшеними умовами праці, меншими енерговитратами в порівнянні з термохімічним процесом отримання покриттів, і забезпечить підвищення корозійної стійкості металів.

КЛЮЧОВІ СЛОВА: радіаційно-хімічне структурування, іонізуюче випромінювання, диференційно-термічний аналіз, макромолекула, епоксидний олігомер

ИССЛЕДОВАНИЕ РАДИАЦИОННО-ХИМИЧЕСКОГО СТРУКТУРИРОВАНИЯ КОМПОЗИЦИЙ НА ОСНОВЕ ЭПОКСИДНЫХ ОЛИГОМЕРОВ

Л.Ф. Подгорная, В.Л. Авраменко, О.Г. Карандашов

Национальный технический университет «Харьковский политехнический институт»

ул. Кирпичова, 2, 61002, Харьков, Украина

Исследованы процессы радиационно-химического структурирования модифицированных эпоксиакриловых композиций в зависимости от природы эпоксидных олигомеров и модификаторов. В качестве эпоксидных олигомеров были выбраны эпоксидиановые олигомеры марок ЭД-20, ЭД-22; в качестве циклоалифатических олигомеров были выбраны

3,4-эпоксигексагидробензаль-3,4-эпокси 1,1-бис-(гидроксиметил)-циклогексан, марки УП-612, а также 3,4-эпоксициклогексилметил-3,3-эпоксициклогексанкарбоксилат, марки УП-632; и диглицидиловый эфир диэтиленгликоля ДЭГ был выбран в качестве алифатического олигомера. Для модификации эпоксидных олигомеров использовали: ненасыщенные акриловые мономеры, такие как акриловая кислота и сложный эфир метилакриловой кислоты; ароматические и алифатические олигоэфирные акрилаты, такие как α, ω-метакрил (бис-диэтиленгликоль) фталат (марки MDP-1), α, ω-метакрилди (диэтиленгликольфталат) (марки MDP-2), α, ω-метакрил (бис-триэтиленгликоль)) фталат (марки MGP-9), три- (оксиэтиленгликоль) -α, ω-диметакрилат (марка TGM-3); продукт конденсации димеризованных жирных кислот льняного масла и полиэтиленполиамина, такого как олигоамид марки L-20; продукт конденсации рицинолевой кислоты, касторового масла и малеинового ангидрида, такого как ненасыщенный полиэфир PE-220.Изучены теплофизические и релаксационные свойства сетчатых полимеров, полученных под действием γ –излучения Co^{60} и ускоренных электронов поглощенной дозой излучения 50-150 кГр при токе в пучке 2-4 мА и энергии электронов 240-300 кэВ. Расстояние от выпускного окна ускорителя до облучаемой поверхности образцов составляло 63-80 мм. Теплофизические свойства отвержденных полимеров оценивали с помощью термомеханических исследований на термомеханографе при подъеме температуры 1 °/мин и давлении 0,54 МПа в интервале температур 293-673K, а также методом дифференциального термического и термогравиметрического анализов на дериватографе системы Л. Паулик, Р. Паулик, Л.Эрдеи в интервале температур 293-973 К со скоростью подъема 7 °/мин. Релаксационные свойства и молекулярную подвижность сетчатых полимеров изучали диэлектрическим методом. Определение тангенса угла диэлектрических потерь осуществляли в температурном интервале 143-393K при частоте 1 кГц цифровым автоматическим мостом переменного тока Р-589. Измерение температуры исследуемого образца проводили с помощью потенциометра от термопары медь-константан, которая находилась в измерительной ячейке вместе с исследуемым образцом. Охлаждение образцов осуществляли путем помещения ячейки в сосуд с жидким азотом. В результате исследований установлено влияние химической природы эпоксидных олигомеров и ненасыщенных модификаторов на процессы формирования структуры и молекулярную подвижность полимеров, полученных в условиях радиационно–химического отверждения. Определено, что при модификации эпоксидных олигомеров акриловой кислотой, метиловым эфиром акриловой кислоты, олигоэфиракрилатами МГФ-9 или ТГМ-3 структурирование композиций на основе алифатического эпоксиолигомера ДЭГ-1 и циклоалифатического олигомера УП-612 осуществляется более эффективно по сравнению с композициями на основе ненасыщенного олигомера ОЭТ и эпоксидиановых олигомеров ЭД-20 и ЭД-22. Установлено, что модификатор олигоамид Л-20, содержащий первичные и вторичные аминогруппы, повышает радиационную чувствительность композиций на основе эпоксидиановых и циклоалифатических олигомеров и уменьшает ингибирующее действие кислорода воздуха. Определен оптимальный состав композиций и основные технологические параметры, позволяющие получать материалы с высокими физико-механическими свойствами и адгезионной прочностью к различным металлам. Применение разработанных материалов в промышленных условиях позволит организовать непрерывный высокоскоростной радиационно-химический процесс получения полимерных покрытий на металлах с улучшенными условиями труда, меньшими энергозатратами по сравнению с термохимическим процессом получения покрытий и обеспечит повышение коррозионной стойкости металлов.

КЛЮЧЕВЫЕ СЛОВА: радиационно-химическое структурирование, ионизирующее излучение, дифференциально-термический анализ, макромолекула, эпоксидный олигомер

CASCADE ENERGY TRANSFER IN INSULIN AMYLOID FIBRILS DOPED BY THIOFLAVIN T, BENZANTHRONE AND SQUARINE DYES

ⓘUliana Tarabara[a]*, ⓘKateryna Vus[a], Mykhailo Shchuka[a], ⓘElena Kirilova[b], Georgiy Kirilov[b], ⓘOlga Zhytniakivska[a], ⓘValeriya Trusova[a], ⓘGalyna Gorbenko[a], Todor Deligeorgiev[c]

[a]*Department of Medical Physics and Biomedical Nanotechnologies, V.N. Karazin Kharkiv National University*
4 Svobody Sq., Kharkiv, 61022, Ukraine
[b]*Department of Chemistry and Geography, Daugavpils University, Vienibas 13, Daugavpils, LV5401, Latvia*
[c]*Faculty of Chemistry and Pharmacy, Sofia University, "St. Kliment Ohridski" 1,*
blv. J. Bourchier, Sofia, 1164, Bulgaria
*Corresponding Author: uliana.tarabara@gmail.com
Received 15 January 2020, revised January 30, 2020; accepted January 31, 2020

The three-step Förster resonance energy transfer (FRET) within the cascade of four dyes, including the classical amyloid marker Thioflavin T as a primary donor, two jumper dyes, benzanthrone ABM and squaraine SQ4, and terminal acceptor SQ1, was tested as a possible tool for detection and characterization of insulin amyloid fibrils. The results obtained confirm the occurrence of highly efficient multistep FRET (msFRET) in the chromophore ensemble in the presence of insulin fibrils formed at elevated temperature under pH 2 (InsF1) or pH 7.4, 0.15 M NaCl (InsF2), while negligible FRET efficiencies were obtained for the control unfibrillized protein, suggesting the specificity of msFRET to cross-β-sheet architecture characteristic of amyloid fibrils. Specifically, the efficiencies of FRET for the donor-acceptor pairs ThT-ABM, ABM-SQ4 and SQ4-SQ1 at maximum acceptor concentrations (~0.4 μM – 1.6 μM) were estimated to be 86%/94%, 48%/34% and 66%/32%, respectively, in the presence of InsF1/InsF2. The most significant differences between InsF1/InsF2 and the control protein were observed for the donor-acceptor pair ThT-ABM, suggesting that ABM is the key mediator in the whole process of msFRET. Assuming the isotropic rotation of the fluorophores, the average donor-acceptor distances were estimated in the presence of InsF1, yielding the values 1.3 nm, 5.3 nm, and 3.9 nm for the ThT-ABM, ABM-SQ4 and SQ4-SQ1 pairs, respectively. The obtained distances are indicative of different fibril binding sites for the chromophores in the insulin fibrils, although due to their high specificity to the fibrillar structure, the dyes are most likely to localize in the surface grooves of β-sheets running along the main axis of amyloid fibril. Remarkably, the differences in the insulin amyloid morphology can be clearly distinguished using msFRET. As evidenced from TEM, InsF2 were thinner, shorter and contained amorphous aggregates, as compared to InsF1. Thus, different amyloid formation pathways under neutral and acidic pH resulted in the changes in the dye affinity for to the fibril binding sites, and, as a consequence, in the distinct msFRET efficiencies, especially for the pair SQ4-SQ1. The ability of ThT to serve as an efficient amplifier for the two near-infrared dyes, SQ4 and SQ1, with the benzanthrone fluorophore ABM as a jumper dye, allows detection of fibrillar insulin in the optical window of the biological samples, with the Stokes shift of the four-chromophore being *ca.* 240 nm. The proposed msFRET-based approach can be employed not only for insulin amyloid detection but also for distinguishing between different amyloid fibril morphologies and gaining further insights into the mechanisms involved in the development of the injection-localized insulin amyloidosis.

KEYWORDS: ABM, cascade resonance energy transfer, insulin amyloid fibrils, quantum yield, Thioflavin T.

Förster resonance energy transfer (FRET) is known as a physical process by which an excited state fluorophore (donor) non-radiatively transfers energy to another fluorophore via distance-dependent long-range dipole-dipole interactions [1]. Due to this feature, FRET technique has proven to be highly informative in the structural characterization of a wide variety of biological macromolecules and their assemblies [1-4]. The efficiency of FRET depends on the distance between the chromophores employed as energy donor and acceptor, orientation of the donor and acceptor transition dipoles, and the donor quantum yield [1,5]. Numerous studies indicate that the maximum FRET efficiency can be achieved via multiple interacting FRET pathways rather than independent channels, by which the energy travels from an initial donor chromophore through the intermediate donors/acceptors onto a final acceptor chromophore [6,7]. Therefore, during the past decades the multistep FRET (msFRET), manifesting itself in the energy transfer within multiple chromophore systems through cascade route, attracts increasing attention [8,9]. To exemplify, the msFRET was applied for protein labeling [10], simultaneous enzyme detection in multicomponent biological samples [9], genotyping of single nucleotide polymorphism [11], DNA sequencing [12], estimating the stoichiometry of protein complexes [13], determination of the tumor necrosis factor [14] and analysis of multiprotein interactions in living cells [15], screening of multiple enzyme inhibitors [7], developing the light harvesting systems and molecular photonic wires [6,7,16,17]. The vast majority of the above implementations of msFRET are based on the application of DNA as a framework for arraying multiple fluorophores at precise positions and controlling the inter-chromophore distances in such a way that the energy transfer occurs on the nanoscale [6,7,11,12,17].

Recently we have found that amyloid fibrils can also serve as a molecular scaffold for controlled positioning of a multitude of chromophores communicating via the two-step FRET [18,19]. Moreover, we have demonstrated that the technique based on the msFRET can be effectively used for the identification and characterization of insulin amyloid fibrils along with classical Thioflavin T (ThT) assay, thus allowing the increase of amyloid detection sensitivity [19,20].

For further investigation of the ability of amyloid fibrils to act as a molecular framework for arraying multiple fluorophores, herein we directed our efforts to the identification of a set of fluorophores capable of reinforcing the amyloid-sensing potential of the classical amyloid marker ThT. More specifically, the aim of the present study was to examine the applicability of the chromophore system, containing Thioflavin T, benzanthrone dye ABM, and two squaraine compounds, SQ1 and SQ4, to detecting and characterizing the insulin amyloid fibrils of different morphology.

EXPERIMENTAL SECTION
Materials
Bovine insulin, dimethyl sulfoxide (DMSO), Tris, Thioflavin T (ThT) were purchased from Sigma. Benzanthrone dye ABM [21], and squaraine dyes, SQ1, SQ4 [19], were synthesized in the Daugavpils University and University of Sofia, respectively. All other reagents were used without further purification.

Preparation of working solutions
The insulin stock solutions 10 mg/ml (InsF1) or 0.3 mg/ml (InsF2) were prepared in 10 mM glycine buffer (pH 2.0) or in 10 mM Tris-HCl buffer (0.15 M NaCl), respectively. The reaction of the protein (stock solutions) fibrillization was conducted at 37 °C for 5 days (InsF2) and for 10 hours, followed by incubation at 55 °C for 8 hours (InsF2) under constant agitation on the orbital shaker (108 and 143 r.p.m. for InsF1 and InsF2, respectively). The kinetics of amyloid formation was monitored using the Thioflavin T assay [22], revealing the dye fluorescence intensity increase at 480 nm *ca.* 142 and 591 times for InsF1 and InsF2, respectively (data not shown). Hereafter, the fibrillar protein and its non-fibrillized counterpart (the insulin solution in glycine or Tris-HCl buffers that was not subjected to heating and agitation) are denoted as InsF1/InsF2 and InsN1, respectively, where indexes 1 and 2 correspond to glycine and TRIS buffers, respectively.

The dyes stock solutions were prepared in DMSO (SQ1 and SQ4) and ethanol (ABM), while ThT was dissolved in 10 mM Tris buffer (pH 7.4). The fluorimetric measurements were carried out in 10 mM Tris-HCl buffer (pH 7.4).

Insulin fibril samples for transmission microscopy were contrasted by 1.5% (w/v) phosphotungstic acid, dried and viewed with the EM-125 electron microscope (Selmi, Ukraine), as described previously [19].

A   B
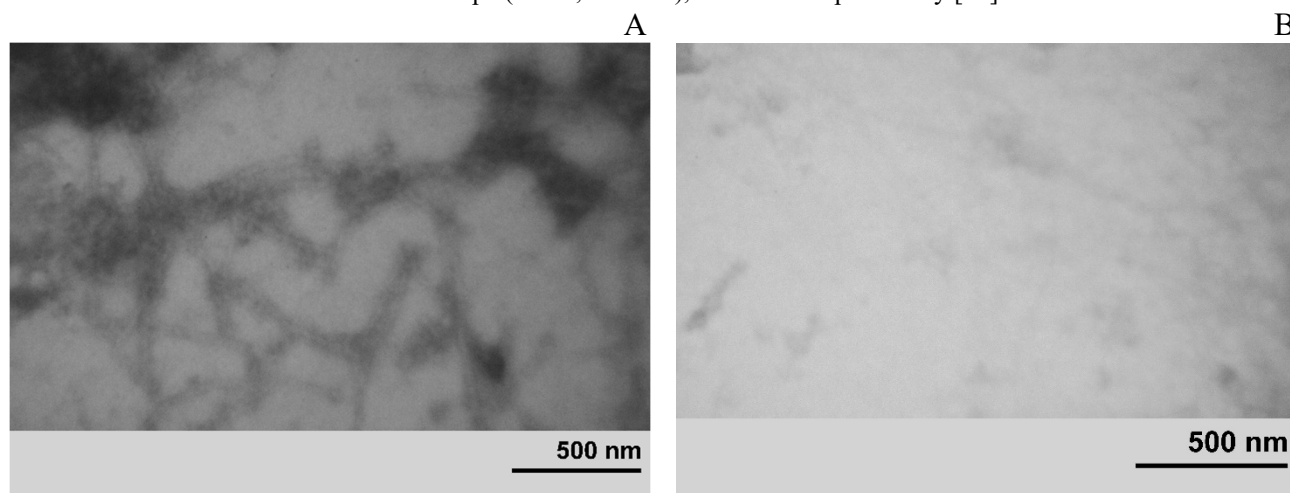

Fig. 1. Transmission electron microscopy photographs of the insulin amyloid fibrils prepared in 10 mM glycine buffer (pH 2) (A) 10 mM Tris-HCl buffer (0.15 M NaCl, pH 7.4) (B).

Spectroscopic measurements
The absorption spectra of the examined dyes were recorded with the spectrophotometer Shimadzu UV-2600 (Japan) at 25 ºC. The dye concentrations were determined spectrophotometrically using the extinction coefficients $\varepsilon_{444}^{EtOH} = 9.3 \cdot 10^3$ M^{-1}cm^{-1}, $\varepsilon_{662}^{DMSO} = 2.3 \cdot 10^5$ M^{-1}cm^{-1}, $\varepsilon_{641}^{DMSO} = 4.21 \cdot 10^5$ M^{-1}cm^{-1} and $\varepsilon_{412}^{water} = 3.6 \cdot 10^4$ M^{-1}cm^{-1} for ABM, SQ1, SQ4 and ThT, respectively. Steady-state fluorescence spectra were recorded with RF-6000 spectrofluorimeter (Shimadzu, Japan). Fluorescence measurements were performed at 25 °C using 10 mm pathlength quartz cuvettes. Fluorescence spectra were recorded within the range 460–800 nm with the excitation wavelength 440 nm. The excitation and emission slit widths were set at 10 nm.

The efficiency of energy transfer was determined from the quenching of the donor fluorescence in the presence of acceptor using the theory described in our previous paper [19]. Briefly, the following formulas were used [1]:

$$E = 1 - \frac{I_{DA}}{I_D} \qquad (1)$$

where I_D and I_{DA}, are fluorescence intensities of the free donor and in presence of the acceptor, respectively. The donor fluorescence recorded upon addition of the acceptor was corrected for inner filter effect [19]. The Förster radius was calculated using the Mathcad 15.0 software and the equations:

$$R_0 = 979\left(\kappa^2 n_r^{-4} Q_D J\right)^{1/6}, \quad J = \int_0^\infty F_D(\lambda)\varepsilon_A(\lambda)\lambda^4 d\lambda / \int_0^\infty F_D(\lambda)d\lambda \tag{2}$$

where J is the overlap integral; $F_D(\lambda)$ is the donor fluorescence intensity, $\varepsilon_A(\lambda)$ is the acceptor molar absorbance at the wavelength λ, n_r is the refractive index of the medium; Q_D is the donor quantum yield; κ^2 is the orientation factor [19]. Finally, quantum yield of the dyes was estimated from the equation:

$$Q_d = Q_s \cdot \frac{(1 - 10^{A_s}) S_d n_d^{2}}{(1 - 10^{A_d}) S_s n_s^{2}} \tag{3}$$

where Q_s is the quantum yield of the standard, A_d and A_s are the absorbances at the donor excitation wavelength, S_d and S_s are the areas under the fluorescence curve, n_d and n_s are the refractive indexes of the solutions in which fluorescence spectra of the donor and standard are measured, respectively.

RESULTS AND DISCUSSION

The three-step sequential FRET was observed in the system of four dyes including the ThT (donor), ABM (the main mediator), squaraine dyes SQ4 (acceptor for ABM) and SQ1 (acceptor for SQ4) in the presence of fibrillar insulin and control unfibrillized protein (Fig. 2). A sequential chromophore addition to InsF1 and to the control unfibrillized protein, starting from the terminal acceptor (SQ1) and ending by the primary donor (ThT), resulted in the following SQ1 fluorescence intensity increases at 680 nm: SQ1+SQ4 (~2), +ABM (~20), +ThT (~100) for InsF1 and SQ1+SQ4 (~1.2), +ABM (~14), +ThT (~15) for the control protein (Fig. 3A,B). Notably, increase in the fluorescence intensity of the terminal acceptor SQ1 (~100 for InsF1) in the presence of ABM in the four-chromophore system was higher than that in the case of 4$^/$-dimethylaminochalcone (DMC) [19], suggesting that the examined benzanthrone dye is better enhancer of SQ1 fluorescence in the msFRET occurring in the insulin amyloid fibrils. As illustrated in Fig. 3C, titration of the fibril-bound ThT with ABM is accompanied by the decrease in ThT fluorescence intensity at 480 nm, allowing the calculation of FRET efficiency. The sample containing InsF1, ThT and ABM was then titrated with SQ4, followed by the titration with SQ1 (data not shown), and FRET efficiencies within the pairs ABM-SQ4 and SQ4-SQ1 were determined. Similar approach was employed to determine the msFRET efficiencies for the donor-acceptor pairs bound to InsF2.
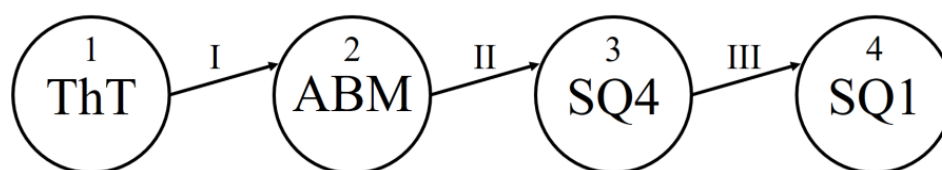

Fig. 2. Scheme of a three-step sequential energy transfer between 4 chromophores.

Interestingly, addition the dyes in the following order: SQ1, SQ4, ABM (0.3 μM), ABM (1.6 μM) to the InsF2-ThT system, resulted in the increase of SQ1 fluorescence at 680 nm by ~4, ~8, ~18, ~75 times, respectively (Fig. 3D). These data indicate that ABM acts as a jumper dye in the FRET between ThT and SQ4, since the squaraine fluorescence intensity increases with increasing the ABM concentration (Fig. 3D). Furthermore, final increase in SQ1 fluorescence at 680 nm was about 100 (18) times for InsF1 (InsF2) at the SQ1, SQ4 and ABM concentrations, 0.46, 0.25, and 0.3 μM, respectively. The differences observed between InsF1 and InsF2 suggest the sensitivity of msFRET to amyloid fibril morphology (Fig.3A,D). The donor quantum yields (Q_d) presented in Table 1 were calculated using eq. (3). Notably, the ThT quantum yield was increased two orders of magnitude upon the dye binding to fibrillar insulin, that is in a good agreement with our previous data [19].

The FRET efficiencies (E) evaluated for the donor-acceptor pairs ThT-ABM, ABM-SQ4 and SQ4-SQ1 at the maximum acceptor concentrations (InsF1: 0.8 μM, 0.4 μM and 1.2 μM; InsF2: 1.6, 0.3 and 0.4 μM for ABM, SQ4 and SQ1, respectively) are given in Table 2. Similar to our previous study with DMC [19], the energy transfer efficiencies for all donor-acceptor pairs in the cascade were higher in the presence of fibrillar insulin, as compared to the control unfibrillized protein, suggesting the specificity of msFRET for amyloid state of polypeptide chain.
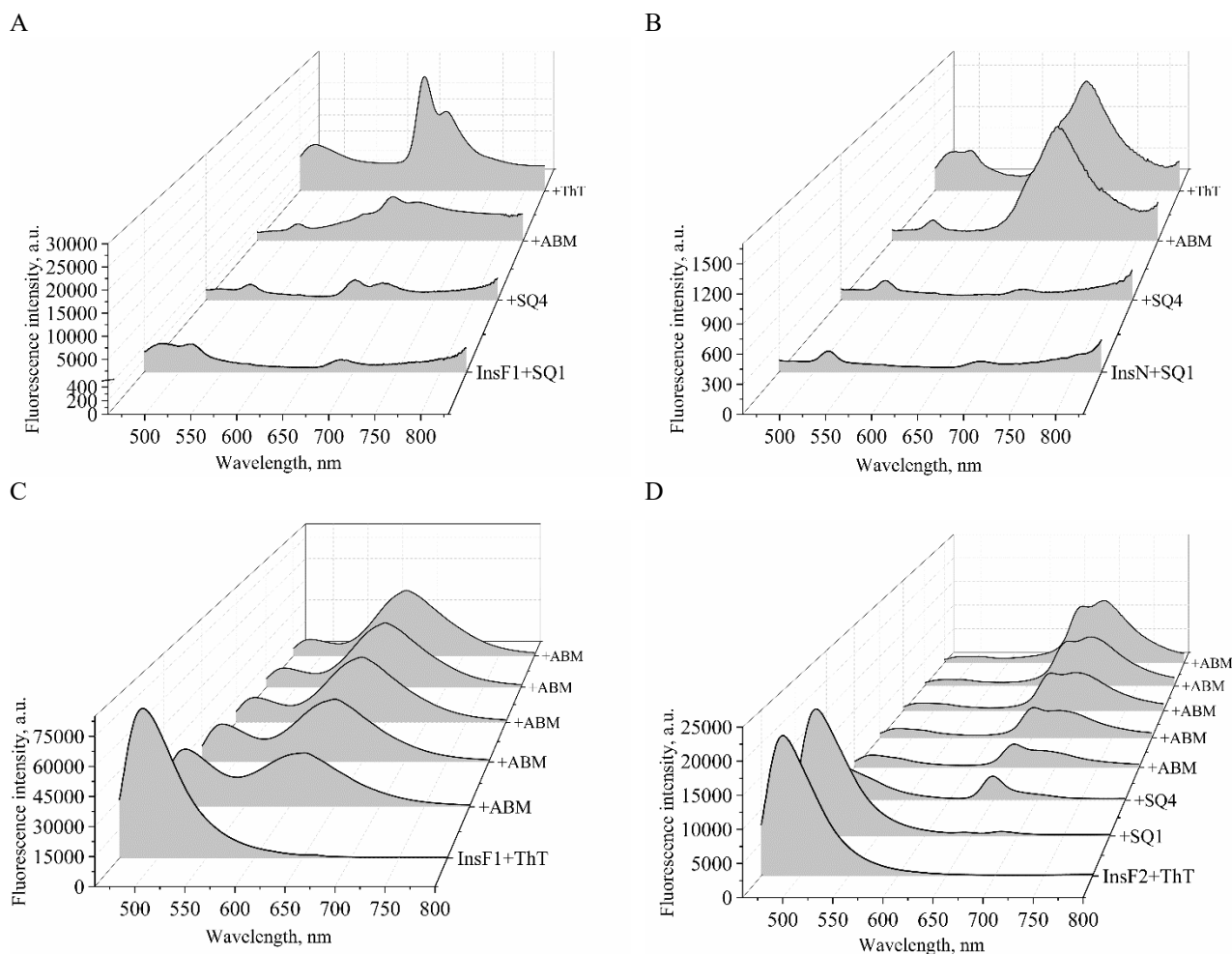
A

B

C

D

Fig. 3. Changes in the emission spectra of the squaraines (SQ1 and SQ4) upon addition of donors (ThT and ABM) in the presence of the fibrillar insulin InsF1 (A) and control protein (B). Fluorescence spectra of fibril-bound ThT upon titration with the main mediator ABM (C) or SQ1, SQ4, ABM (D). The protein and ThT concentrations were 5.6 and 3.6 μM (A–C), 1.8 and 0.16 μM (D), respectively. SQ1 and SQ4 concentrations were 0.46 and 0.25 μM, respectively. ABM concentration was 0.3 μM (A,B), and was varied from 0.2 to 0.8 μM (C) and from 0.3 to 1.6 μM (D). The samples were incubated for 3–16 minutes after addition of each aliquot of the dye stock solutions to the InsF2-ThT mixture (D).

Notably, the benzanthrone dye ABM is the key mediator in a whole msFRET process, because the energy transfer efficiency for the pair ThT-ABM was the highest (Table 2). ABM appeared to be a better mediator than DMC, because only ~ 60 % FRET efficiency was observed for ThT-DMC pair in the presence of insulin amyloid fibrils [19].

Notably, FRET efficiency for the pair Q4-SQ1 was 2-fold lower in InsF2, as compared to that in InsF1 (Table 2). Furthermore, only 4% FRET efficiency was observed for this donor-acceptor pair immediately after the addition of SQ1 to the ThT-ABM-SQ4-InsF2 system, and it reached the value of 32% only after 19 hours of sample incubation at room temperature (Table 2), probably because of steric restrictions for the binding of bulky SQ1 molecule to InsF2. The distinct FRET efficiencies in the ensemble of four dyes in the presence of InsF1 and InsF2 can be explained by variations in fibril morphology resulting from different pH, concentration, and ionic strengths [26]. As seen in Fig. 1A, the mature fibrils of 1.0±0.2 μm in length and 30±6 nm in diameter were formed under acidic pH in the absence of NaCl [27]. Instead, shorter (0.9±0.7 μm), thinner (24±6 nm) and blurred aggregates were observed upon insulin incubation at physiological pH (7.4) and ionic strength 150 mM (Fig. 1B). In fact, InsF2 fibrils seem to be immature, e.g., broken fibrils or protofilaments, resulting in the different appearance of InsF1 and InsF2 structures (Fig. 1) [28]. Thus, a more pronounced loss of insulin tertiary structure induced by acidic pH provides fast and complete maturation (InsF1, Fig. 1A), while some amount of amorphous aggregates are formed at pH 7.4 presumably due to screening of the electrostatic repulsion between the protein molecules (InsF2, data not shown). The latter is in good agreement with the results of Yoshihara and co-workers, who reported common amyloid structural properties of insulin fibrils formed at pH 1.6, 0.1 M NaCl, such as high beta-sheet content and exposed C-terminal and N-terminal parts of the B-chain [28]. In turn, the aggregates prepared at pH 7.4, 0.14 M NaCl were featured by the presence of unordered structures and exposed only the C- terminal part of the B-chain. Remarkably, both electrostatic and hydrophobic intermolecular

interactions govern insulin amyloid fibril assembly, and thus, at low pH insulin molecules exist as monomers, which may form amyloid nuclei.

Table 1

Donor quantum yields in the presence of fibrillar insulin (InsF1)

Donor	Q_d	Standard
ThT	0.011	ThT in buffer ($Q_s=10^{-4}$) [23]
ABM	0.10	DSP-6 in ethanol ($Q_s=0.05$) [24]
SQ4	0.039	Nile Blue in water ($Q_s=0.01$) [25]

In turn, both pH 7.4 and 0.15 M NaCl reduce electrostatic repulsion, enabling amorphous aggregates formation, and, furthermore, it is the insulin dimer, which most likely forms amyloid nuclei in this case [26, 28]. Notably, addition of NaCl resulted in decrease in the lag time of insulin growth at pH 1.6 [26]. Next, 15-times greater lag time and 12-fold slower insulin fibril growth rate were observed in 0.1 M NaCl at pH 7.4, as compared to the corresponding values at pH 1.6, 0.1 M NaCl [26]. Furthermore, insulin amyloid aggregates were not formed at pH 7.4 without stirring, suggesting a slower nucleation than at pH 1.6 (presumably due to slow structural transformations of the insulin dimer).

Table 2

FRET efficiencies in the system containing ThT, ABM, SQ4, SQ1, fibrillar (InsF1/InsF2) or control (InsN1) insulin at the maximum acceptor concentration

Donor-acceptor pair	E_{InsF1}, %	E_{InsN}, %	E_{InsF2}, %
ThT-ABM	86	12	94
ABM-SQ4	48	25	34
SQ4-SQ1	66	4	32

It should also be emphasized that ThT affinity for insulin amyloid fibrils formed at pH 1.6 was about 2-3 times smaller than for the protein aggregates prepared at pH 7.5, although the binding stoichiometry in both cases was reported to be ~0.1 [29]. This fact may result in about 4-fold greater fluorescence increase of ThT in the presence of InsF2, as compared to that in InsF1 (591 and 142 for InsF2 and InsF1, respectively), and, as a consequence, to different FRET efficiencies (Table 2). Interestingly, a very high FRET efficiency was recorded in InsF2 for the ThT-ABM pair, although its value for the pair SQ4-SQ1 was close to that for the control unfibrillized insulin, suggesting low affinity of SQ1 for insulin fibrils prepared at pH 7.4. The observed effect can be explained by the low accessibility of the InsF2 binding sites for SQ1 whose molecule is the longest among the four employed chromophores (SQ1 length is ~2.1 nm [19]). Thus, the InsF1 and InsF2 species can be clearly distinguished using msFRET within the above four-chromophore cascade, specifically, through estimating the FRET efficiency for the SQ4-SQ1 donor-acceptor pair. Furthermore, two types of binding sites were observed for ThT in the insulin fibrils formed at pH 7.4 [29], presumably accounting for a slightly greater FRET efficiency for the ThT-ABM pair in InsF2 as compared to that for InsF1 (Table 2). The above considerations indicate that the examined four-chromophore system can be employed not only for insulin amyloid detection, but also for distinguishing between different amyloid fibril morphologies.

The overlap integral values (J) derived by numerical integration, the Förster radii and the donor-acceptor distances (calculated using the FRET efficiency values at the maximum acceptor concentration, 0.8 µM, 0.4 µM and 1.2 µM for ABM, SQ4 and SQ1, respectively) are presented in Table 3.

Table 3

FRET parameters obtained under assumption of isotropic rotation of the fluorophores in the presence of InsF1

System	J, M^{-1}cm^{-1}nm^4	R_0, nm	r, nm
ThT-ABM	$2.12\cdot10^{14}$	1.8	1.3
ABM-SQ4	$1.27\cdot10^{16}$	5.2	5.3
SQ4-SQ1	$1.20\cdot10^{16}$	4.4	3.9

The pairs ABM-SQ4 and SQ4-SQ1 showed the greatest J values due to small shifts (~22 nm and ~14 nm, respectively) between ABM(SQ4) fluorescence and SQ4(SQ1) absorption maxima, and high extinction coefficients of SQ4(SQ1). The largest value of the Förster radius (Table 3) was obtained for the pair ABM-SQ4 due to the greatest value of SQ4 extinction coefficient. The recovered distances are suggestive of the different binding sites for the chromophores within fibril structure, although due to their high specificity to the fibrillar assemblies, the dyes are most likely to localize in the surface grooves of the β-sheets running along the main fibril axis. Furthermore, the ABM and DMC seem to reside in the different fibril grooves due to two-fold lower ThT-ABM distance (Table 3), as compared to that for the pair ThT-DMC (~2.4 nm) [19]. As a consequence, ABM is localized further from SQ4, while the r value for the DMC-SQ4 pair was 4.5 nm [19]. Notably, similar distances between SQ4 and SQ1 were obtained in the two studies,

providing additional evidence for the similar morphology of insulin amyloid fibrils prepared under acidic pH and elevated temperature [19].

CONCLUSIONS

In summary, cascade FRET within the four-chromophore system containing benzothiazole dye Thioflavin T (primary donor, excited at 440 nm), benzanthrone dye ABM (main mediator), and the two novel squaraine dyes SQ4 and SQ1 (terminal acceptor possessing the emission maximum at 680 nm), was shown to be suitable for detection and characterization of insulin amyloid fibrils prepared at pH 2 (InsF1) or at pH 7.4, 0.15 M NaCl (InsF2). The examined energy transfer cascade produced a greater enhancement of SQ1 fluorescence in the presence of InsF1 compared to that containing DMC instead of ABM [19]. Furthermore, ABM appeared to be the main mediator in a whole msFRET process (occurring in the presence of InsF1/InsF2) due to the highest FRET efficiencies (86 %/94 %) observed for the donor-acceptor pair ThT-ABM. Notably, a negligible msFRET occurred in the presence of control nonfibrillized insulin, suggesting a high specificity of the chromophores to the fibrillar structures. Both, different enhancements of the terminal donor fluorescence and distinct FRET efficiencies in the chain ThT→ABM→SQ4→SQ1 reflect different morphology of the fibrillar species InsF1 and InsF2, suggesting the applicability of msFRET for distinguishing between the various types of insulin aggregates. For instance, about 6-fold greater increase in ThT emission in the presence of InsF2, as compared to that of InsF1, can be due to: i) the greater affinity of ThT for InsF2, and ii) the higher rigidity of InsF2 binding sites for the dye. The estimated donor-acceptor distances for the pairs ThT-ABM, ABM-SQ4 and SQ4-SQ1 in the presence of InsF1, assuming the isotropic rotation of the fluorophores, fall in range 1.3 nm – 5.3 nm, suggesting that the dyes occupy different sites on the amyloid surface, most likely represented by the β-sheet grooves running parallel to the main fibril axis. The obtained results can be useful for the development of sensitive fluorescence techniques for amyloid fibril detection in vivo, based on the cascade FRET within the systems containing classical amyloid marker Thioflavin T, a near-infrared fluorescent dye and effective enhancers of its fluorescence.

ORCID IDs

Uliana Tarabara https://orcid.org/0000-0002-7677-0779, **Kateryna Vus** https://orcid.org/0000-0003-4738-4016,
Elena Kirilova https://orcid.org/0000-0002-9577-5612, **Olga Zhytniakivska** https://orcid.org/0000-0001-9554-0090,
Valeriya Trusova https://orcid.org/0000-0002-7087-071X, **Galyna Gorbenko** https://orcid.org/0000-0002-0954-5053

REFERENCES

[1] J.R. Lakowicz, Principles of fluorescent spectroscopy (Plenum, New York, 1999).
[2] P.R. Selvin, Nature Struct. Biol. **7**, 730-734 (2000), https://doi.org/10.1038/78948.
[3] P. Wu and L. Brand, Anal. Biochem. **218**, 1-13 (1994), https://doi.org/10.1006/abio.1994.1134.
[4] L.M. Loura and M. Prieto, Front. Physiol. **2**, 82 (2011), https://doi.org/10.3389/fphys.2011.00082.
[5] Y. Domanov, G.P. Gorbenko, Biophys. Chem. **99**, 143-154 (2002), https://doi.org/10.1016/S0301-4622(02)00143-6.
[6] S. Buckhout-White, C. Spillmann, W.R. Algar, A. Khachatrian, J.S. Melinger, E.R. Goldman, et al. Nat. Commun. **5**, 5615 (2014), https://doi.org/10.1038/ncomms6615.
[7] J. Hu, M. Liu, C. Zhang, ASC Nano. **13**, 7191-7201 (2019), https://doi.org/10.1021/acsnano.9b02679.
[8] X. Hu, Y. Li, T. Liu, G. Zhang and S. Liu, ACS Appl. Mater. Interfaces. **7**, 15551-15560 (2015), https://doi.org/10.1021/acsami.5b04025.
[9] D. Navarathne, Y. Ner, J.G. Grote, G.A. Sotzing, Chem. Commun. (Camb). **47**, 12125-12127 (2011), https://doi.org/10.1039/C1CC14416B.
[10] G. Ulrich, C. Goze, M. Guardigli, A. Rodda and R. Ziessel, Angew. Chem. Int. Ed. **44**, 3694-3698 (2005), https://doi.org/10.1002/anie.200500808.
[11] X. Duan, S. Wang and Z. Li, Chem. Commun. **2008**, 1302–1304 (2008), https://doi.org/10.1039/B717300H.
[12] A. Aneja, N. Mathur, P.K. Bhatnagar and P.C. Mathur, J. Biol. Phys. **34**, 487-493 (2008), https://doi.org/10.1007/s10867-0089107-y.
[13] V. Raicu, J. Biol. Phys. **33**, 109-127 (2007), https://doi.org/10.1007/s10867-007-9046-z.
[14] L. He, X. Wu, J. Simone, D. Hewgill and P.E. Lipski, Nucleic Acid Res. **33**, 61–73 (2005), https://doi.org/10.1093/nar/gni057.
[15] E. Galperin, V. V. Verkhusha and A. Sorkin, Nature Methods, **1**, 209–217 (2004), https://doi.org/10.1038/nmeth720.
[16] P. Tinnefeld, M. Heilemann and M. Sauer, Chem. Phys. Chem **6**, 217-222 (2005), https://doi.org/10.1002/cphc.200400513.
[17] B. Albinsson, J.K. Hannestad and K. Borjesson, Coordination Chemistry Reviews, **256**, 2399-2413 (2012), https://doi.org/10.1016/j.ccr.2012.02.024.
[18] G. Gorbenko, V. Trusova, T. Deligeorgiev, N. Gadjev, C. Mizuguchi and H. Saito, J. Mol. Liq. **294**, 111675 (2019), https://doi.org/10.1016/j.molliq.2019.111675.
[19] U. Tarabara, M. Shchuka, K. Vus, O. Zhytniakivska, V. Trusova, G. Gorbenko, N. Gadjev and T. Deligeorgiev, East European Journal of Physics, **4**, 58-69 (2019), https://doi.org/10.26565/2312-4334-2019-4-06.

[20] L.M. Loura and M. Prieto, Front. Physiol. **2**, 82 (2011), https://doi.org/10.3389/fphys.2011.00082.

[21] O. Zhytniakivska, V. Trusova, G. Gorbenko, E. Kirilova, G. Kirilov and P. Kinnunen, Вісник Львівського університету. Серія біологічна. **68**, 279-285 (2014), http://nbuv.gov.ua/UJRN/VLNU_biol_2014_68_30.

[22] M. Groenning, J. Chem. Biol. **3**, 1-18 (2010), https://doi.org/10.1007/s12154-009-0027-5.

[23] A.I. Sulatskaya, A.A. Maskevich, I.M. Kuznetsova, V.N. Uversky and K.K. Turoverov, PLoS ONE, **5**, e15385 (2010), https://doi.org/10.1371/journal.pone.0015385.

[24] J.A. Vladimirov and G.E. Dobretsov, *Флуоресцентные зонды в исследовании биологических мембран [Fluorescent probes in study of biological membranes]*, (Nauka, Moscow, 1980), pp. 40. (in Russian)

[25] H.P. Oliveira, A.J. Camargo, L.G. Macedo, M.H. Gehlen and A.B. da Silva, Spectrochim. Acta A Mol. Biomol. Spectrosc. **58**, 3103–3111 (2002), https://doi.org/10.1016/S1386-1425(02)00119-1.

[26] L. Nielsen, R. Khurana, A. Coats, S. Frokjaer, J. Brange, S. Vyas, V.N. Uversky and A.L. Fink, Biochemistry, **40**, 6036-6046 (2001), https://doi.org/10.1021/bi002555c.

[27] J.L. Jiménez, E.J. Nettleton, M. Bouchard, C.V. Robinson, C.M. Dobson and H. Saibil, Proc. Natl. Acad. Sci. USA, **99**, 9196-9201 (2002), https://doi.org/10.1073/pnas.142459399.

[28] H. Yoshihara, J. Saito, A. Tanabe, T. Amada, T. Asakura, K. Kitagawa and S. Asada, J. Pharm. Sci. **105**, 1419-1426 (2016), https://doi.org/10.1016/j.xphs.2016.01.025.

[29] M. Groenning, M. Norrman, J.M. Flink, M. van de Weert, J.T. Bukrinsky, G. Schluckebier and S. Frokjaer, J. Struct Biol. **159**, 483-497 (2007), 10.1016/j.jsb.2007.06.004.

КАСКАДНИЙ ПЕРЕНОС ЕНЕРГІЇ В АМІЛОЇДНИХ ФІБРИЛАХ ІНСУЛІНУ, ДОПОВАНИХ ТІОФЛАВІНОМ Т, БЕНЗАНТРОНОВИМ ТА СКВАРАЇНОВИМИ БАРВНИКАМИ

У. Тарабара[a], К. Вус[a], М. Щука[a], О. Кірілова[b], Г. Кірілов[b], О. Житняківська[a], В. Трусова[a], Г. Горбенко[a], Т. Делігеоргієв[c]

[a]Кафедра медичної фізики та біомедичних нанотехнологій,
Харківський національний університет імені В.Н. Каразіна
м. Свободи 4, Харків, 61022, Україна
[b]Факультет хімії та географії, Даугавпілський університет, Даугавпілс, LV5401, Латвія
[c]Факультет хімії і фармації, Софійський університет, Софія, 1164, Болгарія

Протестовано можливість використання трьохетапного індуктивно-резонансного переносу енергії (IРПЕ) у системі зондів, що включала класичний амілоїдний маркер тіофлавін Т (ThT), бензантроновий медіатор ABM та сквараїнові барвники SQ1, SQ4, для детектування та характеризації амілоїдних фібрил інсуліну. Виявлено високі значення ефективності багатоетапного IРПЕ у даному ансамблі хромофорів за наявності амілоїдних фібрил інсуліну, сформованих при підвищених температурах та pH 2 (InsF1) або pH 7.4, 0.15 M NaCl (InsF2), у той час як незначний IРПЕ спостерігали у нефібрилізованому білку (контроль), що свідчить про специфічність зондів каскаду до крос-β-складчатої архітектури амілоїдних фібрил. Зокрема, ефективність IРПЕ для донорно-акцепторних пар ThT-ABM, ABM-SQ4 та SQ4-SQ1 за максимальної концентрації акцептора (~ 0.4 µM – 1.6 µM) становила 86%/94%, 48%/34% та 66%/8%, відповідно, у присутності InsF1/InsF2. Найбільш суттєві відмінності між InsF1/InsF2 та контрольним білком виявлено для донорно-акцепторної пари ThT-ABM, що свідчить про ключову роль ABM як медіатора у процесі багатоетапного IРПЕ. При оцінці відстаней між донором і акцептором у фібрилярних агрегатах InsF1, за умови ізотропного обертання зондів отримані значення 1.3 нм, 5.3 нм та 3.9 нм для пар ThT-ABM, ABM-SQ4 та SQ4-SQ1, відповідно. Ці результати свідчать про різні сайти зв'язування фібрил для зондів каскаду, хоча завдяки їх високій специфічності до фібрилярних структур, барвники мають бути локалізовані у поверхневих жолобках β-листів, що простягаються уздовж головної осі амілоїдної фібрили. Слід зауважити, що різниця у морфології амілоїдних фібрил може бути чітко охарактеризована за допомогою багатоетапного IРПЕ. Зокрема, за даними електронної мікроскопії виявлено, що фібрили InsF2 були більш тонкими, короткими та містили аморфні агрегати, у порівнянні з InsF1. Вочевидь, різні шляхи формування амілоїдних фібрил при нейтральному та кислому значеннях pH, призвели до різної афінності зондів до сайтів зв'язування фібрил, та, як наслідок, до різних значень ефективності IРПЕ, особливо для пари SQ4-SQ1. Здатність ThT слугувати ефективним підсилювачем для SQ4 та SQ1, що флуоресціюють у ближній інфрачервоній області, при використанні бензантронового флуорофору ABM у якості медіатора дозволяє детектувати фібрили інсуліну в оптичному вікні біологічних зразків завдяки стоксовому зсуву чотирьох-хромофорної системи близько 240 нм. Запропонований підхід, що базується на багатоетапному IРПЕ, можна використовувати не лише для детектування амілоїдних фібрил інсуліну, але і для диференціювання морфології фібрилярних агрегатів та встановлення механізмів розвитку ін'єкційно-локалізованого інсулінового амілоїдозу.

КЛЮЧОВІ СЛОВА: АБМ, каскадний індуктовно-резонансний перенос енергії, аміло�їдні фібрили інсуліну, квантовий вихід, тіофлавін Т.

КАСКАДНЫЙ ПЕРЕНОС ЭНЕРГИИ В АМИЛОИДНЫХ ФИБРИЛЛАХ ИНСУЛИНА, ДОПИРОВАННЫХ ТИОФЛАВИНОМ Т, БЕНЗАНТРОНОВЫМ И СКВАРАИНОВЫМИ КРАСИТЕЛЯМИ

У. Тарабара[a], К. Вус[a], М. Щука[a], Е. Кирилова[b], Г. Кирилов[b], О. Житняковская[a], В. Трусова[a], Г. Горбенко[a], Т. Делигеоргиев[c]

[a]Кафедра медицинской физики и биомедицинских нанотехнологий,
Харьковский национальный университет имени В.Н. Каразина
пл. Свободы 4, Харьков, 61022, Украина
[b]Факультет химии и географии, Даугавпилский университет, Даугавпилс, LV5401, Латвия
[c]Факультет химии и фармации, Софийский университет, София, 1164, Болгария

Протестировано возможность применения трехэтапного индуктивно-резонансного переноса энергии (ИРПЭ) в системе зондов, которая включала классический амилоидный маркер тиофлавин Т (ThT), бензантроновый медиатор ABM и сквараиновые красители SQ1, SQ4, для детектирования и характеризации амилоидных фибрилл инсулина. Обнаружено

высокие значения эффективности многоэтапного ИРПЭ в данном ансамбле хромофоров в присутствии амилоидных фибрилл инсулина, сформированных при повышенных температурах и pH 2 (InsF1) или pH 7.4, 0.15 M NaCl (InsF2), в то время как незначительный ИРПЭ наблюдали в нефибриллизированном белке (контроль), что свидетельствует о специфичности зондов каскада к β-складчатой архитектуре амилоидных фибрилл. В частности, эффективность ИРПЭ для донорно-акцепторных пар ThT-ABM, ABM-SQ4 и SQ4-SQ1 при максимальной концентрации акцептора (~ 0.4 μM – 1.6 μM) составила 86%/94%, 48%/34% и 66%/8%, соответственно, в присутствии InsF1/InsF2. Наиболее существенные отличия между InsF1/InsF2 и контрольным белком обнаружены для донорно-акцепторной пары ThT-ABM, что свидетельствует о ключевой роли ABM как медиатора в процессе многоэтапного ИРПЭ. При оценке расстояний между донором и акцептором в фибриллярных агрегатах InsF1, при условии изотропного вращения зондов получены значения 1.3 нм, 5.3 нм и 3.9 нм для пар ThT-ABM, ABM-SQ4 и SQ4-SQ1, соответственно. Эти результаты свидетельствуют о разных сайтах связывания фибрилл для зондов каскада, хотя благодаря их высокой специфичности к фибриллярным структурам, красители должны локализоваться в поверхностных желобках β-листов, которые простираются вдоль основной оси амилоидной фибриллы. Следует отметить, что различия в морфологии амилоидных фибрилл можно четко охарактеризовать при помощи многоэтапного ИРПЭ. В частности, согласно данным электронной микроскопии, фибриллы InsF2 были более тонкими, короткими и содержали аморфные агрегаты, в отличие от InsF1. Очевидно, разные пути формирования амилоидных агрегатов при нейтральном и кислом значениях pH, обусловливают разную афинность зондов к сайтам связывания фибрилл, и, следовательно, разные значения эффективности многоэтапного ИРПЭ, особенно для пары SQ4-SQ1. Способность ThT служить эффективным усилителем для SQ4 и SQ1, которые флуоресцируют в ближней инфракрасной области, при использовании бензантронового флуорофора ABM в качестве медиатора, позволяет детектировать амилоидные агрегаты инсулина в оптическом окне биологических образцов благодаря стоксовому сдвигу четыреххромофорной системы около 240 нм. Предложенный поход, который базируется на многоэтапном ИРПЭ, можно использовать не только для детектирования амилоидных фибрилл инсулина, но и для дифференцирования морфологии фибриллярных агрегатов и выяснения механизмов развития инъекционно-локализованного инсулинового амилоидоза.

КЛЮЧЕВЫЕ СЛОВА: АБМ, каскадный индуктивно-резонансный перенос энергии, амилоидные фибриллы инсулина, квантовый выход, тиофлавин Т.

STUDY ON CONCEPTUAL DESIGNS OF SUPERCONDUCTING COIL FOR ENERGY STORAGE IN SMES

Md. Abdullah Al Zaman[a]*, **M.R. Islam**[b], **H.M.A.R. Maruf**[c]

aDepartment of Textile Engineering, Northern University Bangladesh, Dhaka, Bangladesh
bDepartment of Physics, University of Chittagong, Chittagong 4331, Bangladesh
cDepartment of Physics, Chittagong University of Engineering and Technology, Chittagong- 4349, Bangladesh
*Corresponding Author: proyashzaman@gmail.com
Received October 12, 2019; revised November 22, 2019; accepted January 21, 2020

Superconducting Magnetic Energy Storage (SMES) is an exceedingly promising energy storage device for its cycle efficiency and fast response. Though the ubiquitous utilization of SMES device is restricted because of the immense cost of cryogenic refrigeration system to sustain the superconducting state but with the continuous evolution of high Tc superconductors, SMES is turning into a major contender to the existing energy storage devices in the future. Among its several parts, the superconducting coil is considered to be the most crucial segment of this technology and the inductance generated in the coil determines the quantity of stored energy. In this paper, the possible geometrical configurations of SMES coil have been demonstrated. High Tc superconducting tapes are usually employed to form these configurations worldwide. BSCCO (Bismuth strontium calcium copper oxide)-2223 tape superconductor has been considered for studying the conceptual designs of superconducting coil of SMES. Before estimating the results, the value of critical current at different magnetic field densities and temperatures have been addressed through the study of superconducting tape characterization. Numerical results and the relationship among the several parameters for both the solenoid and toroid configurations in different specifications have been presented. Based on the results, the size ratio in solenoid and the mean toroid diameter in toroid arrangement is found to play the vigorous roles in the generation of inductance and hence the energy storage. The results also match the propensity of other studies. Suggestions for maximum energy gain from a specific solenoid configuration have been provided. Future research scopes with alternative superconducting tapes and limitations of this study have been briefly conferred.

KEYWORDS: SMES, inductance, energy storage device, solenoid, toroid.

Superconducting magnetic energy storage (SMES) is one of the benedictions of superconductivity. SMES stores energy in the form of magnetic field produced by the flow of direct current in a superconducting coil which has been cryogenically cooled to a temperature below its superconducting critical temperature (Tc). The stored energy can be released back to the network by discharging the coil [1]. Discovery of high-Tc materials as well as the development of other equipment is making SMES a better option in energy storage facilities [2]. SMES is considered as one of the most efficient energy storage systems and its lifetime is also relatively higher than the other storage systems [2]. SMES can be used in several ways like FACTS (Flexible AC Transmission System), UPS (Uninterruptible Power Supplies), System stabilizer and so on [3]. The essential parts of a SMES system consist of superconducting coil with the magnet (SCM), power conditioning system (PCS), cryogenic system (CS) and control unit (CU) [3]. Of them, the superconducting magnet coil or inductor is the most important part for technical as well as electrical perspective. The SCM is considered as the heart of the SMES technology. It is well known that the storage energy depends on fixed operating current I (of course below the critical current, I_c) and the inductance of the magnet coil. The possible way of increasing energy storage is to increase the inductance of the respective coil. Therefore, it is necessary to study the magnet coil which can be done by observing its characteristics. Since the beginning, there have been many experimental and theoretical studies led on this topic. There are three types of coils that may be considered; Solenoid, Multiple solenoid and toroid coil. Here, we will present the study on conceptual designs and theoretical considerations of superconducting magnet coils (solenoid and toroid) of SMES system for energy storage purpose. Before going to the key section, pertinent formulas utilized in this study have been introduced for understanding the study goal.

INDUCTANCE, ENERGY AND VOLUME OF A SMES COIL

When a DC current is passed in a normal conductor the energy would be dissipated due to the resistance of the wire. But when the flow of DC current in a wire made of the material that possesses superconducting behavior, a magnetic field is generated due to the flow under proper condition. This means that the energy will be stored in the form of a magnetic field in a persistent mode and will remain the same until utilized. A very steady DC current will also exist in a closed circuit due to the zero resistance environment of a superconductor. This principle works on a superconducting coil storing electrical energy in the form of magnetic field and the stored energy will be inductive. It can be written in the form [4, 5],

$$E = \frac{1}{2} LI^2 \tag{1}$$

where, L = Inductance of the coil, I = current that flows through the coil.

While designing a SMES system the calculation of inductance of the coil is very important to understand how much energy can be gained from this and how to accumulate or connect the other components including the protection. Typically there are two kinds of SMES magnet topologies:
1. Solenoid and
2. Toroid.

SOLENOID CONFIGURATION

Solenoid configuration is frequently used due to its simple winding process, high stray field and non -uniform stress. Fig.1(a) and 1(b) are showing the construction of the superconducting magnet in the solenoid configuration in a SMES system.

The inductance of a solenoid coil can be written in the form [5],

$$L = \pi\mu_0 \left(\frac{N^2 D_i}{16\beta}\right) \frac{(\alpha+1)^2}{1+0.9\left(\frac{\alpha+1}{4\beta}\right)+0.64\left(\frac{\alpha-1}{\alpha+1}\right)+0.84\left(\frac{\alpha-1}{2\beta}\right)}, \tag{.2}$$

where N is the total number of turns of the solenoid, D_0 is the outer radius and D_i is the inner radius of the solenoid coil. α and β are the size ratios which are determined by the following formulas,

$$\alpha = \frac{D_0}{D_i} \quad and \quad \beta = \frac{H}{D_i}, \tag{3}$$

where H is the total height of the coil and

$$H = W_p n_p \tag{4}$$

where: n_p = the number of pancake and W_p = width of the superconducting tape.
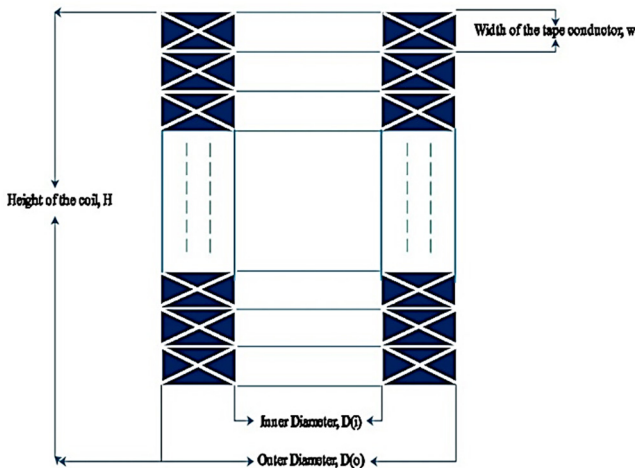

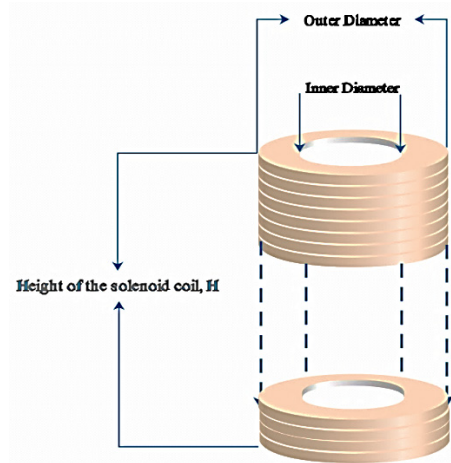| Fig. 1(a) SMES Coil in solenoid configuration | Fig. 1(b). Three dimensional representation of SMES Coil in solenoid configuration |

The total number of turns of the coil N of the solenoid is determined by the relation

$$N = n \times n_p \tag{5}$$

Here, n is the number of turns in each pancake and is written as

$$n = \frac{Outer\ Diameter(D_0) - inner\ diameter\ (D_i)}{2t} \tag{6}$$

where t is the thickness of the tape conductor.

Using Eq. (1) for inductance L and replacing I by I_c , the energy stored in a solenoid coil for a critical current I_c

$$E = \frac{I_c^2}{2} \left\{\pi\mu_0 \left(\frac{N^2 D_i}{16\beta}\right) \frac{(\alpha+1)^2}{1+0.9\left(\frac{\alpha+1}{4\beta}\right)+0.64\left(\frac{\alpha-1}{\alpha+1}\right)+0.84\left(\frac{\alpha-1}{2\beta}\right)}\right\} \tag{7}$$

Here, I_c (>I) is the maximum current sustain in a superconducting coil, determined by the relation

$$I_c = J_c A_{sc}, \tag{8}$$

where J_c= critical current density of the superconducting tape in (A/m^2), A_{sc}= Area through which current flows
And the area (in m^2) can be written as

$$A_{sc} = W_p t \tag{9}$$

The total volume of the SMES coil in solenoid arrangement can be written as (Figure 2)

$$V_1 = \pi r_1^2 H \tag{10}$$

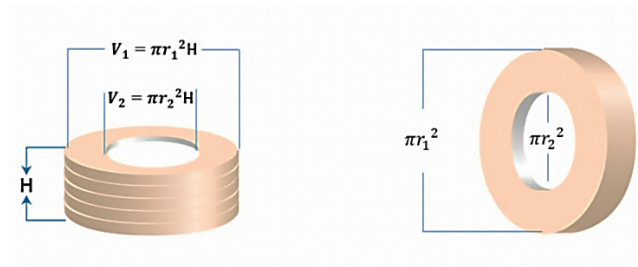And the volume of the inner empty space

$$V_2 = \pi r_2^2 H, \tag{11}$$

Fig. 2. Schematic for volume analysis of SMES coil

where r_1 is the outer radius and r_2 is the inner radius which can be calculated from

$$r_1 = \frac{D_o}{2} \ and \ r_2 = \frac{D_i}{2} \tag{12}$$

So the volume of the superconducting material is

$$V_{SC} = V_1 - V_2 = \pi r_1^2 H - \pi r_2^2 H \tag{13}$$

TOROID CONFIGURATION

In the toroid arrangement, the winding process is relatively complex but there are no limits to the stray field and the stress can be optimized more efficiently than the solenoid arrangement of the superconducting coil for the SMES system [6]. In Fig. 3(a) and 3(b) are showing the construction of the toroid configuration.

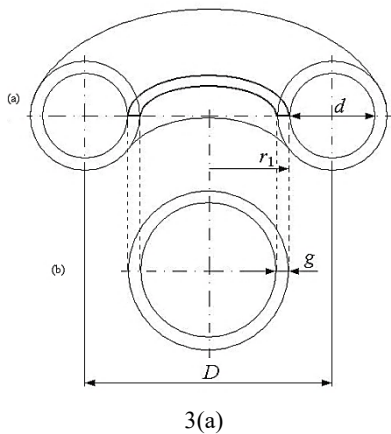3(a)   3(b)

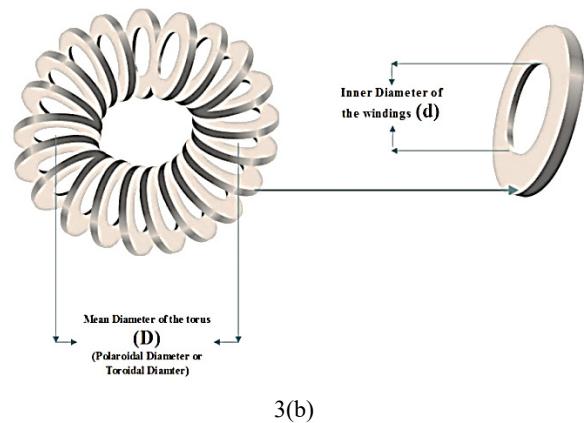Fig. 3(a). SMES Coil[7] in Toroid configuration   Fig. 3(b): Three dimensional representation of SMES Coil in Toroid configuration

In the Fig. 3(a) and 3(b) D is the mean diameter of torus, d is the inner diameter of winding and g is the thickness. For a thin winding torus, the exact analytical expression of inductance is written as [4, 7].

$$L = \frac{\mu_0}{2} [D - \sqrt{D^2 - d^2}], \tag{14}$$

where μ_0 = permeability in the vacuum.
Using equation (14), the energy stored in a toroid coil now can be written as

$$E = \frac{1}{2} L I_c^2 = \frac{\mu_0 I_c^2}{4} [D - \sqrt{D^2 - d^2}] \tag{15}$$

The total section or area of superconductor corresponding to the inner radius shown in Figure 2(b) is [7]

$$A_{sc} = \pi g (D - d - g) \tag{16}$$

Using equation (8) and (16), equation (15) can be written as,

$$E = \frac{\mu_0 J_c^2}{4} \pi^2 g^2 (D - d - g)^2 [D - \sqrt{D^2 - d^2}] \tag{17}$$

The volume of the superconducting material [7]

$$V_{SC} = \pi^2 g (D - d - g)(d + g) \tag{18}$$

Let us define,

$$\alpha = \frac{d}{D} \ and \ \beta = \frac{g}{D} \tag{19}$$

The energy and volume equations in terms of size ratio can be expressed as

$$E = \frac{\mu_0 J_c^2}{4} \pi^2 \beta^2 D^5 (1 - \alpha - \beta)^2 [1 - \sqrt{1 - \alpha^2}] \tag{20}$$

$$V_{SC} = \pi^2 D^2 (1 - \alpha - \beta)(\alpha + \beta) \tag{21}$$

HTS TAPE CHARACTERIZATION

Superconducting tapes or more specifically high temperature superconductor (HTS) tapes plays the major role in determining the quantity of inductance as well as the energy stored in the SMES system. But before utilization we have to understand the characteristics of the tapes that provide the proper idea about the quantity of the inductance that can be generated. Now a days, there are several options to this and the silver coated Bi2223 (Bismuth strontium Calcium Copper Oxide) HTS tape has been chosen for this study. These tapes are responsive to both the perpendicular and parallel magnetic field. The critical current that flows through the tape is also dependent on temperature. Lower the temperature, higher the critical current at a specific magnetic field density [9] [16]. The critical current also differs for perpendicular and parallel magnetic field.

For this study we have only considered the perpendicular component of the magnetic field. Figure 4 is showing the relationship of the current with the magnetic flux density at some certain temperature. From these we can find out the critical current in the HTS tape. These figures are taken from the experimental results [8] determined by Kozak J. et.al. (2009).
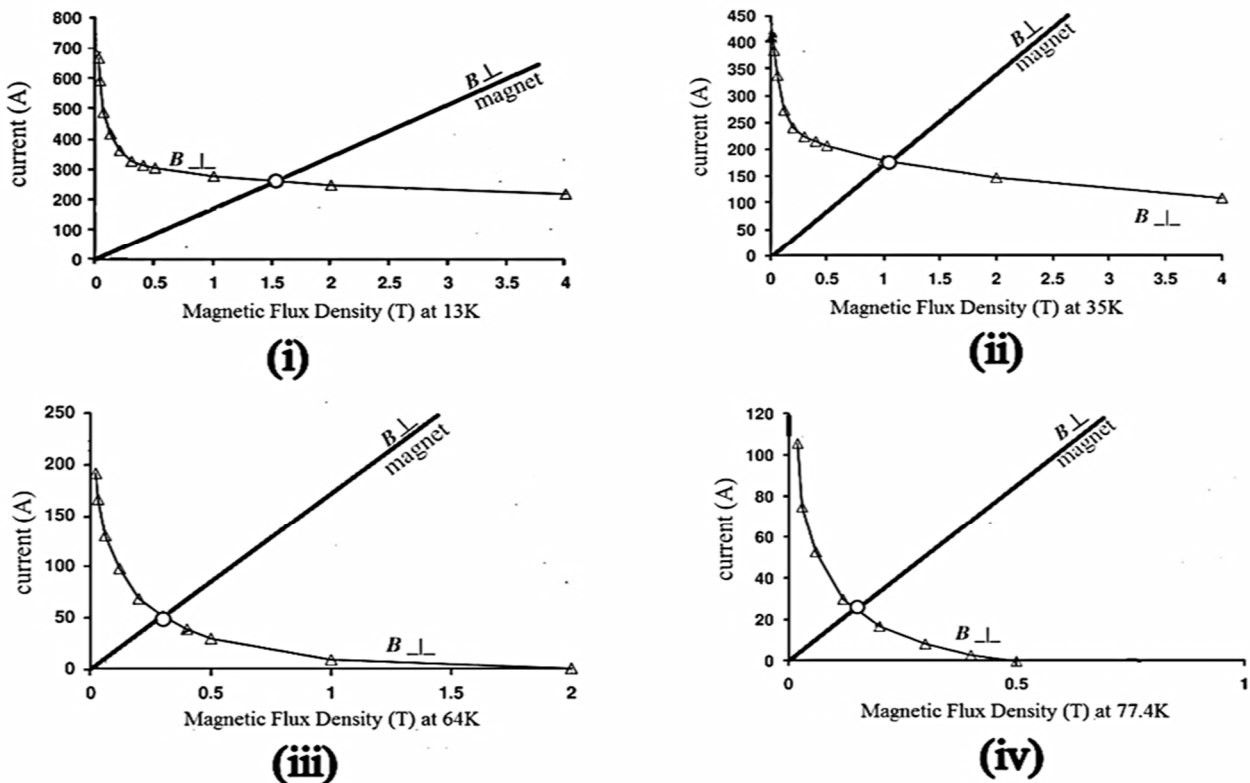

Fig. 4. (i-iv) - I_c-B relationship of Bi2223/Ag HTS tape with the perpendicular field component at different low temperatures [8,9]

From the characterization we have the critical values of current for the different perpendicular magnetic field at some specific temperatures (shown in Table 1).

Table 1.
Value of the critical currents at different temperatures for different perpendicular magnetic field component [8]

Temperature	Magnetic flux density	Critical Current I_C
77K	0.15T	25A
64K	0.30T	50A
35K	1.0T	180A
13K	1.5T	264A

STUDY METHODOLOGY

From section II we can see that the inductance is dependent on the several parameters like the inner diameter, outer diameter etc. for solenoid arrangement and in the toroid arrangement the toroid diameter and inner diameter of the pancake. So, several cases will be considered in this study. After the study of the inductance and energy the volume energy relationship will be presented. A comparison between these two configurations will also be presented. All the primary numerical calculations have been done with the help of SMES-PCC (superconducting magnetic energy storage-parameter calculation & characteristics) computer program developed by us. It is useful in calculating the inductance, energy and some other parameters required for designing a SMES coil [18]. Also MATLAB has been employed for additional calculations. The block diagram (Fig. 5) is showing the considerations and steps in this study.
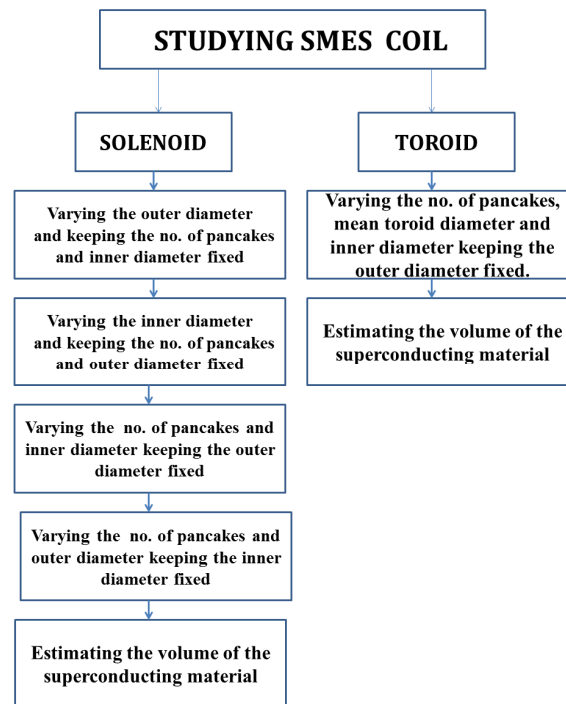

Fig. 5. Block diagram for describing the several steps and considerations in the study.

RESULTS

The tape specification is given in Table 2. As mentioned in the methodology, we have started with a fixed no. of pancake layers and inner diameter and considered some possible cases. Fig. 6 is illustrating the coil specification and the design. All the necessary illustrations have been drawn with **Edraw-Max** software.

Table 2.
Superconducting tape specification [5, 8, 9]

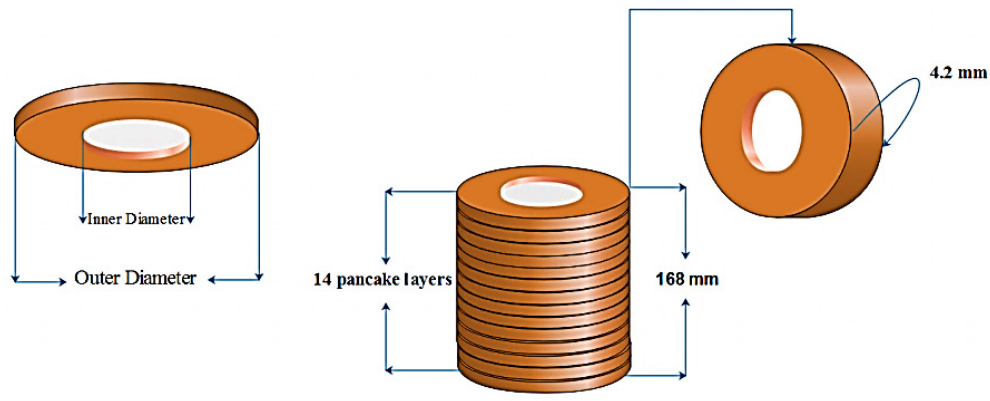| Tape specification	Bi2223/Ag HTS tape
Width of the tape (W_p)	4.2 mm or 0.0042 meter
Thickness of the tape (t)	0.31 mm or 0.00031 meter
Critical current I_c at 77K,0.15T	25A
Critical current I_c at 64K,0.30T	50 A
Critical current I_c at 35K,1.0T	180 A
Critical current I_c at 13K,1.50T	264 A

Fig. 6. Illustration of Pancake layers and solenoid arrangement (for 14 pancakes)

Fig. 7. is illustrating different values of outer diameter while keeping the inner diameter fixed. Fig. 8 is illustrating the considerations for the different values of inner diameter while keeping the outer diameter fixed. In Fig. 9, it is observed that the inductance increases when the inner diameter is retained constant and varying the outer diameter, greater the outer diameter greater the inductance and hence the energy, shown in Fig. 10. The opposite results are obtained when the outer diameter was kept constant and gradually increasing the inner diameter (Fig. 11).
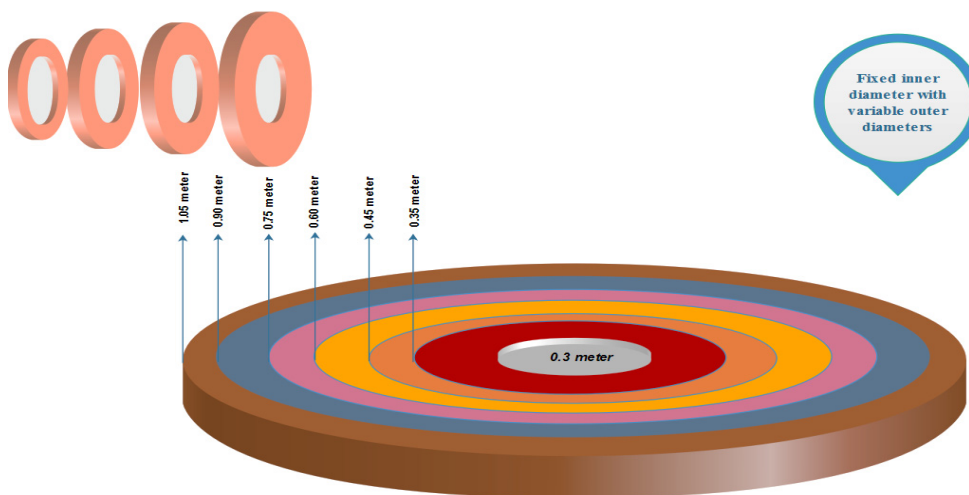

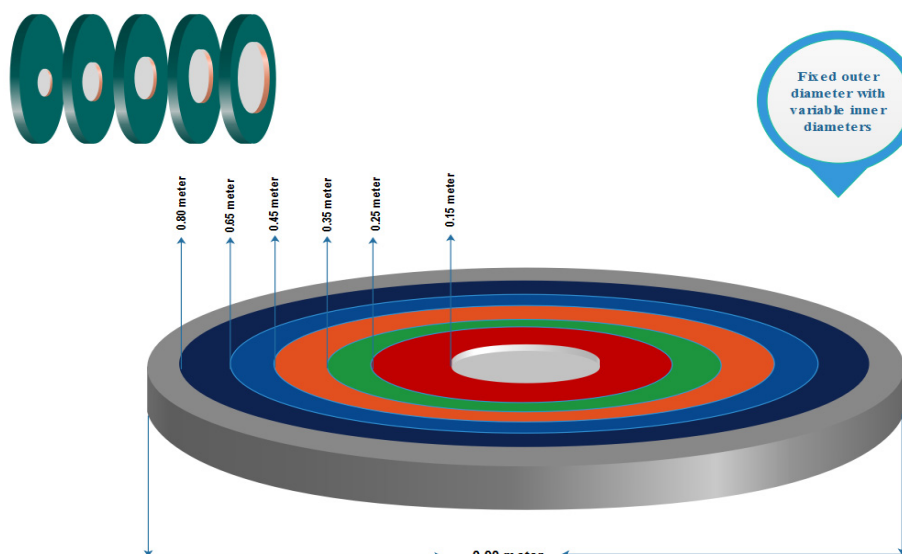Fig. 7. Constant inner diameter with variable outer diameter

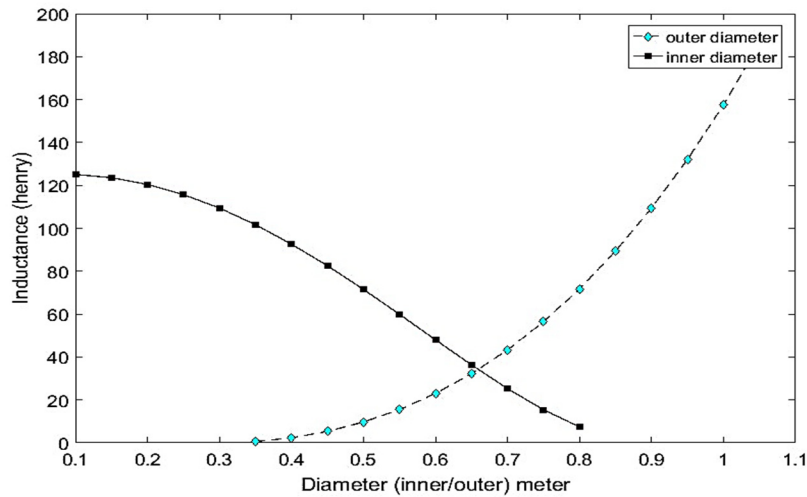Fig. 8. Constant outer diameter with variable inner diameter

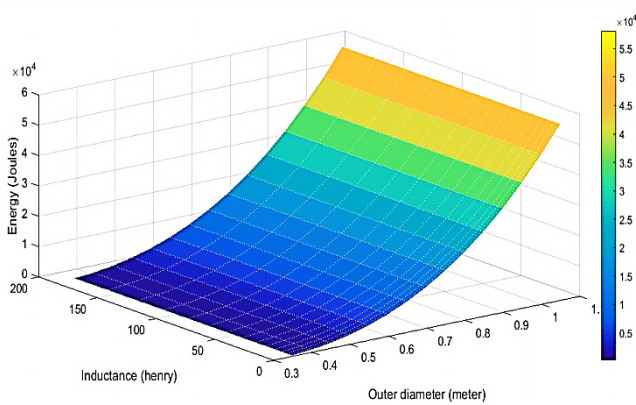Fig. 9. Variation of inductance with inner diameter and outer diameter

Fig. 10. Variation of inductance and energy with inner diameter at 25A @77K, 0.15T (keeping the outer diameter fixed)
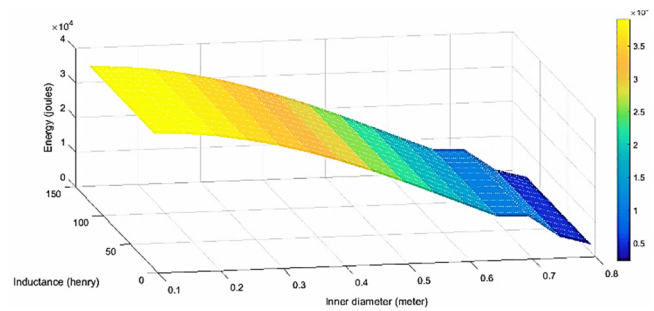
Fig. 11. Variation of inductance and energy with outer diameter at 25A @77K, 0.15T (keeping the inner diameter fixed)
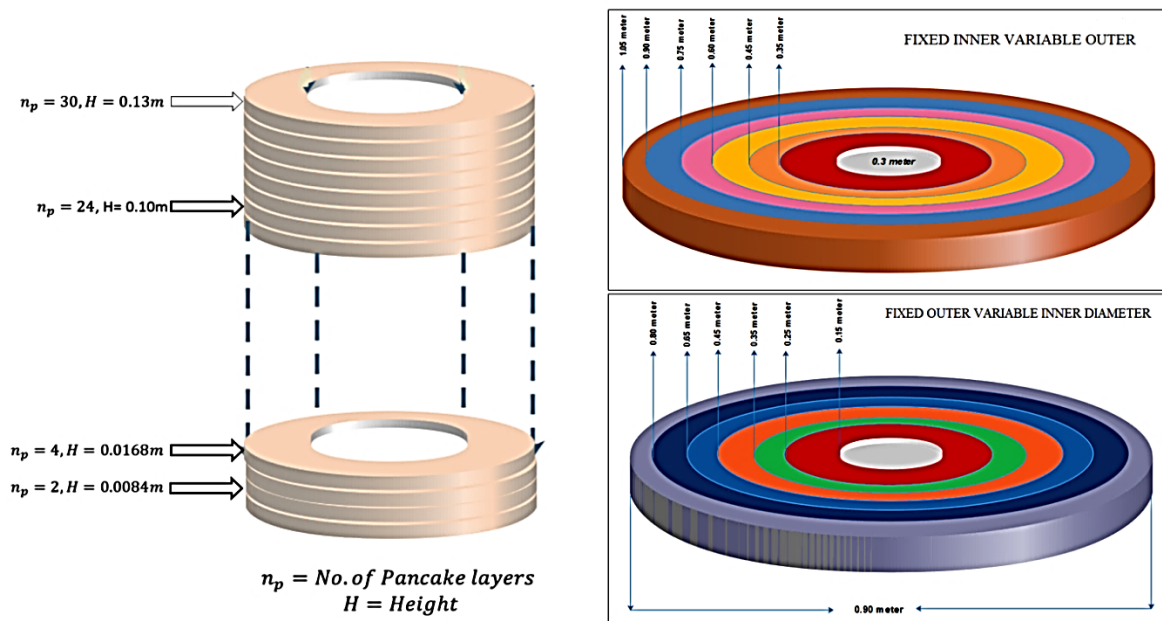
Fig. 12. Variable Pancakes consideration

Now we will observe the variation when the no. of pancakes varies with outer and inner diameters. Fig. 12 is showing the variation of pancakes with outer diameter (keeping inner diameter fixed) and inner diameter (keeping outer diameter fixed).

The calculated results (Fig. 13,14) indicate that the inductance as well as energy increases when the inner diameter is kept constant and vary the outer diameter and pancakes and vice versa. Quite interesting results obtained when we

kept the outer diameter constant and gradually increase the inner diameter and number of pancake layers. In this case the inductance rises up for a certain configuration but ultimately the inductance starts to decrease after reaching a maximum value (Fig. 15).

Fig. 14. Variation of inductance and energy with outer diameter at 25A @77K, 0.15T (Varying pancake layers and keeping the inner diameter fixed)

Fig. 13. Variation of inductance with inner diameter (While outer diameter is fixed) and outer diameter (while inner diameter is fixed)

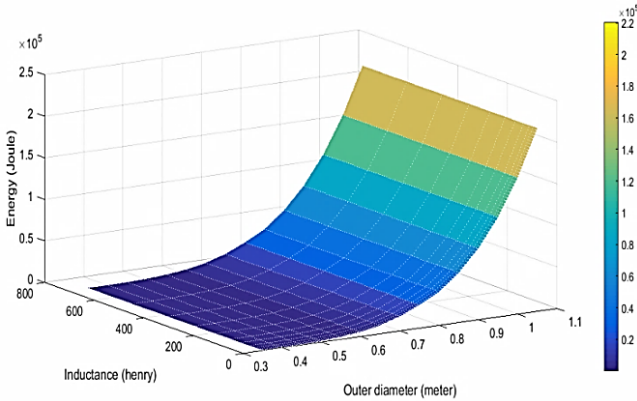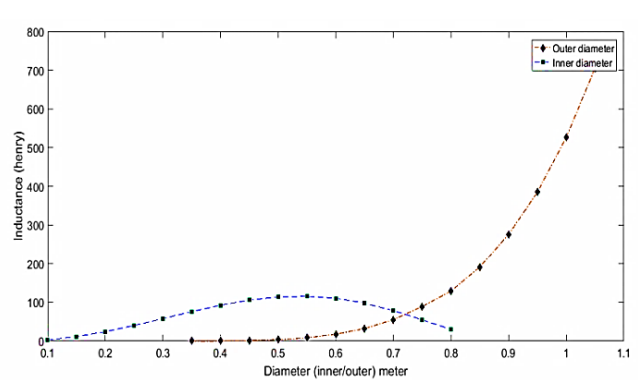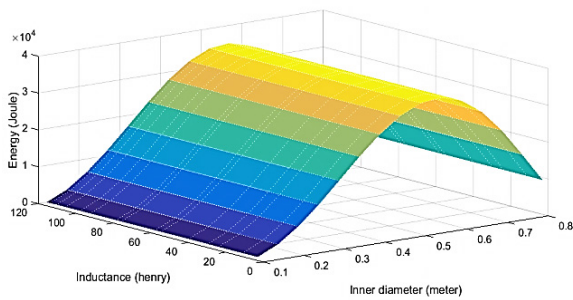Fig. 15. Variation of inductance and energy with inner diameter at 25A @77K, 0.15T (Varying the no. of pancakes and keeping the outer diameter fixed)
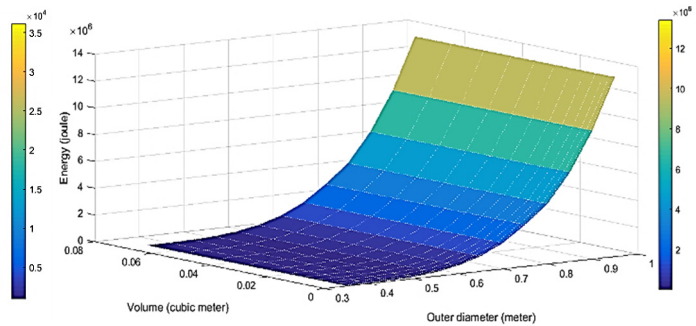
Fig. 16. Variation of Energy with volume and outer diameter at 264A @13K, 1.5T

Now considering the volume of the superconducting materials and the corresponding energy stored. The maximum energy can be obtained when we keep the inner diameter constant and vary the outer diameter at 264A @13K, 1.5T. Considering the variation of pancakes with the constant inner diameter and varying outer diameter, the volume of the superconducting material has been calculated. We see that the energy is positively related with the volume (Fig. 16) i.e. greater the volume greater the energy output.
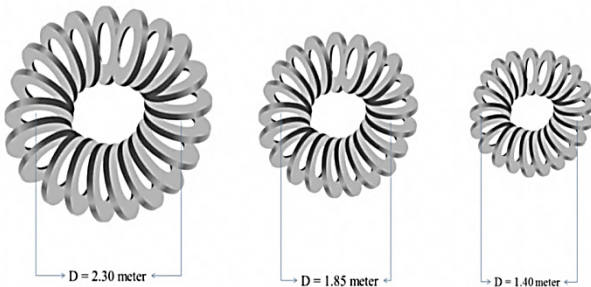
Fig. 17. Toroid design considerations
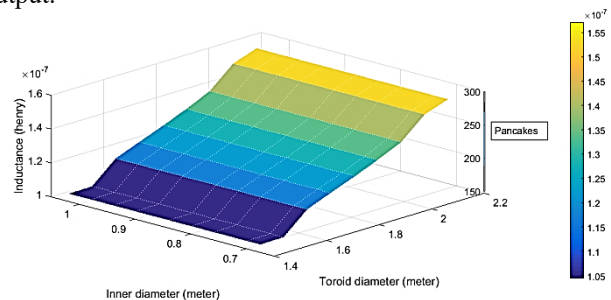
Fig. 18. Relationship between inductance, mean toroid diameter, inner diameter of the pancakes

Now we can study the toroid arrangement of SMES magnet. Fig. 17 is illustrating a few of the considerations. There are mainly two variables that determine the toroid inductance. The first one is the toroid diameter and the next one is the inner diameter of the toroid windings. So keeping the outer diameter fixed, varying the toroid diameter, inner diameter and pancakes we have calculated the values of inductance, shown in Fig. 18.
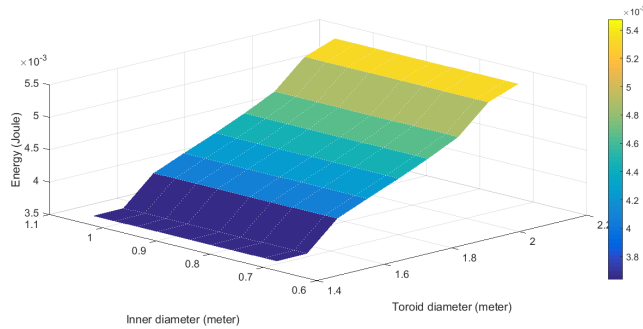
Fig. 19. variation of energy with mean toroid diameter and inner diameter (264 A @13K, 1.5T)
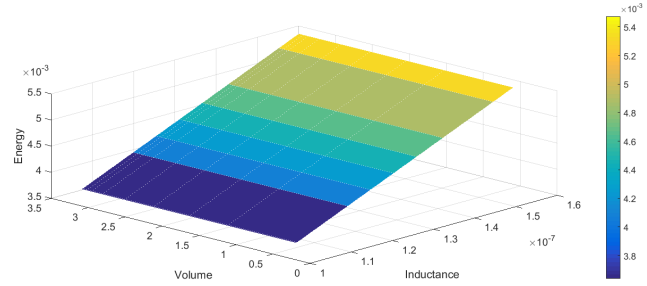
Fig. 20. Relationship among inductance, energy and volume. (At 264A, 13K@1.5T,)

From Fig. 18,19,20 it is clear that the inductance as well as energy in the toroid arrangement increases with the increase of mean toroid diameter as well as the inner diameter.

DISCUSSION AND CONCLUSION

The theoretical considerations of superconducting magnet have been demonstrated in Fig. (6, 7, 8, 12 and 17) and the results are in Fig. 9-11, 13-16, 18-21, provide the understanding of the relationships among the parameters that determines the amount of the energy stored in the system. In the study of the solenoid coils or magnets, it is observed that the outer diameter should be as great as possible to ensure the maximum amount of energy stored considering the smallest possible inner diameter. This can also be understood in terms of size ratio i.e. the ratio between the inner and outer diameter, greater the size ratio greater the inductance. Also the increasing number of pancake raises the amount of stored energy. But when we want to employ less amount of superconducting material and ensure maximum energy we have to optimize the configuration with inner diameter (Fig. 15). In the case of toroid the mean toroid diameter as well as inner diameter of the pancakes plays the most substantial role in determining the quantity of energy stored in the system. The obtained results are completely in coherence with the former theoretical and experimental studies [5, 7, 8, 9, 10, 16]. Though we have neglected the inter-distance between the pancakes in solenoid arrangement but it did not left any major impact on our results. This inter-distance between the pancake layers which is very tiny but definitely contribute to the height of the coil. If not omitted, the results should be the same, determined by others [8, 9].

We have calculated inductance for the toroid arrangement using thin torus winding (low thickness, g). The overall results suggest that the designs we have illustrated (regarding pancake layer, critical current, etc.) are not efficient for this arrangement (toroid), even the material volume does not affect much in stored energy compared to the solenoid arrangement.

It is essential to mention that for our theoretical study we have considered the same critical current for all the configurations while calculating the energy. Practically when the dimensions or the structural parameters changes there should be changes in the magnetic field as well as the critical current. So the practical implementations for some of these configurations will definitely deviate from the theoretical results.

However, for this study BSCCO tape superconductor has been considered but there are some other alternatives like YBCO tapes [13, 14] or the comparatively contemporary MgB_2 based superconductors [15] which are capable of attaining greater current densities ensuring greater amount of energy under the same condition as described in the HTS tape characterization. Also studies can be extended for other conceptual designs with LTS superconductors, like Nb-Ti which has greater current density.

ORCID IDs

Md. Abdullah Al Zaman https://orcid.org/0000-0002-3696-2127, **M.R. Islam** https://orcid.org/0000-0002-0151-2505
H.M.A.R. Maruf https://orcid.org/0000-0002-6031-3573

REFERENCES

[1] X. Luo, J. Wang, M. Dooner and J. Clarke, Applied energy, **137**, 511-536 (2015) https://doi.org/10.1016/j.apenergy.2014.09.081.
[2] W. Yuan and M. Zhang, in: *Handbook of Clean Energy Systems*, edited by J. Yan (John Wiley & Sons, Ltd., 2015). https://doi.org/10.1002/9781118991978.hces210.
[3] M.A. Al Zaman, S. Ahmed and N.J. Monira, in *International Conference on Nanotechnology and Condensed Matter Physics* (Dhaka, Bangladesh, 2018), https://doi.org/10.13140/RG.2.2.20403.53289/1.
[4] W. Hassenzahl, IEEE Transactions on Magnetics, **25**(2), 799-1802 (1989), https://doi.org/10.1109/20.92651.
[5] C. Chao and C. Grantham, in: *AUPEC 2005 Australasian Universities Power Engineering Conference*, edited by M. Negnevitsky (School of Engineering, University of Tasmania, 2005), pp. 375-379.
[6] M.R. Islam, *Study of SMES technology for electric power supply and investigation of its utility and possible implementation in Bangladesh*: *A Project report*, (University of Chittagong, July 2014).
[7] F. Ştefănescu, Annals of the University of Craiova, Electrical Engineering series, **35**, 2011, http://elth.ucv.ro/fisiere/anale/2011/33.pdf.
[8] J. Kozak, M. Majka, L. Jaroszynski, T. Janowski, S. Kozak, B. Kondratowicz–Kucewicz and G. Wojtasiewicz, Journal of Physics: Conference Series, **234**(3), 032034 (2010), https://doi.org/10.1088/1742-6596/234/3/032034.

[9] G. Wojtasiewicz, T. Janowski, S. Kozak, B. Kondratowicz-Kucewicz and M. Majka, Journal of Physics: Conference Series, **97**(1), 012019 (2008), https://doi.org/10.1088/1742-6596/97/1/012019.

[10] J. Kozak, S. Kozak, T. Janowski and M. Majka, IEEE Transactions on Applied Superconductivity, **19**(3), 1981-1984 (2009), https://doi.org/10.1109/TASC.2009.2018753.

[11] A. Morandi, M. Fabbri, B. Gholizad, F. Grilli, F. Sirois and V.M. Zermeño, IEEE Transactions on Applied Superconductivity, **26**(4), 1-6 (2016), https://doi.org/10.1109/TASC.2016.2535271.

[12] S.S. Kalsi, D. Aized, B. Conner, G. Snitchier, J. Campbell, R.E. Schwall, J. Kellers, T. Stephanblome, A. Tromm and P. Winn, IEEE transactions on applied superconductivity, **7**(2), 971-976 (1997), https://doi.org/10.1109/77.614667.

[13] Zhu, J., Yuan, W., Coombs, T.A. and Ming, Q., 2011. Simulation and experiment of a YBCO SMES prototype in voltage sag compensation. Physica C: Superconductivity, **471**(5-6), 199-204 (2011), https://doi.org/10.1016/j.physc.2010.12.015.

[14] K. Higashikawa, T. Nakamura, K. Shikimachi, N. Hirano, S. Nagaya, T. Kiss and M. Inoue, IEEE Transactions on Applied Superconductivity, **17**(2), 1990-1993 (2007), https://doi.org/10.1109/TASC.2007.898947.

[15] R. Hott, R. Kleiner, T. Wolf and G. Zwicknagl, (2013), e-print https://arxiv.org/abs/1306.0429.

[16] B. Kondratowicz-Kucewicz, T. Janowski, S. Kozak, J. Kozak, G. Wojtasiewicz and M. Majka, Journal of Physics: Conference Series, **234**(3), 032025 (2010), https://doi.org/10.1088/1742-6596/234/3/032025.

[17] S. Nomura, H. Tsutsui, S. Tsuji-Iio, H. Chikaraishi and R. Shimada, in *Proceedings of the Fifteenth International Toki Conference on "Fusion and Advanced Technology"*, **81**(20-22) 2535-2539 (2006), https://pascal-francis.inist.fr/vibad/index.php?action=getRecordDetail&idt=18346799.

[18] Md. Abdullah Zaman, https://doi.org/10.13140/RG.2.2.32352.53760.

ДОСЛІДЖЕННЯ КОНЦЕПТУ КОНСТРУКЦІЇ НАДПРОВІДНОЇ КОТУШКИ ДЛЯ ЗБЕРІГАННЯ ЕНЕРГІЇ В ННМЕ

М. Абдулла Аль Заман[a], М.Р. Іслам[b], Х.М.А.Р. Маруф[c]
[a]Кафедра текстильної техніки, Північний університет Бангладеш, Дака, Бангладеш
[b]Кафедра фізики, Університет Чіттагонг, Чіттагонг 4331, Бангладеш
[c]Фізичний факультет, Чіттагонгський інженерно-технологічний університет, Чіттагонг, 4349, Бангладеш

Надпровідний накопичувач магнітної енергії (ННМЕ) – надзвичайно перспективний пристрій для зберігання енергії через ефективність його циклу та швидкий відгук. Хоча повсюдне використання пристрою ННМЕ обмежене через величезну вартість кріогенної системи охолодження для підтримки надпровідного стану, але з постійною еволюцією надпровідників з високим Тс, ННМЕ перетворюється на головного конкурента існуючих пристроїв акумулювання енергії в майбутньому. Серед декількох його частин надпровідна котушка є найважливішим сегментом цієї технології, а індуктивність, що створюється в котушці, визначає кількість накопиченої енергії. У цій роботі продемонстровані можливі геометричні конфігурації котушки ННМЕ. Надпровідні стрічки з високим Тс зазвичай використовуються у всьому світі для формування цих конфігурацій. У роботі розглянута надпровідна стрічка з ВСКМО (вісмут-стронцій-кальцій-мідний оксид)-2223 для вивчення концептуальних конструкцій надпровідної котушки ННМЕ. Спочатку були визначені значення критичного струму при різній щільності магнітного поля та температурі шляхом вивчення характеристик надпровідних стрічок. Представлені чисельні результати та співвідношення між декількома параметрами як для соленоїдної, так і для тороїдної конфігурацій у різних специфікаціях. Виходячи з результатів, встановлено, що співвідношення розмірів у соленоїді та середній діаметр тороїда в розташуванні тороїдів відіграє важливу роль у генерації індуктивності, а отже, і в накопиченні енергії. Результати також відповідають дослідженням інших авторів. Надано пропозиції щодо максимального підсилення енергії для конкретної соленоїдної конфігурації. Також були коротко представлені майбутні сфери досліджень з альтернативними надпровідними стрічками та їх обмеження.
КЛЮЧОВІ СЛОВА: ННМЕ, індуктивність, накопичувач енергії, соленоїд, тороїд.

ИССЛЕДОВАНИЕ КОНЦЕПТА КОНСТРУКЦИИ СВЕРХПРОВОДЯЩЕЙ КАТУШКИ ДЛЯ ХРАНЕНИЯ ЭНЕРГИИ В СНМЭ

М. Абдулла Аль Заман[a], Н.Г. Ислам[b], Х.М.А.Р. Маруф[c]
[a]Кафедра текстильной техники, Северный университет Бангладеш, Дакка, Бангладеш
[b]Кафедра физики, Университет Читтагонг, Читтагонг 4331, Бангладеш
[c]Физический факультет, Читтагонгский инженерно-технологический университет, Читтагонг, 4349, Бангладеш

Сверхпроводящий накопитель магнитной энергии (СНМЭ) – чрезвычайно перспективное устройство для хранения энергии из-за эффективности его цикла и быстрый отклик. Хотя повсеместное использование устройства СНМЭ ограничено из-за огромной стоимости криогенной системы охлаждения для поддержания сверхпроводящего состояния, но с постоянной эволюцией сверхпроводников с высоким Тс, СНМЭ превращается в главного конкурента существующих устройств аккумулирования энергии в будущем. Среди нескольких его частей сверхпроводящая катушка является важнейшим сегментом этой технологии, а индуктивность, создаваемая в катушке, определяет количество накопленной энергии. В этой работе продемонстрированы возможные геометрические конфигурации катушки СНМЭ. Сверхпроводящие ленты с высоким Тс обычно используются во всем мире для формирования этих конфигураций. В работе рассмотрена сверхпроводящая лента с ВСКМО (висмут-стронций-кальций-медный оксид)-2223 для изучения концептуальных конструкций сверхпроводящей катушки СНМЭ. Сначала были определены значения критического тока для различной плотности магнитного поля и температуры путем изучения характеристик сверхпроводящих лент. Представленные численные результаты и соотношение между несколькими параметрами как для соленоидных, так и для тороидальных конфигураций в различных спецификациях. Исходя из результатов, установлено, что соотношение размеров в соленоиде и средний диаметр тороида в расположении тороидов играет важную роль в генерации индуктивности, а следовательно, и в накоплении энергии. Результаты также соответствуют исследованиям проведенными другими авторами. Даны предложения по максимальному усиления энергии для конкретной соленоидный конфигурации. Также были кратко представлены будущие сферы исследований с альтернативными сверхпроводящими лентами и их ограничения.
КЛЮЧЕВЫЕ СЛОВА: СНМЭ, индуктивность, накопитель энергии, соленоид, тороид.

HYDRODYNAMIC MODEL OF TRANSPORT SYSTEM

Oleh M. Pihnastyi[a]*, Valery D. Khodusov[b]**

ᵃNational Technical University "KhPI"
Kyrpychev str. 2, Kharkiv, Ukraine
ᵇV.N. Karazin Kharkiv National University, Kharkov, Ukraine
*Corresponding Author: pihnastyi@gmail.com, **vkhodusov@ukr.net

A hydrodynamic model of production systems with a flow method of organizing production is considered. The basic macro-parameters of the state of the production flow line and the relationship between them are determined. The choice of a lot of moment approximation for modelling the production line is justified. It is shown that the conveyor-type flow line is a complex dynamic system with distributed parameters. The boundary value problem is formulated for the longitudinal vibrations of the conveyor belt when the material moves along the transportation route. It is assumed that there is no sliding of material along the conveyor belt, and the deformation that occurs in the conveyor belt is proportional to the applied force (Hooke's elastic deformation model). The significant effect of the uneven distribution of the material along the transportation route on the propagation velocity of dynamic stresses in the conveyor belt is shown. When constructing the boundary and initial conditions, the recommendations of DIN 22101: 2002-08 were used. The mechanism of the occurrence of longitudinal vibrations of the conveyor belt when the material moves along the transportation route is investigated. The main parameters of the model that cause dynamic stresses are determined. It is shown that dynamic stresses are formed as a result of a superposition of stresses in the direct and reflected waves. Analytical expressions are written that make it possible to calculate the magnitude of dynamic stresses in a conveyor belt and determine the conditions for the occurrence of destruction of the conveyor belt. The characteristic phases of the initial movement of the material along the technological route are considered. The process of the emergence of dynamic stresses with the constant and variable acceleration of the conveyor belt is investigated. The dynamics of stress distribution along the transportation route is presented. It is shown that the value of dynamic stresses can exceed the maximum permissible value, which leads to the destruction of the conveyor belt or structural elements. The transition period is estimated, which is required to ensure a trouble-free mode of transport operation during acceleration or braking of the conveyor belt. The use of dimensionless parameters allows us to formulate criteria for the similarity of conveyor systems.

KEY WORDS: hydrodynamic model of a transport system, two-moment description, Hooke model, balance equations, PDE production model

The methods of statistical physics are one of the tools for modelling production systems with the flow method of organizing production [1], [2]. The developed models of production systems in the hydrodynamic approximation are widely used in the design of highly efficient flow production line control systems at leading world enterprises [3]. The values of the macro parameters of the state of the production system are determined through the values of the state parameters of a large number of products that are in different stages of processing in technological operations along the technological route [4]. The main macro-parameters of the state used to describe production systems with the in-line method of organizing production are the density of products in inter operational backlogs $[\chi]_0(t,S)$ and the intensity of product processing $[\chi]_1(t,S)$ for technological operations. The trajectories of the movement of individual products along the technological route are determined by the laws established by the technological process of manufacturing the finished product and are reflected in the route maps of the enterprise. As a result of technological processing, the product passes from one state to another as a result of exposure to technological equipment and the interaction between individual products [1, 4]. The set of points that specify a continuous change in the state of the product determines the technological path of the product in the phase state space. The change in the condition of the product as a result of the influence of technological equipment occurs as a result of the transfer of technological resources to products. The balance equations for the macroscopic parameters of the production system with the flow type of organization of production are determined, to a large extent, by the technological laws of the interaction of products with each other and technological equipment.

DISTRIBUTED MODEL OF THE PRODUCTION LINE

In a multi-moment approximation, the system of balance equations for the macro parameters of the production flow line has the form [1–3]:

$$\frac{\partial [\chi]_0(t,S)}{\partial t} + \frac{\partial [\chi]_1(t,S)}{\partial S} = \int_0^\infty G(t,S,\mu)d\mu \, , \qquad (1)$$

$$\frac{\partial[\chi]_k(t,S)}{\partial t} + \frac{\partial[\chi]_{k+1}(t,S)}{\partial S} + kf(t,S)[\chi]_{k-1}(t,S) = \int_0^\infty \mu^k G(t,S,\mu)d\mu ,$$

$$\int_0^\infty \mu^k \chi(t,S,\mu)d\mu = [\chi]_k(t,S), \qquad k \geq 0, \qquad f(t,S) = \frac{\partial}{\partial t}\left(\frac{[\chi]_{1\psi}(t,S)}{[\chi]_0(t,S)}\right) + \frac{[\chi]_{1\psi}(t,S)}{[\chi]_0(t,S)}\frac{\partial}{\partial S}\left(\frac{[\chi]_{1\psi}(t,S)}{[\chi]_0(t,S)}\right),$$

where S is the technological position at which the product is in the technological route at a time t (waiting for processing or processing), $S \in [0, S_d]$; $\chi(t,S,\mu)$ is function of the distribution of subjects of labour by state in the phase technological space; $[\chi]_{1\psi}(t,S)$ is the rate of processing products along the technological route at the position determined by the coordinate S (the processing rate of the product in accordance with the technical documentation or equipment data sheet). The pace of processing products $[\chi]_{1\psi}(t,S)$ in most cases is considered a given. $G(t,S,\mu)$ is a function that determines the process of equipment transferring technological resources to the subject of labour [1]. The system of equations (1) is not closed. Closing conditions are determined from the specific operating conditions of the production line. To describe the state of a production system with a flow method of organizing production, in the vast majority of cases, the first two moments $[\chi]_0(t,S)$ or $[\chi]_1(t,S)$ of the distribution function of subjects of labour by the states $\chi(t,S,\mu)$ are used. When constructing models in the one-moment description, the closure condition is often applied:

$$\frac{\partial[\chi]_0(t,S)}{\partial t} + \frac{\partial[\chi]_1(t,S)}{\partial S} = 0 , \qquad [\chi]_1(t,S) = [\chi]_{1\psi}(t,S) .$$

The disadvantage of the one-moment description is that such a description does not provide an opportunity to study the fluctuations of the flow parameters of the production line. To describe production lines for which the presence of fluctuations in flow parameters is of practical importance, a two-moment description can be used:

$$\frac{\partial[\chi]_0(t,S)}{\partial t} + \frac{\partial[\chi]_1(t,S)}{\partial S} = \int_0^\infty G(t,S,\mu)d\mu , \quad \frac{\partial[\chi]_1(t,S)}{\partial t} + \frac{\partial[\chi]_2(t,S)}{\partial S} + f(t,S)[\chi]_0(t,S) = \int_0^\infty \mu G(t,S,\mu)d\mu , \qquad (2)$$

$$[\chi]_2 = \int_0^\infty \mu^2 \chi(t,S,\mu)d\mu = [\chi]_1(t,S)\frac{[\chi]_1(t,S)}{[\chi]_0(t,S)} + \int_0^\infty\left(\mu - \frac{[\chi]_1(t,S)}{[\chi]_0(t,S)}\right)^2 \chi(t,S,\mu)d\mu .$$

Such systems may include conveyor-type production lines, for which fluctuations in flow parameters exceeding the limit level can lead to break down of technological equipment. As an alternative approach for studying fluctuations in the flow parameters of production lines, kinetic models of production lines can be called [5]. However, kinetic models are currently not widely used for designing highly efficient production line control systems. In this regard, the main focus of this article will be on the study of fluctuations in the flow parameters of the production line using a two-moment model in the form (2).

CONVEYOR TYPE PRODUCTION LINE MODEL

Among the models of conveyor systems, two large groups should be distinguished. The first group includes models for calculating the flow parameters of the conveyor line. When building models of this group are used: the finite element method (FEM) [6]; finite difference method (FDM) [7]; Lagrange equations [8]; aggregated equation of state [9,10,11]; equations for neural network layers [12]; system dynamics equations [13] and multiple regression equations [14–16]. The models of the first group are used in the tasks of operational planning of production activities of the enterprise. For a given quality criterion, the algorithms of optimal control of the flow parameters of the transport system are built on the foundation of these models. The second group includes models for the force calculation of structural elements of the transport system [16–22]. Of particular practical interest are the models that determine the conditions for the destruction of the conveyor belt [6,8,23–29]. This allows you to determine the design parameters of the conveyor belt and the dynamic load modes, which ensure the stable operation of the transport system. The energy consumption required for the transport system (belt conveyor type 2LU120V) can be represented by the expression [30–32]:

$$N(t) = N_{xx} + n_1 M(t) , \qquad (3)$$

where N_{xx} is the power of the conveyor idling; n_1 is increment of power consumption with an increase in the mass of cargo on the conveyor by 1 ton. According to the experiment for a belt conveyor type 2LU120V $N_{xx} = 160$(kW), $n_1 = 1{,}11$(kW/t). The theoretical calculation of the standard energy costs required for the operation of the 2LU120V

conveyor line [31, p.62] of length $S_d = 730$ (m), with an average belt speed $a(t) = 3.15$ (m/sec), maximum productivity $[\chi]_1(t,0) = 1450(t/h)$ and mass per linear meter of moving parts $[\chi]_{0C} = 138.1$(kg/m) in the normative loading mode gives the following values model coefficients: $N_{xx} = 123.84$(kW), $n_1 = 1.23$(kW/t). The maximum amount of material in the transport system with a uniform distribution of material on the conveyor belt is $M_{max} \approx 100(t)$ for the maximum allowable linear density $[\chi]_{0\,max} \approx 134(kg/m)$:

$$M_{max} = \frac{[\chi]_1(t,0)}{a(t)} S_d = \frac{1450(t/h)}{3.15(\text{m/sec})} 730(m) \approx 100(t), \qquad\qquad [\chi]_{0\,max} = \frac{M_{max}}{S_d} \approx \frac{100(t)}{730(m)} \approx 134(kg/m).$$

Experimental studies and theoretical calculations show that the maximum allowable linear density $[\chi]_{0\,max}$ and mass per linear meter of moving parts $[\chi]_{0C}$ are comparable quantities. The unit cost of energy for the movement of the material of a unit mass can be represented in the following form

$$\frac{N(t)}{M(t)} = \frac{N_{xx}}{M(t)} + n_1 = n_{xx}\frac{[\chi]_{0C}}{[\chi]_0} + n_1, \tag{4}$$

where n_{xx} is unit costs of electricity for moving a running meter of conveyor belt. Expression (4) demonstrates two ways to reduce the unit cost of energy. The first way is to reduce the weight of a running meter of moving parts $[\chi]_{0C}$, in particular, by changing the thickness of the cross section of the conveyor belt. The second way is to increase the load on conveyor systems $[\chi]_0 \rightarrow [\chi]_{0\,max}$ when applying algorithms to control the speed of conveyor belts [25, 32, 33], which makes it possible to save up to 30% in the specific energy spent on moving the material [25, 30]. As a result of using conveyor belt speed control systems, a 30% reduction in specific energy costs is achieved by increasing the load on conveyor systems, for which the traditional filling level of conveyor belt material is 60–100%. However, as a result of controlling the speed of the belt, there is a constant acceleration and braking of the conveyor belt loaded with material. This causes additional stresses on the material of the conveyor belt and, as a result, its damage. One of the ways to avoid damage to the conveyor belt is to increase the thickness of the conveyor belt, and therefore the mass of a running meter of moving parts $[\chi]_{0C}$. An increase in the mass of a running meter of the conveyor belt leads to an increase in the specific energy costs required to move the extracted material of a single mass. In this regard, in the present work, the main attention is paid to the interconnection of the stream parameters of the conveyor and the design parameters of the conveyor belt.

To build a model of the transport system, we use the two-moment description equations (2) in the following form [35]:

$$\frac{\partial[\chi]_0(t,S)}{\partial t} + \frac{\partial[\chi]_1(t,S)}{\partial S} = \delta(S)\lambda(t), \qquad \frac{\partial[\chi]_1(t,S)}{\partial t} + \frac{\partial[\chi]_2(t,S)}{\partial S} - f(t,S)[\chi]_0(t,S) = \delta(S)\lambda(t)\frac{[\chi]_1(t,S)}{[\chi]_0(t,S)}. \tag{5}$$

The system of equations (5) corresponds to the case when the material does not crumble during transportation along the technological route. We will also assume that the material does not spread along the technological route:

$$\int_0^\infty \left(\mu - \frac{[\chi]_1(t,S)}{[\chi]_0(t,S)}\right)^2 \chi(t,S,\mu)d\mu = P(t,S), \qquad\qquad [\chi]_2 = [\chi]_1(t,S)\frac{[\chi]_1(t,S)}{[\chi]_0(t,S)}. \tag{6}$$

We introduce the notation for the speed of the belt in the equilibrium μ_ψ and nonequilibrium state $\langle\mu\rangle$ [35]:

$$\langle\mu\rangle = \frac{[\chi]_1(t,S)}{[\chi]_0(t,S)}.$$

Taking into account (6), we multiply the first equation (5) by $\left([\chi]_1(t,S)/[\chi]_0(t,S)\right)$ and subtract the result from the second equation (5), we obtain a system of equations for a two-moment description of the transport system:

$$\frac{\partial[\chi]_0(t,S)}{\partial t} + \frac{\partial[\chi]_1(t,S)}{\partial S} = \delta(S)\lambda(t), \qquad [\chi]_0(t,S)\frac{\partial\langle\mu\rangle}{\partial t} + [\chi]_1(t,S)\frac{\partial\langle\mu\rangle}{\partial S} = [\chi]_0(t,S)f(t,S) - \frac{\partial P(t,S)}{\partial S}. \tag{7}$$

For a conveyor line, the force moving the material acts on the element of the conveyor belt and can be represented in the form (Fig. 1):

$$dm \frac{d\langle\mu\rangle}{dt} = R(t, S + dS) - R(t, S) - dF_W , \qquad dm = \left([\chi]_0(t,S) + [\chi]_{0C}\right)dS , \qquad (8)$$

$$R(t, S + dS) = \sigma(t, S + dS)Bh , \qquad R(S) = \sigma(t,S)Bh , \qquad R(t, S + dS) - R(t, S) \approx \frac{\partial R(t,S)}{\partial S}dS ,$$

where dm is total mass acting on the belt; B is width of the conveyor belt;; h – the thickness of the conveyor belt; F_W is the sum of the total resistance to movement of the belt [21, p.12]:

$$F_W = F_H + F_N + F_{St} + F_S .$$

Primary resistances F_H are associated with the friction of resistance along the conveyor belt, with the exception of special resistances. Primary resistance F_H , assuming a linear relationship between the resistances and the transported load, are determined by the expression [21, p.13]:

$$d\,F_H = dS \cdot f_C \cdot g_m \left([\chi]_{0R} + \left([\chi]_0(t,S) + [\chi]_{0C}\right)\cos\delta_C \right) ,$$

where f_C is coefficient of resistance to movement includes rolling resistance of driving rollers and belt indentation resistance [21, p.13]; (m / sec2); $[\chi]_{0R}$ is linear load from rotating parts [21, p.8]; δ_C is conveyor section angle [21, p.9]. The linear load from the rotating parts $[\chi]_{0R}$ can be calculated as the ratio of the mass of the rotating element (roller) m_R to the distance S_R between axes of symmetry of the rotating elements [22, p.153]

$$[\chi]_{0R} = \frac{m_R}{S_R} .$$

The force F_N , taking into account the effect on the movement of secondary resistances, can be expressed in terms of the value of primary resistance to motion F_H [21, p.17]:

$$F_N = (C - 1)F_H .$$

For belt conveyor systems with filling factors φ in the range from 0.7 to 1.1, the standard values of the coefficient C are presented in [21, p.17]. For a conveyor section of length $S_d > 2.0$ km this coefficient is equal $C = 1,05$. The force F_{St} , characterizing the gradient resistance of the conveyor belt and the transported material, is calculated for each section of the part as follows [21, p.17]:

$$d\,F_{St} = dS \cdot sin\delta_C \cdot g_m \left([\chi]_0(t,S) + [\chi]_{0C} \right) .$$

The calculation of the force F_S , associated with special resistances in the transport system, is presented in [21, p.18]. The value of F_S is determined by the design features of the transport system. For most conveyor-type transport systems, it is assumed

$$F_S << F_H .$$

Divide (8) by dm , get the value $f(t,S)$:

$$\frac{d\langle\mu\rangle}{dt} = \frac{1}{\left([\chi]_0(t,S) + [\chi]_{0C}\right)} \frac{\partial R(t,S)}{\partial S} - \frac{1}{\left([\chi]_0(t,S) + [\chi]_{0C}\right)} \frac{\partial F_W}{\partial S} . \qquad (9)$$

For the model under consideration, it is believed that stress and strain are related by a linear relationship

$$\sigma(t,S) = E\varepsilon(t,S) , \qquad \varepsilon(t,S) \approx 10^{-2} , \qquad (10)$$

where E is elastic modulus; ε is relative deformation of the conveyor belt element. If we introduce the absolute elongation of the conveyor belt $\omega(t,S)$ at a point in time t for the technological position S , then the ratio of the elongation $d\omega(t,S)$ of the element of the conveyor belt to the length of the segment dS is the relative deformation of the element

$$\varepsilon(t,S) = \frac{\partial \omega(t,S)}{\partial S} . \qquad (11)$$

If we substitute (9) - (11) in (7) then obtain the equations of oscillation of the conveyor belt

$$\frac{\partial\langle\mu\rangle}{\partial t} + \langle\mu\rangle\frac{\partial\langle\mu\rangle}{\partial S} = \frac{BhE}{\left([\chi]_0(t,S) + [\chi]_{0C}\right)} \frac{\partial^2 \omega(t,S)}{\partial S^2} - \frac{1}{\left([\chi]_0(t,S) + [\chi]_{0C}\right)} \frac{\partial F_W}{\partial S} . \qquad (12)$$
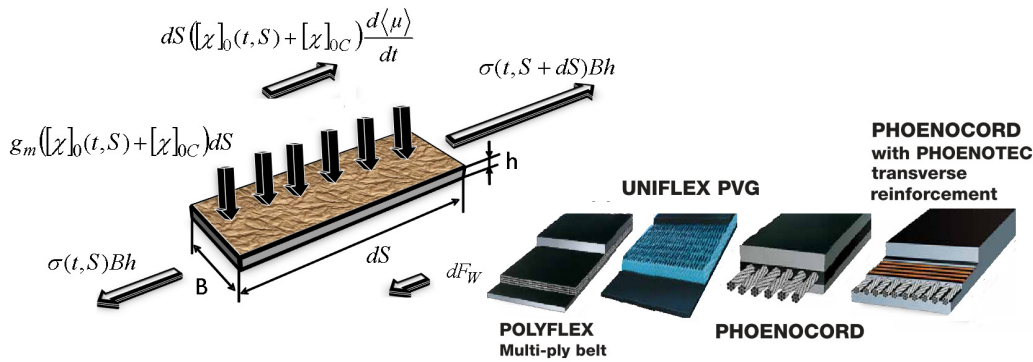
Fig. 1. The forces acting on the element of the conveyor belt

The speed $\langle\mu\rangle$ of the conveyor belt, on which the material is located consists of the speed of the belt in the equilibrium μ_ψ and vibrational $\dfrac{d\omega(t,S)}{dt}$ parts:

$$\langle\mu\rangle = \mu_\psi + \frac{d\omega(t,S)}{dt}, \qquad\qquad \frac{d\omega(t,S)}{dt} = \frac{\partial\omega(t,S)}{\partial t} + \langle\mu\rangle\frac{\partial\omega(t,S)}{\partial S}.$$

Since the relative deformation of the element $\varepsilon(t,S)$ is small (11), then

$$\frac{d\omega(t,S)}{dt} = \frac{\partial\omega(t,S)}{\partial t} + \langle\mu\rangle\varepsilon(t,S) \approx \frac{\partial\omega(t,S)}{\partial t}, \qquad \langle\mu\rangle\varepsilon(t,S) << \frac{\partial\omega(t,S)}{\partial t}. \tag{13}$$

We substitute the expression for the speed of movement of the conveyor belt in the oscillation equation (12), obtain

$$\frac{\partial\mu_\psi}{\partial t} + \frac{\partial^2\omega(t,S)}{\partial t^2} + \left(\mu_\psi + \frac{\partial\omega(t,S)}{\partial t}\right)\frac{\partial}{\partial S}\left(\mu_\psi + \frac{\partial\omega(t,S)}{\partial t}\right) =$$
$$= \frac{BhE}{\left([\chi]_0(t,S)+[\chi]_{0C}\right)}\frac{\partial^2\omega(t,S)}{\partial S^2} - \frac{1}{\left([\chi]_0(t,S)+[\chi]_{0C}\right)}\frac{\partial F_W}{\partial S}. \tag{14}$$

Belt speed for steady motion is a known quantity that is set by program control of the conveyor line

$$f_\psi(t,S) = \frac{\partial\mu_\psi(t,S)}{\partial t} + \mu_\psi\frac{\partial\mu_\psi(t,S)}{\partial S}.$$

One of the main features of conveyor-type transport systems is that within the conveyor section for a steady-state mode of operation, the material at each point of the transport route moves at the same speed, which is equal to the speed of the conveyor belt

$$f_\psi(t) = \frac{\partial\mu_\psi}{\partial t} + \mu_\psi\frac{\partial\mu_\psi}{\partial S}, \qquad\qquad \frac{\partial\mu_\psi}{\partial S} = 0. \tag{15}$$

We introduce the notation

$$C_\chi^2(t,S) = \frac{BhE}{\left([\chi]_0(t,S)+[\chi]_{0C}\right)}, \tag{16}$$

and taking into account expression (15), we represent equation (14) with small perturbations

$$\frac{\partial^2\omega(t,S)}{\partial t^2} + \left(\mu_\psi + \frac{\partial\omega(t,S)}{\partial t}\right)\frac{\partial^2\omega(t,S)}{\partial t\partial S} = C_\chi^2(t,S)\frac{\partial^2\omega(t,S)}{\partial S^2} - \frac{1}{\left([\chi]_0(t,S)+[\chi]_{0C}\right)}\frac{\partial F_W}{\partial S} - f_\psi(t). \tag{17}$$

The speed of the conveyor belt $\langle\mu\rangle$ can have a large gradient, for example as a result of sudden acceleration or deceleration of the conveyor belt. In this paper, we will pay attention to the steady mode for which condition (10) is satisfied, i.e., there are no large gradients for variable speed. Using the passage to the limit using the limit ratio

$$\langle\mu\rangle\frac{\partial^2\omega(t,S)}{\partial t\partial S} = \langle\mu\rangle\frac{\partial\varepsilon(t,S)}{\partial t} \approx \frac{\langle\mu\rangle\varepsilon(t+\Delta t,S)-\langle\mu\rangle\varepsilon(t,S)}{\Delta t}, \tag{18}$$

and taking into account (13), it follows

$$\frac{\langle\mu\rangle\varepsilon(t+\Delta t,S)-\langle\mu\rangle\varepsilon(t,S)}{\Delta t} << \frac{1}{\Delta t}\left(\frac{\partial\omega(t+\Delta t,S)}{\partial t}-\frac{\partial\omega(t,S)}{\partial t}\right) \approx \frac{\partial^2\omega(t,S)}{\partial t^2}. \tag{19}$$

When you change the length of a segment of the transport route, the density $([\chi]_0(t,S)+[\chi]_{0C})$ changes. Let the length of the segment dS changes and becomes equal $(dS+d\omega(t,S))$, $dS >> d\omega(t,S)$. In this case, the linear density will change and becomes equal $([\chi]_0(t,S)+[\chi]_{0C})+(\Delta[\chi]_0(t,S)+\Delta[\chi]_{0C})$. For this segment of the transport route we have

$$dS([\chi]_0(t,S)+[\chi]_{0C})=(dS+d\omega(t,S))([\chi]_0(t,S)+[\chi]_{0C})+(\Delta[\chi]_0(t,S)+\Delta[\chi]_{0C}).$$

Neglecting the value of the second-order of smallness $d\omega(t,S)(\Delta[\chi]_0(t,S)+\Delta[\chi]_{0C})$, we get

$$0 \approx dS(\Delta[\chi]_0(t,S)+\Delta[\chi]_{0C})+\omega(t,S)([\chi]_0(t,S)+[\chi]_{0C}),$$

where from

$$\frac{d\omega(t,S)}{dS} \approx -\frac{\Delta[\chi]_0(t,S)+\Delta[\chi]_{0C}}{[\chi]_0(t,S)+[\chi]_{0C}} \approx \varepsilon.$$

This allows us to represent the square of the function $C_\chi^2(t,S)$ as an expansion in the vicinity of the unperturbed density $[\chi]_{0\psi}(t,S)$

$$C_\chi^2(t,S) \approx \frac{BhE}{[\chi]_{0\psi}(t,S)+[\chi]_{0C}}\left(1-\frac{\Delta[\chi]_{0\psi}(t,S)+\Delta[\chi]_{0C}}{[\chi]_{0\psi}(t,S)+[\chi]_{0C}}\right)=C_\psi^2(t,S)(1-\varepsilon),$$

$$C_\psi^2(t,S)=\frac{BhE}{[\chi]_{0\psi}(t,S)+[\chi]_{0C}}.$$

The function $C_\psi^2(t,S)$ determines the propagation speed of disturbances along the conveyor belt [36]. Thus, using assumption (10) on the linear dependence of stress and relative deformation, the system of equations for determining the vibrations of the conveyor belt takes the form:

$$\frac{\partial[\chi]_0(t,S)}{\partial t}+\mu_\psi(t)\frac{\partial[\chi]_0(t,S)}{\partial S}=\delta(S)\lambda(t), \tag{20}$$

$$\frac{\partial^2\omega(t,S)}{\partial t^2}=C_\psi^2(t,S)\frac{\partial^2\omega(t,S)}{\partial S^2}-\frac{1}{([\chi]_0(t,S)+[\chi]_{0C})}\frac{\partial F_W}{\partial S}-f_\psi(t). \tag{21}$$

We assume that at the initial moment of time the linear density of the material is distributed along the transport route according to the law

$$[\chi]_0(0,S)=H(S)\Psi(S), \qquad H(S)=\begin{cases}0, & S<0, \\ 1, & S\geq 0,\end{cases} \qquad S\in[0;S_d]. \tag{22}$$

We supplement the system of equations (20) with boundary conditions for an equation that describes oscillatory processes in a transport system. Stresses $\sigma(t,0)$ and $\sigma(t,S_d)$ are determined by the tension forces of the conveyor belt T_1 and T_4 (fig.2).

We write the system of equations for the forces T_i, that determine the movement of the belt at the characteristic points of the horizontal conveyor section:

$$T_1=T_2\exp(k_b\alpha); \qquad T_3=T_2+F_{W(2-3)}+F_{\psi(2-3)}; \qquad T_4=k_sT_3, \qquad T_1=T_4+F_{W(4-1)}+F_{\psi(4-1)},$$

$$F_{H(2-3)}=S_d\cdot f_C\cdot g_m([\chi]_{0R}+[\chi]_{0C}), \qquad F_{H(4-1)}=F_{H(2-3)}+f_C\cdot g_m\int_0^{S_d}[\chi]_0(t,S)dS,$$

$$\delta_C=0,$$

$$F_{N(2-3)}=(C-1)F_{H(2-3)}, \qquad F_{N(4-1)}=(C-1)F_{H(4-1)},$$

$$F_{\text{St}(2-3)} = S_d \cdot \sin\delta_C \cdot g_m [\chi]_{0C} = 0, \qquad F_{\text{St}(4-1)} = F_{\text{St}(2-3)} + \sin\delta_C \cdot g_m \int_0^{S_d} [\chi]_0(t,S) dS = 0,$$

$$F_{\psi(2-3)} = f_\psi(t)[\chi]_{0C} S_d, \qquad F_{\psi(4-1)} = f_\psi(t)[\chi]_{0C} S_d + f_\psi(t) \int_0^{S_d} [\chi]_0(t,S) dS,$$

where $F_{\psi(2-3)}$, $F_{\psi(4-1)}$ are forces associated with the acceleration or deceleration of the conveyor belt. We believe that the effects associated with a change in the angular velocity of rotation of the drum are small due to the insignificant magnitude of the moment of inertia of the rollers. Traction moment rotates drum "B". Drum "A" rotates under the action of the frictional force of the belt, resisting movement. Then from the equality

$$T_1 = T_4 + F_{\text{W}(4-1)} + F_{\psi(4-1)} = k_s T_3 + F_{\text{W}(4-1)} + F_{\psi(4-1)} = k_s \left(T_2 + F_{\text{W}(2-3)} + F_{\psi(2-3)}\right) + F_{\text{W}(4-1)} + F_{\psi(4-1)},$$

is determined the tension of the tape at characteristic points

$$T_1 = T_2 \exp(k_b\alpha) = \left(k_s F_{\text{W}(2-3)} + k_s F_{\psi(2-3)} + F_{\text{W}(4-1)} + F_{\psi(4-1)}\right) \frac{\exp(k_b\alpha)}{\exp(k_b\alpha) - k_s}, \qquad (23)$$

$$T_2 = \frac{k_s F_{\text{W}(2-3)} + k_s F_{\psi(2-3)} + F_{\text{W}(4-1)} + F_{\psi(4-1)}}{\exp(k_b\alpha) - k_s},$$

$$T_3 = T_2 + F_{\text{W}(2-3)} + F_{\psi(2-3)} = \frac{k_s F_{\text{W}(2-3)} + k_s F_{\psi(2-3)} + F_{\text{W}(4-1)} + F_{\psi(4-1)}}{\exp(k_b\alpha) - k_s} + F_{\text{W}(2-3)} + F_{\psi(2-3)},$$

$$T_4 = T_2 \exp(k_b\alpha) - F_{\text{W}(4-1)} - F_{\psi(4-1)} = \left(k_s F_{\text{W}(2-3)} + k_s F_{\psi(2-3)} + F_{\text{W}(4-1)} + F_{\psi(4-1)}\right) \frac{\exp(k_b\alpha)}{\exp(k_b\alpha) - k_s} - F_{\text{W}(4-1)} - F_{\psi(4-1)}$$

where k_b is coefficient of adhesion between the drum and the belt; k_s is drum loss coefficient "A"; α is the total girth angle of the drum. For a steel drum in the absence of moisture $k_b \approx 0.3$, $k_s \approx 1.03$ [31] and $\alpha = \pi$ we get $\exp(k_b\alpha) = 2.56$.

Taking into account the values of the acting forces T_1, T_4 (21), we write down the boundary conditions

$$\sigma(t, S_d) = \frac{T_1}{Bh} = E \left.\frac{\partial\omega(t,S)}{\partial S}\right|_{S=S_d} = \frac{1}{Bh}\left(k_s F_{\text{W}(2-3)} + k_s F_{\psi(2-3)} + F_{\text{W}(4-1)} + F_{\psi(4-1)}\right) \frac{\exp(k_b\alpha)}{\exp(k_b\alpha) - k_s}, \qquad (24)$$

$$\sigma(t,0) = \frac{T_4}{Bh} = \frac{T_1 - F_{\text{W}(4-1)} - F_{\psi(4-1)}}{Bh} = E \left.\frac{\partial\omega(t,S)}{\partial S}\right|_{S=0} = E \left.\frac{\partial\omega(t,S)}{\partial S}\right|_{S=S_d} - \frac{F_{\text{W}(4-1)} + F_{\psi(4-1)}}{Bh}.$$

We supplement the system of equations with initial conditions. Consider the steady mode of operation of the conveyor line, when at the initial time there are no oscillations

$$\left.\frac{\partial\omega(t,S)}{\partial t}\right|_{t=0} = 0. \qquad (25)$$

The stress of the conveyor belt at the initial time is determined by the initial distribution of the material along the technological route $\Psi(S)$ and the acceleration of the conveyor belt $f_\psi(t)$. Then

$$\sigma(0,S) = E \left.\frac{\partial\omega(t,S)}{\partial S}\right|_{t=0} = \sigma(0,0) + F_{\text{W}\Psi(4-1)}(0,S) + F_{\psi\Psi(4-1)}(0,S), \qquad (26)$$

$$\sigma(0,0) = \left.\frac{T_4}{Bh}\right|_{t=0} = E \left.\frac{\partial\omega(0,S)}{\partial S}\right|_{S=0},$$

$$F_{\text{H}\Psi(4-1)}(0,S) = f_C \cdot g_m \int_0^S \left([\chi]_{0R} + [\chi]_{0C} + \Psi(\zeta)\right) d\zeta, \qquad F_{\text{N}\Psi(4-1)}(0,S) = (C-1) F_{\text{H}\Psi(4-1)}(t,S),$$

$$F_{\psi\Psi(4-1)}(0,S) = f_\psi(0) \int_0^S \left([\chi]_{0R} + [\chi]_{0C} + \Psi(\zeta)\right) d\zeta, \qquad [\chi]_0(0,S) = \Psi(S).$$

$$F_{W\Psi\,(4-1)}(0,S) = F_{H\Psi\,(4-1)}(0,S) + F_{N\Psi\,(4-1)}(0,S)\,.$$

Combining the system of equations (20), (21) with the boundary (24) and initial (25), (26) conditions, we obtain a two-moment model of the transport system that allows us to study dynamic stresses in the conveyor belt depending on changes in flow parameters $[\chi]_0(t,S), [\chi]_1(t,S)$. Equations (7) and (9) can be used to study the scattering of the material during its transportation.
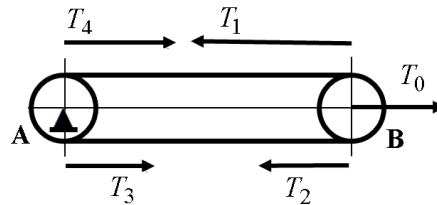

Fig. 2. The scheme of the tension of the conveyor belt

CONVEYOR LINE MODEL IN DIMENSIONAL FORM

Using the notation

$$\tau = \frac{t}{T_d}, \qquad \xi = \frac{S}{S_d}, \qquad \theta_0(\tau,\xi) = \frac{[\chi]_0(t,S)}{[\chi]_{0\max}}, \qquad \psi(\xi) = \frac{\Psi(S)}{[\chi]_{0\max}}, \qquad \gamma(\tau) = \lambda(t)\frac{T_d}{S_d[\chi]_{0\max}},$$

$$g(\tau) = \mu_\psi(t)\frac{T_d}{S_d}, \qquad\qquad \delta(\xi) = S_d\delta(S), \qquad\qquad (27)$$

equation (20) with boundary conditions (22) takes a dimensionless form:

$$\frac{\partial\theta_0(\tau,\xi)}{\partial\tau} + g(\tau)\frac{\partial\theta_0(\tau,\xi)}{\partial\xi} = \delta(\xi)\gamma(\tau), \qquad \theta_0(0,\xi) = H(\xi)\psi(\xi), \qquad 0 \le \gamma(\tau) \le \gamma_{\max}\,. \qquad (28)$$

The solution of equation (28) allows you to determine the state of the linear density of the material $\theta_0(\tau,\xi)$ along the transport route at an arbitrary point in time at an arbitrary point ξ

$$\theta_0(\tau,\xi) = \left(H(\xi) - H(\xi - G(\tau))\right)\frac{\gamma(G^{-1}(G(\tau)-\xi))}{g(G^{-1}(G(\tau)-\xi))} + H(\xi - G(\tau))\psi(\xi - G(\tau)), \qquad G(\tau) = \int_0^\tau g(\alpha)d\alpha, \qquad \tau = G^{-1}(\xi). \qquad (29)$$

The linear density of the material along the transport route $\theta_0(\tau,\xi)$ at an arbitrary point in time τ can be determined, if the intensity $\gamma(\tau)$ of the rock input to the entrance of the conveyor line and the speed of the conveyor belt $g(\tau)$ are known. The material flow along the conveyor line $\theta_1(\tau,\xi)$ can be obtained as a result of the product of the linear density of the material $\theta_0(\tau,\xi)$ and the speed of movement of the material $g(\tau)$

$$\theta_1(\tau,\xi) = \left(H(\xi) - H(\xi - G(\tau))\right)\frac{\gamma(G^{-1}(G(\tau)-\xi))}{g(G^{-1}(G(\tau)-\xi))}g(\tau) + H(\xi - G(\tau))\psi(\xi - G(\tau))g(\tau). \qquad (30)$$

An analysis of the solution (29), (30) is given in [33]. Using the notation

$$\omega_0(\tau,\xi) = \frac{\omega(t,S)}{\omega_{\max}}, \qquad \omega_{\max} = \frac{\sigma_b S_d}{E}, \qquad \theta_C = \frac{[\chi]_{0C}}{[\chi]_{0\max}}, \qquad \theta_R = \frac{[\chi]_{0R}}{[\chi]_{0\max}}, \qquad (31)$$

$$v_b = \frac{Cf_C g_m([\chi]_{0\max} + [\chi]_{0C})S_d}{\sigma_b Bh}, \qquad v_f = \frac{([\chi]_{0\max} + [\chi]_{0C})f_\psi(t)S_d}{\sigma_b Bh}, \quad v_g{}^2 = \frac{BhE}{([\chi]_{0\max} + [\chi]_{0C})}\left(\frac{T_d}{S_d}\right)^2,$$

equation (21), which describes oscillatory processes in a transport system, takes a dimensionless form

$$\frac{\partial^2\omega_0(\tau,\xi)}{\partial\tau^2} = v_g{}^2\frac{\partial^2\omega_0(\tau,\xi)}{\partial\xi^2}\frac{1+\theta_C}{\theta_0(\tau,\xi)+\theta_C} - v_g{}^2(v_b + v_f) - v_g{}^2 v_b\frac{\theta_R}{\theta_0(\tau,\xi)+\theta_C}$$

with boundary conditions (24)

$$\frac{\sigma(t,S_d)}{\sigma_b} = \left.\frac{\partial \omega_0(t,\xi)}{\partial \xi}\right|_{\xi=1} = \left((k_s+1)(v_b+v_f)\frac{\theta_C}{1+\theta_C} + (k_s+1)v_b\frac{\theta_R}{1+\theta_C} + (v_b+v_f)\int_0^1 \frac{\theta_0(\tau,\xi)}{1+\theta_C}d\xi\right)\left(\frac{\exp(k_b\alpha)}{\exp(k_b\alpha)-k_s}\right),$$

$$(32)$$

$$\frac{\sigma(t,0)}{\sigma_b} = \left.\frac{\partial\omega_0(t,\xi)}{\partial\xi}\right|_{\xi=0} = \left.\frac{\partial\omega_0(t,\xi)}{\partial\xi}\right|_{\xi=1} - \frac{F_{W\,(4-1)}+F_{\psi\,(4-1)}}{\sigma_b Bh} = \left.\frac{\partial\omega_0(t,\xi)}{\partial\xi}\right|_{\xi=1} - v_b\frac{\theta_R}{1+\theta_C} - (v_b+v_f)\int_0^1 \frac{\theta_C+\theta_0(\tau,\xi)}{1+\theta_C}d\xi,$$

$$(33)$$

and initial conditions (25), (26)

$$\left.\frac{\partial\omega_0(\tau,\xi)}{\partial\tau}\right|_{\tau=0} = 0,$$

$$(34)$$

$$\frac{\sigma(0,S)}{\sigma_b} = \frac{\partial\omega_0(0,S)}{\partial\xi} = \left.\frac{\partial\omega_0(0,\xi)}{\partial\xi}\right|_{\xi=1} - v_b\int_\xi^1 \frac{\theta_C+\theta_R+\psi(\xi)}{1+\theta_C}d\xi - v_f\int_\xi^1 \frac{\theta_C+\psi(\xi)}{1+\theta_C}d\xi, \quad \theta_0(0,\xi)=\psi(\xi),$$

$$(35)$$

where

$$\frac{\sigma(0,S_d)}{\sigma_b} = \left.\frac{\partial\omega_0(0,\xi)}{\partial\xi}\right|_{\xi=1} = \left((k_s+1)(v_b+v_f)\frac{\theta_C}{1+\theta_C} + (k_s+1)v_b\frac{\theta_R}{1+\theta_C} + (v_b+v_f)\int_0^1 \frac{\psi(\xi)}{1+\theta_C}d\xi\right)\left(\frac{\exp(k_b\alpha)}{\exp(k_b\alpha)-k_s}\right).$$

SOLUTION ANALYSIS FOR SMALL LOADED CONVEYOR LINES

Consider the solution of the system of equations (30)–(35) for the case of the initial movement of the conveyor, when the conveyor line is underloaded. The specific weight of the material along such conveyor lines is small compared to the specific weight of the conveyor belt

$$\theta_0(\tau,\xi) << \theta_C, \qquad \psi(\xi) = \theta_0(0,\xi) << \theta_C.$$

Based on the above assumption, the system of equations (30) - (35) takes the form

$$\theta_1(\tau,\xi) = (H(\xi)-H(\xi-G(\tau)))\frac{\gamma(G^{-1}(G(\tau)-\xi))}{g(G^{-1}(G(\tau)-\xi))}g(\tau) + H(\xi-G(\tau))\psi(\xi-G(\tau))g(\tau).$$

$$\frac{\partial^2\omega_0(\tau,\xi)}{\partial\tau^2} = v_g^2\frac{\partial^2\omega_0(\tau,\xi)}{\partial\xi^2}\frac{1+\theta_C}{\theta_C} - v_g^2 v_f - v_g^2 v_b\left(1+\frac{\theta_R}{\theta_C}\right)$$

$$(36)$$

with boundary conditions (32), (33)

$$\left.\frac{\partial\omega_0(t,\xi)}{\partial\xi}\right|_{\xi=1} = \left((k_s+1)v_b\frac{\theta_C}{1+\theta_C}\left(1+\frac{\theta_R}{\theta_C}\right) + (k_s+1)v_f\frac{\theta_C}{1+\theta_C}\right)\left(\frac{\exp(k_b\alpha)}{\exp(k_b\alpha)-k_s}\right),$$

$$(37)$$

$$\left.\frac{\partial\omega_0(t,\xi)}{\partial\xi}\right|_{\xi=0} = \left.\frac{\partial\omega_0(t,\xi)}{\partial\xi}\right|_{\xi=1} - v_f\frac{\theta_C}{1+\theta_C} - v_b\frac{\theta_C}{1+\theta_C}\left(1+\frac{\theta_R}{\theta_C}\right),$$

and initial conditions (34), (35)

$$\left.\frac{\partial\omega_0(\tau,\xi)}{\partial\tau}\right|_{\tau=0} = 0, \qquad \frac{\partial\omega_0(0,\xi)}{\partial\xi} = \left.\frac{\partial\omega_0(0,\xi)}{\partial\xi}\right|_{\xi=1} - v_b\frac{\theta_C}{1+\theta_C}\left(1+\frac{\theta_R}{\theta_C}\right)(1-\xi) - v_f\frac{\theta_C}{1+\theta_C}(1-\xi).$$

$$(38)$$

During the initial movement of the conveyor belt, three characteristic phases should be distinguished: a) the period of time of the initial start-up, when the conveyor belt goes from rest to moving along the entire route; b) the phase of formation of the static force along the conveyor belt; c) the phase of acceleration of the conveyor belt to the rated speed. Let us dwell on the analysis of the last phase of the start of the conveyor belt. The acceleration phase of the conveyor belt to the rated speed is characterized by a constant value of the traction moment [37, p. 95] and a constant value of the acceleration of the elements of the conveyor belt. This allows us to simplify equation (36)

$$\frac{\partial^2 \omega_0(\tau,\xi)}{\partial \tau^2} = v_1{}^2 \frac{\partial^2 \omega_0(\tau,\xi)}{\partial \xi^2} - v_2{}^2 \,, \tag{39}$$

$$v_1{}^2 = v_g{}^2 \frac{1+\theta_C}{\theta_C}, \qquad v_2{}^2 = v_g{}^2 v_f + v_g{}^2 v_b \left(1+\frac{\theta_R}{\theta_C}\right)$$

with boundary conditions

$$\left.\frac{\partial \omega_0(\tau,\xi)}{\partial \xi}\right|_{\xi=1} = \alpha_1 \,, \qquad\qquad \left.\frac{\partial \omega_0(t,\xi)}{\partial \xi}\right|_{\xi=0} = \alpha_1 - \alpha_{12}\,, \tag{40}$$

$$\alpha_1 = \left((k_s+1)v_b \frac{\theta_C}{1+\theta_C}\left(1+\frac{\theta_R}{\theta_C}\right) + (k_s+1)v_f \frac{\theta_C}{1+\theta_C}\right)\left(\frac{\exp(k_b\alpha)}{\exp(k_b\alpha)-k_s}\right),$$

$$\alpha_{12} = v_b \frac{\theta_C}{1+\theta_C}\left(1+\frac{\theta_R}{\theta_C}\right)+v_f \frac{\theta_C}{1+\theta_C} = \left(v_b \frac{\theta_C}{1+\theta_C}\left(1+\frac{\theta_R}{\theta_C}\right)+v_f \frac{\theta_C}{1+\theta_C}\right)\frac{v_g{}^2 \dfrac{1+\theta_C}{\theta_C}}{v_g{}^2 \dfrac{1+\theta_C}{\theta_C}} = \frac{v_2{}^2}{v_g{}^2 \dfrac{1+\theta_C}{\theta_C}} = \frac{v_2{}^2}{v_1{}^2}\,,$$

and initial conditions

$$\left.\frac{\partial \omega_0(\tau,\xi)}{\partial \tau}\right|_{\tau=0} = 0\,, \qquad \frac{\partial \omega_0(0,\xi)}{\partial \xi} = \alpha_1 - \alpha_{12}(1-\xi)\,, \qquad\qquad . \tag{41}$$

where $v_1{}^2$, $v_2{}^2, \alpha_1$, α_{12} are constant coefficient, $\alpha_{1M}(\tau)$ is the stresses, due to vibration of the traction drum as a result of providing the required traction moment.

The solution to equation (9) is sought in the form

$$\omega_0(\tau,\xi) = \omega_{00}(\tau,\xi) + \omega_{01}(\tau,\xi)\,. \tag{42}$$

Choose a function $\omega_{01}(\tau,\xi)$ in the form

$$\omega_{01}(\tau,\xi) = A(\tau)\xi^2 + B(\tau)\xi + C_{01}\,.$$

where C_{01} is an unknown constant. We define the coefficients $A(\tau)$, $B(\tau)$ in such a way as to ensure the presence of boundary conditions for the function $\omega_{00}(\tau,\xi)$ in the form

$$\left.\frac{\partial \omega_{00}(\tau,\xi)}{\partial \xi}\right|_{\xi=1} = 0\,, \qquad \left.\frac{\partial \omega_{00}(t,\xi)}{\partial \xi}\right|_{\xi=0} = 0\,, \qquad \frac{\partial \omega_{00}(t,\xi)}{\partial \xi} = \frac{\partial \omega_0(t,\xi)}{\partial \xi} - \frac{\partial \omega_{01}(t,\xi)}{\partial \xi}\,.$$

Then the coefficients $A(\tau)$, $B(\tau)$ we obtain as a result of solving the system of equations

$$\left.\frac{\partial \omega_{00}(\tau,\xi)}{\partial \xi}\right|_{\xi=1} = \left.\frac{\partial \omega_0(\tau,\xi)}{\partial \xi}\right|_{\xi=1} - \left.\frac{\partial \omega_{01}(\tau,\xi)}{\partial \xi}\right|_{\xi=1} = \alpha_1 - 2A(\tau) - B(\tau) = 0\,,$$

$$\left.\frac{\partial \omega_{00}(\tau,\xi)}{\partial \xi}\right|_{\xi=0} = \left.\frac{\partial \omega_0(\tau,\xi)}{\partial \xi}\right|_{\xi=0} - \left.\frac{\partial \omega_{01}(\tau,\xi)}{\partial \xi}\right|_{\xi=0} = \alpha_1 - \alpha_{21} - B(\tau) = 0\,.$$

From the solution of the system of equations follows

$$A(\tau) = \frac{\alpha_{12}}{2} = \frac{1}{2}\frac{v_2{}^2}{v_1{}^2}\,, \qquad B(\tau) = \alpha_1 - \alpha_{21} = \alpha_1 - \frac{v_2{}^2}{v_1{}^2}\,,$$

$$\omega_{01}(\tau,\xi) = \frac{1}{2}\frac{v_2{}^2}{v_1{}^2}\xi^2 + \left(\alpha_1 - \frac{v_2{}^2}{v_1{}^2}\right)\xi + C_{01}\,.$$

Substituting solution (42) into equation (39) and into the initial conditions (40), (41), we obtain the initial-boundary value problem for the function $\omega_{00}(\tau,\xi)$

$$\frac{\partial^2 \omega_{00}(\tau,\xi)}{\partial \tau^2} = v_1{}^2 \frac{\partial^2 \omega_{00}(\tau,\xi)}{\partial \xi^2} - \frac{\partial^2 \alpha_{12}}{\partial \tau^2}\left(\frac{\xi^2}{2} - \xi\right)\,, \tag{43}$$

$$\left.\frac{\partial \omega_{00}(\tau,\xi)}{\partial \xi}\right|_{\xi=1} = 0\,,\quad \left.\frac{\partial \omega_{00}(\tau,\xi)}{\partial \xi}\right|_{\xi=0} = 0\,,\quad \left.\frac{\partial \omega_{00}(\tau,\xi)}{\partial \xi}\right|_{\tau=0} = \left.\frac{\partial \omega_0(\tau,\xi)}{\partial \xi}\right|_{\tau=0} - \left.\frac{\partial \omega_{01}(\tau,\xi)}{\partial \xi}\right|_{\tau=0} = 0$$

$$\left.\frac{\partial \omega_{00}(\tau,\xi)}{\partial \tau}\right|_{\tau=0} = \left.\frac{\partial \omega_0(\tau,\xi)}{\partial \tau}\right|_{\tau=0} - \left.\frac{\partial \omega_{01}(\tau,\xi)}{\partial \tau}\right|_{\tau=0} = \left.-\frac{\partial \alpha_{12}}{\partial \tau}\left(\frac{\xi^2}{2} - \xi\right)\right|_{\tau=0}.$$

We consider two cases where the acceleration of the conveyor belt is constant $v_f = v_{f0} = const$ and the case where the acceleration of the conveyor belt varies linearly with time $v_f = v_{f0} + v_{f1}\tau$.

In the case where the acceleration of the conveyor belt is constant $v_f = v_{f0}$, the derivative of the function α_{12} is zero

$$\frac{\partial \alpha_{12}}{\partial \tau} = 0\,,$$

and the boundary value problem (43) takes the form

$$\frac{\partial^2 \omega_{00}(\tau,\xi)}{\partial \tau^2} = v_1^2 \frac{\partial^2 \omega_{00}(\tau,\xi)}{\partial \xi^2}\,,\tag{44}$$

$$\left.\frac{\partial \omega_{00}(\tau,\xi)}{\partial \xi}\right|_{\xi=1} = 0\,,\quad \left.\frac{\partial \omega_{00}(\tau,\xi)}{\partial \xi}\right|_{\xi=0} = 0\,,\quad \left.\frac{\partial \omega_{00}(\tau,\xi)}{\partial \tau}\right|_{\tau=0} = 0\,,\quad \left.\frac{\partial \omega_{00}(\tau,\xi)}{\partial \xi}\right|_{\tau=0} = 0.$$

The solution of problem (44) is presented in the form

$$\omega_{00}(\tau,\xi) = \sum_{n=0}^{\infty} T_n(\tau)X_n(\xi),$$

where the function $X_n(\xi)$ is determined from the solution of the Sturm-Liouville problem. Using the boundary conditions, we write the solutions to the problem in the following form

$$\omega_{00}(\tau,\xi) = \sum_{n=0}^{\infty} T_n(\tau)\cos(\pi n \xi).$$

At the initial time, the rate of change of the function $\omega_{00}(\tau,\xi)$ is zero. From this condition follows

$$\left.\frac{\partial \omega_{00}(\tau,\xi)}{\partial \tau}\right|_{\tau=0} = 0 \quad \Rightarrow \quad \omega_{00}(\tau,\xi) = \sum_{n=0}^{\infty} G_n \cos(\pi n v_1 \tau)\cos(\pi n \xi).\tag{45}$$

The values of the coefficients G_n are determined from the second initial condition

$$\left.\frac{\partial \omega_{00}(\tau,\xi)}{\partial \xi}\right|_{\tau=0} = -\sum_{n=0}^{\infty} \pi n G_n \sin(\pi n \xi) = 0\,.$$

Equality holds if $G_n = 0$. Э This is consistent with the decision

$$\omega_{00}(\tau,\xi) = 0\,.$$

Thus, in the presence of acceleration of the conveyor belt of constant magnitude, there are no oscillations in the belt. Elongation of the tape along the conveyor can be represented by the expression.

$$\omega_0(\tau,\xi) = \omega_{00}(\tau,\xi) + \omega_{01}(\tau,\xi) = \frac{1}{2}\frac{v_2^2}{v_1^2}\xi^2 + \left(\alpha_1 - \frac{1}{2}\frac{v_2^2}{v_1^2}\right)\xi + C_{01}\,.$$

The constant C_{01} is determined from the condition of the minimum allowable stress $\omega_{\min}$, ensuring the adhesion of the tape with the drum to create traction in the transport system with a given limit on the allowable amount of sagging of the tape. This allows us to write down the inequality

$$\omega_{01}(\xi) = \frac{1}{2}\frac{v_2^2}{v_1^2}\xi^2 + \left(\alpha_1 - \frac{v_2^2}{v_1^2}\right)\xi + C_{01} \geq \omega_{\min 0}\,.$$

Taking into account the last condition, we write the solution of the equation in the form

$$\omega_{01}(0) = \frac{1}{2}\frac{v_2{}^2}{v_1{}^2}\xi^2 + \left(\alpha_1 - \frac{v_2{}^2}{v_1{}^2}\right)\xi + \omega_{\min 0}\,.$$

We turn to the second case when the acceleration of the conveyor belt varies with time according to the linear law $v_f = v_{f0} + v_{f1}\tau$. Then

$$\frac{\partial \alpha_{12}}{\partial \tau} = \frac{v_g{}^2 v_{f1}}{v_1{}^2}\,, \qquad v_2{}^2 = v_g{}^2\left(v_{f0} + v_{f1}\tau\right) + v_g{}^2 v_b\left(1 + \frac{\theta_R}{\theta_C}\right),$$

and the boundary value problem (43) takes the form

$$\frac{\partial^2 \omega_{00}(\tau,\xi)}{\partial \tau^2} = v_1{}^2\frac{\partial^2 \omega_{00}(\tau,\xi)}{\partial \xi^2}\,, \tag{46}$$

$$\left.\frac{\partial \omega_{00}(\tau,\xi)}{\partial \xi}\right|_{\xi=1} = 0\,, \qquad \left.\frac{\partial \omega_{00}(\tau,\xi)}{\partial \xi}\right|_{\xi=0} = 0\,, \qquad \left.\frac{\partial \omega_{00}(\tau,\xi)}{\partial \xi}\right|_{\tau=0} = 0\,, \tag{47}$$

$$\left.\frac{\partial \omega_{00}(\tau,\xi)}{\partial \tau}\right|_{\tau=0} = -\frac{v_g{}^2 v_{f1}}{v_1{}^2}\left(\frac{\xi^2}{2} - \xi\right) = Z(\xi)\,. \tag{48}$$

Using the results of the previous problem for the case $v_f = v_{f0} = const$, considering two zero boundaries and one zero initial condition (47), we look for the solution to the initial boundary-value problem (46) in the form

$$\omega_{00}(\tau,\xi) = \sum_{n=0}^{\infty} G_n\,\sin(\pi n v_1\tau)\cos(\pi n\xi)\,. \tag{49}$$

We determine the unknown coefficients G_n from the initial condition (48)

$$\left.\frac{\partial \omega_{00}(\tau,\xi)}{\partial \tau}\right|_{\tau=0} = \pi v_1\sum_{n=0}^{\infty} nG_n\cos(\pi n\xi) = -\frac{v_g{}^2 v_{f1}}{v_1{}^2}\left(\frac{\xi^2}{2} - \xi\right).$$

Emerging dynamic stresses in the conveyor belt can be represented as

$$\frac{\partial \omega_{00}(\tau,\xi)}{\partial \xi} = -\pi\sum_{n=0}^{\infty} nG_n\sin(\pi n v_1\tau)\sin(\pi n\xi) = -\pi\sum_{n=0}^{\infty} nG_n\left(\frac{\cos(\pi n[\xi - v_1\tau]) - \cos(\pi n[\xi + v_1\tau])}{2}\right) = \frac{\Omega(\xi - v_1\tau) - \Omega(\xi + v_1\tau)}{2}$$

.

We transform the solution (49) to the form

$$\omega_{00}(\tau,\xi) = W_1(\xi + v_1\tau) + W_2(\xi - v_1\tau)\,. \tag{50}$$

We define $W_1(\xi + v_1\tau), W_2(\xi - v_1\tau)$ from conditions (47), (48):

$$\left.\frac{\partial \omega_{00}(\tau,\xi)}{\partial \xi}\right|_{\tau=0} = \frac{dW_1(\xi)}{d\xi} + \frac{dW_2(\xi)}{d\xi} = 0\,, \qquad \left.\frac{\partial \omega_{00}(\tau,\xi)}{\partial \tau}\right|_{\tau=0} = v_1\frac{dW_1(\xi)}{d\xi} - v_1\frac{dW_2(\xi)}{d\xi} = -\frac{v_g{}^2 v_{f1}}{v_1{}^2}\left(\frac{\xi^2}{2} - \xi\right) = Z(\xi)\,.$$

Integrating the equalities, we obtain

$$W_1(\xi) + W_2(\xi) = C_{w1}\,, \qquad W_1(\xi) - W_2(\xi) = \frac{1}{v_1}\int_{\xi_0}^{\xi} Z(\alpha)d\alpha + C_{w2}\,.$$

where ξ_0, C_{w1}, C_{w2} is constant coefficients. The constant C_{w1} is equal to zero due to the choice of the form of functions $W_1(\xi)$, $W_2(\xi)$ (50). We solve the system of equations, we find

$$W_1(\xi) = \frac{1}{2v_1}\int_{\xi_0}^{\xi} Z(\alpha)d\alpha + \frac{C_{w2}}{2}\,, \qquad W_2(\xi) = -\frac{1}{2v_1}\int_{\xi_0}^{\xi} Z(\alpha)d\alpha - \frac{C_{w2}}{2}\,. \tag{51}$$

Substituting (51) into (50), we obtain

$$\omega_{00}(\tau,\xi) = \frac{1}{2v_1}\int_{\xi - v_1\tau}^{\xi + v_1\tau} Z(\alpha)d\alpha\,. \tag{52}$$

The expression for the emerging dynamic stresses of the conveyor belt has the form

$$\frac{\partial \omega_{00}(\tau,\xi)}{\partial \xi} = \frac{Z(\xi + v_1\tau) - Z(\xi - v_1\tau)}{2v_1} \qquad (53)$$

The properties of the function $Z(\alpha)$ follow from the boundary conditions (47)

$$\left.\frac{\partial \omega_{00}(\tau,\xi)}{\partial \xi}\right|_{\xi=0} = \frac{Z(v_1\tau) - Z(-v_1\tau)}{2v_1} = 0, \qquad Z(\beta) = Z(-\beta), \qquad (54)$$

$$\left.\frac{\partial \omega_{00}(\tau,\xi)}{\partial \xi}\right|_{\xi=1} = \frac{Z(1 + v_1\tau) - Z(1 - v_1\tau)}{2v_1} = 0, \qquad Z(\beta_{11}) = Z(2 - \beta_{11}), \qquad \beta_{11} = (1 + v_1\tau).$$

Since the function $Z(\beta)$ (54) is even and the value τ is arbitrary, it follows

$$Z(2 - \beta) = Z(\beta) = Z(-\beta), \qquad Z(2 + \beta) = Z(\beta). \qquad (55)$$

The function $Z(\beta)$ is an even function of period 2. The general solution of the problem takes the form

$$\omega_0(\tau,\xi) = \frac{1}{2}\frac{v_2^2}{v_1^2}\xi^2 + \left(\alpha_1 - \frac{v_2^2}{v_1^2}\right)\xi + \omega_{\min 0} + \frac{1}{2v_1}\int_{\xi - v_1\tau}^{\xi + v_1\tau} Z(\alpha)d\alpha,$$

$$\frac{\partial \omega_0(\tau,\xi)}{\partial \xi} = \frac{v_2^2}{v_1^2}\xi + \left(\alpha_1 - \frac{v_2^2}{v_1^2}\right) + \frac{Z(\xi + v_1\tau) - Z(\xi - v_1\tau)}{2v_1}. \qquad (56)$$

We define the point of the transport route at which the maximum dynamic stresses of the conveyor belt occur. We introduce the variable τ_n so that

$$0 \le v_1\tau_n - 2n < 2, \qquad \tau_n = \tau - \frac{2n}{v_1}.$$

Then, due to the periodicity of function (55), it follows

$$Z(\xi + v_1\tau) = Z(\xi + v_1\tau - 2n) = Z\left(\xi + v_1\left(\tau - \frac{2n}{v_1}\right)\right) = Z(\xi + v_1\tau_n) = Z(\beta_1), \qquad \beta_1 = \xi + v_1\tau_n,$$

$$Z(\xi - v_1\tau) = Z(\xi - v_1\tau + 2n) = Z\left(\xi - v_1\left(\tau - \frac{2n}{v_1}\right)\right) = Z(\xi - v_1\tau_n) = Z(\beta_2), \qquad \beta_2 = \xi - v_1\tau_n.$$

We calculate the value of dynamic stresses (53) arising in the conveyor belt

$$\frac{\partial \omega_{00}(\tau,\xi)}{\partial \xi} = \frac{Z(\xi + v_1\tau) - Z(\xi - v_1\tau)}{2v_1} = Z_0(\beta_1,\beta_2), \qquad Z(\beta) = v_d\left(\frac{\beta^2}{2} - \beta\right), \qquad v_d = -\frac{v_g^2 v_{f1}}{v_1^2}.$$

The expression for the function $Z_0(\beta_1,\beta_2)$ for different ranges of values β_1, β_2 is presented in table 1. The function $Z_0(\beta_1,\beta_2)$ is linear with respect to the variable ξ, has an increasing section and a decreasing section. The inflexion point of the function determines the extreme value of the dynamic stress (Fig. 3).

Table

Dynamic stresses $Z_0(\beta_1,\beta_2)$ in the conveyor belt

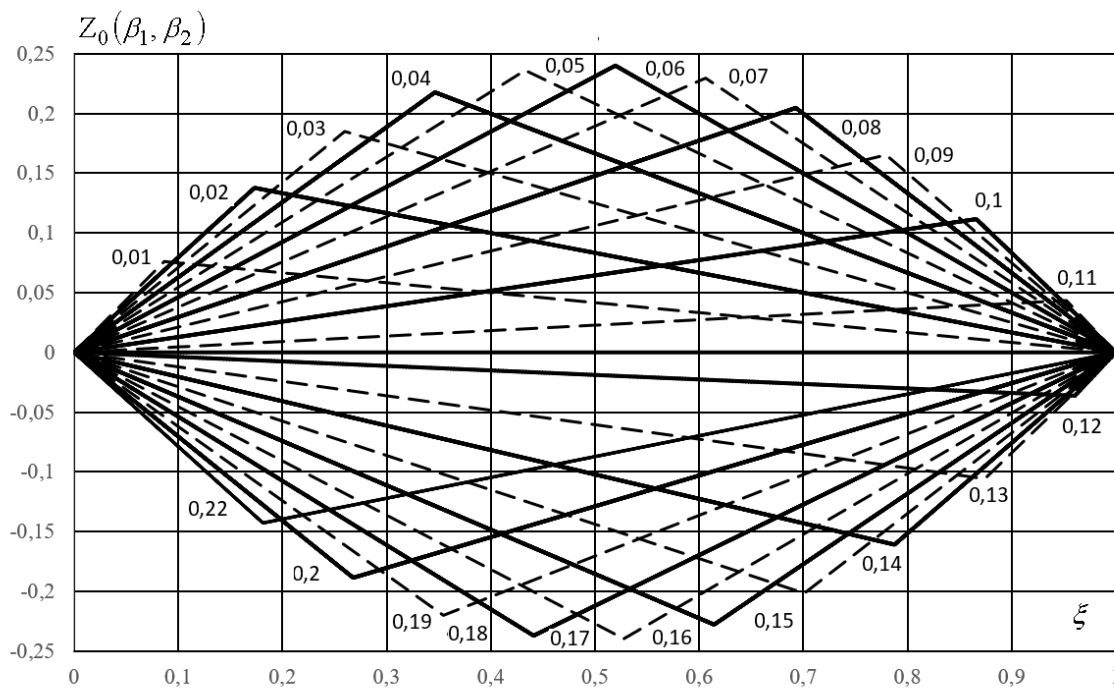| No	Вид функции $Z_0(\beta_1,\beta_2)$	$-2 \le \beta < -1$	$-1 \le \beta < 0$	$0 \le \beta < 1$	$1 \le \beta < 2$	$2 \le \beta < 3$
1	$Z_0(\beta_1,\beta_2) = v_d\tau_n(\xi - 1)$			β_1, β_2		
2	$Z_0(\beta_1,\beta_2) = v_d\xi(\tau_n - 1/v_1)$		β_2	β_1		
3	$Z_0(\beta_1,\beta_2) = v_d\xi(\tau_n - 1/v_1)$		β_2		β_1	
4	$Z_0(\beta_1,\beta_2) = v_d\xi(\tau_n - 1/v_1)$	β_2			β_1	
5	$Z_0(\beta_1,\beta_2) = v_d(\tau_n - 2/v_1)(\xi - 1)$	β_2				β_1
6	$Z_0(\beta_1,\beta_2) = v_d(\tau_n - 2/v_1)(\xi - 1)$		β_2			β_1
7	$Z_0(\beta_1,\beta_2) = v_d\tau_n(\xi - 1)$			β_2	β_1	

Fig. 3. Conveyor belt dynamic stresses $Z_0(\beta_1, \beta_2)$ for times $\tau = 0.01 \cdot m$, $m = 0,1,2...$

Using (56), we determine the condition under which the value of the dynamic voltage is an insignificant part of the magnitude of the static voltage has the form

$$\frac{v_2^2}{v_1^2}\xi + \left(\alpha_1 - \frac{v_2^2}{v_1^2}\right) \approx \frac{v_2^2}{v_1^2}\xi >> \left|\frac{Z(\xi + v_1\tau) - Z(\xi - v_1\tau)}{2v_1}\right| \approx |v_d\tau_n\xi|.$$

This implies

$$\frac{v_{f1}\tau_n}{v_{f0} + v_b} << 1.$$

Dynamic stresses do not affect the acceleration of the conveyor belt under the condition of a slow change in the value of the acceleration over a typical period of time τ_n

$$v_{f1} << \frac{v_{f0} + v_b}{\tau_n}.$$

CONCLUSION

Using the statistical method of modelling production systems in a two-moment description, a model of a conveyor transport system is presented. A feature of this model is the ability to take into account the effect of uneven distribution of material along the transport route on the propagation of emerging dynamic stress disturbances in the conveyor belt. The elastic properties of the conveyor belt are taken into account in accordance with the Hooke model. Calculation of resistances in the transport system is made in accordance with DIN 22101: 2002-08. The characteristic mode of operation of transport conveyor systems during acceleration of the conveyor section is considered in detail. In the approximation, when the conveyor system starts and the loading of the conveyor section is negligible, the conditions for the occurrence of dynamic stresses are determined. These expressions can be used to calculate the static and dynamic stresses of the conveyor belt.

ORCID-IDs
Oleh M. Pihnastyi https://orcid.org/0000-0002-5424-9843, **Valery D. Khodusov** https://orcid.org/0000-0003-1129-3462

REFERENCES
[1] N.A. Azarenkov, O.M. Pihnastyi and V.D. Khodusov, Reports of the National Academy of Sciences of Ukraine, **2**, 29-35 (2011), http://dspace.nbuv.gov.ua/handle/123456789/37227.
[2] O.M. Pihnastyi, Problems of Atomic science and technology, **3**, 322–325 (2007), http://dspace.nbuv.gov.ua/handle/123456789/111018.
[3] O.M. Pihnastyi, Belgorod State University Scientific Bulletin, **31**(1), 147–157 (2014), https://ssrn.com/abstract=3404364.

[4] O.M. Pihnastyi, Scientific bulletin of National Mining University, **4**, 104–111 (2017), http://nbuv.gov.ua/UJRN/Nvngu_2017_4_18.

[5] N.A. Azarenkov, O.M. Pihnastyi and V.D. Khodusov, Reports of the National Academy of Sciences of Ukraine, **12**, 36-43 (2014), https://doi.org/10.15407/dopovidi2014.12.036.

[6] D. He, Y. Pang, G. Lodewijks and X. Liu. Powder Technology, **327**, 408–419 (2018), http://dx.doi.org/10.1016/j.powtec.2018.01.002.

[7] T. Mathaba and X. Xia, Energies, **8**(12), 13590–13608 (2015), https://doi.org/10.3390/en81212375.

[8] G. Yang, Sensors & Transducers, **81**(10), 210–218 (2014), https://www.sensorsportal.com/HTML/DIGEST/P_2492.htm.

[9] A.A. Reutov, in: IOP Conference Series: Earth and Environmental, **87**, (2017), https://doi.org/10.1088/1755-1315/87/8/082041.

[10] I.A. Halepoto and S. Khaskheli, Indian Journal of Science and Techology, **9**(47), 1–6 (2016), http://dx.doi.org/10.17485/ijst%2F2016%2Fv9i47%2F108658.

[11] L. Ristic, M. Bebic and B. Jeftenic, Electronics, **17**, 30–39 (2013). http://dx.doi.org/10.7251/ELS1317030R.

[12] L. Xinglei, Yu. Hongbin, in: *Proceedings of the 3rd International Conference on Mechanical Engineering and Intelligent Systems* (ICMEIS, 2015), pp. 789–793, https://doi.org/10.2991/icmeis-15.2015.148.

[13] E. Wolstenholm, Dynamica, **6**(2), 25–35 (1980), https://www.systemdynamics.org/assets/dynamica/62/6.pdf.

[14] M. Andrejiova, D. Marasova, Acta Montanistica Slovaca, **18**(2), 77–84 (2013), https://actamont.tuke.sk/pdf/2013/n2/2andrejiova.pdf.

[15] P. Markos and A. Dentsoras, FME Transactions, **46**, P.313–319 (2018), https://scindeks-clanci.ceon.rs/data/pdf/1451-2092/2018/1451-20921803313M.pdf

[16] M. Bajda, R. Krol, Procedia Earth and Planetary Science, **15**, 702–711 (2015), https://doi.org/10.1016/J.PROEPS.2015.08.098.

[17] A. Kumar and L.P. Singh, International journal of engineering sciences & research technology system, **6**(9), 337–341 (2017), http://www.ijesrt.com/issues%20pdf%20file/Archive-2017/September-2017/43.pdf

[18] V. Pasika, P. Koruniak, P. Nosko, O. Bashta and Yu. Tsibrii, Bulletin of NTU "KhPI": Series: New solutions in modern technologies. 45(1321), P.47–58 (2018). https://doi.org/10.20998/2413-4295.2018.45.07.

[19] Shirong Zhang, Xiaohua Xia, in: IEEE AFRICON–2009, (Nairobi, Kenya, 23–25 September 2009), pp. 17-27. https://doi.org/10.1109/AFRCON.2009.5308257.

[20] S. Gramblička, R. Kohár and M. Stopka, Procedia Engineering, **192**, 259-264 (2017), https://doi.org/10.1016/j.proeng.2017.06.045.

[21] *DIN 22101:2002-08. Continous conveyors. Belt conveyors for loose bulk materials. Basics for calculation and dimensioning*. [Normenausschuss Bergbau (FABERG), DIN Deutsches Institut für Normung e.v. Normenausschuss Maschinenbau (NAM)], (2002), pp. 51.

[22] V.A. Budishevsky and A.A. Sulima, *Theoretical foundations and calculations of transport of energy-intensive industries*, (1999). pp. 216, http://ea.donntu.org:8080/jspui/handle/123456789/10466. (in Russian)

[23] M. Alspaugh, 2004, in*: MINExpo-2004*, (New York, Las Vegas, NV, USA, 2004), pp. 17-27, http://fliphtml5.com/pfyf/pccg/basic.

[24] B. Karolewski and P. Ligocki, Maintenance and reliability, **16**(2), 179-187 (2014), http://yadda.icm.edu.pl/yadda/element/bwmeta1.element.baztech-ce355084-3e77-4e6b-b4b5-ff6131e77b30/c/karolewski_2014-02-02_en.pdf.

[25] H. Lauhoff, Bulk Solids Handling Publ. **25**(6), 368-377 (2005), http://synergy-eng.com/pdf/BSH-2005_Beltspeed_Lauhoff.pdf.

[26] N.F. Timerbaev, A.R. Sadrtdinov, D.B. Prosvirnikov, A.A. Fomin and V.V. Stepanov, in: IOP Conf. Series: Earth and Environmental Science (IPDME 2017), **87**, 1–9 (2017), https://doi.org/10.1088/1755-1315/87/8/082047.

[27] C.A. Wheeler, in: *International Materials Handling Conference (Beltcon) 12*, (Johannesburg, South Africa, 2003), pp.1–11. http://www.saimh.co.za/beltcon/beltcon12/paper1208.htm.

[28] Y. Lu and Q. Li, Measurement and Control, **52**, 441-448 (2019), https://doi.org/10.1177/0020294019840723.

[29] A. Harrison, Bulk Solids Handling, **28**(4), 242-247 (2008), https://static.wpe.au.syrahost.com/var/m_c/c1/c10/35361/296385-bsh2008_non-linear_dynamics.pdf?download.

[30] A. Semenchenko, M. Stadnik, P. Belitsky, D. Semenchenko and O. Stepanen, Eastern-European Journal of Enterprise Technologies, **4**/1, 42–51 (2019), https://doi.org/10.15587/1729-4061.2016.75936.

[31] V.V. Degtjarev, *Нормирование топливно-энергетических ресурсов и регулирование режимов энергопотребления* [*Rationing of fuel and energy resources and regulation of energy consumption modes*], (Nedra, Moscow, 1983), pp. 225, http://www.xn--80affsqimkl5h.xn--p1ai/_ld/7/735__-.pdf. (in Russian)

[32] O.M. Pihnastyi, Scientific bulletin of National Mining University, **6**, 44-51 (2019).

[33] J. Antoniak, Transport Problems, **5**(4), 5-14 (2010), http://transportproblems.polsl.pl/pl/Archiwum/2010/zeszyt4/2010t5z4_01.pdf.

[34] O.M. Pihnastyi and V.D. Khodusov, Bulletin of the South Ural State University. Ser. Mathematical Modelling, Programming & Computer Software (Bulletin SUSUMMCS), **10**, 67-77 (2017), https://doi.org/10.14529/mmp170407.

[35] O.M. Pihnastyi. Statistical theory of production systems, (Kharkiv: KhNU, 2007), pp. 388.

[36] R. Pascual, V. Meruane and G. Barrientos, in: *Proceedings of the XXVI Iberian Latin-American Congress on Computational Methods in Engineering CILAMCE 2005* (CILAMCE-2005, Santo, Brazil, 2005), Paper CIL0620, http://citeseerx.ist.psu.edu/viewdoc/download?doi=10.1.1.494.34&rep=rep1&type=pdf.

[37] A.O. Spivakovsky and V.A. Dyachkov, *Транспортные машины* [*Transporting machines*], (Mechanical Engineering, Moscow, 1983), pp. 487. (in Russian)

ГІДРОДИНАМІЧНА МОДЕЛЬ ТРАНСПОРТНОЇ СИСТЕМИ

О.М. Пигнастий[a], В.Д. Ходусов[b]
[a]Національний технічний університет «ХПІ», 61002
Україна, м.Харків, вул. Кирпичева, 2
[b]Харківський національний університет імені В.Н. Каразіна
61022, Україна, Харків, пл. Свободи, 4

Розглянуто гідродинамічна модель виробничих систем з потоковим методом організації виробництва. Визначено основні макропараметри стану виробничої потокової лінії і взаємозв'язку між ними. Обгрунтовано вибір багатомоментного наближення для моделювання виробничої потокової лінії. Показано, що конвеєр конвеєрного типу це складна динамічна система з розподіленими параметрами. Сформульовано крайову задачу про поздовжні коливання конвеєрної стрічки при

русі матеріалу по маршруту транспортування. Передбачається, що ковзання матеріалу уздовж конвеєрної стрічки відсутня, а деформація, що виникає в конвеєрній стрічці пропорційна доданої силі (модель пружних деформацій Гука). Показано суттєвий вплив нерівномірності розподіл матеріалу уздовж маршруту транспортування на швидкість поширення динамічних напружень в конвеєрній стрічці. При побудові граничних і початкових умов використані рекомендації DIN 22101: 2002-08. Досліджено механізм виникнення поздовжніх коливань конвеєрної стрічки при русі матеріалу по маршруту транспортування. Визначено основні параметри моделі, які є причиною виникнення динамічних напружень. Показано, що динамічні напруги формуються в результаті суперпозиції напружень в прямій і відбитої хвилі. Записані аналітичні вирази, що дозволяють розрахувати величину динамічних напружень в конвеєрній стрічці і визначені умови виникнення руйнувань конвеєрної стрічки. Розглянуто характерні фази початкового руху матеріалу по технологічному маршруту. Досліджено процес виникнення динамічних напружень при постійному і змінному прискоренні конвеєрної стрічки. Представлена динаміка поширення напруг уздовж маршруту транспортування. Показано, що величина динамічних напружень може перевищувати гранично допустиме значення, що призводить до руйнування конвеєрної стрічки або конструктивних елементів. Зроблено оцінку тривалості перехідного періоду, яка потрібна для забезпечення безаварійного режиму функціонування транспортної при прискоренні або гальмуванні конвеєрної стрічки. Використання безрозмірних параметрів дозволяє сформулювати критерії подібності транспортних систем конвеєрного типу.

КЛЮЧОВІ СЛОВА: гідродинамічна модель транспортної системи, двох-моментний опис виробництва, модель Гука, балансові рівняння, PDE-модель виробництва

ГИДРОДИНАМИЧЕСКАЯ МОДЕЛЬ ТРАНСПОРТНОЙ СИСТЕМЫ

О.М. Пигнастый[a], В.Д. Ходусов[b]
[a]Национальный технический университет «ХПИ»
61002, Украина, г. Харьков, ул. Кирпичева, 2
[b]Харьковский национальный университет имени В.Н. Каразина
61022, Украина, Харьков, пл. Свободы, 4

Рассмотрена гидродинамическая модель производственных систем с поточным методом организации производства. Определены основные макропараметры состояния производственной поточной линии и взаимосвязи между ними. Обоснован выбор много моментного приближения для моделирования производственной поточной линии. Показано, что поточная линия конвейерного типа – это сложная динамическая система с распределенными параметрами. Сформулирована краевая задача о продольных колебаниях конвейерной ленты при движении материала по маршруту транспортировки. Предполагается, что скольжение материала вдоль конвейерной ленты отсутствует, а деформация, возникающая в конвейерной ленте пропорциональна приложенной силе (модель упругих деформаций Гука). Показано существенное влияние неравномерности распределение материала вдоль маршрута транспортировки на скорость распространения динамических напряжений в конвейерной ленте. При построении граничных и начальных условий использованы рекомендации DIN 22101:2002-08. Исследован механизм возникновения продольных колебаний конвейерной ленты при движении материала по маршруту транспортировки. Определены основные параметры модели, которые являются причиной возникновения динамических напряжений. Показано, что динамические напряжения формируются в результате суперпозиции напряжений в прямой и отраженной волны. Записаны аналитические выражения, позволяющие рассчитать величину динамических напряжений в конвейерной ленте и определены условия возникновения разрушений конвейерной ленты. Рассмотрены характерные фазы начального движения материала по технологическому маршруту. Исследован процесс возникновения динамических напряжений при постоянном и переменном ускорении конвейерной ленты. Представлена динамика распространения напряжений вдоль маршрута транспортировки. Показано, что величина динамических напряжений может превышать предельно допустимое значение, что приводит к разрушению конвейерной ленты или конструктивных элементов. Произведена оценка продолжительности переходного периода, которая требуется для обеспечения безаварийного режима функционирования транспортной при ускорение (торможение) конвейерной ленты. Использование безразмерных параметров позволяет сформулировать критерии подобия транспортных систем конвейерного.

КЛЮЧЕВЫЕ СЛОВА: гидродинамическая модель транспортной системы, двух моментное описание производства, модель Гука, балансовые уравнения, PDE-модель производства

INSTRUCTIONS FOR PREPARING MANUSCRIPT IN EAST EUROPEAN JOURNAL OF PHYSICS

[1]N.N. Author*, [2]N.N. Co-author(s)
[1]Affiliation of first author
[2]Affiliation of second author (if different from first Authors)
*E-mail: corresponding_authors@mail.com, [1]ORCID ID
E-mail: co_authors@mail.com, [2]ORCID ID

Each paper must begin with an abstract. The abstract should be typed in the same manner as the body text (see below). Please note that these Instructions are typed just like the manuscripts should be. The abstract must have at least 1800 phonetic symbols, supplying general information about the achievements, and objectives of the paper, experimental technique, methods applied, significant results and conclusions. Page layout: the text should be printed on the paper A4 format, at least 5 pages, with margins of: Top - 3, Bottom, Left and Right - 2 cm. The abstract should be presented in English (only for foreign authors), Ukraine and Russian.

KEYWORDS: there, must, be, at least, 5 keywords

This is introduction section. This paper contains instructions for preparing the manuscripts. The text should be prepared in .doc format (using MS Word).

INSTRUCTIONS

The text should be typed as follows:
• **title**: Times New Roman, 12 pt, ALL CAPS, bold, 1 spacing, centred;
• **authors**: name, initials and family names; Times New Roman, 12 pt, bold, 1 spacing, centred;
• **affiliation(s)**: Times New Roman, 9 pt, italic, 1 spacing, centred;
• **abstract**: Times New Roman, 9 pt, 1 spacing, justified;
• **body text**: Times New Roman, 10 pt, 1 spacing, justified; paragraphs in sections should be indented right (tabulated) for 0.75 cm;
• **section titles**: Times New Roman, 10 pt, bold, 1 spacing, centred, without numbering, one line should be left, blank above section title;
• **subsection titles**: Times New Roman, 10 pt, bold, 1 spacing, centred, without numbering in accordance to the section (see below), one line should be left blank above subsection title;
• **figure captions**: width of the figure should be 85 or 170 mm, figures should be numbered (Fig. 1) and titled below figures using sentence format, Times New Roman, 9 pt, 1 spacing, centred (if one line) or justified (if more than one line); one line should be left blank below figure captions;
• **table captions**: width of the table should be 85 or 170 mm, tables should be numbered (Table 1.) and titled above tables using sentence format, Times New Roman, 10 pt, 1 spacing, centred (if one line) or justified (if more than one line), tables should be formatted with a single-line box around the outside border and single ruling lines between rows and columns; one line should be left blank below tables;
• **equations**: place equations centred, numbered in Arabic (1), flush right, equations should be specially prepared in MathType; one line should be left blank below and above equation.

Additional instructions

Numerated figures and tables should be embedded in your text and placed after they are cited. Only black and white drawings and sharp photographs are acceptable. Letters in the figures should be 3 mm high. The figures should be presented in one of the following graphic formats: jpg, gif, pcx, bmp, tif.

REFERENCES

Cite references in AIP style (https://guides.lib.monash.edu/citing-referencing/aip). Numbering in the order of referring in the text, e.g. [1], [2-5], etc. References should be listed in numerical order of citation in the text at the end of the paper (justified), Times New Roman, 9 pt, 1 spacing.

Journal Articles
[1]   T. Mikolajick, C. Dehm, W. Hartner, I. Kasko, M. J. Kastner, N. Nagel, M. Moert and C. Mazure, Microelectron. Reliab. **41**, 947 (2001).
[2]   S. Bushkova, B.K. Ostafiychuk and O.V. Copaiev, Physics and Chemistry of Solid State. **15**(1), 182-185 (2014), http://page.if.ua/uploads/pcss/vol15/!1501-27.pdf. (in Ukrainian)
[3]   M. Yoshimura, E. Nakai, K. Tomioka and T. Fukui, Appl. Phys. Lett. **103**, 243111 (2013), http://dx.doi.org/10.7567/APEX.6.052301.

E-print resourses with collaboration research
[4]   M. Aaboud et al. (ATLAS Collaboration), Eur. Phys. J. C, **77**, 531 (2017), http://dx.doi.org/10.1140/epjc/s10052-017-5061-9
[5]   Sjöstrand et al., *Comput. Phys. Commun.* **191,** 159-177 (2015), http://arxiv.org/abs/1410.3012.
[6]   Boudreau, C. Escobar, J. Mueller, K. Sapp, and J. Su, (2013), http://arxiv.org/abs/1304.5639.

Books
[7]   S. Inoue and K.R. Spring, *Video Microscopy*: *The fundamentals*, 2nd ed. (Plenum, New York, 1997), pp. 19-24.
[8]   I. Gonsky, T.P. Maksymchuk and M.I. Kalinsky, *Біохімія Людини [Biochemistry of Man],* (Ukrmedknyga, Ternopil, 2002), p. 16. (in Ukrainian)
[9]   V.V. Mal'tsev, *Металлография промышленных цветных металлов и сплавов [Metallography of industrial nonferrous metals and alloys],* (Moscow, Metallurgiya, 1970), p. 364. (in Russian)
[10] M. Garkusha, *Основи Фізики Напівпровідників [Fundamentals of Semiconductor Physics]* (Vysshaja shkola, Moscow, 1982), http://gagago.ru/g20-osnovi-fiziki-napivprovidnikiv-pidruchnik-dlya-tehniku.html.

Book Chapters
[11] M. Gonzalez-Leal, P. Krecmer, J. Prokop and S.R. Elliot, in: *Photo-Induced Metastability in Amorphous Semiconductors*, edited by A.V. Kolobov (Wiley-VCH, Weinheim, 2003), pp. 338-340.
[12] A. Kochelap and S.I. Pekar, in: *Теория Спонтанной и Стимулированной Хемилюминесценции Газов [Theory of Spontaneous and Stimulated Gas Chemiluminescence]* (Naukova dumka, Kyiv, 1986), pp. 16-29. (in Russian)

Conference or symposium proceedings
[13] C. Yaakov and R.Huque, in: *Second International Telecommunications Energy Symposium Proceedings*, edited by E. Yow (IEEE, New York, 1996), pp. 17-27.
[14] V. Nikolsky, A.K. Sandler and M.S. Stetsenko, in: *Автоматика-2004: Матеріали 11 Міжнародної Конференції по Автоматичному Управлінню [Automation-2004: Materials of the 11th International Conference on Automated Management]* (NUHT, Kyiv, 2004), pp. 46-48. (in Ukrainian)

Patent
[15] I.M. Vikulin, V.I. Irha and M.I. Panfilov, Patent Ukraine No. 26020 (27 August 2007). (in Ukrainian)

Special Notes
1. Use International System of Units (SI system). 2. It is undesirable to use acronyms in the titles. Please define the acronym on its first use in the paper. 3. Refer to isotopes as ^{14}C, ^{3}H, ^{60}Co, etc.

Наукове видання

СХІДНО-ЄВРОПЕЙСЬКИЙ ФІЗИЧНИЙ ЖУРНАЛ
Номер 1, 2020

EAST EUROPEAN JOURNAL OF PHYSICS
No 1, 2020

Збірник наукових праць
англійською, українською, російською мовами